Online Chemical Characterization of Volatile Organic Compounds and Aerosol Particles at Urban and Rural Locations

Zur Erlangung des akademischen Grades einer

DOKTORIN DER NATURWISSENSCHAFTEN (Dr. rer. nat.)

von der KIT Fakultät für

Bauingenieur-, Geo- und Umweltwissenschaften

des Karlsruher Instituts für Technologie (KIT)

genehmigte DISSERTATION von

Junwei Song

aus

Anhui, China

Tag der mündlichen Prüfung: 11.07.2022

Referent: Prof. Stefan Norra

Korreferent: Prof. Thomas Leisner

Karlsruhe (2023)

Erklärung

Hiermit erkläre ich, dass ich die vorliegende Dissertation, abgesehen von der Benutzung der angegebenen Hilfsmittel, selbständig verfasst habe.

Alle Stellen, die gemäß Wortlaut oder Inhalt aus anderen Arbeiten entnommen sind, wurden durch Angabe der Quelle als Entlehnungen kenntlich gemacht.

Diese Dissertation liegt in gleicher oder ähnlicher Form keiner anderen Prüfungsbehörde vor.

Karlsruhe (2022)

Junwei Song

Acknowledgements

I want to thank the China Scholarship Council (CSC) for financial support to pursue my PhD study. Thanks to KIT Graduate School for Climate and Environment (GRACE) for offering various courses for developing personal skills and providing funds for attending academic conferences and summer school.

There is a long list of people who have contributed greatly to the completion of this dissertation. Specifically, I would like to thank go to my direct supervisor, Dr. Harald Saathoff, for his support and guidance through these last four years. You are always patient to help me get through different kinds of scientific problems. I appreciated all your contributions of time, ideas and funding to make my Ph.D. experience wonderful. Without your help, I would not have grown as much as I have over my time at IMK-AAF. Grateful thanks to my official supervisors, Prof. Stefan Norra and Prof. Thomas Leisner for their valuable advice on my PhD study and scientific career.

Thanks to my colleagues at IMK-AAF for daily accompany, sharing work and lives, exchanging ideas and giving help. I really enjoy the warm working atmosphere with all of you. Thank you, Linyu Gao, Feng Jiang, Hengheng Zhang, Harald Saathoff, Tobias Schorr, Franziska Vogel, Nsikanabasi Silas Umo, Marco Zanatta, Frank Schwarz, Georg Scheurig, Buschbacher, Jens Nadolny, Stefen Vogt, Tomasz Chudy, Olga Dombrowski, and Susanne Bolz. Special thanks to formed AAF colleagues, Xiaoli Shen and Wei Huang for teaching me how to use the mass spectrometers, prepare the chamber and field campaigns and analyze the data at the first year of my PhD study. Thanks to some other former colleagues, Barbara Bertozzi, Magdalena Vallon and Yvette Gramlich for giving me many advice to adjust the new life in Germany.

Thanks to the colleagues at KIT-AGW, Reiner Gebhardt, Stefan Norra and Jonas Bauer for their technical support in the field campaigns at Durlacher Tor. I gratefully acknowledge the help of Dr. Ralf Tillmann for offering remote help in the field campaign when our instruments had technical issues at Eifel forest site. Thanks to Dr. Georgios I. Gkatzelis for sharing the results of data analysis from the Eifel forest campaign.

Finally, big thanks to my family members, especially my parents, older sister and brother-in-law for their unconditional love and encouragement. Last but not least, thanks to my girlfriend, Linyu for her love, accompany and encourage. Without their support, none of this thesis would been started and finished.

Abstract

Volatile organic compounds (VOCs) are key precursors for the formation of organic aerosol particles (OA), and have a strong impact on air quality and climate change. Over the last decades, the air quality in western Europe has been improving by reducing anthropogenic emissions. However, pollution episodes with high OA concentrations still occur frequently. To assess the role of OA in these pollution episodes, I want to determine the sources and evolution processes of VOCs and OA particles in urban and rural locations in Germany by the state-of-the-art mass spectrometers including a proton-transfer-reaction mass spectrometer (PTR-MS) and an aerosol mass spectrometer (AMS).

As a prerequisite for my work, I characterized the performance of a new PTR-MS coupled with a new particle inlet (CHARON) and a fast gas chromatograph (FastGC) in simulation chamber and field experiments. The OA determined by the CHARON correlated linearly ($R > 0.9$) with that measured by the AMS, and the CHARON total OA mass to AMS can reach up to ~60% in field campaigns. The oxygen to carbon (O:C) ratios of OA compounds detectable by CHARON-PTR-MS are in the range of 0.25-0.50, close to that for semi-volatile organic aerosol derived from the AMS. The CHARON can detect less-oxygenated organic molecules typically with up to 1-5 oxygen atoms per molecule. Good agreements were also found for calibrated VOC species measured by CHARON-PTR-MS and a Vocus-PTR-MS. A FastGC was calibrated and applied for a fast separation of monoterpene isomers from forest emissions.

During two field campaigns at an urban kerbside of downtown Karlsruhe in southwest Germany in summer 2019 and winter 2020, I identified that $PM_{2.5}$ mostly consists of OA particles with an average contribution of 60 ± 9% in summer and 44 ± 18% in winter. Source apportionment of OA by positive matrix factorization (PMF) revealed that OA was dominated by secondary organic aerosol (SOA) with 82 ± 8% in summer and 48 ± 7% in winter, while only few contributions of primary traffic emissions (6 ± 5 to 11 ± 9%) were found for both seasons. During a summertime heatwave episode, high contributions of SOA to $PM_{2.5}$ mass were identified, mainly formed from the oxidation of biogenic VOCs. Wintertime pollution was caused by various sources including local industrial emissions, long-range transport of Saharan dust, and regional anthropogenic emissions.

By PMF analyses I discovered the sources of OA particles and VOCs at a rural site in the north of Karlsruhe in summer 2021. Both PMF results revealed the important role of OA and VOC factors related to secondary oxidation processes, which showed high contributions of 80 ± 10% to total OA and 56 ± 12% to total VOC concentrations. Furthermore, I characterized two heatwave episodes with nighttime OA mass increases and particle growth (rates: 3.5-4.0 nm h^{-1}). The efficient particle growth was correlated with stagnant conditions with relatively lower temperatures and high relative humidity (RH), and can be attributed to gas-to-particle partitioning of semi-volatile oxygenated organic aerosol (SV-OOA,78%-93%) formed from oxidation of monoterpenes.

During a summer field campaign in a stressed pine forest in the Eifel in western Germany, I identified that a nearby biogas power plant was an important source for methane, monoterpenes (max. 53.5 ppb) and aromatic compounds. The diurnal variations of isoprene showed higher concentrations during daytime due to higher emissions. However, monoterpenes and sesquiterpenes showed an opposite diurnal variation with lower concentrations during daytime, which was due to their rapid photochemical consumption. During a heatwave episode, the diurnal variations of less-oxygenated and semi-volatile monoterpene-derived organic products ($C_{10}H_{16}O_{1-3}$) showed significant increases at nighttimes. However, more-oxygenated organic products ($C_{10}H_{16}O_{4-5}$) with low volatility increased during daytime, indicating strong photochemical oxidation of monoterpenes. In contrast, lower temperature and higher RH at nights favor the partitioning of semi-volatile organic components; e.g., fractionation of $C_{10}H_{16}O_{1-3}$ to particle phase increases with 0.005-0.006 per % increase in RH. These results provide insights into the evolution of BVOCs and their atmospheric oxidation processes and demonstrate the capability of state-of-the-art PTR-MS instruments for such studies.

This dissertation improves our knowledge of composition, sources and evolution of atmospheric organic compounds in urban and rural locations in Germany. This work also provides insights into complex interaction of biogenic and anthropogenic emissions in the real atmosphere in response to more frequent extremely weather (e.g., heatwave) in western Europe.

Zusammenfassung

Flüchtige organische Verbindungen (VOCs) sind wichtige Vorläufer für die Bildung von organischen Aerosolpartikeln (OA), und beide haben einen starken Einfluss auf die Luftqualität und den Klimawandel. In den letzten Jahrzehnten wurde die Luftqualität in Westeuropa durch die Reduzierung anthropogener Emissionen verbessert. Allerdings kam es häufig zu Belastungsepisoden mit hohen OA-Konzentrationen. Um die Rolle von OA in diesen Verschmutzungsepisoden zu bewerten, wollte ich die Quellen und Evolutionsprozesse von VOCs und OA-Partikeln in städtischen und ländlichen Gebieten in Deutschland mit modernsten Massenspektrometern einschließlich einer Protonentransferreaktion bestimmen-Massenspektrometer (PTR-MS) und ein Aerosol-Massenspektrometer (AMS).

Als Voraussetzung für meine Arbeit charakterisierte ich die Leistungsfähigkeit eines neuen PTR-MS gekoppelt mit einem neuen Partikeleinlass (CHARON) und einem schnellen Gaschromatographen (FastGC) in Simulationskammer- und Feldexperimenten. Folglich korreliert die vom CHARON ermittelte OA linear (R >0,9) mit der vom AMS gemessenen, und die CHARON-Gesamt-OA-Masse zu AMS kann in der Feldkampagne bis zu ~60 % erreichen. Die Verhältnisse von Sauerstoff zu Kohlenstoff (O:C) der mit CHARON gemessenen OA lagen im Bereich von 0,25–0,50, nahe dem für halbflüchtiges organisches Aerosol, das aus dem AMS stammt. Der CHARON kann weniger sauerstoffhaltige organische Moleküle typischerweise mit der Anzahl der Sauerstoffatome von 1-5 erkennen. Gute Übereinstimmungen wurden auch für kalibrierte VOC-Spezies gefunden, die mit CHARON-PTR-MS und einem Vocus-PTR-MS gemessen wurden. Die FastGC wurde für die Umgebungsluft angewendet und charakterisiert erfolgreich die Monoterpen-Isomere aus den Kiefernemissionen.

Während zweier Feldkampagnen an einem städtischen Bordstein in der Innenstadt von Karlsruhe im Südwesten Deutschlands im Sommer 2019 und im Winter 2020 habe ich festgestellt, dass $PM_{2,5}$ hauptsächlich aus OA-Partikeln besteht, mit einem durchschnittlichen Beitrag von 60 ± 9 % im Sommer und 44 ± 18 % im Winter. Ich habe die Analyse der positiven Matrixfaktorisierung (PMF) für die Quellenzuordnung von OA verwendet. OA wurde von sekundären organischen Aerosolen (SOA) mit 82 ± 8% im Sommer und 48 ± 7% im Winter dominiert, während in beiden Jahreszeiten nur wenige Beiträge der primären Verkehrsemissionen (6 ± 5 – 11 ± 9%) gefunden wurden. Ich charakterisierte eine sommerliche Hitzewelle, die hohe Beiträge von SOA zur $PM_{2,5}$-Masse zeigte,

die hauptsächlich aus der Oxidation von biogenen VOCs entstanden. Ich habe auch eine Winterverschmutzung charakterisiert, die durch verschiedene Quellen verursacht wurde, darunter lokale Industrieemissionen und Ferntransport von Saharastaub und anthropogenen Emissionen in Westeuropa.

Während einer Feldkampagne auf einem ländlichen Standort im Norden von Karlsruhe im Sommer 2021 habe ich PMF-Analysen verwendet, um die Quellen von OA-Partikeln und VOCs einzeln zu untersuchen. Beide PMF-Ergebnisse zeigten die wichtige Rolle von OA- und VOC-Faktoren im Zusammenhang mit sekundären Oxidationsprozessen, die hohe Beiträge von 80 ± 10 % zur Gesamt-OA- und 56 ± 12 % zur Gesamt-VOC-Konzentration zeigten. Darüber hinaus charakterisierte ich zwei Hitzewellenepisoden mit durchschnittlicher nächtlicher OA-Massenzunahme und Partikelwachstumsrate (3,5-4,0 nm h^{-1}). Die Massenzunahme von OA und Partikeln erfolgte bei stagnierenden Bedingungen mit niedrigen Temperaturen und hoher relativer Luftfeuchtigkeit (RH), die hauptsächlich auf die Gas-zu-Partikel-Partitionierung von halbflüchtigem, sauerstoffhaltigem, organischem Aerosol (SV-OOA,78%-93%) aus der Monoterpen-Oxidation gebildet.

Bei einer Feldkampagne in einem gestressten Kiefernwald in der Eifel in Westdeutschland stellte ich fest, dass das nahe gelegene Biogaskraftwerk eine wichtige Quelle für Monoterpene (max. 53,5 ppb) war. Die tageszeitlichen Schwankungen von Isopren zeigten tagsüber höhere Konzentrationen aufgrund hoher Emissionen. Monoterpene und Sesquiterpene zeigten jedoch eine entgegengesetzte tageszeitliche Variation mit geringeren Konzentrationen während des Tages, was auf ihren schnellen photochemischen Verbrauch über die Emissionen zurückzuführen war. Ich habe eine Episode charakterisiert, die die Hitzewelle mit den vollständigen Datensätzen von CHARON-PTR-MS und Vocus-PTR-MS abdeckt. Während dieser Episode zeigten die täglichen Schwankungen von weniger sauerstoffreichen und halbflüchtigen, von Monoterpenen abgeleiteten organischen Produkten ($C_{10}H_{16}O_{1-3}$) die Zunahmen in den Nächten. Allerdings nahmen mehr sauerstoffhaltige organische Produkte ($C_{10}H_{16}O_{4-5}$) mit geringer Flüchtigkeit tagsüber zu, was auf eine starke photochemische Oxidation von Monoterpenen während des Tages hinweist. Im Gegensatz dazu begünstigen niedrigere Temperaturen und höhere relative Luftfeuchtigkeit in den Nächten die Verteilung halbflüchtiger organischer Komponenten. Ich habe die relativ erhöhten Fraktionen von $C_{10}H_{16}O_{1-3}$ in der Partikelphase auf 0,005–0,006 durch die RH-Erhöhung von 1 % berechnet. Diese Ergebnisse geben Einblicke in die Entwicklung von BVOCs und ihre atmosphärischen

Oxidationsprozesse und demonstrieren die Leistungsfähigkeit modernster PTR-MS-Instrumente für solche Studien.

Diese Dissertation erweitert unser Wissen über Zusammensetzungen, Quellen und Entwicklungen atmosphärischer organischer Verbindungen in städtischen und ländlichen Gebieten in Deutschland. Diese Arbeit liefert auch Einblicke in das komplexe Zusammenspiel von biogenen und anthropogenen Emissionen in der realen Atmosphäre als Reaktion auf häufigere Extremwetter (z. B. Hitzewelle) in Westeuropa.

Contents

List of Figures

Abbreviations

AAE	Absorption Ångström exponent
ACSM	Aerosol Chemical Speciation Monitor
AIDA	Aerosol Interaction and Dynamics in the Atmosphere
AMS	Aerosol Mass Spectrometer
AVOC	Anthropogenic volatile organic compounds
BBOA	Biomass burning organic aerosol
BC	Black carbon
BLH	Boundary layer height
BVOC	Biogenic volatile organic compounds
CH_4	Methane
CHARON	CHemical anlysis of Aerosol ONline inlet
CIMS	Chemical ionization mass spectrometer
CO	Carbon monoxide
CO_2	Carbon dioxide
COA	Cooking-related organic aerosol
DMA	Differential mobility analyzer
d_m	Mobility diameter
d_{va}	Aerodynamic diameter
EI	Electron Ionization
FastGC	Fast Gas Chromarography
FIGAERO	Filter Inlet for Gases and AEROsols
FT-ICR-MS	Fourier transform ion cyclotron resonance mass spectrometry
GC-/LC-MS	Gas/Liquid Chromarography-Mass Spectrometer
GLV	Green leaf volatiles
H:C	Hydrogen-to-carbon ratio
H_3O^+	Hydronium ion
HO_2	Hydroperoxyl radicals
HOA	Hydrocarbon-like organic aerosol
HR-TOF-AMS	High-resolution Time-of-Flight Aerosol Mass spectromter
HYSPLIT	Hybrid Single-Particle Lagrangian Integrated Trajectory

I^-	Iodide ion
IDA	IONICON Data Analyzer
KITcn	Karlsruhe Institute of Technology Campus north
LCU	Liquid Calibration Unit
LO-OOA	Less oxygenated organic aerosol
LV-OOA	Low-volatility oxygenated organic aerosol
m/z	Mass-to-charge ratio
ME-2	Multilinear Engine algorithm
MO-OOA	More oxygenated organic aerosol
MOSES	Modular Observation Solutions for Earth Systems
MS	Mass Spectrometry
NH_3	Ammonia
NH_4	Ammonium
NO	Nitric oxide
NO_2	Nitrogen dioxide
NO_3	Nitrate
NO_3·	Nitrate radicals
NR-PM_1	Non-refractory PM_1
NR-$PM_{2.5}$	Non-refractory $PM_{2.5}$
O:C	Oxygen-to-carbon ratio
O_3	Ozone
O_x	Odd oxygen
OA	Organic Aerosols
OH·	Hydroxyl radicals
PBL	Planetary Boundary Layer
PMF	Positive Matrix Factorization
POA	Primary Organic Aerosol
p$OrgNO_3$	Particle organic nitrate
PTOF	Particle Time-of-Flight
PTR-ToF-MS	Proton-transfer-reaction Time of Flight Mass Spectrometer
RH	Relative humidity

RO_2	Organic peroxy radicals
SO_2	Sulfur dioxide
SO_4	Sulfate
SOA	Secondary organic aerosol
SV-OOA	Semi-volatile oxygenated organic aerosol
VOC	Volatile Organic Compounds
WD	Wind direction
WS	Wind speed

1. Introduction

The Earth's atmosphere contains thousands of organic compounds, both in the gas and particulate phases. Volatile organic compounds (VOCs) are significant gas precursors responsible for the formation of tropospheric ozone (O_3) and secondary organic aerosol (SOA) (Hallquist et al., 2009; McFiggans et al., 2019; Stevenson et al., 2013). They play important roles in the troposphere, influencing local and regional air quality, human health and climate change both directly and indirectly (IPCC, 2021; Seinfeld and Pandis, 2016a). VOCs have many emission sources of both anthropogenic and biogenic origins. After VOCs are emitted into the atmosphere, they can react with various atmospheric oxidants including hydroxyl radicals (OH·), ozone and nitrate radicals (NO_3·) to produce SOA. As shown in Figure 1 (Shrivastava et al., 2017), the interaction between anthropogenic and biogenic emissions has a direct influence on the formation and aging of SOA. Furthermore, the physicochemical properties of SOA including phase state and volatility are associated with the conditions with ambient temperature and relative humidity. Determining the sources and evolution processes of organic compounds and demonstrating their roles in new particle formation, growth and evaporation are needed to estimate their environmental impacts on air quality and climate.

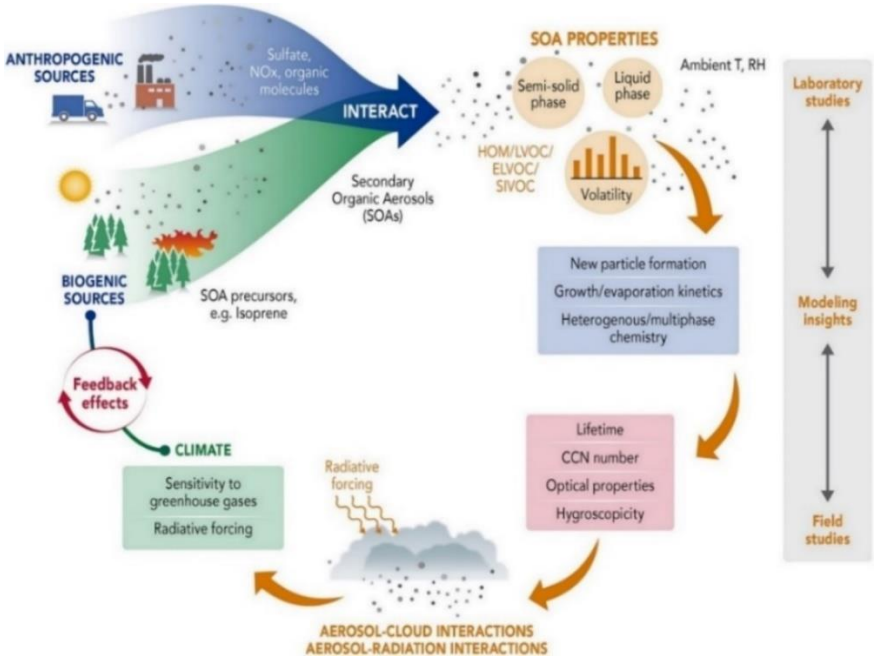

Figure 1. Interactions between anthropogenic and biogenic emissions for SOA formation. Fundamental SOA properties including phase and volatility affect new particle formation, growth/evaporation, and multiphase reactive kinetics of these particles (Shrivastava et al., 2017).

1.1 Volatile organic compounds (VOC)

With respect to their emission sources, VOCs can be grouped into biogenic and anthropogenic VOCs. On a global scale, the biogenic VOC (BVOC) emissions are one order of magnitude higher than the anthropogenic ones (AVOC), accounting for 75-90% of the total emissions of VOCs (Guenther et al., 2012). However, some anthropogenic VOC species like benzene and toluene have adverse impacts on air quality and human health especially in urban environments (Nurmatov et al., 2013; Volkamer et al., 2006). Despite some VOCs might have lower emissions, they have large contributions to SOA due to their high reactivity and SOA formation potential (Shrivastava et al., 2017). Therefore, the emissions and SOA formation potential are the most important factors for assessing the role of VOCs in SOA production.

1.1.1 Biogenic VOCs

The global BVOC emissions are dominated by isoprene (C_5H_8, 465 Tg C yr^{-1}) (Guenther et al., 2012), which can be emitted from many tree species such as deciduous trees. It is well known that isoprene emission from the trees is dependent on both light and temperature (Guenther et al., 1993; Kuhn et al., 2002). Previous studies have reported that little isoprene emissions were observed during nighttime, while high emissions and concentrations of isoprene were found for high temperatures and intensive sunlight during daytime (Hellén et al., 2018; Kuhn et al., 2002). This diurnal behavior of isoprene emissions is more pronounced in summertime (Hakola et al., 2012; Yáñez-Serrano et al., 2015). The yield of SOA from isoprene can vary between 1% to 30% relative to the total amount of isoprene oxidized by $OH\cdot$, O_3 and $NO_3\cdot$ radicals (Surratt et al., 2010). Even with a yield as low as 1%, isoprene is estimated to contribute substantially to the global SOA budget due to its large emissions (Guenther et al., 2012; Stadtler et al., 2018).

Monoterpenes ($C_{10}H_{16}$) are a class of terpenes that consist of two isoprene units (Figure 2), and include many isomeric species such as α/β-pinene, limonene, Δ^3-carene, camphene, myrcene and sabinene. Total annual monoterpene emissions are estimated to be ~160 Tg C yr^{-1}, of which α-pinene is the largest contributor (~50 Tg C yr^{-1}) (Guenther et al., 2012). Similar to isoprene, many tree species including Scot pine, Norway spruce, birch and oak trees can emit large amounts of monoterpenes. However, the light- and temperature-dependence of monoterpene emissions are closely associated with the tree species. For example, the emissions of monoterpenes are dependent on both light and temperature above Amazonian rainforest with mainly deciduous tree species

(Jardine et al., 2015a; Kuhn et al., 2002; Yáñez-Serrano et al., 2018). However, the monoterpene emissions are mainly controlled by the temperature rather than light in boreal forests mainly with conifer trees (Hellén et al., 2018; Kontkanen et al., 2016; Taipale et al., 2011). Furthermore, the composition in emissions of monoterpene isomers varies from the tree species. Generally, α/β-pinene are two of the most abundant monoterpenes, emitting from the trees in the Amazonian rainforest (Yáñez-Serrano et al., 2018). However, other monoterpenes such as Δ^3-carene are also important in boreal forest (Hellén et al., 2018) and Δ^3-carene emits similar amounts as α-pinene for Scot pine trees (Bäck et al., 2012). Monoterpenes have high reactivities towards various atmospheric oxidants. They can undergo several oxidation steps to produce low-volatility organic compounds that eventually leads to the formation of SOA and particle growth (Ehn et al., 2014; Mohr et al., 2017; Mohr et al., 2019; Zhang et al., 2015). Over the last decades, the yield, kinetics, chemical composition of SOA from the oxidation of various monoterpenes by OH radicals, O_3 and NO_3· radicals were studied extensively not only in field observations but also in the simulation chambers based on substantial progress in technical tools (e.g., simulation chambers and mass spectrometry) (Docherty et al., 2005; Ehn et al., 2014; Huang et al., 2018b; Saathoff et al., 2009; Yu et al., 1999a; Yu et al., 1999b; Zhang et al., 2015). The formation mechanism of monoterpene-derived SOA at different conditions (e.g., NO_x, SO_2, humidity, temperature, seed aerosol) were extensively investigated in the simulation chamber studies (Huang et al., 2018b; Kristensen et al., 2014; Ng et al., 2017; Ng et al., 2007a; Saathoff et al., 2009). In field observation, Xu et al., (2015) have shown that monoterpene-derived SOA can be greatly mediated by anthropogenic NO_x emissions in southeastern United States. Zhang et al., (2018) have found that monoterpene-derived SOA can account for approximately half of total fine OA during summertime in the southeastern United States.

Sesquiterpenes, with the molecular formula of $C_{15}H_{24}$, are a class of terpenes that consists of three isoprene units (Figure 2), and has less global emissions (30 Tg yr^{-1}) than monoterpenes (Guenther et al., 2012). Compared to monoterpenes, the tree emissions of sesquiterpenes are less studied due to its very high reactivity and thus low ambient concentrations challenging the instrumentation (Fischer et al., 2021; Hellén et al., 2018; Kim et al., 2009). Sesquiterpenes consist of many isomeric species such as β-caryophellene, α/β-farnesene, α-humulene and longifonene and are dominated by β-caryophellene for conifer tree emissions. Previous measurements at boreal forests estimated that the sesquiterpenes contributed around 20% of that of monoterpene emissions (Hakola et al., 2006;

Rinne et al., 2007). Consistently, the concentrations of sesquiterpenes were much lower than monoterpenes from the measurements at boreal forests (Fischer et al., 2021; Hellén et al., 2018). However, the relative importance of sesquiterpenes emissions to monoterpene ones varied for different biospheres. For instance, Hellén et al., (2020) reported that the emissions of sesquiterpenes mainly β-caryophellene were higher than monoterpene emissions at a sub-Arctic wetland in a growing season in 2018. Regarding the studies available on sesquiterpenes (Hakola et al., 2006; Hellén et al., 2018), its emissions are mainly dependent on the temperature as monoterpenes. Even though sesquiterpenes are only a minor fraction of the total BVOCs, they are recognized to play an important role in the atmospheric chemistry due to their relatively high SOA yields and their high reactivity with atmospheric oxidants (Griffin et al., 1999; Hellén et al., 2018). Compared to monoterpenes, the contribution of sesquiterpene oxidation to SOA formation has been often overlooked due to challenges in measuring these highly reactive organic compounds in the ambient. Recently, Barreira et al., (2021) have reported that the oxidation of sesquiterpenes could have a more contribution to SOA formation compared to monoterpene-derived products in some periods of springtime at a hemi-boreal forest.

In addition to isoprene and terpenes, the plants can also emit significant amounts of oxygenated VOCs (OVOCs) such as green-leaf volatiles (GLVs, mainly C_5- and C_6- aldehydes, alcohols and esters) especially under the influence of stresses (e.g., human cuttings, drought and herbivore attack) (Holopainen and Gershenzon, 2010). Green leaf volatiles are produced from the biochemical conversion of fatty acids (e.g., linoleic and linolenic acids) within plant cells (Ameye et al., 2018). The major GLVs include 3-hexenal, 2-hexenal, 3-hexenol, 1-hexenol, hexanal and 3-hexenyl acetate. The global emissions of GLVs are relatively small (< 4.9 Tg yr^{-1} for 3-hexenal) based on the BVOC emission modelling studies (Guenther et al., 2012; Sindelarova et al., 2014). The emissions of GLVs can be increased significantly due to the influence of stress. For instance, the cutting activities of tree leaf and grass can lead to large emissions of GLVs along with terpeniods (Fall et al., 1999; Ruuskanen et al., 2011). Under the stress of drought and high temperature, a significant increase emissions and concentrations of GLVs were observed for boreal forest downy birches (Hellén et al., 2021) and in Amazonian rainforest (Jardine et al., 2015b). Plants can even emit more GLVs in order to response the stress of herbivore attack such as bark beetle (Scala et al., 2013). In addition to the increased GLV emissions, the bark beetle infestation can lead to increases in the emissions of terpenoids as well (Amin et al., 2012; Ghimire et al., 2016). In recent years, the

outbreaks of bark beetle become more widespread in European forests especially during spring to summer months (Hlásny et al., 2021), possibly leading to an increase of GLVs emissions in the future. GLVs can be oxidized by O_3 and OH· to form low volatility products that produce SOA with mass yields from 0.7 to 20% (Hamilton et al., 2009; Mentel et al., 2013). In addition, the aqueous production of SOA from GLVs can be attributed by excited triplet states and OH reactions, which form low volatility products at a rate that is approximately half that from the gas-phase reactions of GLVs (Richards-Henderson et al., 2015; Sarang et al., 2021).

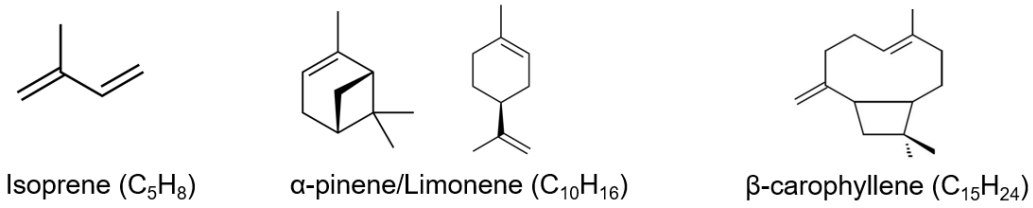

Figure 2. Structural formulae of isoprene, monoterpenes (α-pinene and limonene) and β-caryophellene.

1.1.2 Anthropogenic VOCs

The global emissions of AVOCs comprise of mainly single-ring aromatic hydrocarbons (Henze et al., 2008). Generally, single-ring aromatic hydrocarbons such as benzene, toluene, xylenes and trimethylbenzene are released from traffic, biomass burning and industrial solvent usage. The emissions of single-ring aromatic hydrocarbons depend on several factors such as source strength, the fuel type, and combustion efficiency. For example, the combustion of diesel and gasoline fuels produce totally different AVOC profiles (Lopes et al., 2014). Since these single-ring aromatic hydrocarbons are significantly contributed by the traffic, their diurnal variations often show the peaks in the morning and evening rush hours in urban areas or at highly traffic-influenced regions (Baudic et al., 2016; Gkatzelis et al., 2021; Wang et al., 2020; Yuan et al., 2012). These sing-ring aromatic hydrocarbons can react with OH radicals during daytime to form anthropogenic SOA. The yield of SOA from the oxidation of single-ring aromatic hydrocarbons are related to the NO_x level (Henze et al., 2008; Johnson et al., 2005; Ng et al., 2007b). Under high NO_x conditions, less SOA is formed from the oxidation of sing-ring aromatic hydrocarbons since RO_2 + NO reactions increased and other reaction pathways (RO_2+RO_2 and RO_2 + HO_2) are reduced.

Biomass burning including forest fire and residential wood combustion can make a significant contribution to VOCs in the atmosphere (Bruns et al., 2017; Languille et al., 2020). On a regional

scale, residential wood combustion can play an important role in the variations of VOCs (Languille et al., 2020). Based on laboratory burning experiments (Bruns et al., 2017; Coggon et al., 2016), wood combustion can release a lot of VOC species including hydrocarbons (e.g., alkanes, alkenes, aromatics), aldehydes, ketones, alcohols, acids, phenols, substituted phenols and furans, etc. It is always of significance to find the specific marker species for distinguishing the contribution of biomass burning. Acetonitrile has been widely used as a tracer for biomass burning (Huangfu et al., 2021; Warneke et al., 2006). Some laboratory burning experiments have found less acetonitrile emitted from residential wood combustion, but more released from the open fires (e.g., forest and agricultural fires) (Bruns et al., 2017; Coggon et al., 2016). In urban areas, acetonitrile could be contributed by other sources such as traffic (Huangfu et al., 2021) and solvent use (Languille et al., 2020), thus it is not a good tracer for residential wood combustion. Compared to acetonitrile, furfural can be regarded as a specific tracer for residential wood combustion based on laboratory burning studies. In addition, many biomass burning VOCs (e.g., phenols, substituted phenols and furans) with high reactivity and functionality have been found as important precursors for SOA formation (Bruns et al., 2016; Joo et al., 2019; Nakao et al., 2011).

1.2 Organic aerosol particles (OA)

Atmospheric aerosol particles such as $PM_{2.5}$ (particulate matter with diameter less than 2.5 μm) can adversely affect human health, and influence climate change by modifying atmospheric radiative fluxes and cloud formation processes (Burnett et al., 2014; IPCC, 2021; Seinfeld and Pandis, 2016b). Atmospheric organic aerosol particles (OA) represent a major contribution (20%-90%) to submicron particulate matter (PM_1) (Jimenez et al., 2009; Zhang et al., 2011). OA can be divided into primary organic aerosol (POA) and secondary organic aerosol (SOA). POA is the direct emissions such as traffic, biomass burning and cooking, while SOA is formed via oxidation of VOCs. Both BVOCs and AVOCs can be oxidized to produce low-volatility organic compounds, which can nucleate new particle clusters or condense on pre-existing particles resulting in the formation of SOA (Hallquist et al., 2009; Shrivastava et al., 2017). In addition, POA in the condensed phased can undergo chemical transformation and aging, contributing to the SOA mass. Many studies have reported that SOA represent a major fraction of the total OA mass burden (Crippa et al., 2014; Jimenez et al., 2009; Zhang et al., 2011). The full characterization on the chemical composition, sources and evolution processes of OA is crucial to elucidate the environmental effects it causes.

Source apportionment of OA in non-refractory fine aerosol particles (NR-PM_1 or NR-$PM_{2.5}$) have been studied extensively using Aerodyne aerosol mass spectrometers (AMS) or aerosol chemical speciation monitors (ACSM) data and employing positive matrix factorization (PMF) analysis (Canonaco et al., 2015; Crippa et al., 2014; Zhang et al., 2011). With the AMS-PMF method, OA are generally deconvolved into different factors including POA, i.e., fossil hydrocarbon-like OA (HOA) dominantly by traffic emissions, cooking OA (COA), biomass burning OA (BBOA) and SOA, i.e., semi-volatile oxygenated OA (SV-OOA) and low-volatility oxygenated OA (LV-OOA). Over the last two decades, many field studies with AMS measurements were conducted with the PMF method to investigate the sources of OA in PM_1 globally e.g., Europe (Crippa et al., 2013a), American (Zhang et al., 2011), Asian countries (Zhou et al., 2020). Crippa et al., (2013a) provided an overview on the source apportionment of OA from 25 AMS data sets across Europe using PMF. They reported that the contribution of direct traffic emissions to total OA mass varied between 3% to 24%. The influence of traffic emissions on OA were strongly depended on the sampling location with more contribution at urban sites. The contribution of biomass burning to total OA ranged between 5% to 27%, which was strongly dependent on the measurement seasons with more contribution in winter. The AMS-PMF method can also resolve different OOA factors according to their oxidation degree and volatility. Generally, SV-OOA showed a low oxygen-to-carbon ratio (O:C) and had a good correlation with semi-volatile species like nitrate. In contrast, LV-OOA had a higher O:C value, and showed a good correlation with low-volatility aerosol species like sulfate. Therefore, SV-OOA and LV-OOA can also be defined as less-oxygenated OA (LO-OOA) and more-oxygenated OA (MO-OOA) based on the oxygenation degree (Zhou et al., 2020). It should be noted that the AMS-PMF method has no ability to apportion SOA to specific sources. Many chamber and field experiments generate a database of mass spectra from different OA sources or organic compounds measured by the AMS. With these reference mass spectra, a constrained AMS-PMF via multilinear engine algorithm (ME-2) can be done for improving the separation of POA factors. For example, POA factors such as HOA, COA and BBOA can well resolved from constrained AMS-PMF method compared to unconstrained one (Canonaco et al., 2013; Zhu et al., 2018). Besides, Slowik et al., (2010) firstly performed a PMF analysis with a unified dataset of OA measured by AMS and VOCs measured by a proton-transfer reaction mass spectrometer (PTR-MS). This application of PMF analysis to a unified AMS/PTR-

MS dataset can increase details regarding the composition of SOA factors compared to the analysis from individual AMS OA dataset.

In addition to emissions sources, the variability of OA is also strongly driven by the meteorological conditions. The temperature and relative humidity play significant roles in the formation processes of SOA. For instance, high relative humidity may favor the aqueous phase formation of SOA. Increasing temperature may lead to the evaporation of semi-volatile OA (Sun et al., 2011). Higher temperatures are usually accompanied with intensive solar radiation, which favors photochemical production of SOA (Duan et al., 2020; Huang et al., 2020). Furthermore, high temperatures and strong solar radiation can also enhance the emissions of BVOCs leading to enhanced photochemical formation of SOA (Canonaco et al., 2015). Variations of OA are also closely linked to wind speeds and directions. In urban areas, the streets are flanked by buildings creating a canyon-like environment, which can modify the wind conditions (Baker et al., 2004; Ketzel et al., 2002; Kumar et al., 2008). The winds with high speeds along the canyon direction can efficiently remove air pollutants. The wind direction cross canyon plays a less important role in the dilution processes. Furthermore, low wind speeds within canyons can result in poor dispersion conditions, and thus the accumulation and mixing of primary pollutants and secondary pollutant formation in downtown areas. In rural areas with less anthropogenic source emissions, while pollution episodes could be caused by the formation of SOA locally and/or the long-range transport of OA. It is important to study the variations of OA in various ambient environments for different meteorological conditions, which would be useful to improve our understanding in the cause of air pollution and atmospheric chemical processes. In this dissertation, I conducted two field campaigns at an urban site focusing on the variations of OA sources in context of seasonality and meteorology. The major results are presented in section 3.2. In addition, I conducted three field campaigns in two different rural sites focusing on the sources and chemical processes of OA and VOCs. The major results are presented in sections 3.3 and 3.4.

1.3 Recent advances in VOCs and OA measurements

1.3.1 VOC measurement techniques

The most comprehensive VOC measurements often involve gas-chromatographic separation and detection using mass spectrometry (GC-MS). The GC has been widely used for the separation of many different compounds based on their retention times in the chromatographic columns (Noziere

et al., 2015). However, the VOC measurement with GC-MS has the drawbacks of time-intensive, leading to low time-resolution (> 1 h). Besides, it requires some pre-processing steps for the GC-MS analysis including preconcentration to achieve the lowest detection limit and removal of O_3 and water to avoid interferences.

Real-time chemical ionization mass spectrometry like PTR-MS and iodide-CIMS (I^--CIMS) can overcome these limitations of GC-MS, allowing a high time resolution and sensitive VOC measurement (Blake et al., 2009; Lee et al., 2014; Yuan et al., 2017). PTR-MS utilizing hydronium ion (H_3O^+) as a reagent ion can detect a wide spectrum of organic analytes from non-oxidized to medium less oxidized organic molecules. Although PTR-MS is a relatively soft ionization techniques, it still has some fragmentation for some VOC species especially for terpenoids and large molecular weight VOCs depending on the strength of collisional energy in the drift tube of PTR-MS (Yuan et al., 2017). Fragmentation of protonated molecules create unique product ion distributions that must be known in order to perform a reliable quantification of the target VOCs (Kari et al., 2018; Pang, 2015; Tani et al., 2003). Comparatively, I^--CIMS using iodide (I^-) as a reagent ion can well detect the oxygenated organic molecules but not the non-oxidized ones. Furthermore, I^--CIMS is a soft ionization technique with negligible fragmentation (Lee et al., 2014). Even though PTR-MS and I^--CIMS can detect many organic molecules, it is not possible to have authentic standards for all species to get a fully qualitative and quantitative analysis on organic molecules. Based on many laboratory calibrations, most organic molecules showed a similar reaction kinetic with the reagent ion H_3O^+. Therefore, PTR-MS can still quantify the signals of uncalibrated organic species with an accuracy of ±30 % via a simple reaction kinetics approach (Holzinger et al., 2019). In contrast, the sensitivity of I^--CIMS can vary by several orders of magnitude for different oxidized organic compounds (Bi et al., 2021a; Iyer et al., 2016; Lopez-Hilfiker et al., 2016). This may pose significant limitations in the quantitative measurement of organic compounds by I^--CIMS in ambient atmosphere especially when there are no authentic standards available for the targeted species. In this dissertation, I particularly focused on the quantification of terpenoids including isoprene, monoterpenes and sesquiterpenes by a new PTR-MS, which are useful to study the kinetics and chemical processes of BVOC oxidation and their contribution to SOA formation. The fragmentation of theses terpenoids are well characterized for a new PTR-MS, which are important for better interpreting the complex PTR-MS mass spectra.

Another issue is that both PTR-MS and I^--CIMS cannot separate the VOC isomers compared to conventional GC-MS. To combine the advantages of high time resolution from PTR-MS or I^--CIMS and separation capability of GC, a GC can be coupled to PTR-MS or I^--CIMS to allow the real-time isomer detection with time resolution of minutes to hours (Bi et al., 2021b; Bsaibes et al., 2020; Claflin et al., 2021; Materic et al., 2015). Materić et al., (2015) have coupled a FastGC module to the PTR-MS (FastGC-PTR-MS), which can separate the gas standard or tree samples containing different monoterpenes in the laboratory. Bsaibes et al., (2020) have used a FastGC-PTR-MS to separate the monoterpene isomers from the dynamic enclosure experiments in a mixed holm oak (Quercus ilex) forest. However, the FastGC-PTR-MS has relatively high detection limits (e.g., 0.8-1.2 ppb for monoterpenes) compared to the real-time VOC measurement by the PTR directly (Bsaibes et al., 2020; Materić et al., 2015). Recently, Claflin et al., (2021) have developed a GC with thermal desorption preconcentration unit coupled to Vocus-PTR, which can achieve average detection limits of 1.6 ppt across a range of monoterpenes and aromatics at a time resolution of hours. The FastGC-PTR-MS has been well characterized in laboratory or successfully applied for measuring the air with high concentrations of VOCs e.g., dynamic enclosure chamber (Bsaibes et al., 2020) and indoor air (Claflin et al., 2021). The application of the FastGC-PTR-MS for ambient environments has not been reported. Although the fast-GC-PTR-MS has high detection limits, its application for the intensive observation periods in high VOC concentrations would be still very helpful to provide complementary information of isomer detection. During my PhD study, I deployed the FastGC-PTR-MS in a field campaign in summer 2021 for the intensive observation periods with high VOC concentration during nighttime, which were discussed in Section 3.2. In this dissertation, I applied the FastGC-PTR-MS in the simulation chamber and field measurements, which allowed me to study the chemical processes of VOC isomers.

1.3.2 OA measurement techniques

Various offline and online techniques have been developed to characterize and quantify OA particles. Offline techniques are based on the filter collection and subsequent laboratory analysis including gas/liquid-chromatography MS (GC-/LC-MS) and fourier transform ion cyclotron resonance mass spectrometry (FT-ICR-MS) (Noziere et al., 2015; Smith et al., 2009), which usually provide detailed information of chemical composition such as molecular composition (GC-/LC-MS) and functional groups (e.g., FT-ICR-MS). Offline techniques generally have low time resolution with hours to weeks due to sample collection and laboratory analysis. Furthermore, these

techniques are time and labor-intensive and suffer from the organic compound loss or detection interferences during the periods of filter sample collection, storage and preprocessing steps.

There are also many online techniques used for detecting organic aerosol such as AMS, FIGAERO-I^--CIMS and CHARON-PTR-MS. AMS is the most widely used online aerosol measurement techniques utilizing electron ionization (EI) (Canagaratna et al., 2007; DeCarlo et al., 2006). It can provide size-resolved chemical composition of non-refractory aerosol particles (organics, sulfate, nitrate, ammonium and chloride) at a time-resolution of minutes. Even though AMS can quantify the mass concentration of bulk OA, it cannot provide the specific chemical composition and molecular information of OA due to the ionization at high electronic energy (70 eV) resulting in substantial fragmentation. Compared to the EI method, chemical ionization techniques like PTR-MS and CIMS with relatively low ionization energy (< 10 eV) can minimize the impact of fragmentation to achieve molecular information. With particle inlets coupled to CIMS and PTR-MS, they can also allow the online measurement of OA particles at a molecular level. The Filter Inlet for Gaes and AEROsols (FIGAERO) coupled to the I^--CIMS (FIGAERO-I^--CIMS) can significantly reduce the sample collection time to minutes with high sampling flowrates (~10 lpm), leading to a better time-resolution of OA particles compared to conventional filter-based offline techniques (Thornton et al., 2020). However, the subsequent thermal desorption of the samples is required more time, thus FIGAERO-I^--CIMS only provides semi-continuous measurement of OA (>30 min). FIGAERO-I^--CIMS can detect thousands of oxygenated organic molecules, while its quantification is often limited due to the lack of authentic standards and the large variabilities of sensitivity among different organic species (Lee et al., 2014). The CHemical Analysis of aeRosol ONline inlet (CHARON) coupled to the PTR-MS has been developed that provides online measurements of organic aerosol particles at a time resolution of 1 s (Eichler et al., 2015; Muller et al., 2017). With the ionization by H_3O^+, CHARON-PTR-MS can detect a series of organic molecules from non-oxidized to medium oxidized organic molecules and is well-suited for a quantitative bulk organic aerosol analysis (Leglise et al., 2019). Although the PTR-MS is a relatively soft ionization technique, significant fragmentation in the CHARON-PTR still occurs for oxygenated compounds such as *cis*-pinonic acid (Gkatzelis et al., 2018b). However, the fragmentation can be minimized by adjusting the electric field strength of the PTR drift tube (Gkatzelis et al., 2018b; Leglise et al., 2019). More recently, a correction algorithm has been derived from 26 oxidized organic compounds relevantly found in atmospheric organic aerosol,

which can improve the quantitative analysis of organic aerosol (Leglise et al., 2019). As introduced above, each instrument has its own advantages and disadvantages, the combined usage of different online techniques would improve the chemical characterization of OA. It should always keep in mind that characterizing their measurement capability are prerequisites for studying the atmospheric aerosol chemistry.

1.4 Research objectives

It is challenging to assess the environmental impacts of organic compounds due to the complexity of their chemical composition, sources, and transformation processes in the atmosphere. In this context, this dissertation aims to provide a substantial contribution to characterize the evolution of VOCs and OA particles in urban and rural atmospheres with the-state-of-art mass spectrometry. My major research questions are listed as follows:

(1) What is the performance of the new PTR-ToF-MS with a particle inlet (CHARON) in comparison with established mass spectrometers like the AMS, FIGAERO-I^--CIMS and Vocus-PTR-MS?
(2) Can simultaneous measurements of the compositions of VOC and or OA particles be used to learn about atmospheric conversion processes of VOCs to OA particles?
(3) What are the contributions of anthropogenic and biogenic sources on OA and VOC levels in urban and rural areas?
(4) What is the impact of meteorology (e.g., heat waves) on the variations of OA and VOC levels in urban and rural areas?
(5) What are the atmospheric chemical processes controlling the evolution of VOCs and OA particles under different meteorological conditions?

I present major results to answer these research questions in the following sections. In section 3.1, the measurement capability of a new PTR-MS coupled to a CHARON inlet and a FastGC on VOCs and OA were characterized in simulation chamber and field experiments in comparison to other online mass spectrometers. In section 3.2, the relative roles of anthropogenic and biogenic emissions to OA were investigated at an urban kerbsite of downtown Karlsruhe in summer and winter. Please note that I have published the results from my studies in downtown Karlsruhe already as first-author (Song et al., 2022). In section 3.3, the sources and nighttime chemical processing of VOCs and OA were investigated at a rural site 10 km north of downtown Karlsruhe. In section 3.4,

the variations of VOCs and their contributions to SOA formation were investigated in a stressed pine tree forest.

2. Methodology

2.1 Instrumentation and software

To achieve the research objectives and answer the open questions, I conducted several simulation chamber and field experiments. I mainly used two mass spectrometers including an aerosol mass spectrometer (AMS) and a proton-transfer-reaction mass spectrometer (PTR-MS) to measure the chemical composition of aerosol particles and VOCs. In addition, I also used several auxiliary instruments with some technical support from my colleagues. I will introduce these instruments in the following.

2.1.1 Aerosol mass spectrometer (AMS)

The AMS (Aerodyne) is a powerful instrument for online measurement of the size-resolved chemical composition of non-refractory aerosol particles including total organic mass (OA) and inorganic species sulfate (SO_4) and nitrate (NO_3) and ammonium (NH_4). A schematic of the AMS is showed in Figure 3 and the details of AMS operation is provided elsewhere (Canagaratna et al., 2007; DeCarlo et al., 2006). The instrument consists of several parts: sample system, sizing region, vaporization and ionization systems. Briefly, the ambient air is sampled directly via an aerodynamic lens which focuses aerosol particles with size ranging from 0.07 to 2.5 μm. At the exit of the lens, a supersonic expansion accelerates the particles into the sizing region (particle time-of-flight, PToF), where particle size is determined by the corresponding particle flight time. Subsequently, the particles are heated by a vaporizer at 600 °C, and the resulting vapors are ionized by electron impact (70 eV) and characterized by a time-of-flight mass spectrometer. The AMS can be operated alternatingly in V mode for determining the particle mass concentration and size distribution, and in W mode for measuring the highest resolution mass spectra ($m/\Delta m$ >5000). In this study, the AMS was usually operated in V mode in chamber experiments, while was operated alternatingly with 1 min in V mode and 1 min in W mode for the field measurements. In both chamber and field experiments, essentially V mode data were finally reported and W mode data were only used for the peak fitting. It is important to note that, particles can bounce off the vaporizer, which could lead to the underestimation of aerosol mass concentrations (Middlebrook et al., 2012). Therefore, a collection efficiency (CE) of the AMS is needed to be calculated for correction. In this dissertation, CE values (~0.4-0.7) were determined based on a comparison with the reference scanning mobility particle sizer (SMPS) in the chamber experiments, while a particle composition

dependent CE value (CDCE, ~0.5) was used to correct the AMS data in field measurements. At the beginning and end of each campaign, the ionization efficiency of the AMS was calibrated using ~300 nm ammonium nitrate (NH_4NO_3) or ammonium sulfate ($(NH_4)_2SO_4$) aerosol particles. Operation and calibration of the AMS in the chamber and field experiments were performed by me and Linyu Gao.

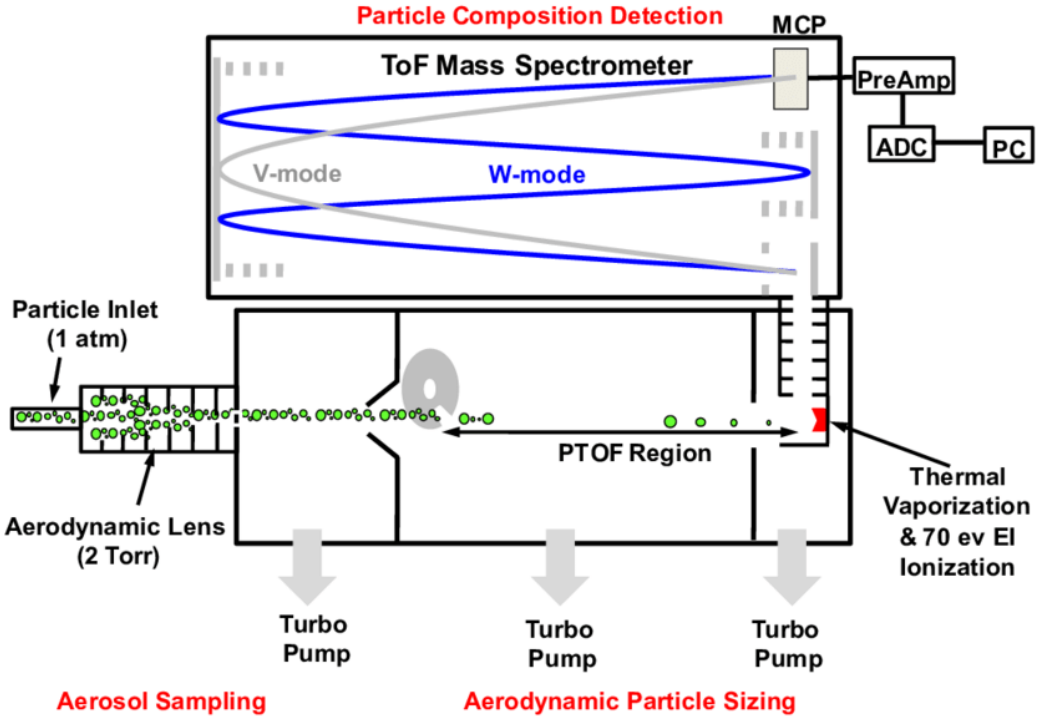

Figure 3. A schematic of the HR-ToF-AMS (Canagaratna et al., 2007)

2.1.2 Proton-transfer-reaction mass spectrometer (PTR-MS)

The PTR-ToF-MS is a powerful instrument for real-time measurements of many VOCs e.g., aromatics, terpenes, alcohols and carbonyls and with a detection limit as low as several pptv. A schematic of this instrument is shown in Figure 4a. Furthermore, the PTR-MS was also used for distinguishing the isomers of VOCs by application of a fast gas chromatography (FastGC) module and for measuring the chemical composition of volatile aerosol particle components with a CHARON inlet. In this dissertation, I used a new conventional PTR-ToF-MS (Model 4000, Ionicon Analytik) coupled with a CHARON inlet before May 2020. After that the PTR-ToF-MS achieved an upgrade to improve the sensitivity by a factor of ~10 via installing an ion funnel. On October 2020, another upgrade of the PTR-ToF-MS was made with the addition of a FastGC. Since then,

the PTR-TOF-MS coupled with the CHARON inlet and a FastGC allow me to measure VOCs and their isomers and volatile aerosol components in intermittent measurements with one instrument.

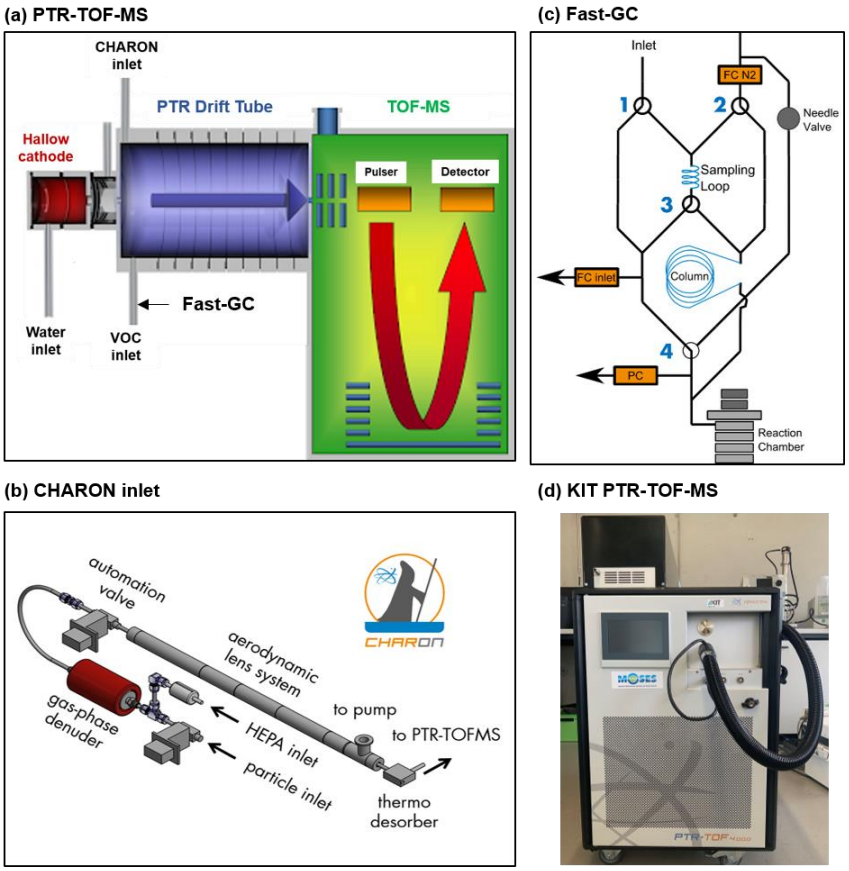

Figure 4 Schematic of the (a) PTR-ToF-MS, (b) CHARON inlet (adapted from Ionicon Analytik, GmbH https://www.ionicon.com/technologies/details/charon, last access: 01.04.2022) , (c) a Fast-GC (Romano et al., 2014) and (d) a photo of the PTR-ToF-MS at KIT (Photo: J. Song, 02.2020).

Generally, a PTR-TOF-MS consists of three major parts including an ion source, a drift tube and a time-of-flight mass spectrometer (Jordan et al., 2009; Yuan et al., 2017). The regent ions mainly consisting of hydronium ions (H_3O^+) produced from water vapor inside a hollow cathode discharge. Then H_3O^+ ions are introduced into a drift tube, where they are reacting with the gas sample. The VOCs with higher proton affinity than water (691 kJ mol^{-1}) can be charged via proton transfer reaction from the H_3O^+ ions ($VOC + H_3O^+ \rightarrow VOC{\cdot}H^+ + H_2O$). Subsequently, the protonated ions ($VOC{\cdot}H^+$) are detected by a time-of-flight mass spectrometer. The concentration of VOCs can be calculated using Eq (1)

$$[VOC \cdot H^+] = [H_3O^+]_0 \cdot (1 - e^{-k[VOC]t}) \approx [H_3O^+]_0 \cdot [VOC] \cdot k \cdot t \quad (1)$$

where $[VOC{\cdot}H^+]$ is the measured concentration of protonated product ions, $[H_3O^+]_0$ is the concentration of reagent ion which are typically in large excess, k is the reaction rate constant for the proton-transfer reaction, $[VOC]$ is the concentration of VOC species and t is the reaction time. Since the H_3O^+ ions are in excess of the sample molecules in the drift tube, so Eq (1) can be approximated given on its right side. Following Eq (1), the quantification of VOCs is mainly related to the amount of H_3O^+ and the reaction rate constant. The values of k were determined experimentally for many compounds based on previous studies (Cappellin et al., 2012; Sekimoto et al., 2017). Based on the known rate constants, other VOC species can be estimated with an uncertainty of ~50% (Cappellin et al., 2012). A default k value of 2×10^{-9} cm^3 s^{-1} is assumed as the default rate constant for uncalibrated VOC species. In addition, the response of the PTR-MS to different VOCs depends on the transmission efficiency relative to H_3O^+ from the drift tube to the detector of the MS. This transmission curve typically can be obtained from a calibration with many VOCs over a wide mass range. Although the proton transfer reaction with H_3O^+ ions is a relatively soft ionization process, some protonated ions still undergo fragmentation, which increase the complexity of PTR mass spectra interpretation. Generally, setting low electric fields in the drift tube can efficiently reduce the fragmentation. However, this will increase the formation of water cluster ions, which can react with some VOCs as well. Therefore, a compromise between reduced fragmentation and the suppression of water cluster ion formation required for setting the electric field in the drift tube (Yuan et al., 2017). It should be noted that these sources for quantification errors can be minimized by calibration with corresponding VOC species, e.g., from reference gas mixtures.

Conventional PTR-TOF-MS like our instrument has typically sensitivities ranging from tens to hundreds of counts per second per ppbv (cps/ppbv) for the majority of VOCs in the ambient air (Yuan et al., 2017). However, these sensitivities still limit the research focusing on the highly reactive VOC species or intermediate oxygenated organic compounds, which are often showing very low concentrations (ppt) in the atmosphere. To improve the instrument sensitivity (Barber et al., 2012), only recently ion funnels can be installed between the drift tube and the detector, which minimize the transmission loss of ions. After that our instrument has the sensitivity to thousands of cps/ppb. Before the upgrade of ion funnel, the time resolution of PTR-MS for real-time VOC measurement was set to 1s and the drift tube was set with a temperature of 120 °C and a pressure of ~2.8 mbar, resulting a reduced electric field (E/N) value of 127 Td. The CHARON vaporizer

was set with a temperature of 150 °C, and the PTR drift tube was automatically optimized to 100 Td at CHARON measurement mode. After the upgrade, the time resolution of PTR-MS for real-time VOC measurement was kept at 1 or 10 s and the drift tube was set with temperature varying from 80-120 °C in different chamber and field campaigns. The drift tube showed a reduced electric field from ~87-92 Td based on the temperature setting. The CHARON was then optimized with the drift tube of 57-60 Td after the upgrade. In this dissertation, the PTR-MS was calibrated with a series of VOCs at the beginning and end of each field and chamber campaign. Before June 2020, the PTR-MS was calibrated with one gas canister (Ionicon Analytik GmbH) containing methanol, acetonitrile, acetone, isoprene, benzene, toluene, *m,o,p*-xylenes, trimethylbenzene, 1,2-dichlorobenzene and 1,2,4-trichlorobenzene at a mixing ratio of ~100 ppb for each species with an accuracy of 10%. After that, it was calibrated with a gas cylinder (Ionicon Analytik GmbH) including methanol, acetone, isoprene, benzene, toluene, xylenes, 1,3,5-trimethylbenzene, α-pinene and limonene at a mixing ratio of ~100 ppb for each species with an accuracy of 10%. I also used two calibrated mass flow controllers (Bronkhorst, Netherlands) with the maximum flowrate of 10 lpm and 0.1 lpm (accuracy ~5%) respectively to dilute the gas standard to achieve the target concentration range (0.01-50 ppb). Therefore, I can calibrate the PTR-MS with a series of diluted gas standard as well. I compared the sensitivities for the reference compounds before and after the installation of the ion funnel as shown Figure 5. It can be clearly seen that about one order of magnitude increase in sensitivity was found for most calibrated VOCs after the installation of the ion funnel. Besides, additional calibrations were done for some single VOC by generating dedicated mixing ratios in a 6 L glass bulb measuring their vapor pressures with high precision pressure sensors (MKS Baratron). The VOCs for single calibration include isoprene (≥ 99%, Sigma Aldrich), α-pinene (98%, Sigma Aldrich), β-pinene (≥ 99%, Sigma Aldrich), Δ^3-carene (≥ 98%, Sigma Aldrich), β-cymene (99%, Sigma Aldrich), acetaldehyde (99.5%, Acros Organics), 2,3-pentanodinoe (97%, Sigma Aldrich) and 3-pentanone (99%, Sigma Aldrich). Calibration for VOCs of low volatility like β-caryophyllene (≥ 98%, Roth GmbH, Karlsruhe) was done with a liquid calibration unit (LCU, Ionicon Analytik GmbH) as shown in Figure 6. In the LCU, a defined volume of a solution of the low volatile compound is quantitatively evaporated into a heated tube and diluted. β-caryophyllene showed significant fragmentation inside the PTR-MS measurement, I calculated the relative percentage of β-caryophyllene-related ions measured by the PTR-MS for chamber studies and/or calibration carefully. As shown in Figure 6, the parent ion of β-

caryophyllene (*m/z*205.20, $C_{15}H_{25}^{+}$) fragmented to form several smaller ions. Finally, the relative contribution of *m/z*205.20 to total signals were relatively constant (39.7% ± 1.5%) among different days in the chamber campaign of SOA19b with the same instrument setting. Therefore, I can well quantify the concentration of β-caryophyllene with an accuracy of 20% considering both uncertainties from LCU and the fragmentation pattern.

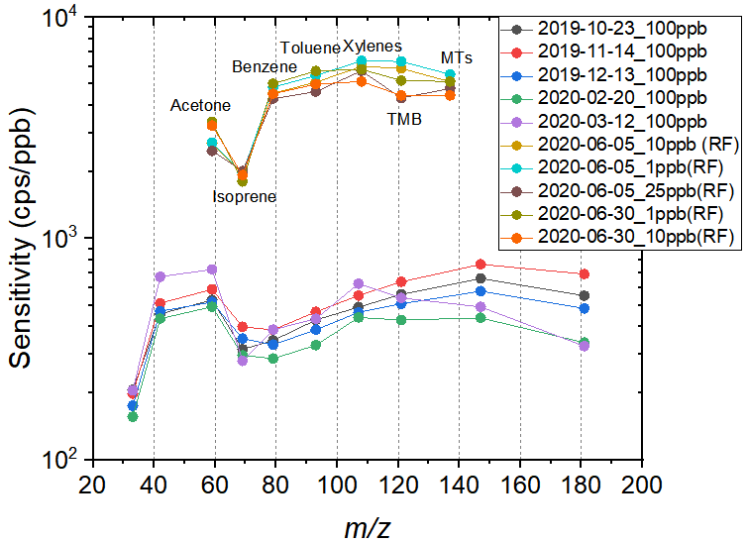

Figure 5 Comparison of sensitivities for calibrated species before and after the installation of ion funnel (RF) in different time.

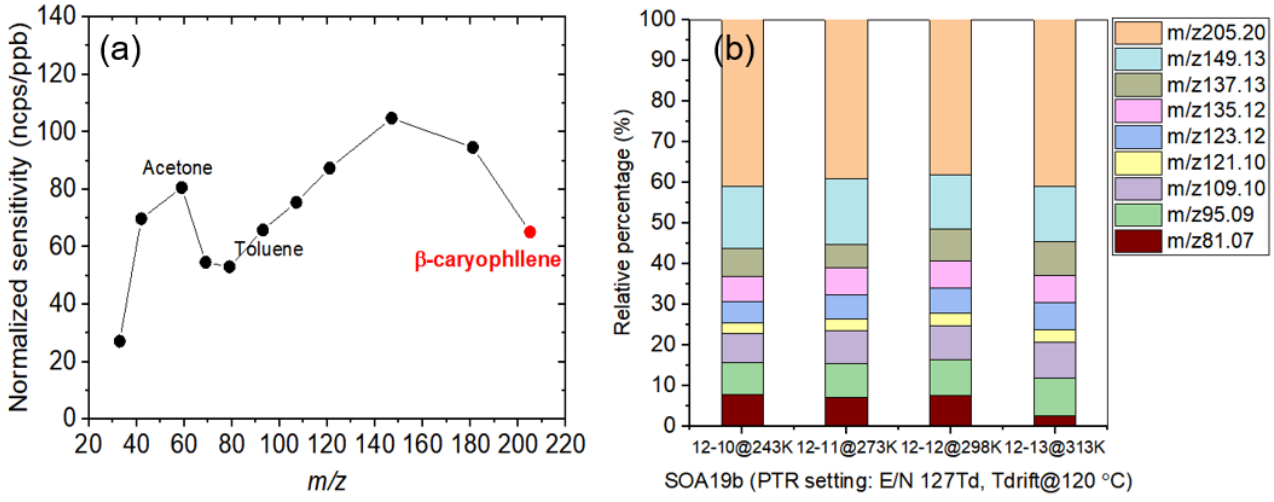

Figure 6 (a) Normalized sensitivity of β-caryophyllene calculated from the calibration via a LCU compared to the calibration of other species via a gas canister. (b) Relative percentage of β-caryophyllene parent (*m/z*205.20) and fragmented ions estimated in the four chamber experiments during the SOA19b campaign. The setting of PTR drift tube was given in the title of x axis.

Although PTR-MS can distinguish VOC of different *m/z* with high mass resolution (> 4000), it cannot separate VOC isomers directly. Therefore, a FastGC was installed in front of the PTR-MS, which allows to separate VOC isomers such as xylenes, monoterpenes and sesquiterpenes. A detailed description of the FastGC can be found elsewhere (Materic et al., 2015; Romano et al., 2014). Briefly, the FastGC module consists of a nonpolar pure dimethyl polysiloxane GC column (MXT-1, 0.25 mm ID, 0.25 μm df, Restek, Bellefonte, PA), a sample loop, a 10-port-valve and an additional flow controller (Figure 4c). Compared to a traditional GC column, the MXT-1 is resistively heated, which allows for very fast heating rates (>10 °C s^{-1}) to separate the VOC isomers. The low thermal mass of the heating module also ensures fast cooling rates (from 200 °C to 50 °C in less than 20 s). The FastGC mode can be activated when required while not affecting the normal PTR-MS operation otherwise. In this dissertation, the following instrumental parameters were used in FastGC run with a gas standard: PTR drift tube: E/N 92 Td; fastGC: (a) carrier gas flow of 6 mL/min under standard conditions and (b) injection time 4 s and temperature ramp consisting of 10 s at 40 °C, heating to 50 °C at 0.2 °C s-1, heating to 100 °C at 3 °C s^{-1}, and heat to 200 °C at 2.5 °C s^{-1}, 40 s at 200 °C. The temperature ramp was optimized for separating monoterpenes. The system was cooled to 40 °C at 16 °C s-1, after which it was ready for the next injection in less than 30 s. High purity nitrogen (> 99.999%) and synthetic air were used as a carrier and make-up gas respectively. In chamber and field experiments, FastGC-PTR-MS was set at a time resolution of 5 min including 1-2 min online VOC measurements and 3-4 min for a FastGC measurement, which allows to detect the total VOCs and their isomer composition with a reasonable time resolution compared to atmospheric concentration variations. An example of FastGC run for a gas standard was shown in Figure 7. It can clearly be seen that the FastGC can well separate the VOC isomers such as xylenes (*m/p*-xylene and *o*-xylene) and monoterpenes (α-pinene and limonene).

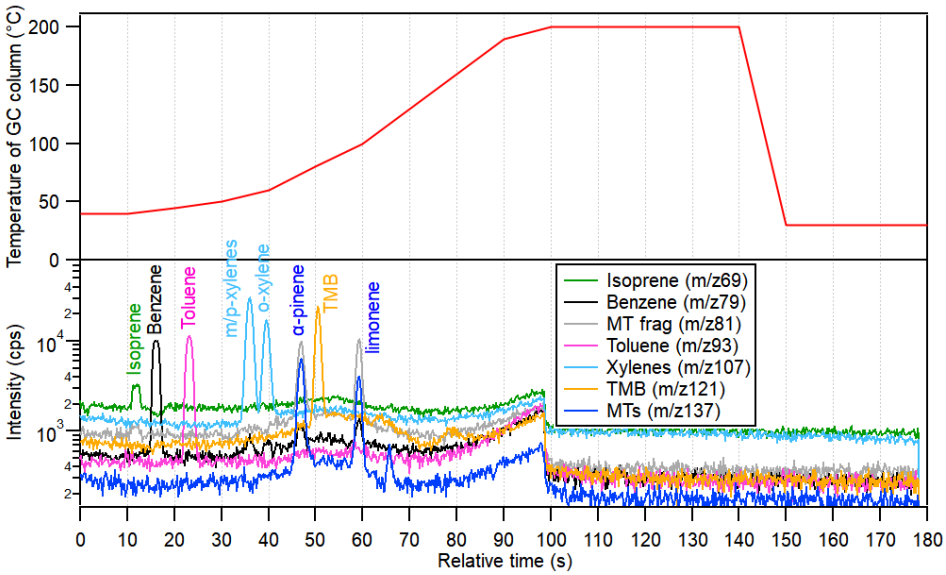

Figure 7 Example of FastGC measurement for a gas standard containing isoprene, benzene, toluene, m/p/o-xylenes, trimethylbenzene (TMB), α-pinene and limonene. The upper and bottom panels show the temperature ramp and chromatograms of the FastGC respectively.

In addition to VOC measurement, PTR-MS can be used to measure chemical compositions of aerosol in real time with a CHARON particle inlet. Figure 4b shows a schematic of the CHARON inlet (Eichler et al., 2015; Muller et al., 2017). The CHARON inlet consists of a monolith charcoal denuder for stripping off gaseous organics, an aerodynamic lens for enriching particles in the instrument subsampling flow, and a thermo-desorption unit for particle evaporation prior to chemical analysis. The monolith charcoal denuder can remove all gas-phase compounds with an efficiency of >99.999% and transmit the particles efficiently. The thermos-desorption unit consisted of a heated Siltek/Sulfinert-treated stainless steel tube, which was operated at a temperature of 150 °C and an absolute pressure of 7-8 mbar. A high-efficiency HEPA filter (ETA filter model HC01-5N-B, Aerocolloid LLC, Minneapolis, MN, USA) was periodically placed upstream of the gas-phase denuder for determining the instrumental background of particulate phase. A scroll pump (Varian TriScroll 600, Agilent Inc., Santa Clara, CA, USA) was used for maintaining a ~550 sccm sampling flow through the CHARON inlet. At the beginning and/or end of each campaign, the enrichment factor of the CHARON inlet was determined using an external calibration with size-selected ammonium nitrate particles (NH_4NO_3, ~60-700 nm) that are counted using a condensation particle counter (CPC). Figure 8 shows the enrichment factor of CHARON determined in different campaigns compared to the certification from the manufacturer (Ionicon

Analytik GmbH). The enrichment factor was calculated with an average of 18.9 ± 2.1 for the particles in the size range of 150 to 700 nm in this study. Particles in the size below 150 nm are less efficiently enriched.

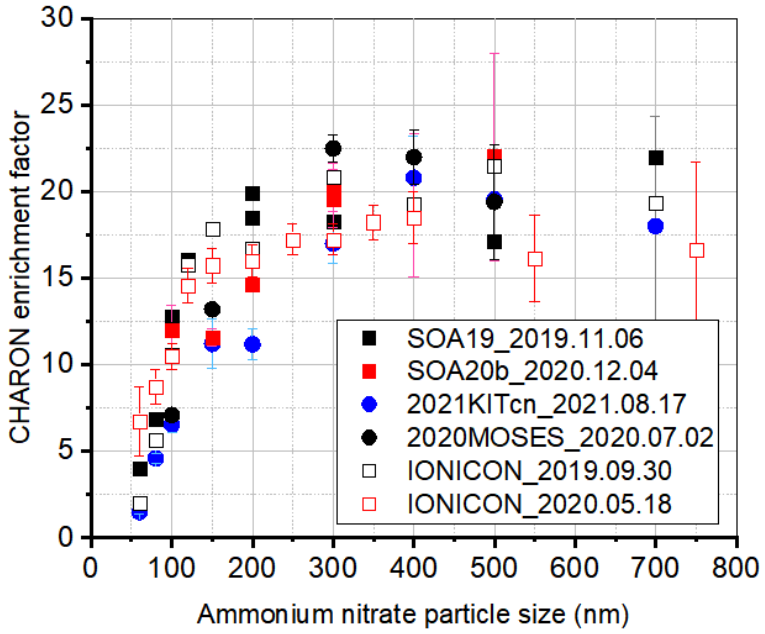

Figure 8 Enrichment factor of CHARON inlet determined by the size-selected ammonium nitrate particles in the different campaigns compared to the certificated results from the manufacturer (IONICON).

2.1.3 Software tools for analysis of AMS and PTR-MS data

The AMS data were analyzed by the IGOR-based software package SQUIRREL (version 1.60C) and PIKA (version 1.20C). Based on the data acquired during the HEPA filtered air measurement periods, the standard fragmentation table was adjusted to refine the gaseous contributions to the measured CO_2^+ signal and the $^{16}O^+$ to $^{14}N^+$ ratio for air signals. To account for the effect of particle bouncing loss, chemical-composition-based collection efficiencies (CDCE) were applied to calculate the mass concentration of aerosol species (Middlebrook et al., 2012). The elemental ratios of organics including oxygen-to-carbon and hydrogen-to-carbon ratios (O/C and H/C) were calculated from the V mode data based on the 'Improved-Ambient (I-A)' method (Canagaratna et al., 2015).

The PTR-MS mass spectra were analyzed by IONICON software tools including PTR Viewer 3.3.12 and the relatively new Ionicon Data Analyzer (IDA 1.0.0). These two software tools allow the analysis of PTR-MS data with the following characteristics: (i) multiple file analysis, (ii) mass

calibration, (iii) peak detection and deconvolution and (iv) quantification and suggestion of elemental composition. In the PTR Viewer and IDA, the mass calibrations can be done using three or four ion peaks: *m/z*21.022 (H_3O^+), *m/z*59.491 ($C_3H_7O^+$), *m/z*203.943 ($C_6H_5I^+$) and *m/z*330.848 ($C_6H_5I_2^+$). In the PTR Viewer, chemical formulas for each ion mass were assigned using a peak list produced from the software and which I complemented with the dedicated data from the growing PTR-MS literature database (Pagonis et al., 2019; Yáñez-Serrano et al., 2021). A high-resolution peak fitting algorithm was then manually adjusted for individual peak shapes and PTR Viewer calculated ion counts for each peak, performing a baseline correction, and correcting for mass discrimination in the time-of-flight following common standard PTR-MS data analysis procedures. The concentrations of compounds that have not been calibrated were determined based on measured transmission curve coefficients and an estimated ion-molecule rate constant reported by Cappellin et al. (2012). In the IDA, chemical composition for each ion mass were assigned automatically. The ion-molecule rate constant for each ion mass can be automatically determined depending on the properties of chemical composition (Müller et al., 2013; Titzmann et al., 2010). Besides, IDA has coupled a function tool for the background correction and the separation of VOC and particle data. Furthermore, an algorithm for correcting the data of CHARON particle measurement is added in this function tool (Leglise et al., 2019), thus IDA is very efficient for the CHARON data analysis. For the FastGC measurement, PTR-MS Trace Analyzer 1.0.5 was used for evaluate the peak area of each VOC in the fastGC chromatogram. The peak area was converted to the mixing ratios by dividing the relative peak area obtained in the FastGC calibration with corresponding gas standard.

Furthermore, high-resolution mass spectra of OA particles measured by the AMS and VOCs measured by the PTR-MS were further analyzed with a positive matrix factorization (PMF) software with a PMF3.exe algorithm in robust mode to determine the sources of OA and VOCs (Paatero and Tapper, 1994a). Positive matrix factorization (PMF) is an advanced multivariate factor analysis tool widely used to identify and quantify the sources of atmospheric pollutants including VOCs and OA. PMF is a bilinear receptor model which represents the measured time series of chemical compounds as a linear combination of factor contributions and their corresponding time-dependent concentrations (Paatero and Tapper, 1994b). This principle is described in the following equation:

$$X = GF + E \quad (2)$$

where X is the input chemical dataset matrix, G is the source contribution matrix, F is the source profiles matrix and E is the so-called residual matrix. These factors resolved from PMF analysis can be related to emission sources, and/or atmospheric processes, depending on their chemical and temporal characteristics.

Over the last two decades, PMF has been extensively used for source apportionment of OA measured by many AMS studies over the globe (Canonaco et al., 2013; Crippa et al., 2014; Ulbrich et al., 2009; Zhang et al., 2011; Zhou et al., 2020). PMF has also been widely used to determine source contributions of VOCs measured by the PTR-MS in different environments including urban areas (Gkatzelis et al., 2021; Kaltsonoudis et al., 2016; Wang et al., 2021; Wang et al., 2020; Yuan et al., 2012), rural areas (Vlasenko et al., 2009) and forests (Li et al., 2021a; Vestenius et al., 2021). In this dissertation, only organic mass at *m/z* 12-120 in V mode measured by the AMS in field campaigns were included in the PMF analysis as ions at larger *m/z* tended to have a low signal-to-noise ratio (SNR). I followed the PMF procedures for the data-processing and factor-selecting steps according to Ulbrich et al., (2009) and Zhang et al., (2011). The PMF was typically run from one to eight factors with the rational parameter (f_{Peak}) varying from -1 to 1 with steps of 0.2. In a field campaign at KIT campus north during summer in 2021, a concentration matrix and an error matrix for 89 ions measured by PTR-MS were set as the input files for the PMF analysis. The PMF was run from one to eight factors with the rational parameter (f_{Peak}) varying from -1 to 1 with steps of 0.2 as well. In this dissertation, I did all PMF analysis for AMS-measured OA and PTR-MS-measured VOCs, evaluated the PMF solutions and interpreted the results carefully.

2.1.4 Auxiliary instruments

In all experiments during my PhD study, a series of auxiliary instruments for particle, gas and meteorological measurements were also used and briefly introduced here.

Chemical ionization mass spectrometer: A chemical ionization mass spectrometer (CIMS) equipped with a Filter Inlet for Gases and AEROsols (FIGAERO) (Aerodyne Research Inc.) using iodide as the reagent ion to measure both gas-phase and particle-phase components. The FIGAERO-I^--CIMS has been described in detail by Lopez-Hilfiker et al. (Lopez-Hilfiker et al., 2014). In chamber experiments, the gas-phase compounds were measured online by the I^--CIMS, while the particles were collected on the PFTE filters and analyzed offline. In the field, particle samples were collected for the intensive measurement periods, then transported to the laboratory

for offline analysis. After the particle collection, the particle samples were stored in a freezer at -20 °C prior to the analysis by a FIGAERO-CIMS via a desorption program. Briefly, particles were thermally desorbed by a flow of ultra-high-purity (> 99.999%) nitrogen heated from a laboratory temperature of about 25 °C to 200 °C for 15 min, and soaked at 200 °C for 20 min. The evaporated compounds were measured by the downstream by CIMS. The data analysis was done with the Tofware 3.2.5 software (Aerodyne Research Inc. and TOFWERK). Please note that operations and data analysis of the FIGAERO-CIMS were performed by Linyu Gao and Feng Jiang.

Vocus-PTR-MS: In a field campaign in the Eifel forest in June 2020, a Vocus-PTR-MS (Tofwerk, AG, Switzerland) was used to measure VOCs in comparison to the CHARON-PTR-MS measurement I did. Details about the Vocus-PTR-TOF are well described elsewhere (Krechmer et al., 2018; Li et al., 2020). Compared to conventional PTR-MS, Vocus-PTR-MS was developed for the measurement of more oxygenated VOCs via optimization of the reagent-ion source and deployment of a focusing ion-molecular reactor. The Vocus-PTR-MS improves the detection limit of more oxygenated organic molecules via ion loss minimization using a focusing ion-molecular reactor and high sample flow through the reactor chamber. In the campaign, the calibration of Vocus-PTR-MS was conducted with a homemade gas canister containing of methanol, acetonitrile, acetaldehyde, acetone, isoprene, 2-butanone, 3-pentanone, methyl vyny1 ketone, 1-butanol, benzene, toluene, o-xylene, chlorobenzene, α-pinene, and norpinone. At the end of the campaign, a cross-calibration of Vocus-PTR-MS and CHARON-PTR-MS was performed with a commercial gas standard (Ionicon Analytik, GmbH). Vocus-PTR-MS data were recorded, saved, analyzed, and processed at 1 min time resolution using the Tofware software (Aerodyne Research Inc. and TOFWERK) in Igor Pro. Operation of Vocus-PTR-MS and its calibration was performed by Dr. Ralf Tillman, and data analysis was performed by Dr. Georgios Gkatzelis (both Forschungszentrum Jülich, IEK-8).

Optical particle counter (OPC): Fidas200 (Palas, Germany) is an optical particle counter (OPC) which uses Lorenz–Mie scattered light analysis of single particles to determine particle size, mass and number concentrations. It can continuously measure the aerosol particles in the size range 0.18–18 µm and provide the mass concentrations of PM_1, $PM_{2.5}$ and PM_{10}. Fidas200 was operated with a flowrate of 5 L min^{-1} and with a time resolution of 1 s. Operations and data analysis of the Fidas200 were performed by Dr. Harald Saathoff providing the time series of $PM_{2.5}$ and PM_{10} mass concentrations in 1min or 10 min time resolution.

Condensation particle counter (CPC): Particle number concentration was measured regularly with two CPCs (CPC3022A and CPC3776, TSI Inc., USA) with 1-butanol as a working fluid. The CPC3022A and CPC3776 measure the total number concentrations of particle size >2.5 nm and >7 nm, respectively. In the field campaign at KIT campus north, 2021, a water-based CPC (CPC3789, TSI Inc., USA) was also used to measure the particle number concentrations. All CPCs were set up to collect the data every min. Operations and data analysis of the CPCs were performed by Dr. Harald Saathoff.

Scanning Mobility Particle Sizer (SMPS): I used a SMPS was used for measuring the particle size distribution, which consists of a differential mobility analyzer (DMA, TSI 3080) and a CPC (CPC3022). The SMPS was set at a 1 L/min to collect the data every 7 min covering the size range 13.6–700 nm. I also used a NanoScan SMPS Nanoparticle Sizer 3910 (TSI) to measure particle size distributions from 10 to 420 nm at a time resolution of 1 min in the field experiments. Its internal CPC uses isopropyl alcohol as a working fluid.

Aethalometers: Black carbon (BC) was measured by three aethalometers (Alas et al., 2020) including AE51 and MA200 (AethLabs, USA) and AE33 (Magee Scientific, USA). AE51 draws ambient air on quartz filter-based strip which then measures BC using single 880 nm LED. The flowrate of AE51 was set at 100 mL min^{-1} to collect data every 5 min. MA200 can continuously collect aerosol particles on a filter tape and measures the optical attenuation (ATN) at five wavelengths (880, 625, 528, 470, and 375 nm). MA200 was operated with a flow rate of 150 mL min^{-1} and a time resolution of 5 min. AE33 is a dual-spot aethalometer and measures the aerosol light absorption at seven wavelengths (370, 470, 520, 590, 660, 880 and 950 nm). AE33 was operated with a flow rate of 5 L min^{-1} and a time resolution of 1 min. The mass of particles that absorb light at 880 nm for the MA200 and AE33 is considered to represent BC. The wavelength dependence of the absorption is expressed as the absorption Ångström exponent (AAE). BC from fossil fuel (BC_{ff}) and biomass burning (BC_{bb}) have different AAE values of 1 for the former and 2.0 for the latter (Sandradewi et al., 2008b). To investigate the relative importance of fossil fuel and biomass burning, the AAE was determined using two absorption values at 880 nm and 470 nm for the MA200, while that was determined using two absorption values at 950 nm and 470 nm for the AE33. Operations and data analysis of the AE51, AE33 and MA200 were performed by Feng Jiang and Dr. Harald Saathoff.

Gas monitors: Trace gases were regularly measured via the FEP sampling tubes with different gas monitors i.e., carbon dioxide (CO_2, NGA2000, Rosemount Inc.), ozone (O_3, O341M, Environment SA), nitrogen dioxide (NO_2, AS32M, Environment SA), and sulfur dioxide (SO_2, AF22M, Environment SA). In a field campaign at KITcn in July to August 2021, a cavity ring-down spectroscopy (G2103, Picarro, USA) was used to measure the concentration of NH_3. Operations and data analysis of the gas monitors were performed by Dr. Harald Saathoff providing the time series of their concentrations. In a field campaign at Eifel forest in June 2020, trace gas data including CO_2, CO, CH_4 and H_2O were measured by a cavity ring-down spectroscopy (G2401-m, Picarro, USA), and NO, NO_2 and O_3 were measured by a commercial ozone chemiluminescence analyzer CraNOx (Cranox II, Eco Physics). Operations and data analysis of the gas monitors in Eifel forest campaign were performed by Dr. Ralf Tillmann and Dr. Georgios Gkatzelis providing the time series of their concentrations.

Meteorological data, boundary layer heights, back trajectories: Meteorological data of ambient air temperature, relative humidity, atmospheric pressure, radiation, wind direction and speed and precipitation were mainly obtained from a compact sensor (WS700, Lufft). In the field campaigns at Durlacher Tor, complementary meteorological data were obtained from top of the KIT Physics Building provided by IMK-TRO. Hourly boundary layer height (BLH) data over the field measurement region (0.25×0.25 latitude/longitude data) were retrieved from the European Centre for Medium-Range Weather Forecasts ERA5 reanalysis to investigate its impact on the variations of ambient air pollutants (Hersbach et al., 2020). To investigate the source regions and transport of aerosol particles at field observations, three-day air mass back-trajectories with an arrival height of 100 m were calculated for every hour using the National Oceanic and Atmospheric Administration (NOAA) Air Resources Laboratory Hybrid Single-Particle Lagrangian Integrated Trajectory (HYSPLIT) model (Stein et al., 2015). The hourly back-trajectories were further grouped into different clusters, which were visualized using the IGOR-based Zefir tool (Petit et al., 2017).

2.2 AIDA simulation chamber campaigns

The AIDA simulation chamber is designed to simulate the formation processes of aerosol and cloud at atmospherically relevant conditions (Figure 9). Detailed descriptions of the AIDA chamber can be found elsewhere (Möhler et al., 2003; Saathoff et al., 2009; Wagner et al., 2006). Briefly, it consists of an aluminum cylinder with a volume of 84.5 m^3 that can be operated under a wide range

of temperatures (183–333 K), pressures (1–1000 hPa), RH (0–200%) and at different warming and cooling rates. The AIDA chamber was connected a series of gas and particle instruments for studying the chemical processing of aerosols. Recently, a LED-based light source has been installed at the AIDA chamber for simulating solar radiation allowing to study aerosol photochemistry (Vallon et al., 2022).

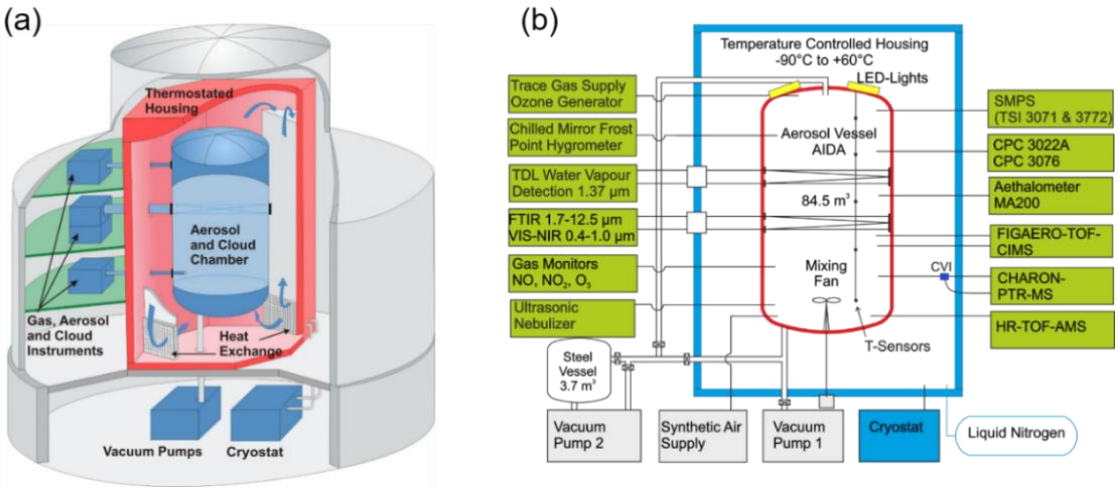

Figure 9. Schematic of the AIDA chamber (a) and main instrumentation (b)

I have participated in seven chamber campaigns (SOA19a, SOA19b, SOA20a, SOA20b, SOA21a, SOA21b and INCAS19) during my PhD study period (

Table 1). The chamber campaigns from SOA19a to SOA21a aimed at studying the chemical processes of SOA from single or mixed biogenic and anthropogenic VOC oxidation (e.g., isoprene/α-pinene/β-caryphellene/toluene/indole). Furthermore, the impact of different conditions such as temperature (213-313 K), with or without light, with or without NO_2 on the SOA yields, formation mechanisms and physicochemical (e.g., volatility) and optical properties were also investigated. In these chamber campaigns, I mainly operated AMS and PTR-MS, did the calibrations for both instruments and the subsequent data analysis. During SOA19a and SOA19b, I quantified the concentrations of organic aerosol and VOCs (e.g., 2,3-pentanodione, formaldehyde, acetaldehyde), which were used in kinetic calculations for studying the photochemistry of aerosol particles and VOCs. During SOA19b, I quantified the concentrations of β-caryophyllene measured by the PTR-MS. Importantly, I did additional PTR-MS calibrations for β-caryophyllene measurements via a LCU method. This was a new method for calibrating this low volatility compounds, which improves the accuracy of β-caryophyllene quantification by PTR-MS. With the results of β-caryophyllene measurement, my colleagues can further calculate the yield of SOA formed from β-caryophyllene ozonolysis and its kinetics. Based on these contributions, I am a co-author of two publications (Gao et al., 2022; Vallon et al., 2022). I also participated in a chamber campaign (INCAS19) with the contribution of AMS operation and data analysis. This campaign investigated the ice nucleation ability of internally mixed particles composed of crystalline ammonium sulfate and α-pinene-derived SOA. The corresponding AMS measurement results in INCAS19 have been published in my co-authored paper (Bertozzi et al., 2021). I also contributed to other chamber campaigns including SOA20a, SOA20b, SOA21a and SOA21b mainly by providing VOC concentrations. I also taught a new PhD student in operation of the aerosol mass spectrometer and its basic theory as well as the data analysis skills in the campaign of SOA20a. For the campaigns of SOA20b, SOA21a and SOA21b, I offered substantial contributions especially in the operation of CHARON-PTR-MS and data analysis. Furthermore, I taught another new PhD student in operation of the CHARON-PTR-MS and its data analysis with newest IONICON software tools (PTR viewer and IDA).

I have also made use of these AIDA chamber campaigns, which provide good opportunities to characterize the measurement capability of a new PTR-MS coupled with a new CHARON inlet and a Fast-GC. In this dissertation, I also combined these chamber measurement results to interpret the field observations.

Table 1 AIDA chamber campaigns with the research topics, and my major contributions

Name	Date	Research topic	Contributions	Results
SOA19a	Mar. 2019	Study of biogenic SOA chemistry	Operation of AMS	co-authored paper (Vallon et al., 2022)
INCAS01	Apr. 2019	Ice nucleation of ammonium sulfate mixed with SOA	Operation of AMS and data analysis	co-authored paper (Bertozzi et al., 2021)
SOA19b	Nov. 2019	Study of biogenic SOA chemistry	Operation of AMS and PTR-MS, data analysis	co-authored papers (Gao et al., 2022; Vallon et al., 2022)
SOA20a	Mar. 2020	Study of anthropogenic SOA chemistry	Operation of PTR-MS and data analysis	Analysis ongoing
SOA20b	Nov. 2020	Study of biogenic/anthropogenic SOA chemistry	Operation of PTR-MS and data analysis	Analysis ongoing
SOA21a	Mar. 2021	SOA surface chemistry and photochemistry	Operation of PTR-MS and data analysis	Analysis ongoing
SOA21b	Nov. 2021	Study of brown carbon from toluene and indole oxidation	Operation of PTR-MS and data analysis	Analysis ongoing

2.3 Field campaigns at urban, rural and forest sites

During my PhD study, I have participated in four field campaigns to study the characteristics of aerosol particles and trace gases in different environments including urban, rural and forest areas (Figure 10 and Figure 11). The detailed information of each field campaign with the research topics and my contributions are summarized in Table 2. The main findings from this field campaign are given in section 3.3, which will be summarized for another first-author manuscript. The mass spectrometers including AMS, CHARON-PTR-MS, FIGAERO-CIMS and Vocus-PTR-MS are marked in Figure 11, and the main instruments available in each field campaign is given in Table 3.

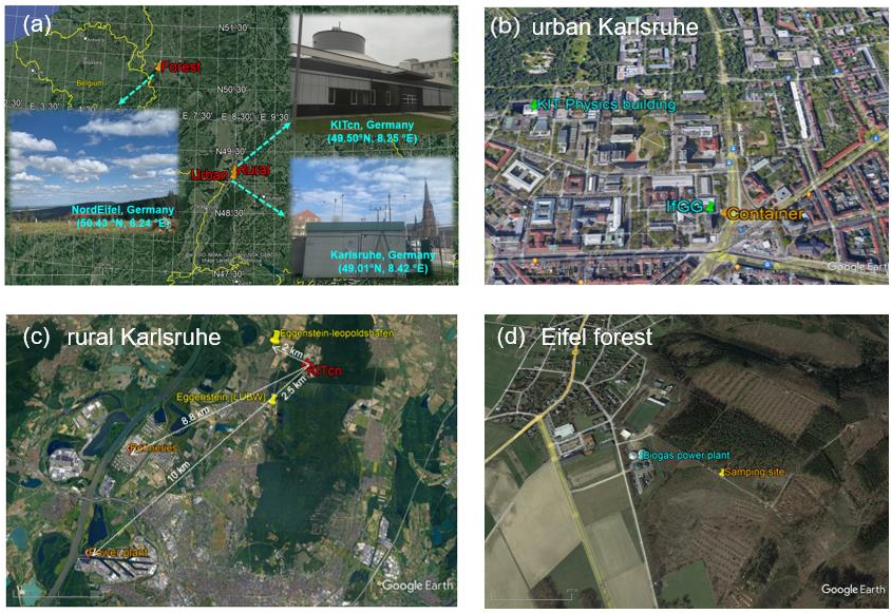

Figure 10. (a) Map of sampling sites for field campaigns in urban, rural and forest areas: (b) urban kerbsite of Karlsruhe (Durlacher Tor), (c) rural site north of Karlsruhe (KIT campus north); (d) Eifel forest, western Germany.

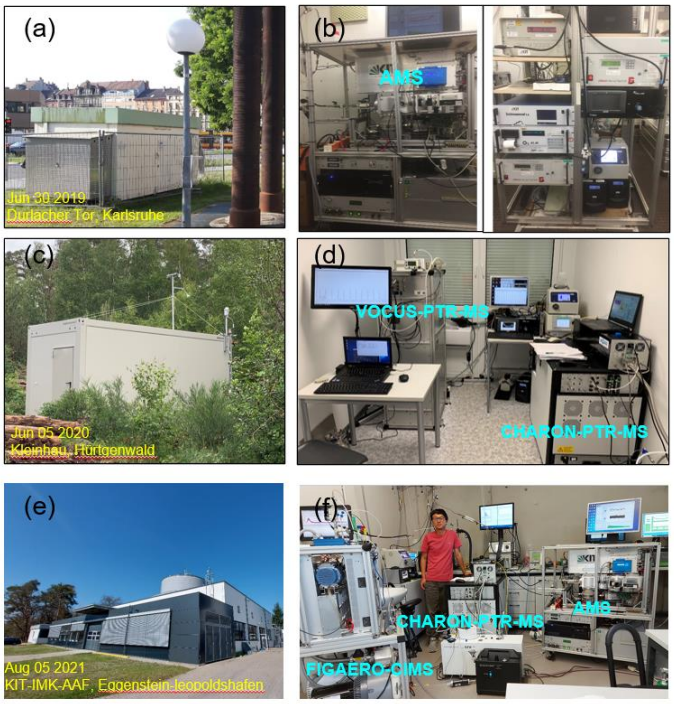

Figure 11. Measurement containers/room and main instrumentation during field campaigns at (a-b) Durlacher Tor (Photo: J. Song, 06.2019), (c-d) Eifel forest (Photo: J. Song, 06.2020), and (e-f) KIT campus north (Photo: H. Saathoff, 08.2021). The mass spectrometers (AMS, PTR-MS and CIMS) are marked.

Urban site in downtown Karlsruhe. I have performed two field campaigns (2019DT and 2020DT) at Durlacher Tor in downtown Karlsruhe (49.01° N, 8.42° E) in southwest Germany in summer (June 28th to July 29th, 2019) and winter (February 21st to March 31st, 2020) (Figure 10). The city of Karlsruhe is located in the upper Rhine valley and can be regarded as a moderately-low polluted city with actually 304000 inhabitants. Generally, the predominant wind directions in Karlsruhe are southwest in summer and northeast in winter due to channeling in the Rhine valley. The measurements are performed in a container located in front of the Institute of Geography and Geoecology (IfGG) on the campus of the Karlsruhe Institute of Technology (KIT). It is next (~5 m) to the central traffic junction Durlacher Tor, which can be considered as an urban street canyon site (Linke et al., 2016; Norra and Stuben, 2004). This site is located on the northeastern periphery of downtown Karlsruhe, approximately 8 km east of a 912 MW coal-fired power plant "Rheinhafen-Dampfkraftwer", 10 km southeast of the refinery "Mineralölraffinerie Oberrhein", and less than 1 km south of rural and forest regions. Therefore, the air quality at this site is influenced by local traffic and downtown emissions, but also depending on meteorological conditions, by anthropogenic and biogenic emissions in the vicinity of the city as well as regional transport. During these two campaigns, I mainly operated two mass spectrometers including the AMS and the CHARON-PTR-MS. My research objectives of these two field campaigns are (1) to characterize the temporal variations of urban aerosol particles and trace gases; (2) to investigate the sources of aerosol species and trace gases; and (3) to elucidate the major factors for the air pollution episodes. The results and discussion are presented in section 3.1, and have been published in the journal of Atmospheric Environment (Song et al., 2022).

During these two campaigns, I also contributed to another research topic for studying the spatial distributions of aerosol particles and heat islands in the east part of downtown Karlsruhe. I built a particle sensor box consisting of two particle sensors (SDS011, Nova fitness and OPC-N3, Alphasense) for measuring the concentrations of $PM_{2.5}$ and PM_{10}. It can be amounted to a bike trailer for providing spatial distributions of $PM_{2.5}$ and PM_{10} concentrations based on bicycle measurements. I did the calibrations of these two particle sensors before and after the bicycle measurements. I am a co-author of a corresponding publication which is still under review (Norra et al., 2022). Besides, I was teaching master students and a PhD student to operate these particle sensors during the bicycle measurements.

Rural site at KIT campus north (11 km north of Karlsruhe). I have participated in two field campaigns conducted at a rural site in winter (February 20th to March 16th, 2021) and summer (July 16th to August 16th, 2021). The sampling site is located at the building of the IMK-AAF on the campus north of KIT (KITcn). The sampling site is far from the main roads, and there is almost no traffics except morning working hours (~7:00-9:00) and late afternoon (~16:00). The campus is mostly surrounded by the Hardwald forest dominated by pine trees, which are the largest contributors for monoterpenes and sesquiterpenes. Besides, the sampling site is 2-3 km east of the village "Eggenstein-Leopoldshafen", a mainly rural residential area, ~11 km north of downtown Karlsruhe, ~8-10 km northeast of industrial areas including a coal-fired power plant "Rheinhafen" and a refinery "MIRO". Therefore, the measurement site could be subject to the biogenic and anthropogenic emissions depending on the meteorological conditions. It is an ideal site to study their relative contributions to trace gas and aerosol particles and the interaction processes. The research topic for the winter campaign is to characterizing the impacts of biomass burning and Saharan dust on aerosol particles in rural Karlsurhe in wintertime. I operated the CHARON-PTR-MS and analyzed the data for providing the concentrations of VOCs and aerosol particles subsequently. I organized the summer campaign for studying the variations of VOCs and SOA formation in rural Karlsruhe. I operated two mass spectrometers (AMS and PTR-MS) and a series of auxiliary instruments (e.g., OPC, CPC and SMPS). In particular, I made the first test measurement with the FastGC for the ambient air during the summer campaign. In this dissertation, the major results from the summer campaign are given in Section 3.2. I will summarize the main findings and prepare for a first-author manuscript. The data analysis of CHARON-PTR-MS during winter campaign are still ongoing, and the results will contribute another co-authored publication focusing the impact of biomass burning on brown carbon.

Forest site in Kleinhau. I have participated a field campaign belonging to MOSES (Modular Observation Solutions for Earth Systems) project in June 2020. It was a joint measurement campaign in a stressed pine forest with the collaboration with researchers from Institute of Energy and Climate Research, Troposphere (IEK-8), Jülich. The sampling site is situated at the Eifel forest in North Rhine-Westphalia, western Germany. The sampling site is located in ~500 m southeast of small town "Kleinhau" in the Hürtgenwald and about 250 m east of a biogas power plant (BioEnergie Kleinhau GmbH). The measurement area is largely composed of Norway spruce and some European beech trees, which are important contributors to BVOCs and especially terpene

emissions. In addition, it is known that these trees can suffer from different abiotic (drought and high temperature) and biotic stresses (bark beetle attacks), which can change the emissions of BVOCs (Ghimire et al., 2016). The research topic for this campaign is to compare two high-sensitivity PTR-MS instruments (CHARON-PTR-MS and Vocus-PTR-MS) and to study the variations of VOCs and their contributions to SOA formation at a stressed forest. During the campaign, I mainly operated the CHARON-PTR-MS for measuring the VOCs and aerosol particles. My research objectives are (1) comparison of VOC measurements between two high-sensitivity PTR-MS instruments; (2) concentration and variations of VOCs, and meteorological effects and (3) contribution of VOC oxidation to SOA formation. The main findings from this field campaign are given in section 3.3, which will be summarized for another first-author manuscript.

Table 2 Field campaigns with the research topics, my contributions and tentative publications

Name	Time	Research topic	Contribution	Results
19DT	Jul. 2019	Characteristics of aerosol particles and trace gases in downtown Karlsruhe	Operation of AMS and data analysis, support of bicycle-based particle measurements	first-author paper (Song et al., 2022); co-author paper (in review)
20DT	Mar. 2020	Characteristics of aerosol particles and trace gases in downtown Karlsruhe	Operation of AMS and PTR-MS and data analysis	first-author paper (Song et al., 2022)
20MOSES	Jun. 2020	Variations of VOCs and their contribution to SOA formation in Eifel forest	Operation of CHARON-PTR-MS and data analysis	first-author paper (in preparation)
21KITcn	Feb. 2021	Wintertime biomass burning/Saharan dust events in rural Karlsruhe	Operation of PTR-MS and VOC data analysis	Analysis ongoing
21KITcn	Jul. 2021	Variations of VOCs and their impacts to SOA formation in rural Karlsruhe	Operation of AMS and PTR-MS and data analysis	first-author paper (in preparation)

Table 3 Main instruments used in the different field campaigns

Measured parameter	Instrument	2019 DT	2020 DT	2020 MOSES	2021 KITcn
Meteorological parameters	WS700 (Lufft GmbH)	x	x	x	x
Particle number concentration (>7 nm)	CPC3022 (TSI Inc.)	x	x		
Particle number concentration (>2.5 nm)	CPC3776 (TSI Inc.)	x	x	x	
Particle number concentration (> 2 nm)	CPC3789 (TSI Inc.)				x
Particle size distribution (10-410 nm, d_m)	NanoScan-SMPS (TSI Inc.)	x	x	x	x
Particle size distribution (13.6-670 nm, d_m)	SMPS (TSI Inc.)				x
O_3	O341M (Environment SA)	x	x		x
NO_2	AS32M (Environment SA)	x	x		x
SO_2	AF22M (Environment SA)	x	x		
CO_2	NGA2000 (Rosement Inc.)	x	x		
NH_3/H_2O	G2103 (Picarro)				x
$NO/NO_2/O_3$	Cranox II (Eco Physics)			x	
$CO/CO_2/CH_4/H_2O$	G2401 (Picarro)			x	
PM_1, $PM_{2.5}$ and PM_{10} mass	FIDAS200 (Palas GmbH)			x	x
Black carbon	AE51/MA200 (Aethlabs Inc.) or AE33 (Magee Scientific Co.)	x	x	x	x
Particle mass and size (0.07-2.5 µm, d_{va})	HR-ToF-AMS (Aerodyne Research Inc.)	x	x		x
VOCs	Vocus-PTR-MS (Tofwerk Aerodyne)			x	
VOCs/semi-volatile particles	CHARON-PTR-MS (IONICON Analytik GmbH)		x	x	x
VOC isomers	FastGC-PTR-MS (IONICON Analytik GmbH)				x
Oxygenated organic molecules (gas/particle phase)	FIGAERO-CIMS (Aerodyne Research Inc.)	x	x		x

3. Results and discussion

3.1 Characterization of a new CHARON/FastGC-PTR-MS

After my training on the new PTR-MS at the headquarters of the manufacturer (IONICON) and its transfer to the KIT, I performed a thorough characterization of the instrument and the upgrades it received during my PhD work. This work is going beyond a standard characterization of a mass spectrometer as it includes validating new measurement strategies. Furthermore, it is the prerequisite for the application of the PTR-MS in simulation chamber experiments and field measurements.

3.1.1 Characteristics of the CHARON-PTR-MS in a chamber experiment

In addition to gas-phase measurement, I used the PTR-MS to measure chemical compositions of particles employing the CHARON inlet. To make full use of this instrument, the CHARON-PTR-MS was operated alternatingly for measuring VOCs and particles. During AIDA simulation chamber experiments, I set the CHARON-PTR-MS to an alternating measurement cycle including (1) 1min HEPA filter measurement to determine the particle (free) background, (2) 5 min CHARON particle measurement, (3) 1 min transition for the equilibration of the instrument, (4) 5 min VOC measurement and (5) another 1 min transition. Figure 12 presents an example with the employment of CHARON-PTR-MS in an AIDA simulating chamber experiment on 5th December 2019. At the beginning of this experiment, I set the CHARON-PTR-MS for measuring the VOCs only. The added amount of isoprene and α-pinene were quantified by the PTR-MS with 19.5 ± 1.0 ppb and 19.4 ± 1.0 ppb, respectively. Subsequently, ~370 ppb O_3 was added to oxidize the VOC precursors to form a small amount of SOA mass (~10 µg m^{-3}) within 10 min. Then tetramethylethylene (TME) was added into the chamber, which can react with the excess of O_3 to form OH radicals. Correspondingly, a large amount of SOA was formed with a mass increase of ~70 µg m^{-3}. When the VOC precursors were mostly depleted and the SOA mass was relatively stable, I switched the CHARON-PTR-MS for alternatingly measuring organic compounds in both gas and particles. In this experiment, the AIDA chamber was further heated (2.5 K h^{-1}) overnight from an initial temperature of 273 K to 293 K on next day morning for studying the evaporation of the SOA. During the chamber heating up period, the CHARON-PTR-MS performed alternating measurements, which provides a good opportunity to compare the CHARON-PTR-MS with other instruments like SMPS, AMS and FIGAERO-CIMS.

As shown in Figure 12c, relatively high background values of total organic signals were observed for the HEPA filter measurements during this experiment. Note that the organic signals shown here are without any instrumental background correction. In fact, these relatively high background values were mainly due to contributions of smaller ions, which mostly showed higher instrumental background. Generally, the sampling background correction was made via subtracting the average values of HEPA filter measurements. In this experiment, the signals of HEPA filter measurements showed a similar trend with the total organic signals directly measured by the CHARON. The changes of the HEPA background showed a relative standard deviation of ~16%, thus it was not very accurate to correct the sampling background with the average value of the HEPA background. In contrast, I can apply the interpolated HEPA filter background subtraction for improving the accuracy of the CHARON measurements.

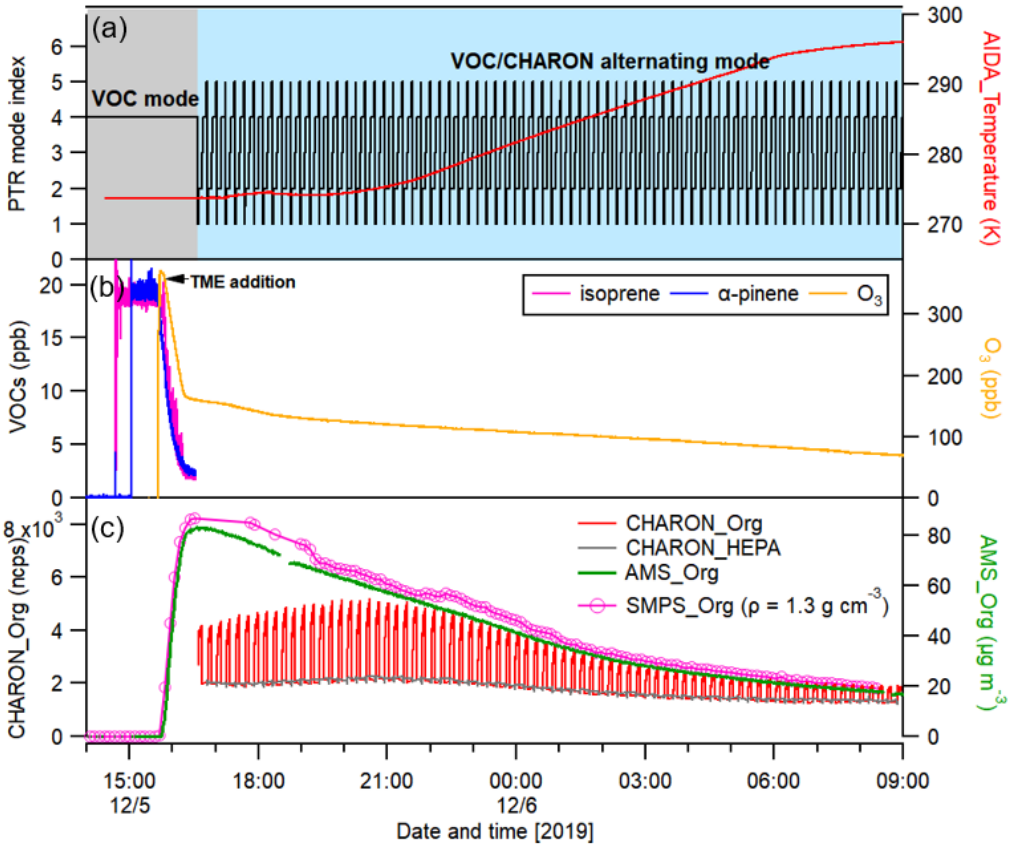

Figure 12 An example of AIDA chamber experiment with employing the new CHARON-PTR-MS on 12/05/2019. (a) measurement mode index of CHARON-PTR-MS, (b) isoprene, α-pinene and O_3 concentrations. Added tetramethyethylene (TME) reacted with excess O_3 to form OH radicals. (c) total organic signals measured by the CHARON and organic mass measured by the AMS and derived from SMPS with a density of 1.3 g cm^{-3}. A gap between CHARON organic signals compared to AMS and SMPS before 21:00 is due to the size effect on CHARON inlet.

Figure 13 shows an example with three alternating measurement cycles of CHARON-PTR-MS employed in this experiment. It can clearly be seen (Figure 13b) that the intensity of the primary ions (H_3O^+) and internal mass calibration ions ($C_6H_5I^+$) dropped significantly during the transition time, which was caused by the switch between VOC inlet and CHARON inlet to the PTR drift tube. However, it comes back to a stable level within 10 s, thus 1 min transition time was sufficient for stabilizing the instrumental conditions. When looking at the evolution of total organic signals in each CHARON cycle (Figure 13c), it always needs a certain time for the PTR response to reach a stable plateau. If assuming the last data point in each CHARON cycle as the maximum value, the relative change of organic signal can be estimated over the time of single CHARON measurement cycle (300 s). As shown in Figure 13d, it takes around 180 s then 90% of total organic signals can be detected by the CHARON. Furthermore, the total organic signals can be further divided into different mass range groups including *m/z*50-100, *m/z*100-150, *m/z*150-200 and *m/z*>200. The organics in *m/z*100-150 and *m/z*150-200 showed similar trend and required 180 s for detecting 90% signals in a single CHARON cycle. However, the organics in *m/z*>200 need a bit more time (~240 s) for getting 90% signals. This can be explained by the lower-volatility of organic compounds with higher molecular mass (Piel et al., 2021). In contrast, the organics in *m/z*50-100 can reach up 90% already in 60s. As discussed before, these smaller ions were mostly affected by the gas background. Finally, I used the data points measured at the last two minutes (120 s) in each single CHARON cycle for the quantification of organics. Please keep in mind that extending the measurement time of the CHARON cycles would be valuable for detecting the low-volatility organic compounds, but reduce the time resolution of VOC measurement correspondingly. Therefore, my results provide not only the general analysis strategy of CHARON-PTR-MS data, but also recommendations for other similar instrumental setting for alternatingly measuring gas and particle phases.

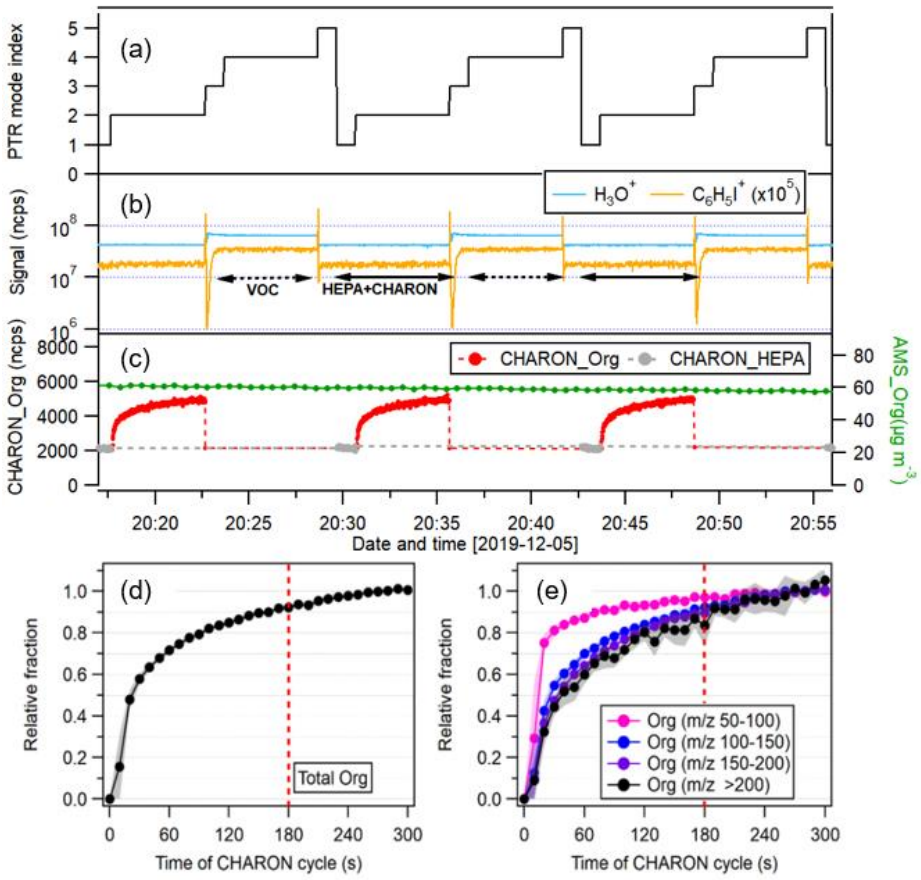

Figure 13 Time series for three alternating measurement cycles of CHARON-PTR-MS (a) PTR mode index, (b) signal evolution of reagent and mass calibration ions (H_3O^+ and $C_6H_5I^+$) (c) total organic signal measured by the CHARON and via HEPA particle filter along with the AMS-measured organic mass (d-e) relative fraction of signal of total organic and individual organic groups with different mass ranges. The fractions are normalized to the final maximum data points in each CHARON cycle. The red dash line shows the time point (~180 s) when ~90% of organic signals were detected by the CHARON.

After the corrections of sampling background and instrumental response, I can convert accurately the CHARON-measured organic signal to the mass concentrations in comparison to other instruments. As shown in Figure 12, there was a significant gap between total organic signals detected by the CHARON-PTR-MS relative to the AMS or SMPS-measured organic mass. This was related to the reduced enrichment efficiency of CHARON aerodynamic system for smaller particles (<150 nm) as mentioned in the section 2.1.2. Based on the particle size evolution measured by the SMPS (Figure 14), the organics measured by the CHARON-PTR-MS can be corrected further to remove the size effect. Finally, a good linear agreement (R = 0.99) was observed for the organic mass measured by the CHARON-PTR-MS with correction of size effect and the AMS as

shown in Figure S1 in the appendix. However, the contribution of CHARON-PTR-MS-measured organic mass to the total organic mas (AMS & SMPS) was only (19.2 ± 1.7)%, which was lower than the fraction of 80 ± 10 % reported in a previous study (Gkatzelis et al., 2018a). Currently, there is no explanation for the underestimation of organic mass detected by the CHARON-PTR-MS in this study. I discussed this issue with the manufacturer (IONICON), and proposed some potential reasons for the underestimation e.g., particle loss in the sampling line, unaccounted higher molecules and/or systematical errors. However, so far, this systematic problem could not be solved. Please note, the AMS and CHARON-PTR-MS measure similar bulk O/C ratios while the FIGAERO-I$^-$-CIMS clearly measures higher oxidized compounds with higher O/C ratios (Figure 14c).

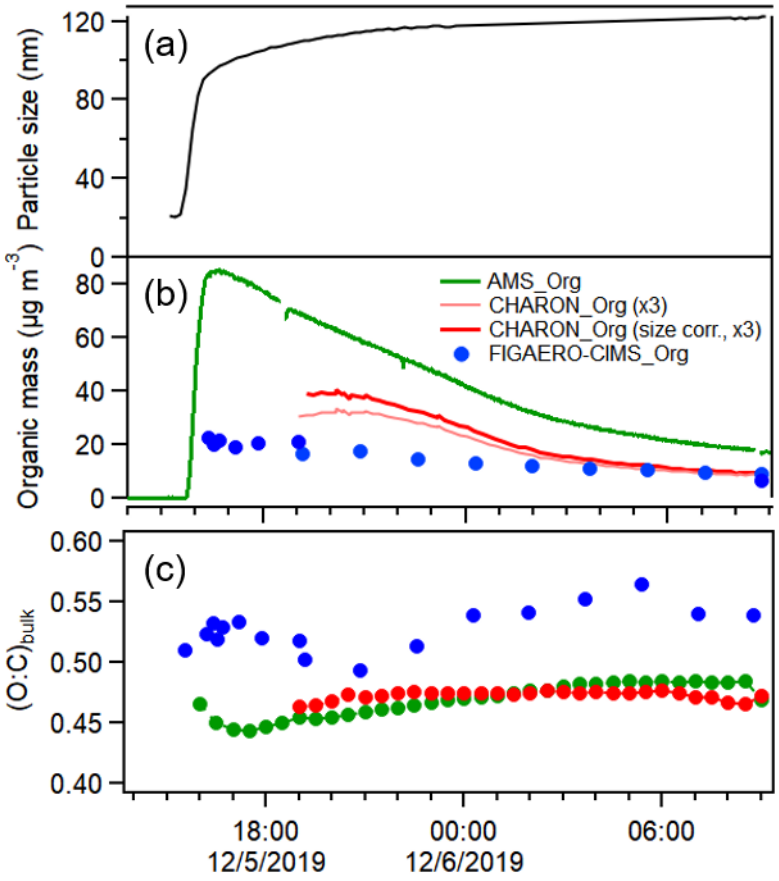

Figure 14 Time series of (a) mean particle diameter measured by SMPS (b) organic mass measured by AMS, CHARON and FIGAERO-CIMS; the CHARON-measured organic mass was corrected by the size effect (dark red). (c) O:C ratios of bulk organics from three mass spectrometers (AMS green, CHARON red, and FIGAERO blue).

Furthermore, the mass spectra of SOA formed from isoprene and α-pinene oxidation by the CHARON-PTR-MS and FIGAERO-CIMS were compared (Figure 15). The results indicate that CHARON-PTR-MS can well detect less-oxidized organic compounds like $C_{10}H_{16}O_3$, $C_{10}H_{14}O_{1\text{-}5}$, $C_9H_{14}O_{3\text{-}4}$, $C_8H_{12}O_{1\text{-}5}$ and $C_7H_{10}O_4$. Comparatively, FIGAERO-CIMS can better detect more-oxidized organic compounds like $C_{10}H_{16}O_{3\text{-}7}$, $C_{10}H_{14}O_{4\text{-}6}$, $C_9H_{14}O_{4\text{-}6}$ and $C_8H_{12}O_{4\text{-}6}$. The mass spectrum of the CHARON-PTR-MS showed significant signals for the lower mass range (*m/z*<120), which were attributed to the fragmentation ions. In contrast, only few ions were detected in the lower mass range of mass spectrum by FIGAERO-CIMS. A previous study reported that the fragmentation of CHARON-PTR-MS was mostly due to the organic molecules losing H_2O or other neutral ions like CO (Gkatzelis et al., 2018b). For example, CHARON-PTR-MS can detect $C_{10}H_{14}O_3$ in this study, while no signals for these molecules in the mass spectrum of FIGAERO-CIMS. Therefore, it was robust to characterize $C_{10}H_{14}O_3$ as a fragment ion produced from the fragmentation of $C_{10}H_{16}O_3$ by losing one H_2O. Note that the CHARON-PTR-MS only measured the mass up to *m/z*254 in this experiment, thus the detection of higher molecular weight compounds was not available. In this experiment, the dominant organic compounds were detected in lower mass range (>*m/z*254) as shown in the FIGAERO-CIMS mass spectrum. In addition, McFiggans et al. (2019) found that isoprene can suppress the dimer formation of α-pinene which were typically in the higher mass range (>*m/z*254). Therefore, the impact of much higher molecular weight (>*m/z*254) compound fragmentation to smaller mass seems to be negligible for the CHARON-PTR-MS.

I also made the comparison of CHARON-PTR-MS and FIGAERO-CIMS measurement for 9 moderately oxidized compounds formed from the oxidation of isoprene and α-pinene. The results indicate that most of them are detected in both instruments showing a linear response ($R^2 > 0.8$). The relative sensitivities of the two instruments to these compounds, indicated by the variations of the slopes appear to change by a factor of 10. It should be note that the sensitivity of CHARON-PTR-MS measured signal is for bulk aerosol without any fragmentation correction. Furthermore, the uncertainty of FIGAERO-CIMS may also lead to some differences compared to CHARON-PTR-MS. However, good linear response for some well-known organic compounds such as $C_8H_{12}O_4$ (terpenylic acid) and $C_{10}H_{16}O_3$ (pinonic acid) between these two instruments still show comparable performance in this experiment. Quantification of these but also of unknown compounds by CHARON-PTR-MS is possible also without calibration with an uncertainty of 40%,

or better (20%) if calibrated with authentic standard compounds like *cis*-pinonic acid (Leglise et al., 2019). By comparing both mass spectra, it is possible to quantify these compounds also in FIGAREO-CIMS data, for which the sensitivities can vary over several orders of magnitude.

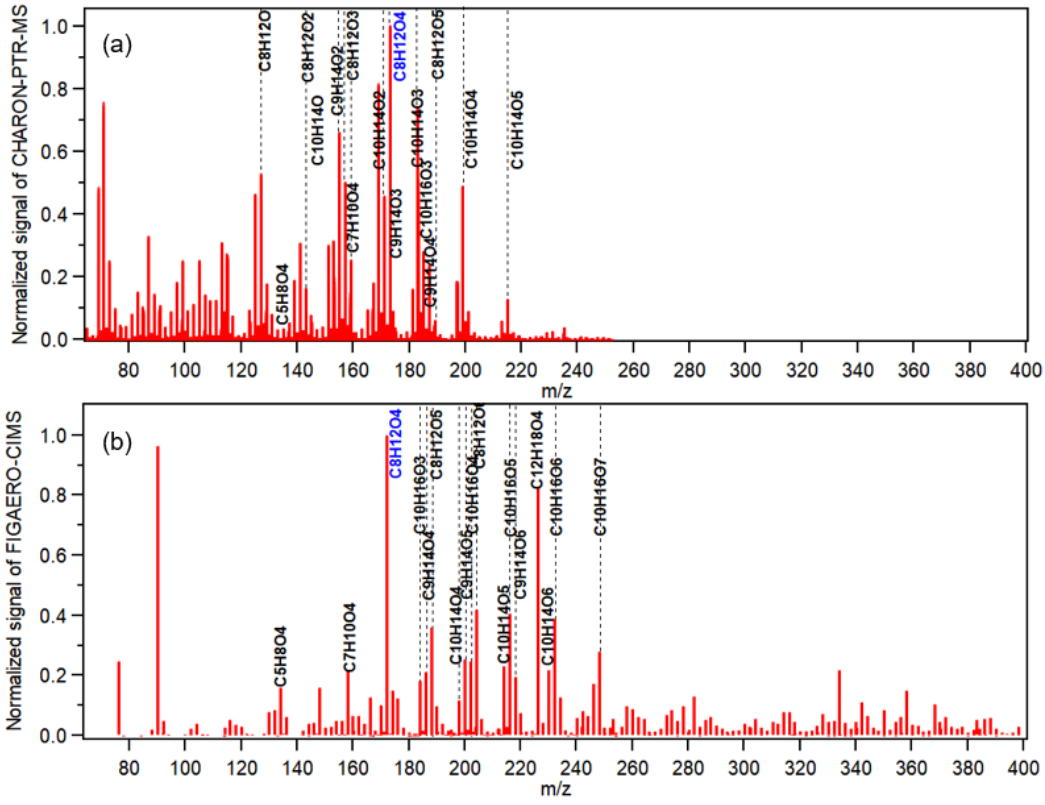

Figure 15 Mass spectra from (a) CHARON-PTR-MS and (b) FIGAERO-CIMS for SOA formed from the oxidation of ab isoprene - α-pinene mixture. The signal intensities are normalized to the maxima at $C_8H_{12}O_4$ (blue).

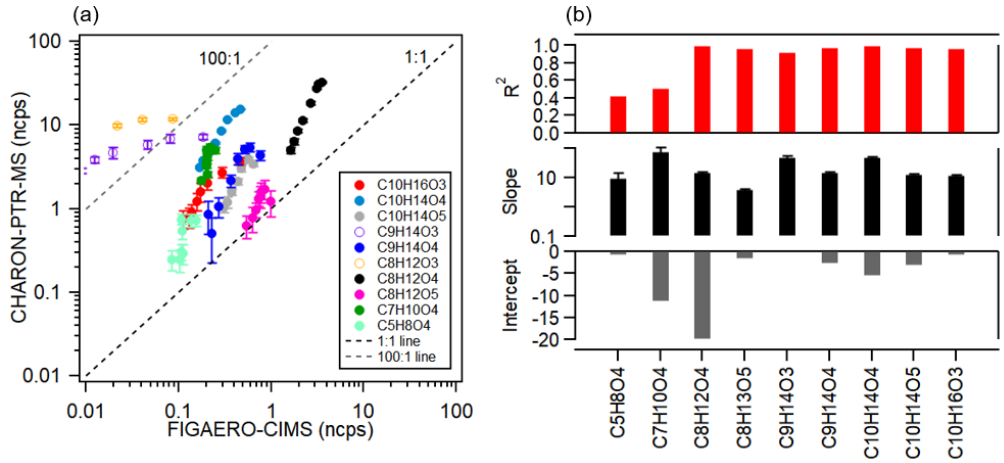

Figure 16 Comparison between FIGAERO-CIMS and CHARON-PTR-MS for some moderately oxidized compounds formed by the oxidation of isoprene and α-pinene. (a) scatter plot and (b) linear fit results.

3.1.2 Characteristics of the CHARON-PTR-MS in field campaigns

In addition to simulation chamber experiments, I also deployed the CHARON-PTR-MS in different field campaigns including 2020DT in winter, 2020MOSES in summer, 2021KITcn in winter and summer. Before starting the summer campaign of 2020MOSES, the CHARON-PTR-MS was upgraded to an ion funnel improving the sensitivity by one order of magnitude. I collaborated with the researchers from Forschungszentrum Jülich during this campaign. They deployed another high-sensitivity Vocus-PTR-MS for measuring VOCs and OVOCs. This was a good opportunity to compare VOC measured by these two high sensitivity PTR-MS. Figure 17 shows the time series of some VOC species including isoprene, benzene, toluene, monoterpenes and sesquiterpenes measured by both instruments during this campaign. Note that the CHARON-PTR-MS (PTR4000) showed transmission losses for detecting higher masses (*m/z*>200) during the period 1 of 5^{th}-22^{nd} June. Thus, the data of sesquiterpenes (*m/z* 205) were only available during period 2 corresponding to measurement days from 22^{nd}-30^{th} June. I performed also comparisons for other VOC species including some OVOC species as shown in Figure 18. Generally, good agreements were observed for most of these VOC and OVOC species measured by these two instruments ($R > 0.7$). The correlation slope values of CHARON-PTR-MS to Vocus-PTR-MS varied by up to two orders of magnitude for different VOC. However, most VOC species especially for calibrated species (e.g., isoprene, benzene, toluene and monoterpenes) showed a slope approaching one. I will present more results from these PTR measurements for this field campaign in section 3.4.

I also made a comparison of total organic mass measured by the CHARON-PTR-MS and the AMS in the summertime field campaign of 2021KITcn (Figure 19). There was a good agreement of total organic mass measured by the CHARON-PTR-MS and the AMS ($R = 0.93$). The CHARON-measured organics on average accounted for 61 ± 10% of the AMS mass. The O:C ratios of CHARON-measured organics were always lower than those measured by the AMS. This was likely due to some low-volatility organic compounds were not well detected by the CHARON-PTR-MS. In fact, based on the PMF analysis, low-volatility oxygenated organic aerosol comprised of a large fraction (53%) to total OA mass measured by the AMS. Furthermore, the O:C ratios of CHARON-measured OA were within the range of 0.25-0.40, close to the values (0.26-0.51) for HOA and SV-OOA by the PMF analysis of AMS-measured OA.

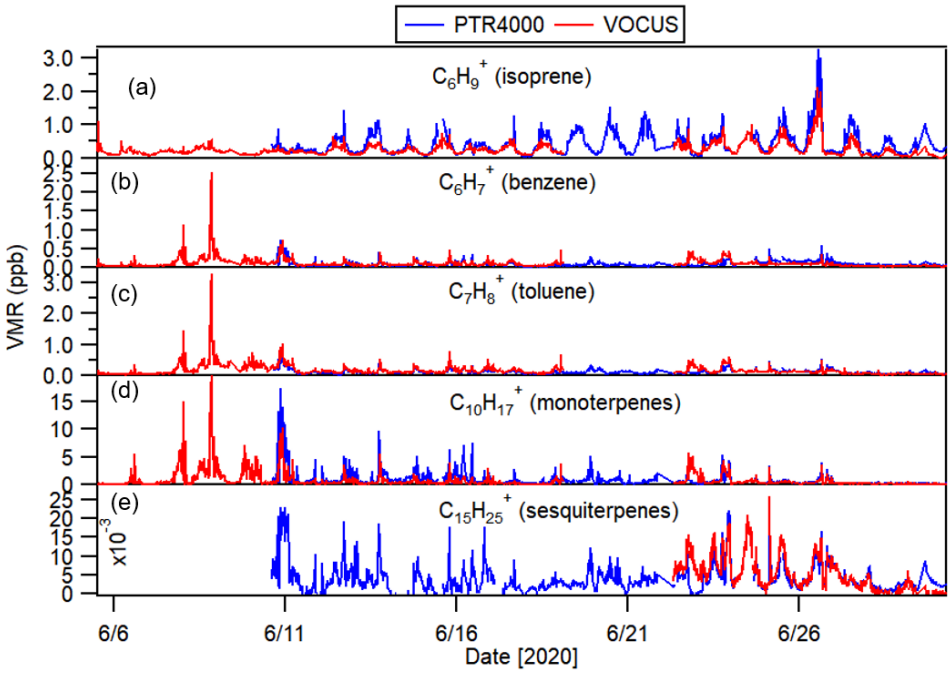

Figure 17 Time series of selected VOCs measured by the PTR4000 and VOCUS-PTR. (a) isoprene, (b) benzene, (c) toluene, (d) monoterpenes and (e) sesquiterpenes. The data of sesquiterpenes from the PTR4000 are not available for 5th-22nd June due to transmission losses.

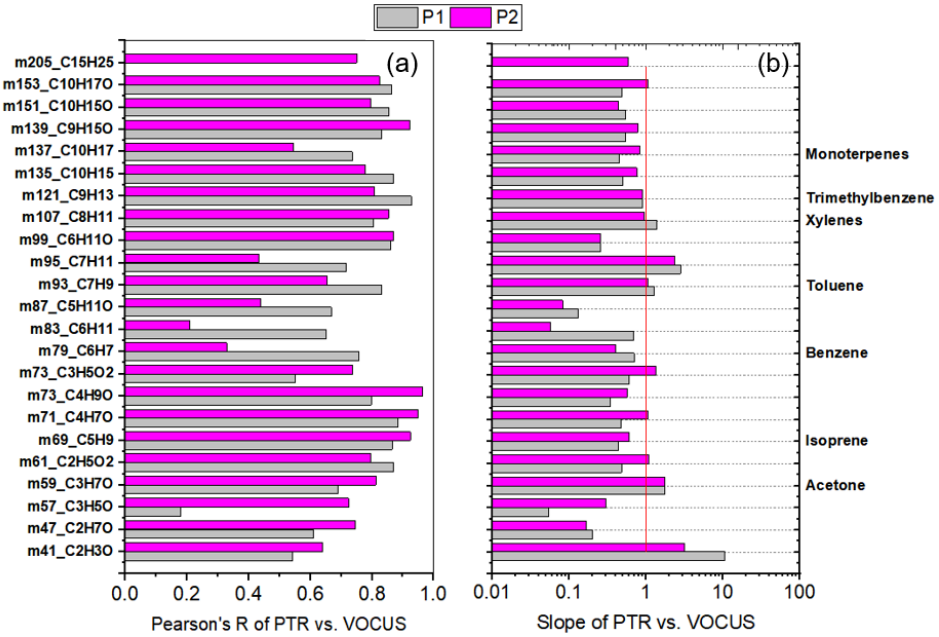

Figure 18 Comparison results of VOC species measured by the CHARON-PTR-MS and VOCUS-PTR-MS during period 1 (P1: 5th-22nd, June) and period 2 (P2: 22nd-30th, June) in the summer campaign of 2020MOSES. (a) correlation coefficients with Pearson's R and (b) slope between CHARON-PTR-MS and VOCUS-PTR-MS. The slope value of 1 is indicated by a red line.

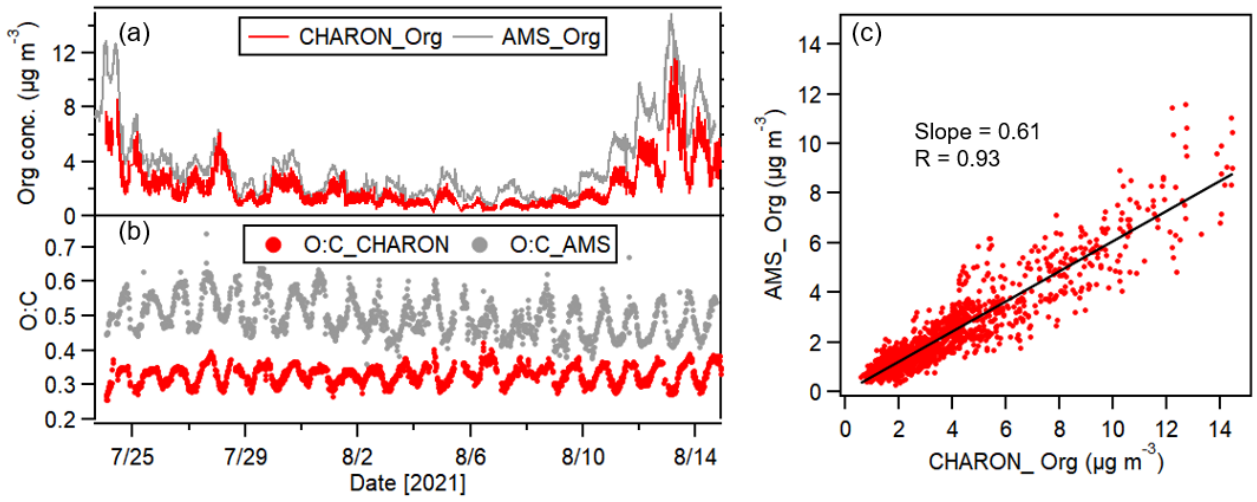

Figure 19 Time series of organic mass concentrations (a) and O:C ratios (b) measured by the CHARON-PTR-MS and AMS in the field campaign at KIT campus north in summer 2021. (c) linear fit of organic mass between the CHARON and AMS.

3.1.3 Characteristics of the FastGC-PTR-MS in chamber and field experiments

In this section, I will demonstrate the capability of the FastGC-PTR-MS for quantifying monoterpene isomers in the AIDA chamber. A mixture of several monoterpenes was oxidized by an excess of ozone, allowing to determine the reaction rate constants of each monoterpene in a single experiment. Furthermore, the FastGC-PTR-MS was deployed at a summer campaign focusing the monoterpene isomers in ambient air.

Figure 20 shows the time series of two ions $C_{10}H_{17}^+$ and $C_6H_9^+$ measured by the FastGC-PTR-MS after successively adding five monoterpenes (a-pinene, β-pinene, limonene, Δ3-carene and myrcene) into the AIDA chamber at room temperature (~293 K). $C_{10}H_{17}^+$ is the monoterpene protonated molecular ion, and $C_6H_9^+$ is the major monoterpene fragment ion. In this experiment, each full run of the FastGC-PTR-MS was set at a time resolution of 5 min, including a real-time VOC measurement of 90 s and a FastGC measurement of 210 s. During the real-time VOC measurements, the signal intensity of $C_{10}H_{17}^+$ and $C_6H_9^+$ showed a gradual increase after the addition of the monoterpenes step by step. In FastGC measurement mode, more peaks appeared in the chromatography with the addition of the monoterpene isomers. These results indicate that FastGC-PTR-MS can well detect these monoterpenes in both measurement modes. Furthermore, when looking at a single chromatogram from a single FastGC-PTR-MS run for these five monoterpenes, it can be clearly seen that FastGC can well separate the monoterpene isomers.

Fragmentation can complicate the interpretation of real-time measurements where there are multiple ions associated with one compound (Claflin et al., 2021; Kari et al., 2018). In the present study, the fragmentation patterns of monoterpenes can be calculated based on the real-time VOC measurement. The fraction of $C_{10}H_{17}^+$ to total signals was ~40% for the α-pinene only, while the fraction decreased slightly to 38% for the mixture of α-pinene and β-pinene. With the subsequent addition of limonene, the fraction of $C_{10}H_{17}^+$ decreased to ~35% for the mixture of α-pinene, β-pinene and limonene. This suggests that limonene showed more fragmentation compared to α-pinene and β-pinene. After adding Δ^3-carene, the fraction of $C_{10}H_{17}^+$ increased back to 38%, and no significant changes after the addition of myrcene were observed. The results showed a small difference (~5%) in the fragmentation among different monoterpene isomers based on the real-time VOC measurement. In fact, the fragmentation of monoterpenes in FastGC measurement more is also within this difference (5%). Therefore, the fragmentation will not introduce a significant bias in the quantification of total monoterpenes with a fixed fragmentation pattern by our PTR-MS instrument. Similarly, Claflin et al., (2021) also reported that all monoterpenes (α-pinene, β-pinene, camphene, Δ^3-carene, and limonene) showed a 1:1 ratio for the fragment ion $C_6H_9^+$ to $C_{10}H_{17}^+$ measured by the GC-Vocus-PTR. Note that the relative fragmentation in different PTR can vary depending on the PTR-MS parameters e.g., collisional energy of the drift tube. Based this discussion, it can be concluded that our PTR-MS can accurately quantify the monoterpenes with a similar fragmentation pattern (37% for $C_{10}H_{17}^+$ and 63% for fragment ions) for all monoterpenes in chamber experiments or field measurements.

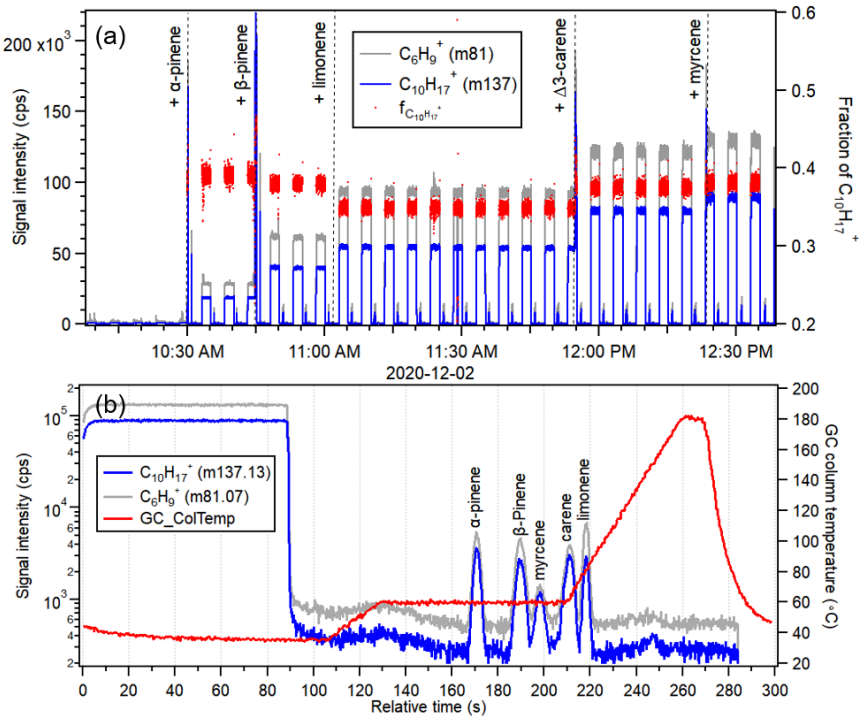

Figure 20 (a) Time series of $C_{10}H_{17}$+ and $C_6H_9^+$ measured by the FastGC-PTR-MS after successively adding five monoterpenes (a-pinene, β-pinene, limonene, Δ3-carene and myrcene) into the AIDA chamber on 2020-12-02. $fC_{10}H_{17}^+$ is the fraction of this monoterpene ion compared to all fragment ions. (b) A single run of the FastGC-PTR-MS including 90 s direct VOC and 210 s FastGC measurements along with the FastGC temperature ramp.

Subsequently, these five monoterpenes were oxidized by different levels of O_3 and OH· radicals in the chamber to produce organic aerosol particles as shown in Figure 21. The first addition of O_3 was around 50 ppb, total monoterpenes showed a significant decrease from ~55 ppb to 30 ppb within 50 min reaction time, leading to the formation of organic aerosol with a mass concentration of ~27 µg m^{-3}. During this time, myrcene was almost fully depleted. After that, a second addition of more O_3 led to the consumption of total monoterpenes to ~20 ppb within another 50 min reaction time, and limonene was fully depleted. An increase of the organic aerosol mass loading by a factor of three was observed simultaneously. Then a third addition of O_3 to ~730 ppb led to the further depletion of monoterpenes (~7.5 ppb) and α-pinene was almost depleted within 35 min reaction time. Simultaneously, the mass concentrations of organic aerosol increased by ~18 µg m^{-3}, Finally, tetramethylethylene (TME) was continuously added into the chamber (~30 min), reaction with the excess of O_3 to form OH· radicals. The remaining monoterpenes (Δ3-carene and β-pinene) were fully oxidized by the OH· radicals. At this stage, the mass concentration of organics increased by ~76 µg m^{-3}, which was contributed by the oxidation of the remaining monoterpenes and other

intermediate compounds produced from the former ozonolysis of monoterpenes. With the real-time VOC and FastGC measurements, the mixing ratios of total monoterpenes and isomers can be quantified simultaneously by the PTR-MS. Over the course of this experiment, the lowest mixing ratios of each monoterpene isomer were approaching the limit of detection (LODs) ranging from 0.2 to 0.6 ppb. These values were similar to the previously reported LODs (1-2 ppb) for the monoterpene separation by a FastGC-PTR-MS system (Materic et al., 2015). Therefore, it would be useful to deploy the FastGC-PTR-MS for the ambient measurement regarding the advantages of high time resolution and low LOD for monoterpene separation.

Furthermore, based on the decay of monoterpene isomer mixing ratios with the successive addition of O_3, the rate constants of monoterpene isomers reacting with O_3 could be determined. These rate constants of monoterpene isomers ozonolysis were determined also in previous studies at 296 ± 2 K using a combination of absolute and relative rate techniques (Atkinson et al., 1990). The experimentally determined rate constants for the monoterpenes followed the order of myrcene > limonene > α-pinene > β-pinene> Δ^3-carene, which is consistent with the fact that Δ^3-carene and myrcene have the highest and lowest reactivity towards O_3 (Atkinson et al., 1990). Therefore, a small amount of O_3 (~15 ppb) can fully consume the myrcene, while Δ^3-carene kept at 2 ppb during high O_3 levels (700 ppb). The rate constants determined for limonene, α-pinene, β-pinene and Δ^3-carene are in good agreement with literature data (Atkionson et al., 1990). This indicates that FastGC-PTR-MS can provide evolution information of monoterpene isomers in high time resolution, which is very useful for kinetic studies. Particularly, we can determine the rate constants of different monoterpene isomers in one experiment by one instrument. This can minimize the uncertainty derived from multiple experiments and/or different instruments. Note that the experimentally measured rate constant for myrcene (9.54×10^{-18} cm^3 $molecules^{-1}$ s^{-1}) was two time higher than the literature value (4.9×10^{-18} cm^3 $molecules^{-1}$ s^{-1}). This overestimation could be due to a part of myrcene simultaneously reacted with the formed OH radicals after the ozonolysis of monoterpenes. Based on the literature (Atkinson et al., 1990), myrcene has higher reaction rate constant with OH radicals (21.3×10^{-18} cm^3 $molecules^{-1}$ s^{-1}) compared to other studied monoterpenes ($5.3\text{-}16.9 \times 10^{-18}$ cm^3 $molecules^{-1}$ s^{-1}) in this study. Furthermore, the OH. reaction rate of myrcene is relatively higher than its ozonolysis rate. The kinetic modelling for this experiment is ongoing, which could improve the calculation accuracy of reaction rate constant, and provide the insights of ozonolysis and OH reaction processes of monoterpene mixture.

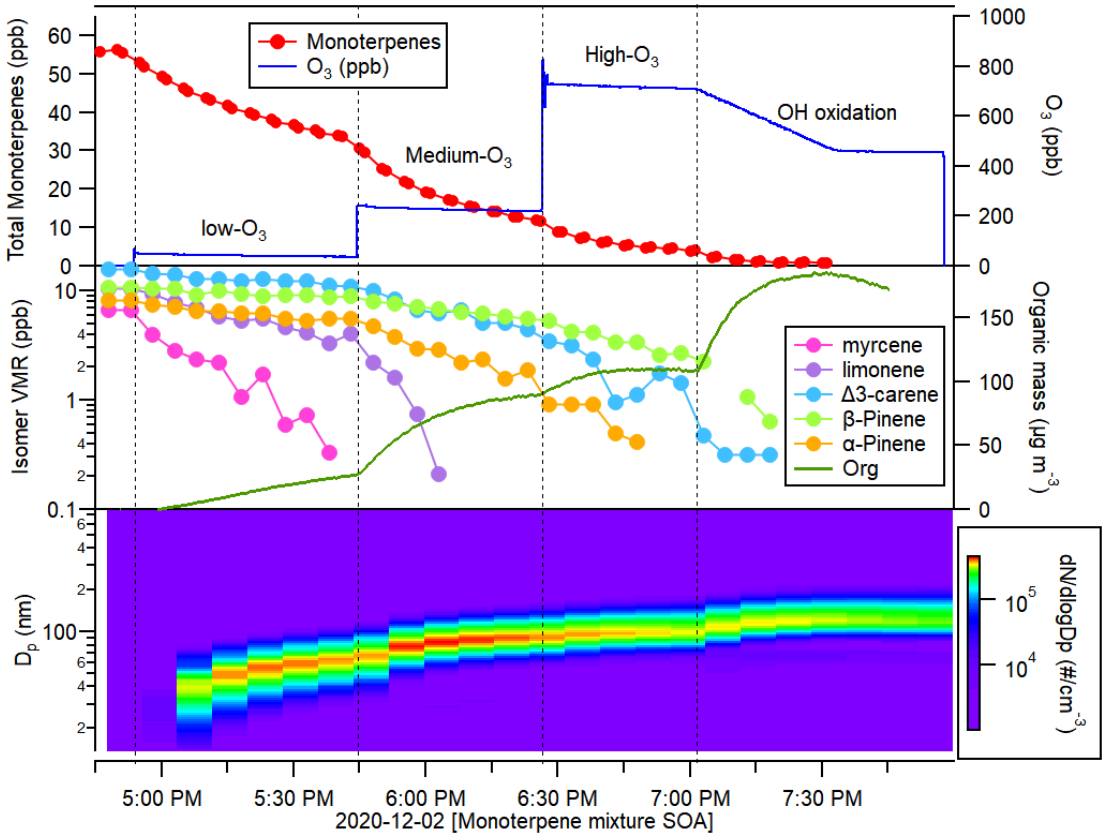

Figure 21 Ozonolysis and OH oxidation of five monoterpenes in the AIDA chamber (a) evolution of total monoterpenes and O_3; (b) evolution of single monoterpene concentrations and organic aerosol mass concentration measured by the AMS; (c) evolution of the particle size distribution measured by the SMPS.

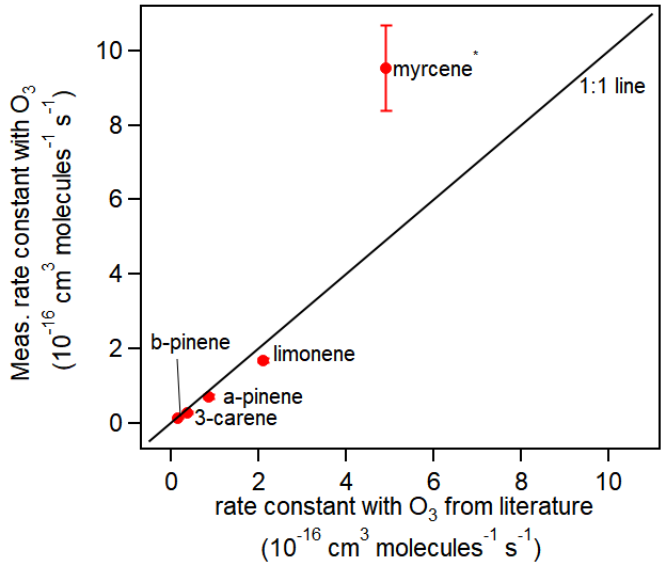

Figure 22 Comparison of the measured rate constant of O_3 with five different monoterpenes compared to literature values (Atkinson et al.,1990) at 296 K. The uncertainty is shown in error bar.

The FastGC-PTR-MS was also deployed for the ambient measurement in a field campaign at a rural site in summer 2021. In this campaign, the FastGC-PTR-MS was operated episodically for the intensive measurement periods. Firstly, the chromatogram of the FastGC for a gas standard and ambient air were compared as shown in Figure 23. It can be clearly be seen that three monoterpene isomers were measured for ambient air by the FastGC, and two isomers could be identified as α-pinene and β-pinene according to my calibrations. The retention time of one uncalibrated monoterpene was within that for α-pinene and β-pinene. Compared to previous studies with the GC-PTR-MS, camphene showed a retention time within that for α-pinene and β-pinene (Claflin et al., 2021; Materic et al., 2015). Even though the separation capability could be different among different GC columns, the relative retention time should be similar. Therefore, it was reasonable to speculate that the uncalibrated monoterpene was camphene. In the chromatogram for the ambient air, also toluene and m/p-xylenes were detected by the FastGC. However, no peak was visible for o-xylene in the chromatogram, suggesting that it was below the detection limit. Consistently, in real-time VOC measurements, the total xylenes showed low mixing ratios (< 1 ppb) during the entire measurement period. The results indicate that anthropogenic VOC emissions were small at this rural location. In contrast, high concentrations of total monoterpenes (>10 ppb) were observed frequently during nighttime, most like steaming from the surrounding pine forest. In the present study, the FastGC-PTR-MS detected α-pinene, β-pinene, camphene as major monoterpenes in the ambient air. This agrees with the typical composition of monoterpenes emitted from pine trees (Janson, 1993; Kainulainen et al., 1992; Räisänen et al., 2009).

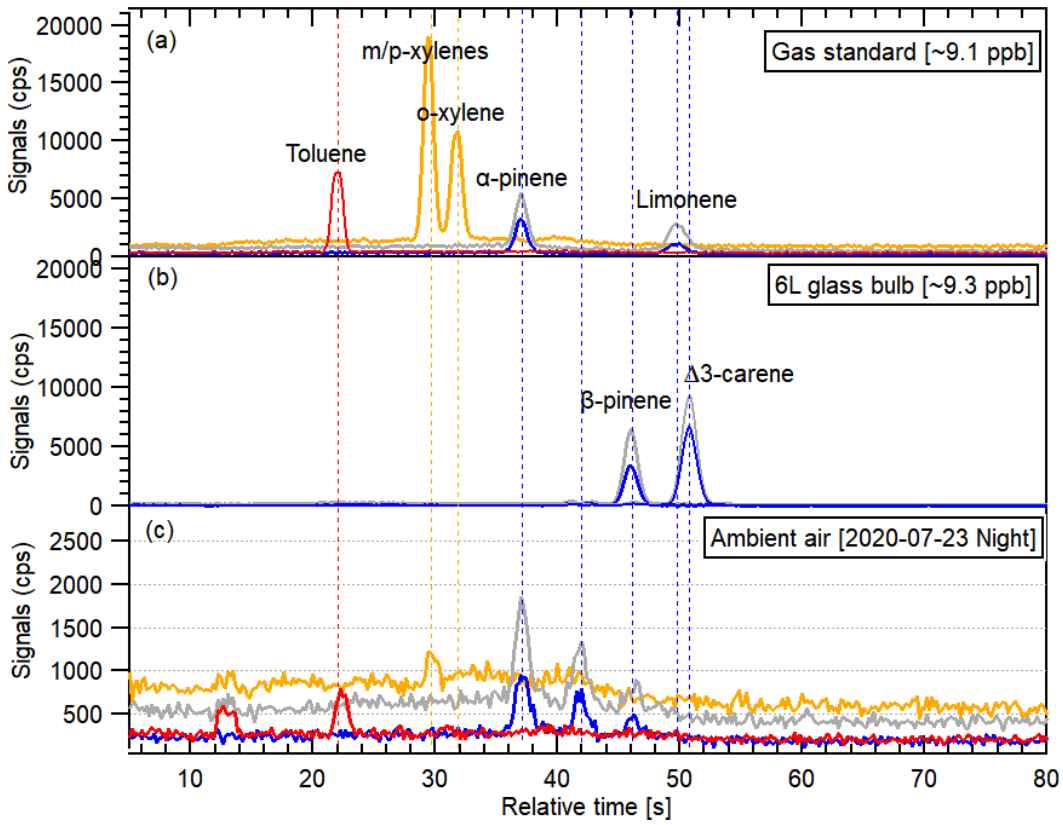

Figure 23 FastGC-PTR-MS chromatograms demonstrating the separation of C_7 and C_8 aromatics and monoterpenes in (a) gas standard, (b) gas standard with a 6-liter glass bulb and (c) ambient air measured at night of 07/23/2020 at KIT campus north. The dash lines showed the midpoint of relative retention time with the compounds labeled.

3.1.4 Summary

To summarize, OA determined by the CHARON correlated linearly (R> 0.9) with that measured by the AMS, and the CHARON total OA mass to AMS can reach up to ~60% in the field campaigns. The oxygen to carbon (O:C) ratios of CHARON-measured OA were within the range of 0.25-0.50, close to that for semi-volatile organic aerosol derived from the AMS. The CHARON can detect less-oxygenated organic molecules typically with the number of oxygen atom of 1-5. Good agreements were also found for calibrated VOC species measured by CHARON-PTR-MS and a Vocus-PTR-MS. The FastGC was applied for the ambient air and can successfully characterize the monoterpene isomers from the pine tree emissions.

3.2 Characteristics of particles and trace gases in downtown Karlsruhe

Over the last decade, many studies based on modern aerosol mass spectrometers like the AMS have improved our understanding on urban aerosol chemistry and air pollution in western European megacities (Crippa et al., 2013b; Freutel et al., 2013). However, few of them were focusing on some of the large number of medium size and typically less polluted cities like Karlsruhe. Even though particle mass concentrations are generally lower in less polluted cities with lower anthropogenic emissions, still short-term pollution episodes with high particle mass concentrations occurred frequently. In this section, I present the results of online characterization of NR-$PM_{2.5}$ using an AMS complemented by collocated measurements of meteorological conditions and trace gases at an urban kerbside in the city of Karlsruhe, southwest Germany, during summer 2019 and winter 2020. The motivation for this study is (1) to characterize the compositions of $PM_{2.5}$ aerosol particles and estimate their potential sources; (2) to investigate the impact of meteorological conditions on $PM_{2.5}$ aerosol species; and (3) to elucidate the major factors for the air pollution episodes with highest $PM_{2.5}$ mass loadings under certain meteorological conditions like heatwaves. I have published the main results from these two field campaigns already (Song et al., (2022), and summarized them in the following.

3.2.1 Temporal variations of aerosol composition and trace gases

The meteorological parameters measured above the container roof (3.5 m a.g.l) and on top of the KIT Physics building (60 m a.g.l) were compared (Figure S2). There were good agreements of temperature, relative humidity and precipitation measured at these two positions. The weather was relatively warm and dry with an average temperature of 3.4 ± 5.8 °C and an average relative humidity (RH) of 57.8 ± 20.2% in summer. In winter, it was colder and more humid with an average temperature of 9.5 ± 4.0 °C and RH of 66.9 ±15.9%. As shown in Figure 24, there were large discrepancies of wind speeds and directions measured at the two different measurement positions. At the container roof, the wind speeds were lower with averages of 0.8 ± 0.4 m s^{-1} in summer and 1.6 ± 0.8 m s^{-1} in winter, and the wind directions were relatively constant over the measurement periods (Figure 24). In contrast, the wind speeds were significantly higher at 60 m above ground on top of the KIT Physics building, where the wind directions were more variable. These results indicate the street canyon effect that the northeast winds in summer were diverted to northwest at the container position, and the predominant southwest winds in winter were channeled to the south.

This was especially visible for wind directions from the west, which were blocked by the nearby tall buildings (e.g., IfGG building of KIT campus south).

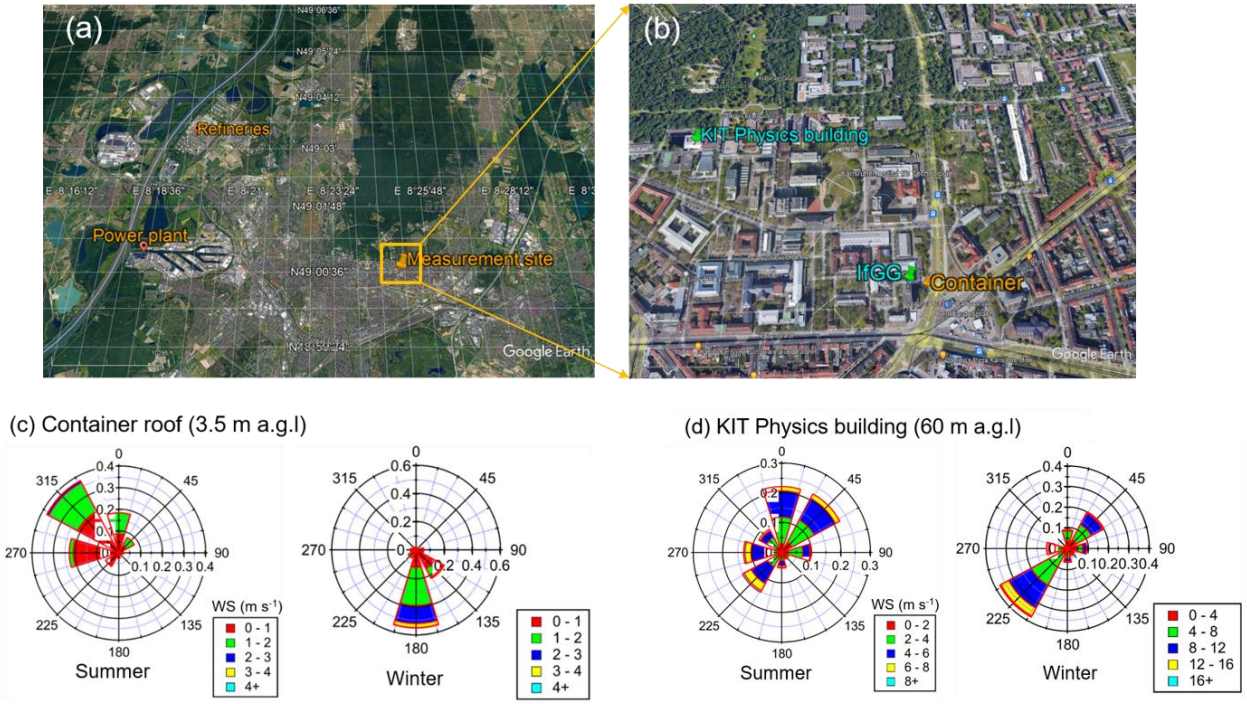

Figure 24. (a) Map of the measurement site in Karlsruhe, Germany and two local industrial emission sites, refinery and power plant (©Google Earth); (b) position of the measurement container in front of the Institute of Geography and Geoecology (IfGG) and ~530 m southeast of the KIT Physics building; (c) and (d) show the wind roses measured at container roof (3.5 m a.g.l) and KIT Physics building (60 m a.g.l) for the two measurement periods, respectively.

Figure 25 shows the time series of temperature, relative humidity, trace gases (O_3, NO_2 and SO_2) and $PM_{2.5}$ and PM_{10} mass concentrations measured by the daily filters (gravimetric), and on-line by OPC in comparison with the NR-$PM_{2.5}$ species measured by AMS. The average concentration of O_3 in summer (36.9 ± 19.6 ppb) was higher than in winter (29.2 ± 10.7 ppb). The concentrations of NO_2 were comparable for both seasons with averages of 9.4 ± 6.3 ppb and 8.8 ± 7.2 ppb in summer and winter, respectively. NO_2 showed frequent spikes over the measurement periods mainly due to the nearby traffic emissions. The data of SO_2 were only available for the winter campaign due to failure of the SO_2 monitor in summer. Generally, very low concentrations of SO_2 (< 1 ppb) were observed. However, we found that SO_2 showed occasionally spikes up to 5 ppb during afternoon to evening hours when the wind direction was from the local industrial source regions in the west. Despite the street canyon effect, local industrial emissions could be still transported downward to the sampling site with enhanced vertical mixing from afternoon to

evening (Figure 24). A similar effect has been shown also by measurements and transport model calculations for SO_2 for a location 10 km north of Karlsruhe in a previous study (Shen et al., 2019).

Good correlations of NR-$PM_{2.5}$ by the AMS and $PM_{2.5}$ by the OPC and the filter samples were observed in both summer and winter (Figure S3). Some differences with lower value for the AMS can be explained because the AMS cannot measure refractory components such as dust and BC. The average mass concentrations of NR-$PM_{2.5}$ (5.8 ± 2.8 µg m^{-3}) were higher in summer than those measured in winter (3.9 ± 3.6 µg m^{-3}). For BC, lower values were also observed in winter (0.46 ± 0.46 µg m^{-3}) compared to those in summer (0.69 ± 0.42 µg m^{-3}). Actually, I had expected higher aerosol concentrations in winter. However, during March 2020, most probably frequent stormy periods with substantial rain caused corresponding dilution, wet deposition, and hence lower average mass concentrations. Nonetheless, for two episodes (E1 and E2) with special weather conditions, I observed significantly enhanced $PM_{2.5}$ mass concentrations, which were higher than the World Health Organization annual limit value (10 µg m^{-3}). Episode 1 (E1, 22-27 July 2019) had five consecutive days with daily maximum temperature over 30 °C and is thus classified as a heatwave episode. Episode 2 (E2, 13-31 March 2020) is classified as a transitional episode with the meteorology switching from relatively warm and humid conditions (13-20 March 2020) to cold and dry conditions (22-31 March 2020) in winter. I focus especially on the driving factors for these air pollution episodes, which will be discussed in-depth in section 3.2.4.

In both seasons, organics represented the major fraction of $PM_{2.5}$ particle mass, accounting on average for 60 ± 12% and 44 ± 10% of NR-$PM_{2.5}$ plus BC mass in summer and winter respectively. The average contributions of sulfate and ammonium to the total NR-$PM_{2.5}$ plus BC mass were comparable in summer (18 ± 9% and 6 ± 4%) and winter (13 ± 7% and 9 ± 4%), while the contribution of nitrate significantly increased from 6 ± 4 % in summer to 22 ± 8 % in winter. This is expected because nitrate is a semi-volatile component, which partitions into the particle phase at lower temperatures in winter. The seasonal composition profile of NR-$PM_{2.5}$ plus BC observed in this study is comparable to those of NR-PM_1 plus BC in other European cities e.g, Paris and Barcelona (Crippa et al., 2013a; Minguillon et al., 2016). In this study, $PM_{2.5}$ was mainly contributed by PM_1 as indicated by the OPC, therefore the difference between NR-$PM_{2.5}$ and NR-PM_1 was negligible.

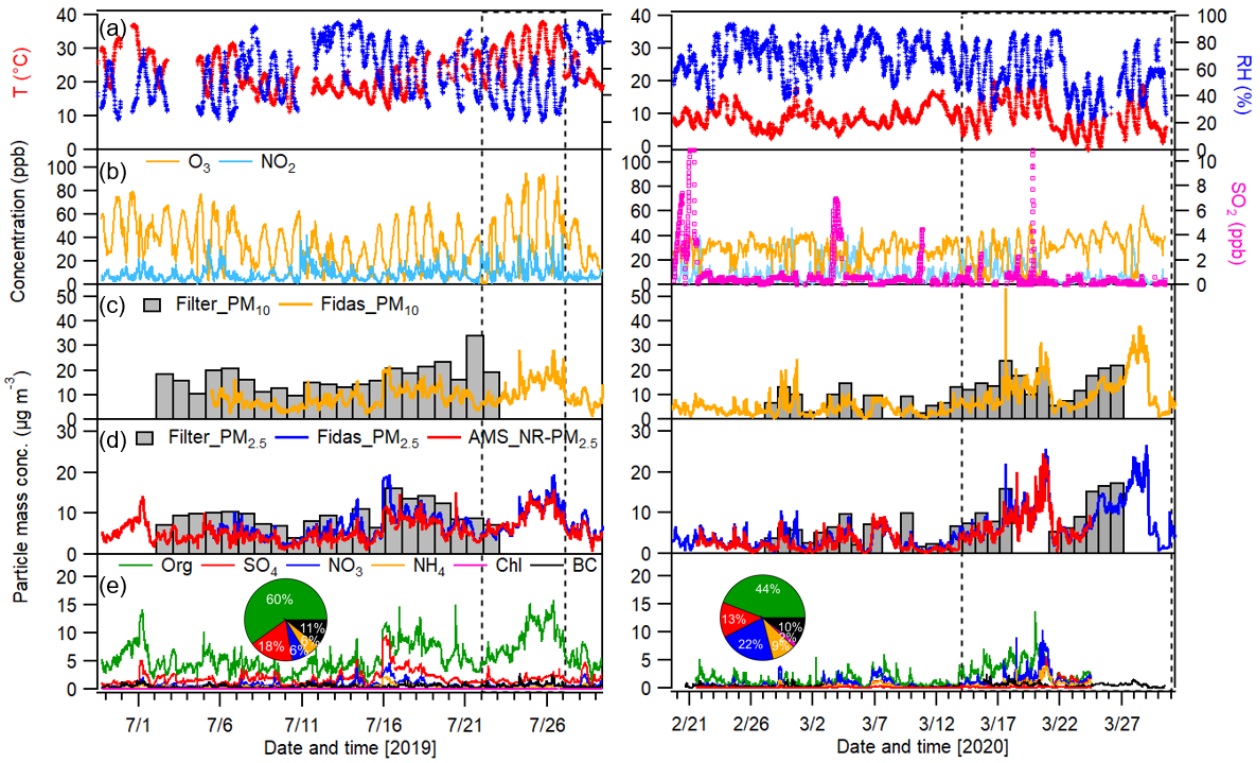

Figure 25. Time series of (a) temperature (T) and relative humidity (RH); (b) trace gases (O_3, NO_2, SO_2), the SO_2 data were not available in summer due to instrument failure; (c-d) PM_{10} and $PM_{2.5}$ mass concentrations obtained from daily filters, Fidas-OPC and NR-$PM_{2.5}$ from AMS; and (e) organics (Org), sulfate (SO_4), nitrate (NO_3), ammonium (NH_4) and chloride (Chl) and black carbon (BC) in summer 2019 (left) and winter 2020 (right). Pie charts show the relative contribution of aerosol components to total NR-$PM_{2.5}$ + BC mass. The two episodes marked by dashed lines are discussed in more detail in the main text.

3.2.2 Diurnal variations of aerosol components and trace gases

The diurnal behavior of $PM_{2.5}$, NR-$PM_{2.5}$ species, and BC during the two seasons is shown in Figure 26. The diurnal variations of meteorological parameters, trace gases, and particle number concentrations are presented in Figs. S4-S5. Given that the measurement site was only 5-10 m away from a major road, I compared the diurnal patterns on weekdays and weekends to investigate the impact of traffic on aerosol particles and trace gases. Since in Karlsruhe, the traffic activities do usually not decrease significantly on Saturday, we defined weekdays as being from Monday to Saturday and weekends only include Sunday.

The diurnal variations in meteorological conditions did not change significantly between weekdays and Sundays in both seasons, except that higher relative humidity was occasionally observed during Sundays in summer. Total $PM_{2.5}$, BC, NO_2, and particle number concentrations

showed two peaks in the morning (7:00-9:00) and evening hours (21:00-23:00) at weekdays in both seasons. The period of 7:00-9:00 typically corresponds to the morning rush hours in Karlsruhe. Therefore, the morning peaks indicate the important contribution of primary traffic emissions. As expected, these pollutants showed less pronounced peaks at 7:00-9:00 on Sundays with less traffic. However, I can observe enhanced BC, NO_2 and particle number concentrations on Sunday evenings (21:00-23:00). These increased evening values observed for every day are not only related to primary emissions but also to a reducing planetary boundary layer (PBL) height. According to the ERA5 reanalysis data, lower PBL heights were found during evenings in both seasons (Figure S6). Furthermore, lower wind speeds were observed during evenings, which could lead to an accumulation of air pollutants.

The diurnal behaviors of NR-$PM_{2.5}$ compounds varied significantly for both seasons. In summer, slightly higher mass concentrations of organics were observed during nighttime, which was likely associated with low PBL heights and nighttime chemistry (Huang et al., 2019a; Shen et al., 2019). However, organics showed a clear peak at evening hours (20:00-21:00) in winter. This peak was related to the biomass burning emissions, which will be validated in the following section. No significant differences in diurnal variations of organics were found between weekdays and Sundays for both seasons. Sulfate and ammonium showed relatively flat diurnal cycles at weekdays in both seasons, similar to previous observations at European urban sites (Crippa et al., 2013a; Crippa et al., 2013b; Huang et al., 2019b; Lanz et al., 2010). This is explained by the fact that ammonium sulfate is typically formed on a regional scale. In present study, I also found several cases with rapid increase sulfate and ammonium from afternoon to evening in summer (e.g., 1st and 16th July) as shown in Fig. S7. These cases always occurred along with the shift of westerly winds with high speeds to northerly winds with low speeds. The westerly winds may bring the industrial emissions from local coal-fired power plant in the west of sampling site (Figure 24). Subsequently enhanced vertical mixing processes during nighttime lead to the accumulation of ammonium sulfate within the street canyon. Nitrate exhibited an even stronger increase over the nights from Saturday to Sunday in summer. Note that higher RH (> 80%), lower temperatures (< 20 °C) and lower WS were observed during the nights from Saturday to Sunday in summer. Under such meteorological conditions during nighttime, nitrate can be formed effectively via gas to particle conversions and subsequently accumulation in the street canyon. Besides, nitrate showed a fast decrease during summer daytime due to the evaporation processes at higher temperatures.

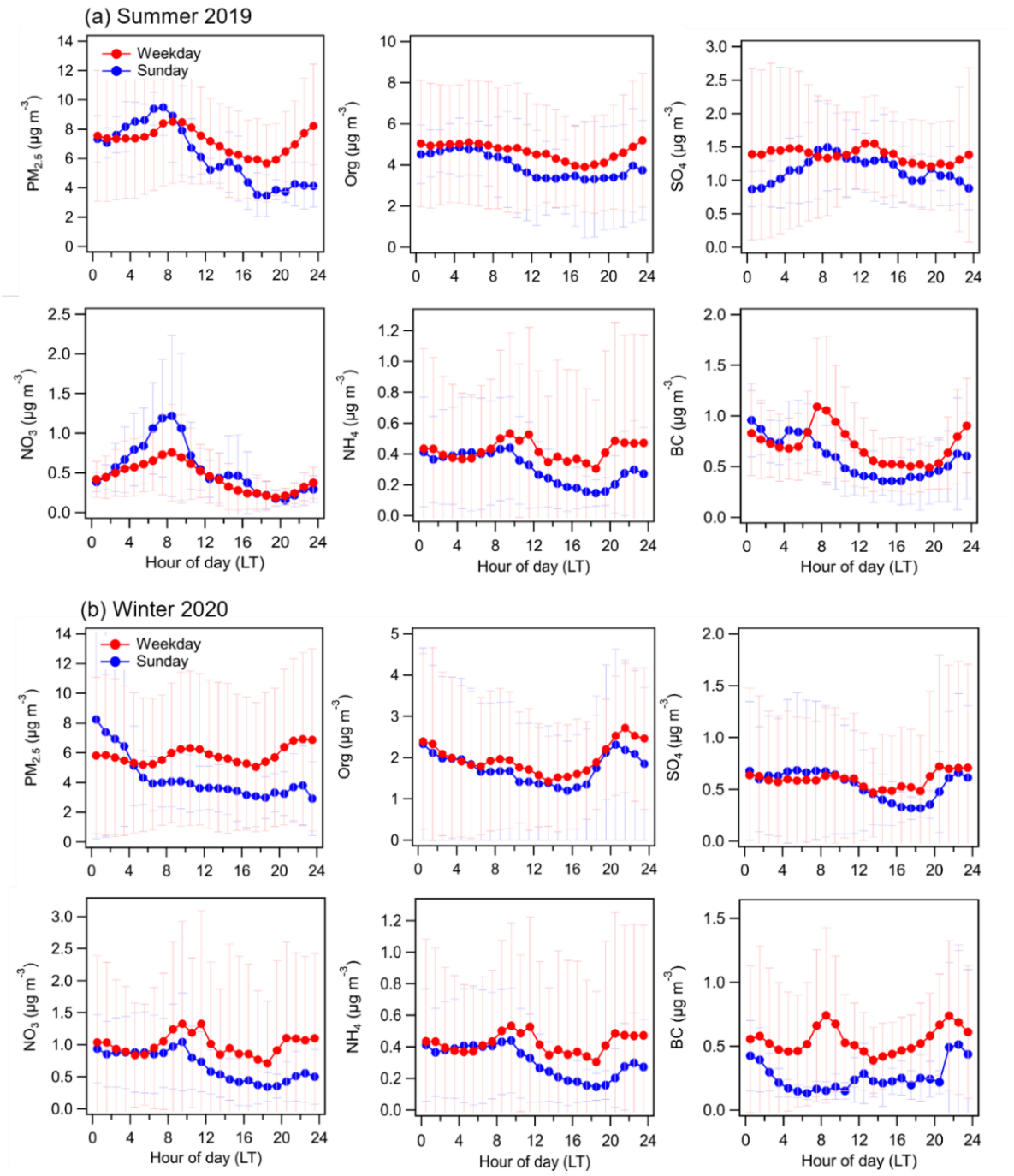

Figure 26. Diurnal variations of $PM_{2.5}$, NR-$PM_{2.5}$ species including organics (Org), sulfate (SO_4), nitrate (NO_3) and ammonium (NH_4) and BC over the entire measurement periods in (a) summer 2019 and (b) winter 2020. The circles represent the hourly data averaged over weekdays (Monday-Saturday, red) and Sundays (blue). For both summer and winter, the NR-$PM_{2.5}$ data are available for five Sundays (~720 data points). The error bars show ± one standard deviation.

3.2.3 Seasonally source apportionment of OA

In this study, positive matrix factorization (PMF) was employed for source apportionment based on organic aerosols measured by AMS. The mass spectra, time series, diurnal behavior, and relative contributions of all OA factors identified for summer and winter are shown in Figure 27 and Figure 28, respectively.

Hydrocarbon-like OA (HOA) was identified in both summer and winter. HOA mass spectra were characterized with low O:C ratios (0.17 in summer and 0.12 in winter) and high H:C ratios (1.90 in summer and 1.96 in winter). The mass spectra of HOA were dominated by alkyl fragments ($C_nH_{2n\pm1}$), which were similar to those reported for other urban sites (Crippa et al., 2014; Lanz et al., 2010; Mohr et al., 2012; Mohr et al., 2009; Sun et al., 2011). In both seasons, HOA showed good correlations with $C_4H_9^+$ (R = 0.90 in summer, 0.97 in winter), a tracer ion of primary traffic emissions (Canagaratna et al., 2010; Mohr et al., 2009). BC showed similar temporal variations as HOA, but there were no strong correlations (R = 0.41-0.43) in both seasons. I investigated the relative influence of traffic and biomass burning sources on BC measured by the MA200 using the method described by (Sandradewi et al., 2008a), which is shown in the Figure S8. The BC was dominated by traffic sources in summer, while it was also significantly influenced by biomass burning in winter. In fact, there were many BC spikes with and without concurrent increase of HOA in summer morning rush hours, which lead to a weak correlation of BC and HOA. This may be explained by different HOA/BC emission ratios of different vehicles and fuel types of the cars passing the traffic junction. Generally, gasoline vehicles have higher emission ratios of HOA/BC (0.9-1.7) than diesel vehicles (0.03-0.61) (DeWitt et al., 2015). In this study, the median ratio of HOA/BC was 0.48 in summer, suggesting the traffic was dominated by diesel engine emissions. Furthermore, HOA showed good correlations with benzene, toluene and xylenes measured by the PTR-MS during winter (Fig. S9, R = 0.6-0.7), indicating that HOA was mainly traffic related. The contributions of HOA to total OA were on average 6 ± 5% in summer and 11 ± 9% in winter. The HOA contributions were compared well with that in total OA in NR-PM_1 (11 ± 6%) measured at 17 urban sites throughout Europe (Crippa et al., 2014), but lower than the fractions (19-26%) reported in Asian roadside environment (Lee et al., 2015; Yao et al., 2021). Note that our AMS system cannot measure ultrafine particles (< 70 nm) effectively due to focusing limits of the aerodynamic lens. Therefore, the HOA contribution in this study can be considered as a lower estimate in $PM_{2.5}$ for European urban areas. In general, ultrafine particles are related to traffic

emissions in urban environments (Hofman et al., 2016; Shi et al., 1999). I calculated the wintertime diurnal pattern of ultrafine particles with sizes from 2.5 nm to 7 nm based on the difference of two CPCs. These ultrafine particles showed similar diurnal patterns as HOA indicating that they were from common traffic emissions.

In this study, COA was observed in both seasons and its mass spectra were characterized with relatively high fractions of hydrocarbon ions ($C_nH_{2n\pm1}$) and slightly oxygenated ions such as $C_4H_7^+$ (*m/z*55), $C_4H_9^+$ (*m/z*57), $C_3H_3O^+$ (*m/z*55) and $C_3H_5O^+$ (*m/z*57). The O/C ratios of COA were 0.23 in summer and 0.25 in winter, which are comparable to the values of COA reported for other urban areas, (Mohr et al., 2012; Sun et al., 2011). Compared to HOA, the mass spectrum of COA showed a higher ratio (> 2) between the fraction of *m/z*55 to *m/z*57 in total organic signals in both summer and winter, which is consistent with previous studies (Crippa et al., 2013a; Mohr et al., 2012). In both seasons, COA correlated well with an ion $C_6H_{10}O^+$ (R = 0.94 in summer and 0.77 in winter), a tracer for cooking activities reported by many studies in urban atmospheres (Crippa et al., 2014; Mohr et al., 2012). The diurnal variation of COA was only characterized with one pronounced peak in the evening hours (20:00-22:00) corresponding to dinnertime. The contribution of COA to total OA mass was on average 12 ± 7% in summer and 16 ± 11% in winter, consistent with average values of ~15% OA in PM_1 reported in previous studies at European urban sites (Crippa et al., 2013a; Mohr et al., 2012).

Biomass burning-related OA (BBOA) was only determined in winter. This was in line with the fact that wood combustion is typically used for residential heating during wintertime in Europe (Crippa et al., 2014; Crippa et al., 2013a; Lanz et al., 2010). The mass spectrum of BBOA showed a higher fraction of $C_2H_4O_2^+$ (1.41% at *m/z*60) compared to that in non-BBOA (0.3%) (Crippa et al., 2014; Cubison et al., 2011; DeCarlo et al., 2008). As reported by previous studies (Cubison et al., 2011; Lanz et al., 2010; Mohr et al., 2012), AMS-measured $C_2H_4O_2^+$ mainly derived from the fragmentation of anhydrous sugars such as levoglucosan. In this study, I observed good correlations of $C_2H_4O_2^+$ with the levoglucosan-related fragmentation ions of $C_6H_9O_4^+$ and $C_4H_5O_2^+$ in the particle phase measured by the CHARON-PTR-MS (Fig. S9) (Muller et al., 2017). Therefore, $C_2H_4O_2^+$ can be regarded as a good tracer for biomass burning. Consequently, BBOA showed a strong correlation with that of $C_2H_4O_2^+$ (R = 0.92). Furthermore, BBOA had a good correlation (R = 0.78) with furfural measured by PTR-MS, a tracer for wood combustion (Bruns et al., 2017; Coggon et al., 2016). Based on the results above, it is robust to attribute BBOA to the residential

wood combustion. The concentration of BBOA showed a strong increase during nighttime and reach the maximum at ~20:00-21:00, which was associated with strong emissions from residential heating activities and a shrinking PBL height. To our best knowledge, wood combustion is actually less used in the downtown Karlsruhe, but more widely in the surrounding rural areas. The O/C ratio of BBOA (0.69) in this study was higher than those reported for fresh biomass burning emissions (0.15-0.5) (Ortega et al., 2013), but close to that of aged or transported BBOA (0.5-0.87) (Gilardoni et al., 2016; Rodelas et al., 2019). Recent field measurements and chamber studies (Gilardoni et al., 2016; Kodros et al., 2020; Rodelas et al., 2019) suggested primary BBOA can undergo rapid dark aging within a few hours especially for high relative humidity. In this study, we observed higher relative humidities (> 60%) during nighttime in winter, which could promote aqueous-phase processing of BBOA within the street canyon. The contribution of BBOA to total OA is on average 25 ± 12%, making biomass burning emissions the second largest contributor to organic aerosol particle mass in winter. This is at the upper end of the range of BBOA contributions to total OA (5-27%) in PM_1 as reported by Crippa et al. (2014) for 17 different locations in Europe but comparable to values of (3-39%) observed for traffic environments in the Helsinki metropolitan area in winter (Pirjola et al., 2017).

Two types of oxidized organic aerosols (OOAs) of different volatility (SV-OOA and LV-OOA) were identified from the PMF analysis of AMS OA mass spectra for both seasons. They can be regarded as representative of secondary organic aerosol (SOA) (Crippa et al., 2014; Jimenez et al., 2009). In summer, the mass spectrum of SV-OOA showed a O/C ratio of 0.35, which was within the range of SV-OOA (0.35 ± 0.14) (Ng et al., 2010). Unexpectedly, SV-OOA is poorly correlated with nitrate (R = 0.24) over the entire summer measurement period, suggesting that they have different sources and/or formation processes. Nitrate can be formed rapidly from traffic-related NO_2 emissions at morning rush hours, which deteriorates the correlation of SV-OOA and nitrate. If considering the data during nighttime (00:00-06:00) with less traffics, the correlation between SV-OOA and nitrate was improved to R = 0.45. Furthermore, a strong correlation of SV-OOA and nitrate was observed during the heatwave episode (R = 0.90), reflecting the volatile nature of these compounds. In summer, the average contribution of SV-OOA to total OA was 19 ± 10%. This is lower than the average fraction 34% ± 11% of SV-OOA to OA in NR-PM_1 determined by Crippa et al. (2014) for 17 different locations in Europe for spring and autumn. In summer, LV-OOA was separated into two factors LV-OOA1 and LV-OOA2. The two LV-OOA factors showed similar

mass spectral patterns, yet their temporal variations differ greatly. LV-OOA1 and LV-OOA2 showed O/C ratios of 0.70 and 0.72 respectively, which were close to those of LV-OOA (0.6-1.0) in previous studies (Crippa et al., 2013b; Jimenez et al., 2009). LV-OOA1 showed better correlation with sulfate (R = 0.53) compared to other factors (< 0.2), suggesting that LV-OOA1 was related to regional transport. In contrast, LV-OOA2 showed a better correlation with O_x ($O_x = NO_2 + O_3$, R = 0.57) compared to other factors, suggesting that it was attributed by photochemical oxidation processes. LV-OOA1 showed a relatively flat diurnal trend, while LV-OOA2 showed significant enhancements during daytime as O_3 and radiation increased. In addition, significant increases of LV-OOA2 were found during days with influence of local air masses, while LV-OOA1 showed a decrease correspondingly (Fig. S10). Therefore, LV-OOA1 was associated with regional transport and LV-OOA2 was attributed by local photochemical oxidation processes in summer. The contributions of LV-OOA1 and LV-OOA2 to total OA were 26 ± 17% and 38 ± 17%, and their total contribution is higher than LV-OOA (50% ± 16%) determined for 17 different locations in Europe for spring and autumn (Crippa et al., 2014).

In winter, SV-OOA and LV-OOA showed higher O/C ratios of 0.55 and 1.00, respectively. Similar to the results in summer, the mass spectrum of SV-OOA showed a predominant fraction of $C_2H_3O^+$, while CO_2^+ was the prominent peak in LV-OOA mass spectrum. The diurnal profile of SV-OOA was anti-correlated to that of temperature as summertime SV-OOA. LV-OOA correlated well with both nitrate and sulfate (Pearson's R: 0.83 and 0.77) but not with O_x, indicating that LV-OOA was associated with regional transport as summertime LV-OOA1. Moreover, higher mass concentrations of LV-OOA were observed during daytime along with higher WS, indicating that LV-OOA was associated with regional transport in winter again. Overall, the contributions of SV-OOA and LV-OOA to total OA in winter were 14% ± 10% and 34% ± 20% respectively.

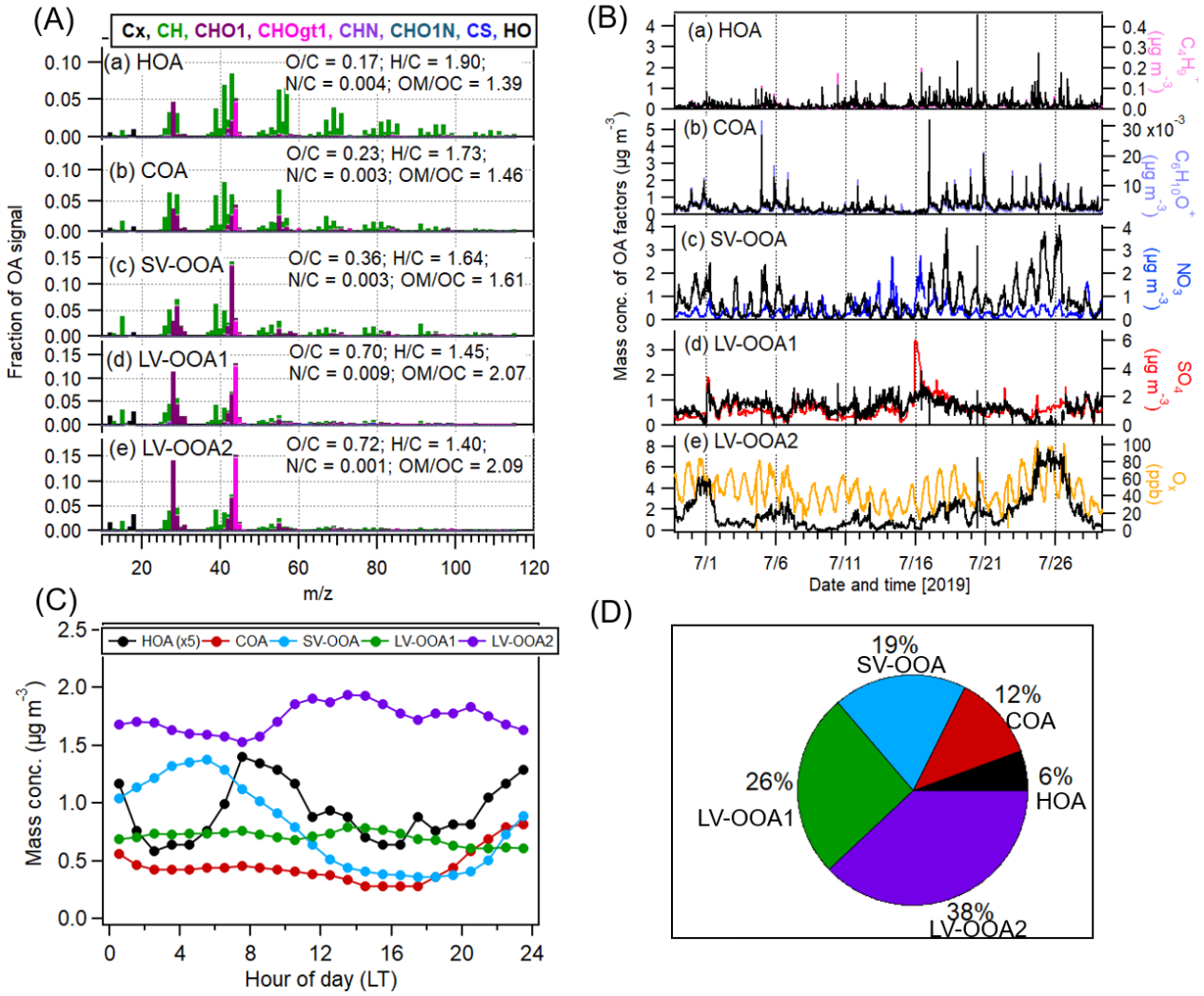

Figure 27. Mass spectra (A) and time series (B) of five PMF-resolved organic aerosol (OA) factors at Durlacher Tor, Karlsruhe for summer 2019. The time series of additional tracers including fragment ions ($C_4H_9^+$ and $C_6H_{10}O^+$), nitrate (NO_3), sulfate (SO_4) and O_x (= O_3 + NO_2) are given for comparison. HOA = hydrocarbon-like OA; COA = cooking-related OA; SV-OOA = semi-volatile oxidized OA and LV-OOA = low-volatile oxygenated OA (LV-OOA1 and LV-OOA2). (C) and (D) show the diurnal patterns and relative contributions of OA factors, respectively.

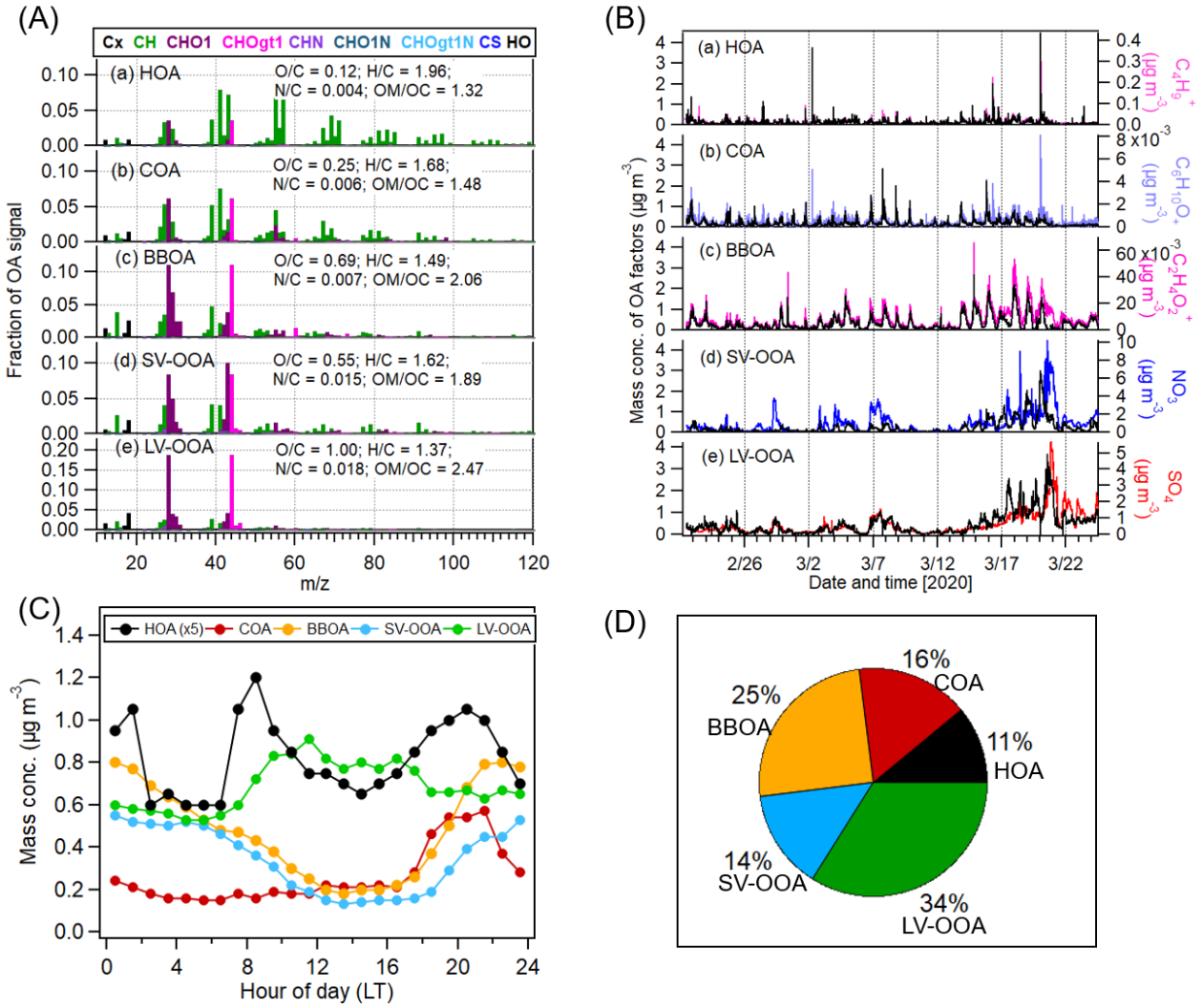

Figure 28. Mass spectra (A) and time series (B) of five PMF-derived organic aerosol (OA) factors at Durlacher Tor, Karlsruhe for winter 2020. The time series of additional tracers including fragment ions ($C_4H_9^+$, $C_6H_{10}O^+$ and $C_2H_4O_2^+$), nitrate (NO_3), sulfate (SO_4) are given for comparison. HOA = hydrocarbon-like OA; COA = cooking-related OA; BBOA = biomass burning-related OA; SV-OOA = semi-volatile oxygenated OA; LV-OOA = low-volatile oxygenated OA. (C) and (D) show the diurnal patterns and relative contributions of OA factors, respectively.

3.2.4 Factors controlling air pollution episodes

Summer heatwave (Episode 1): As mentioned above, a 5-day summer heatwave episode with significant enhancements of $PM_{2.5}$ mass loadings was observed from July 22nd to 26th 2019. As shown in Figure 29, organic components were the largest contributor, accounting for 80 ± 6% of NR-$PM_{2.5}$ mass, followed by sulfate (13 ± 5%) and nitrate (4 ± 2%) during this episode. Organics are mainly comprised by SOA including SV-OOA, LV-OOA1, and especially LV-OOA2. In this episode, the average temperature and relative humidity were 28.9 ± 5.5 °C and 45.2 ± 16.2% respectively. High temperatures can favor emissions of biogenic VOCs, leading to the subsequent production of SOA. The wind conditions measured at the KIT Physics Building show the influence of air masses originating from forested areas in northeast and east of the measurement site, which was consistent with the results of back-trajectory analysis. Therefore, the formation of SOA was possibly attributed to local biogenic emissions in this heatwave episode.

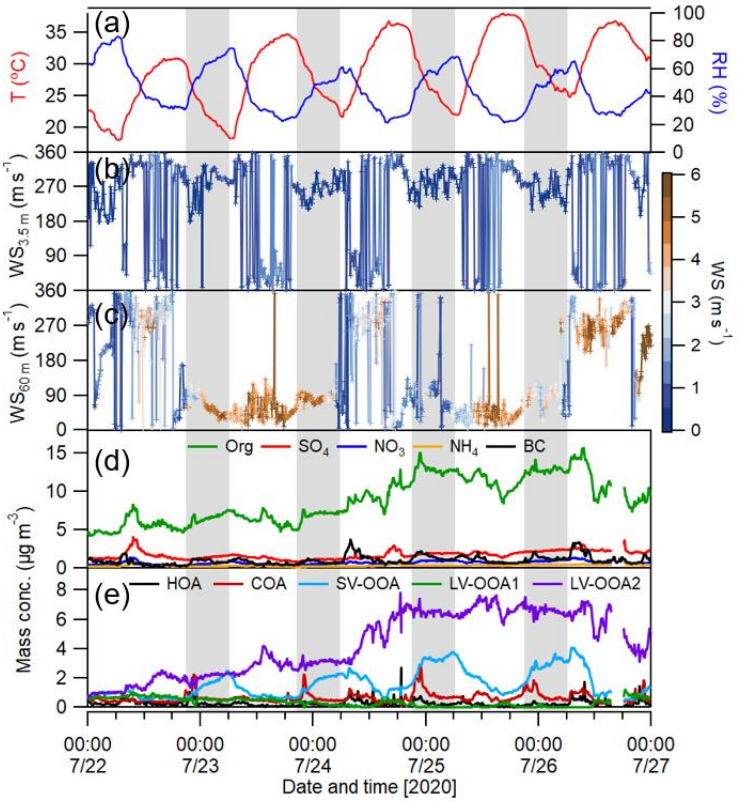

Figure 29. Time series of (a) temperature and relative humidity; (b-c) wind speed and wind direction above the container roof (3.5 m a.g.l) and the KIT Physics building (60 m a.g.l); (d-e) mass concentrations of NR-$PM_{2.5}$ aerosol species and BC and organic aerosol factors during the heatwave episode from 22nd to 26th July in 2019. The grey areas represent the nighttime.

High concentrations of SV-OOA were observed during nighttime of this heatwave episode. Similar diurnal behavior of SV-OOA was also observed in previous summertime measurements at a rural site north of Karlsruhe, showing a strong influence of nighttime chemistry of biogenic VOCs for organic nitrate formation (Huang et al., 2019a; Shen et al., 2019). In this study, I calculated the functionality of organic nitrate ($pOrgNO_3$) based on the intensity ratio of NO_2^+ and NO^+ ions by the AMS (Huang et al., 2019a; Kiendler-Scharr et al., 2016). Consequently, a strong correlation was observed between $pOrgNO_3$ and SV-OOA (R = 0.96). Furthermore, the mass concentrations of $pOrgNO_3$ showed good correlations (Fig. S11, R = 0.56-0.83) with the indicator of nitrate radical production ($[NO_3] = [NO_2]*[O_3]$) during the nighttime (Huang et al., 2019a). These results indicate the importance of nighttime chemistry on $pOrgNO_3$ from BVOC oxidation and thus SV-OOA formation even for urban areas.

In contrast to the diurnal pattern of SV-OOA, the concentrations of LV-OOA2 showed a continuous increase during the heatwave episode while LV-OOA1 was decreasing (Figure 29). This was consistent with above result that LV-OOA1 was associated with the regional transport, while LV-OOA2 was mainly from the local photochemical formation. Therefore, continuous increasing of LV-OOA2 mass indicates the important role of local photochemical oxidation during the heatwave episode. The LV-OOA2 mass showed an exponential relationship with air temperature, which was associated with biogenic VOC emission and oxidation. Generally, the emissions of biogenic VOCs especially for monoterpenes exponentially depend on the air temperature (Guenther et al., 1993). There were no measurements of VOCs in summer, I obtained the molecular composition information of oxygenated OA from the filter samples analyzed by CIMS (Fig. S12). In summer, the highest contribution of the molecule $C_8H_{12}O_5$ (2-hydroxyterpenylic acid) was found, which can be regarded as a marker compound of α-pinene SOA (Claeys et al., 2009). Therefore, it is reasonable to speculate that SOA (especially LV-OOA2) is mainly of biogenic origin even near the traffics. Furthermore, the ratios of LV-OOA/SV-OOA also correlated well with temperature during the heatwave episode, which could be fitted with an exponential function as shown in Fig. 7. In addition to the biogenic emissions, increasing air temperatures could also enhance the atmospheric oxidation capacity (Tsigaridis and Kanakidou, 2007), possibly leading to a more efficient transformation of SV-OOA to LV-OOA. Strong positive correlations of air temperature with O_x and O/C ratios of bulk OA were observed (Figure 30), confirming the enhanced atmospheric oxidation capacity during the heatwave episode. Please note

that SV-OOA evaporation at higher temperatures also leads to higher LV-OOA/SV-OOA ratios. Overall, low WS, air mass origins from forested areas with increasing biogenic emissions, and high temperatures with enhanced oxidation potential support formation and accumulation of biogenic SOA. Therefore, biogenic SOA can play an important role in aerosol pollution even near the traffic during summertime.

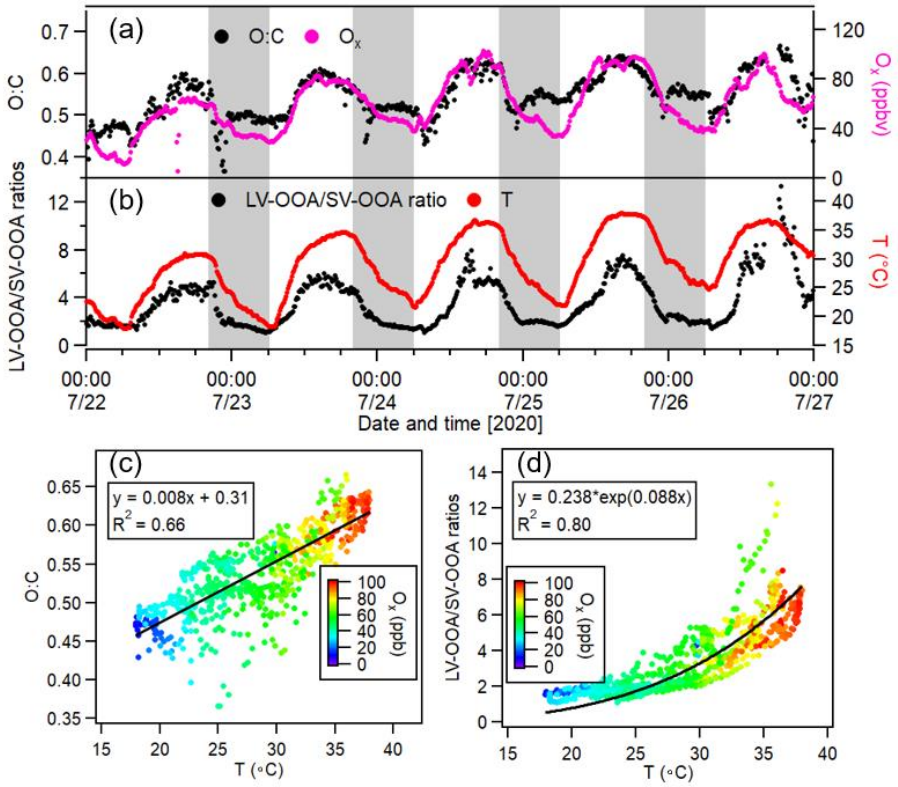

Figure 30. Time series of (a-b) O:C ratios of total organics, O_x concentration, LV-OOA/SV-OOA ratios and temperature. The grey areas represent the nighttime. (c-d) relationships between T and O:C ratios of total organics, and LV-OOA/SV-OOA ratios colored by the O_x concentrations during the heatwave from 22nd to 26th July in 2019.

Winter transitional period (Episode2): In winter, an episode with significantly increasing $PM_{2.5}$ mass was found from March 13th to and 21st and again from March 22nd to 30th, 2020 (Figure 31). Based on the meteorological conditions, this episode was further divided into two stages as Stage 1 (March 13th to 21st) and Stage 2 (March 22nd to 30th). Stage 1 represents a relatively warm and humid period with an average temperature of 12 ± 4 °C and RH of 61 ± 14%. After a heavy rain event on March 21st, it transited to Stage 2 with colder and dryer conditions (T: 5 ± 3 °C and RH: 43 ± 14%). During Stage 1, low WS were measured at both container roof and KIT Physics building, thus these stagnant conditions allowed an accumulation of air pollutant. In contrast, high WS and constant northeasterly wind directions during Stage 2 (except for March 28th) could dilute the air

pollutants from urban emissions. The back-trajectory analysis also showed that the air masses changed from local/regional with short transport distance during Stage 1 to long-range transport during Stage 2.

Please note that the local government issued a strict lockdown beginning on March 17th, 2020 because of the COVID-19 pandemic. The lockdown measures may lead to reduced local anthropogenic emissions such as traffic and restaurant emissions. There is a dramatic decrease of NO_2 mixing ratios on March 21st leading to lower values during Stage 2 compared to Stage 1 but not after starting of the lockdown date on March 17th. Similarly, traffic-related VOCs (e.g., benzene, toluene and xylenes) were reduced significantly on March 21st rather than March 17th (Fig. S9). There is no decrease in BC values nor particle number concentrations observed on March 17th as well. These results suggest that COVID-19 lockdown measures were much less effective for air quality than the change in wind conditions on March 21st. In addition, there was no significant decrease observed for O_3 on March 17th. Furthermore, high concentrations of O_3 were observed as NO_2 decreased during Stage 2, which could be explained by reduced O_3 titration (Sicard et al., 2020).

Furthermore, high contributions of OA to NR-$PM_{2.5}$ were found during Stage 1, which was mainly associated with a high fraction of BBOA during nighttime. Consistently, the molecular composition of OA from the filter samples analyzed by CIMS also showed the largest contribution by $C_6H_{10}O_5$ (levoglucosan, Fig. S12). This indicates that biomass burning plays an important role in contributing to high aerosol mass loadings in winter. The contribution of BBOA to total OA gradually decreased as the nighttime temperature increases over the Stage 1 (Fig. 8). This could be explained to some extent by the fact that residential heating activities are reduced during relatively warmer nighttime. With reduced BBOA contributions, SOA (SV-OOA + LV-OOA) became the dominant contributors to total OA during Stage 1. Especially at end of Stage 1 (March 20th), the largest contribution of SOA was found. Furthermore, a strong and fast increase of sulfate, nitrate and ammonium was observed especially during the evening of March 20th, leading to the highest concentration of $PM_{2.5}$ during Stage 1. In fact, before the build-up of secondary inorganic aerosol components, there was a local industrial plume arriving at our sampling site. This point is confirmed by bivariate plots that show high concentrations of SO_2 for winds coming from the west to northwest, where the local refinery and power plant are located. After receiving this plume of industrial emission, the meteorological conditions became very stagnant with WS dropping down

to 0-1 m s^{-1}, which promotes the secondary formation of aerosol particles and accumulation. Therefore, highest mass concentrations of $PM_{2.5}$ were mainly caused by secondary aerosol formation from industrial emissions within the street canyon during Stage 1.

The high mass concentrations of $PM_{2.5}$ observed during the Stage 2 were mainly build-up between March 27-28th. Since the AMS data is not available for Stage 2, I used the results from other colocated instruments to illustrate the reason. During March 27-28th, we found a significant difference between $PM_{2.5}$ and PM_{10} mass concentrations measured by the OPC, indicating a higher fraction of coarse particles ($PM_{2.5-10}$). This day can be identified as a Saharan dust event, which is not unusual for late winter and early spring (February-April) in western Europe (Rieger et al., 2017; Zhang et al., 2021). The back-trajectory analysis by HYSPLIT shows that the air masses at 3000 m a.g.l on March 28th were coming from the Sahara Desert (Fig. S13). This Saharan dust event was also confirmed by transport model calculations with ICON-ART (ICOsahedral Nonhydrostatic-Aerosol and Reactive Trace gases) (Rieger et al., 2015). Please note, that the air masses at 100 m a.g.l and 1000 m a.g.l originated from the upper troposphere over central European countries e.g., Slovakia and Czechia on March 28th. During the Saharan dust period, a sharp increase of anthropogenic pollutants including BC, NO_2, benzene and toluene were also observed during the evening of March 27th, which is related to accumulation as the WS and PBL height decreased. Besides, there was no significant change of number concentrations of ultrafine particles. Therefore, the possibility of enhanced local traffic emissions or secondary formation processes for the relatively sharp increase can be excluded. Based on results above, I conclude that high $PM_{2.5}$ mass concentrations during Stage 2 were mainly related to long-range transport of Saharan dust and from anthropogenic sources in central Europe including subsequent accumulation in the street canyons.

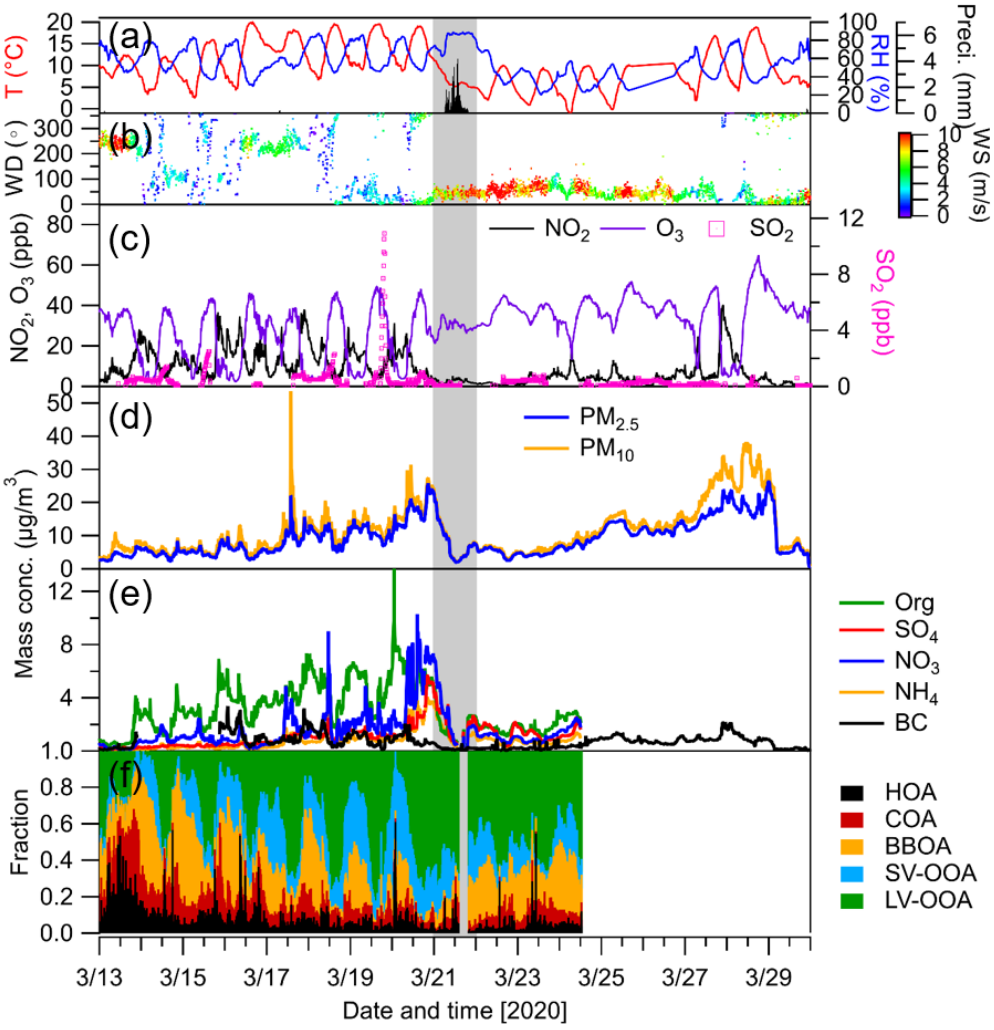

Figure 31. Time series of (a-b) meteorological parameters; (c) trace gases; (d) PM_{10}, $PM_{2.5}$ by the Fidas-OPC; (e) NR-$PM_{2.5}$ aerosol species and (f) fraction of organic aerosol factors from a PMF analysis of AMS data during the transitional episode in winter 2020. The episode is further divided into two stages by a heavy rain day on 21 March as indicated by the grey area.

3.2.5 Summary

The chemical composition and sources of NR-$PM_{2.5}$ were investigated by a HR-ToF-AMS during summertime (July 2019) and wintertime (February-March 2020) at an urban kerbside of southwest Germany. The average mass concentration of $PM_{2.5}$ was higher in dry and hot summer (7.0 ± 3.5 µg m^{-3}) than in cold and humid winter (5.8 ± 2.8 µg m^{-3}) with frequent wet scavenging. The non-$PM_{2.5}$ mostly consists of organic aerosol (OA) with 60 ± 9% in summer and 44 ±10% in winter. PMF analysis was used to investigate the sources of organic aerosol and revealed that SOA (SV-OOA + LV-OOA) was the major contributor with 82 ± 26% in summer and 48 ± 22% in

winter. Besides, residential wood combustion BBOA contributed the second-largest fraction (25 ± 12%) of the OA but only in winter. An in-depth analysis on two pollution episodes demonstrated the importance of meteorology on the variations of $PM_{2.5}$ composition and sources. In a summer heatwave episode, high $PM_{2.5}$ concentrations were mainly caused by the build-up of SOA (SV-OOA+LV-OOA) from biogenic VOC oxidation. A wintertime transitional episode was caused by various sources including local industrial emissions and regional transport of Saharan dust as well as anthropogenic emissions in central Europe. Overall, it was possible to identify the reasons for specific aerosol pollution episodes under certain meteorological conditions. This is very useful to understand the formation and evolution of $PM_{2.5}$ in urban environments and thus for the establishment of new strategies to improve urban air quality in Karlsruhe and similar cities in Europe.

3.3 Characteristics of VOCs and OA at a rural site north of Karlsruhe

This section presents the major results of a field campaign conducted at a rural site on KIT campus north from July to August 2021 (Figure 32). At a nearby location (Linkenheim), a previous study in summer 2016 found a large discrepancy between modelled and measured OA mass concentration (Shen et al., 2019). This discrepancy could be related to many factors such as missing sources of OA or unknown formation mechanism in the model. Furthermore, higher concentrations of OA were observed during nighttime along with frequent particle growth events. Highly functionalized organonitrates were found to be important contributors to the nighttime aerosol mass loading and particle growth (Huang et al., 2019a). Based on the diurnal variations and molecular composition, these organonitrates were mainly from the oxidation of biogenic VOC by NO_3· radicals during nighttime. However, it lacked of VOC measurements in summer 2016, which limits our understanding on the relative influence of the interaction of biogenic and anthropogenic compounds during these nighttime chemical processes. During the campaign in 2021, my research motivation was to estimate the source contribution of biogenic and anthropogenic emissions to OA and VOCs and to investigate the chemical evolution processes during nighttime particle growth events and corresponding controlling factors.

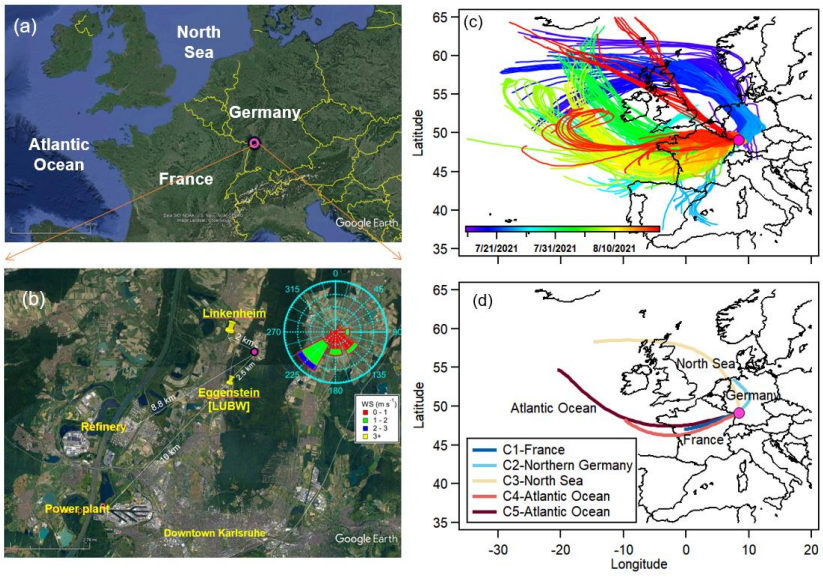

Figure 32. (a) Map of the measurement site (pink cycle) on the KIT campus north near Eggenstein-Leopoldshafen and (b) Locations of the state environmental agency (LUBW) air quality monitoring station, the sampling site for a previous study in summer 2016 (north of Linkenheim) and two industrial emission sources (a refinery and a power plant) near the Karlsruhe habor. The wind rose plot inserted is representative for the whole measurement period. (c-d) Air mass back-trajectories colored by the measurement date and grouped into five different clusters (C1-C5).

3.3.1 Overview of field observations

Figure 33 presents the time series of meteorological parameters including wind directions (WD) and speeds (WS), temperature (T), relative humidity (RH), and precipitation along with the history of air masses. The average temperature and relative humidity (± 1σ) were 20.2 ± 4.3 ^{o}C and 70.5 ±17.3%, respectively. The history of air mass origins during the entire measurement period was investigated by a HYSPLIT back-trajectory analysis (Figure 32). All air masses can be further grouped into five different clusters. The first and second clusters (C1 and C2) were classified as continental air masses, with routes via France and northern Germany, respectively. In contrast, the three other clusters (C3, C4 and C5) are characterized as marine air masses, which all were initially originating from the Atlantic Ocean. The third air mass cluster (C3) passed over the North Sea and northern Germany, while the fourth and fifth ones (C4-C5) mainly came via France to the measurement site. The origins of air masses were consistent with the wind conditions. The continental air mass clusters of C1 and C2 had lower wind speeds (< 2 m s^{-1}), with different directions with southwestern winds from urban Karlsruhe in C1 and eastern/southeastern winds from rural/forest areas in C2. Therefore, C1 could bring the urban emissions to the sampling site in contrast to C2. Besides, the marine air mass clusters (C3-C5) showed higher wind speeds with more frequent rainfall, which could efficiently remove the aerosol particles by dilution and wet deposition.

The data of NO_2 and O_3 were not complete due to technical issues with the gas monitors at the site of KIT campus north (KITcn). The hourly data of trace gases (O_3, NO_2, NO, SO_2) from the nearby Eggenstein air quality station was used in this study (Fig. S14). The average concentration of O_3 was 21.8 ± 13.5 ppb in this study period. The average concentrations of NO_2 and NO were 5.8 ± 4.0 ppb and 1.4 ± 3.5 ppb, respectively. As shown in Fig. S15, a good agreement was found for the available data of O_3 at these two locations. Eggenstein station is much closer to a main road, thus higher traffic may lead to high concentrations of NO_2 and NO. However, there was less traffic at both locations during nighttime, thus a similar level of NO_2 can be expected. The average concentration of SO_2 was 0.23 ± 0.47 ppb. Some SO_2 spikes occurred during daytime, which were related to the transport of industrial plumes from the upwind coal-fired power plant and refinery (Figure 32). Ammonia (NH_3) is responsible for the neutralization reaction of sulfuric acid (H_2SO_4) and nitric acid (HNO_3) to form particulate nitrate and sulfate in the atmosphere. In this study, the average concentration of NH_3 was 6.3 ± 2.5 ppb with a peak value of ~41 ppb measured on midday

of 23rd July. Ammonia can come from various sources at different environments such as traffic in urban areas (Artíñano et al., 2018), agricultural actives or livestock husbandry in rural areas (Ma et al., 2021). There was no livestock husbandry nearby our sampling site, so the NH_3 peak in 23rd July was likely caused by agricultural actives.

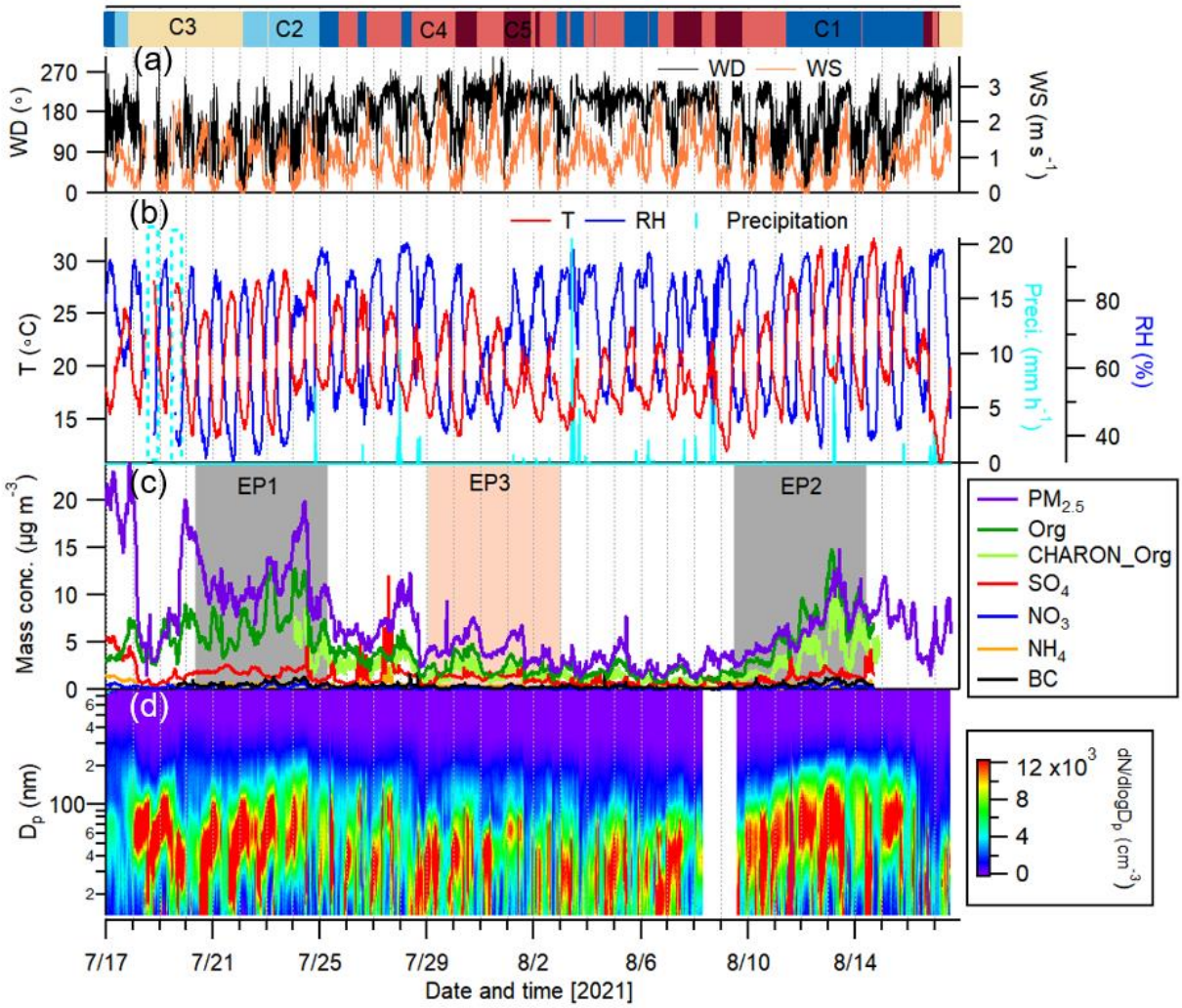

Figure 33. Time series of (a) wind speed and directions (WS and WD) along with air mass clusters; (b) temperature (T) and precipitation (the dashed box shows a meteorological data missing period); (c) mass concentrations of $PM_{2.5}$, NR-$PM_{2.5}$ composition measured by the AMS, organics measured by the CHARON-PTR-MS and BC and (d) particle size distributions measured by the SMPS. Two grey shaded areas in (c) are marked as the pollution Episodes 1 and 2 compared to one clean Episode 3 (pink).

Figure 34 shows the time series of selected VOCs including isoprene, monoterpenes, sesquiterpenes, aromatic hydrocarbons (benzene, toluene, C_8-aromatics and C_9-aromatics) and three OVOCs (acetone, formic acid and ethanol). Isoprene, monoterpenes and sesquiterpenes are

the most important biogenic precursors for SOA formation. During the entire measurement period, the average concentrations of isoprene and monoterpenes were 1.61 ± 0.96 ppb and 1.71 ± 2.48 ppb, respectively. The average concentration of isoprene was slightly higher than the mean value of 0.6 ppb reported by the Vocus-PTR-MS measurement in the French Landes forest in summer 2018 (Li et al., 2020). However, the average concentration of monoterpenes was lower than the value (6.0 ppb) reported in that study. In our study, the average concentration of sesquiterpenes was 6.5 ± 14.8 ppt with the maximum value of ~93 ppt. This was lower than the average value of sesquiterpenes (~100 ppt) observed at a Norway spruce-dominated forest in central Germany in August 2011 (Bourtsoukidis et al., 2014). Note that the variations of BVOCs could be related to many factors including meteorological conditions (e.g., temperature, radiation), oxidant levels, tree species. The concentrations of aromatic hydrocarbons were generally low (<1 ppb) during the entire measurement period, indicating that there was less influence of anthropogenic emissions. Acetone was one of the most abundant OVOCs with an average of 3.83 ± 1.62 ppb in this study. In addition, two other OVOCs, formic acid and ethanol had average concentrations of 1.01 ± 0.73 ppb and 0.07 ± 0.12 ppb, respectively. These OVOCs originate from primary sources (e.g., traffic) but also secondary oxidation processes.

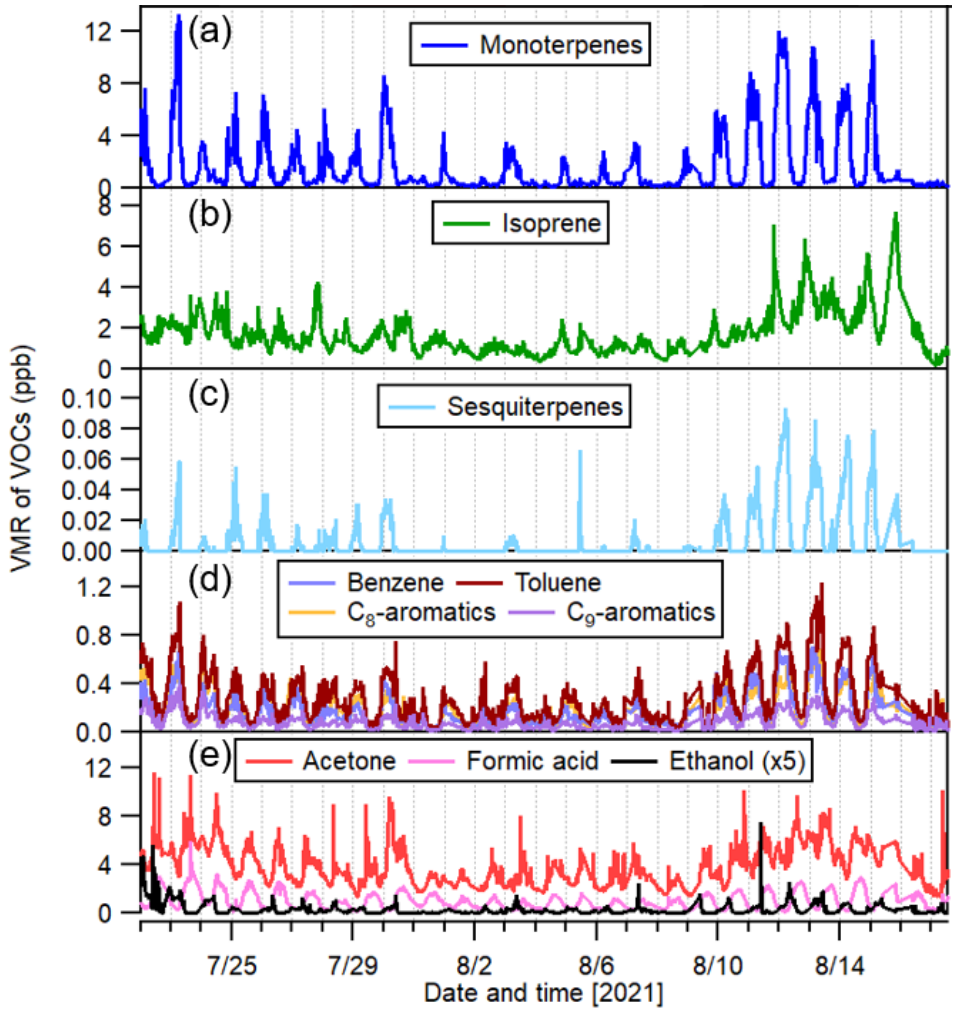

Figure 34. Time series of selected VOCs measured by the PTR-MS (a) monoterpenes, (b) isoprene, (c) sesquiterpenes, (d) benzene, toluene, C_8-aromatics and C_9-aromatics, (e) acetone, formic acid and ethanol.

Good agreements were found for $PM_{2.5}$ or PM_1 concentrations measured by different instruments (OPC, AMS and SMPS) during the entire measurement period (Fig. S16). The mass loadings of NR-$PM_{2.5}$ measured by the AMS varied from <1.1 to 18.1 µg m^{-3} with an average of 6.2 ± 3.5 µg m^{-3}. Organics and sulfate were the two most abundant components, accounting for 67 ± 12 % and 24 ± 10% of the NR-$PM_{2.5}$ mass respectively, followed by ammonium (6 ± 2%) and nitrate (3 ± 1%). A comparison was made for the composition of $PM_{2.5}$ with a previous study conducted in summer 2016 at Linkenheim about 2 km northwest of the measurement site (Figure 32) (Huang et al., 2019a). The average mass concentration of organics (4.2 ± 2.8 µg m^{-3}) in 2021 were slightly lower than those measured in 2016 (5.0 ± 3.3 µg m^{-3}). Sulfate and nitrate also showed slightly lower mass concentration with 1.39 ± 0.96 µg m^{-3} and 0.20 ± 0.16 µg m^{-3}, respectively in 2021 compared

to those observed in 2016 with 1.72 ± 0.78 μg m^{-3} and 0.85 ± 0.81 μg m^{-3}. Besides, the average mass concentration of BC was lower in 2021 (0.4 ± 0.3 μg m^{-3}) than that in 2016 (0.8 ± 0.7 μg m^{-3}). Lower particle mass concentrations may be caused by wet deposition during more rainfall days in summer 2021 (e.g., 25th July to 10th August). Besides, the Linkenheim measurement site was much close a road (~30 m) with more traffic, which can cause higher concentrations of BC and nitrate.

In Figure 33, two pollution episodes (EP1 and EP2) and one clean episode (EP3) were marked. EP1 and EP2 were from 12:00 19th July to 12:00 24th July and from 12:00 9th August to 12:00 14th August with average mass concentrations of NR-$PM_{2.5}$ plus BC of 10.5 μg m^{-3} and 8.8 μg m^{-3}, respectively. EP3 was from 0:00 29th July to 0:00 3rd August with average NR-$PM_{2.5}$ plus BC mass concentration of 4.4 μg m^{-3}. The relative composition of NR-$PM_{2.5}$ plus BC was dominated by the organics during all three episodes (Figure 35), while EP3 showed a high contribution of sulfate (28%) compared to EP1 and EP2. EP1 and EP2 can be further characterized as heatwave episodes with the meteorology of consecutive daytime maximum temperature > 25 ˚C and low RH (<50%). Both EP1 and EP2 were under influence of continental air masses, while the wind rose plots showed that EP1 was associated with local air from the forest, while EP2 had air from urban Karlsruhe during daytime and stagnant conditions during nighttime (< 1 m s^{-1}). EP3 was characterized by prevailing southwestern winds, which could carry SO_2 or sulfate from the upwind industrial sources (coal-fired power plant) to the sampling site. Therefore, the meteorology, air mass origins, sources and local chemical processes may play important roles in the variations of $PM_{2.5}$ compositions and the formation of air pollution episode. In addition, the frequent occurrence of nighttime particle growth events was observed during EP1 and EP2 (Figure 33 and Fig. S17), which were linked to BVOC emissions and SOA formation processes as discussed in the following section.

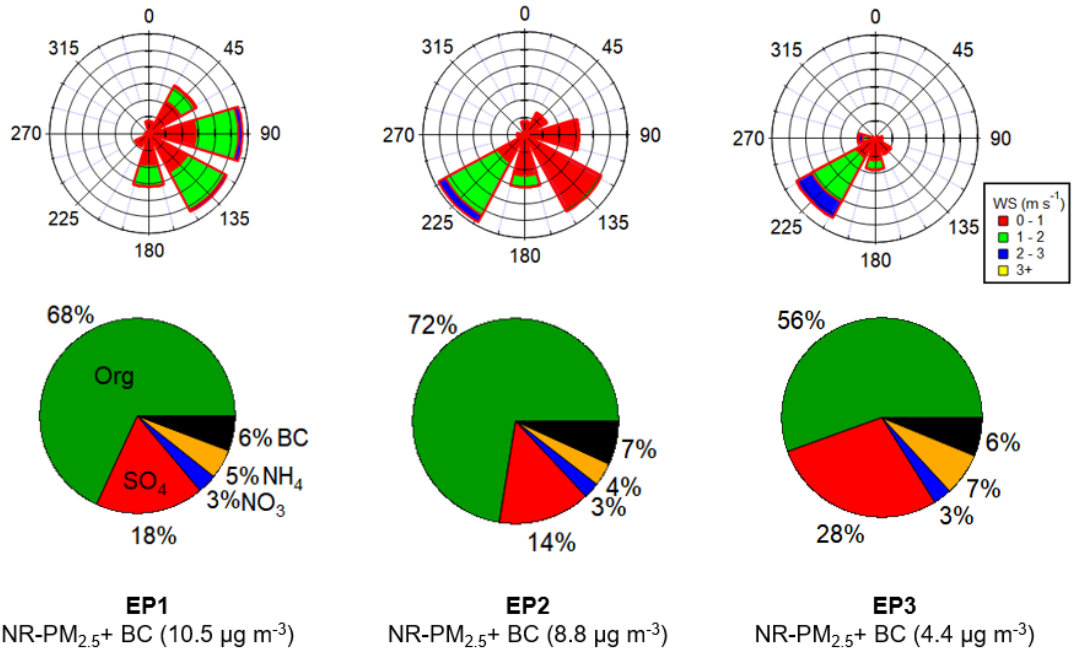

Figure 35 Wind rose plots and relative contribution of each species to total mass of NR-$PM_{2.5}$ plus BC during three characteristic episodes (EP1&2: moderately polluted, EP3: relatively clean).

3.3.2 Diurnal variations of aerosol components and trace gases

Figure 36 presents the diurnal variations of meteorological parameters, NR-$PM_{2.5}$ compositions and their precursors and selected VOCs as well as BC during the entire measurement period to provide insight into their sources and atmospheric processes. As expected, high temperature and intensive radiation were observed during daytime (6:00-20:00), which promotes photochemical reactions. Consistently, the diurnal variation of O_3 showed a significant increase during daytime. In contrast, high relative humidity (> 80%) and low temperature during nighttime may promote a partitioning of gases to the particle phase. Furthermore, low wind speeds (< 1 m s^{-1}) and reduced boundary layer height during nighttime indicate stagnant meteorological conditions.

The diurnal variation of OA was characterized by slightly higher concentrations at night than daytime, which was associated with nighttime chemical processes and/or a shrinking boundary layer. By linking the diurnal variations of OA factors, high concentrations of OA during nighttime were mainly caused by enhanced semi-volatile organic aerosol. High relative humidity and lower temperatures promote the condensation of semi-volatile organic compounds, leading to an increase of organic aerosol mass. Nitrate as a semi-volatile inorganic component showed a nighttime increase as well. This shows the important role of meteorology and nighttime chemistry in driving

the diurnal variations of semi-volatile aerosol species. Besides, nitrate showed a similar peak with NO_2 at morning hours (7:00-9:00), which was related to traffic emissions at the morning rush hours on the campus. Another peak of NO_2 was observed at early evening hours (21:00-23:00), but this was not observed for nitrate. As discussed before, the variation of NO_2 observed at Eggenstein air quality station was strongly influenced by traffic emissions. The discrepancy between nitrate and NO_2 at early evening hours suggests that nighttime chemistry may lead to continuous increase of nitrate rather than primary traffic emissions. The nitrate measured by AMS includes inorganic (e.g., ammonium nitrate) and organic nitrate (Fig. S18). I calculated the diurnal variations of inorganic and organic nitrate based on a method proposed by Kiendler-Scharr et al., 2016 and Farmer et al., et al., 2010. Consequently, organic nitrate showed a significant increase during nighttime and reached maximum values at 4:00. In contrast, inorganic nitrate showed peak values with large deviations at morning working hours (7:00-9:00), similar to that of BC. It can be concluded that inorganic nitrate and BC were associated with traffic emissions during morning hours of working days. Besides, sulfate and ammonium showed similar diurnal variations with only small increases during daytime. Their precursors SO_2 and NH_3 also showed similar diurnal trends. In the atmosphere, SO_2 can be oxidized by O_3 or OH radicals to form sulfuric acid and is subsequently neutralized by reaction with NH_3 leading to the formation of ammonium sulfate. As discussed above, southwesterly winds with high speeds occurred mainly during daytime, which could bring SO_2 or ammonium sulfate from the upwind power plant to our sampling site. Meanwhile, high concentrations of O_3 were found during daytime. Therefore, the diurnal variations of sulfate and ammonium were driven by the air mass transport and daytime photochemical processing.

The diurnal variation of isoprene showed higher concentrations during daytime than nighttime. High ambient temperatures and intensive radiation during daytime can lead to high emissions of isoprene from the plants (Guenther et al., 1993; Kuhn et al., 2002). Besides, isoprene can also be removed by the chemical reactions with OH· radicals and ozone during daytime. Therefore, the increase of isoprene during daytime indicated that the isoprene emissions were higher than the chemical removal. In contrast, the diurnal variations of monoterpenes showed higher concentrations during nighttime than daytime. Unlike the light dependence of isoprene emissions, monoterpene emissions are found to be mainly controlled by temperature (Hellén et al., 2018). During daytime, the concentration of monoterpenes dropped to low levels (<0.5 ppb), which was caused by the increased PBL height and the rapid photochemical oxidation. At night, monoterpenes

can be continuously emitted and accumulate under stagnant conditions with low photochemical activity. Their oxidation occurs then mainly via remaining ozone and NO_3· radicals. Opposite diurnal variations of isoprene and monoterpenes were also observed in previous studies at other European forest sites e.g., Landes forest (Li et al., 2020) and boreal forest (Hakola et al., 2012; Li et al., 2021a). In addition, a Fast-GC was used occasionally during nighttime with a focus on the separation of monoterpenes (Figure 37). The results showed that three monoterpene isomers including α-pinene, β-pinene, and camphene were observed in this campaign. α-pinene accounted for the majority of the monoterpene mixing ratio (~45%) during nighttime. Similar to the diurnal variations of monoterpenes, higher concentrations of sesquiterpenes were observed during nighttime, while they were not detectable during daytime. The diurnal variations of benzene and toluene showed higher concentrations during nighttime than daytime. Since there were no strong traffic emissions at night, higher nighttime concentration of benzene and toluene could be due to reducing PBL heights and lower wind speeds. During daytime, benzene and toluene showed higher concentrations at morning rush hours (7:00-9:00), but no pronounced peaks were observed compared to other traffic-related species like BC. This could be explained by the rapid photochemical consumption of benzene and toluene during daytime. The diurnal variation of ethanol showed a clear peak at morning hours (8:00-9:00) similar to BC, and subsequently dropped to very low concentrations during the rest of daytime. In the atmosphere, ethanol can be released from many sources e.g., traffic, wood combustion, emissions from volatile chemical products (VCP) and/or secondary oxidation processes (Gkatzelis et al., 2021). In this study, we can exclude the impacts of wood combustion or VCP emissions as there were no such anthropogenic activities on the campus. The morning peak of ethanol might point to the emissions from the ethanol-gasoline fueled cars on the campus. In addition, the diurnal variations of acetone and formic acid showed higher concentrations during daytime, suggesting that these two oxygenated VOCs were formed by photochemical processes.

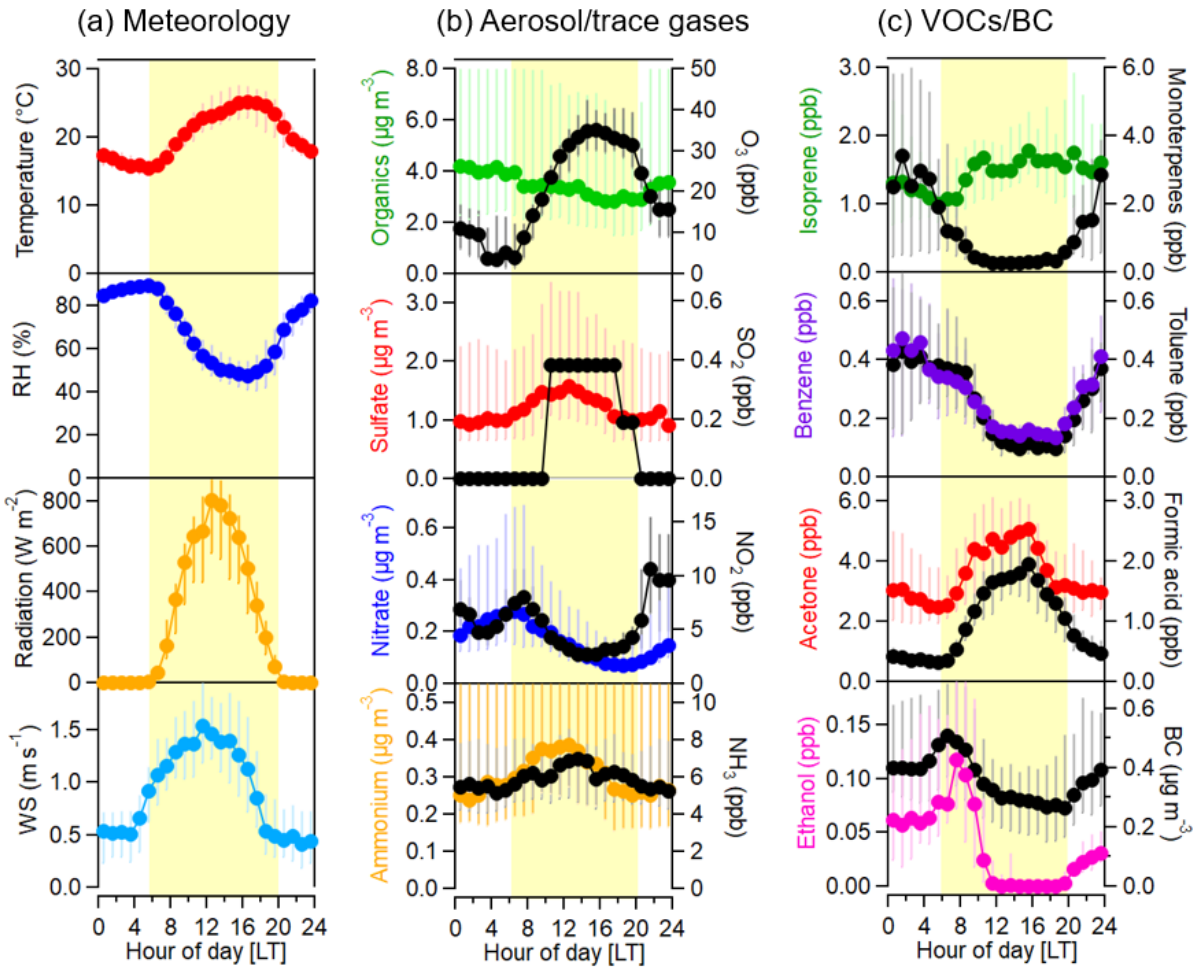

Figure 36. Diurnal variations of (a) meteorological parameters including temperature, relative humidity (RH), solar radiation and wind speeds (WS); (b) aerosol and trace gases including organics, sulfate, nitrate, ammonium, O_3, SO_2, NO_2 and NH_3; (c) VOCs including isoprene, monoterpenes, benzene, toluene, acetone, formic acid, ethanol and BC during the entire measurement period. All data are shown in medians with the whiskers of 25th and 75th percentile values. The yellow shaded areas represent the daytime from 06:00-20:00 local time.

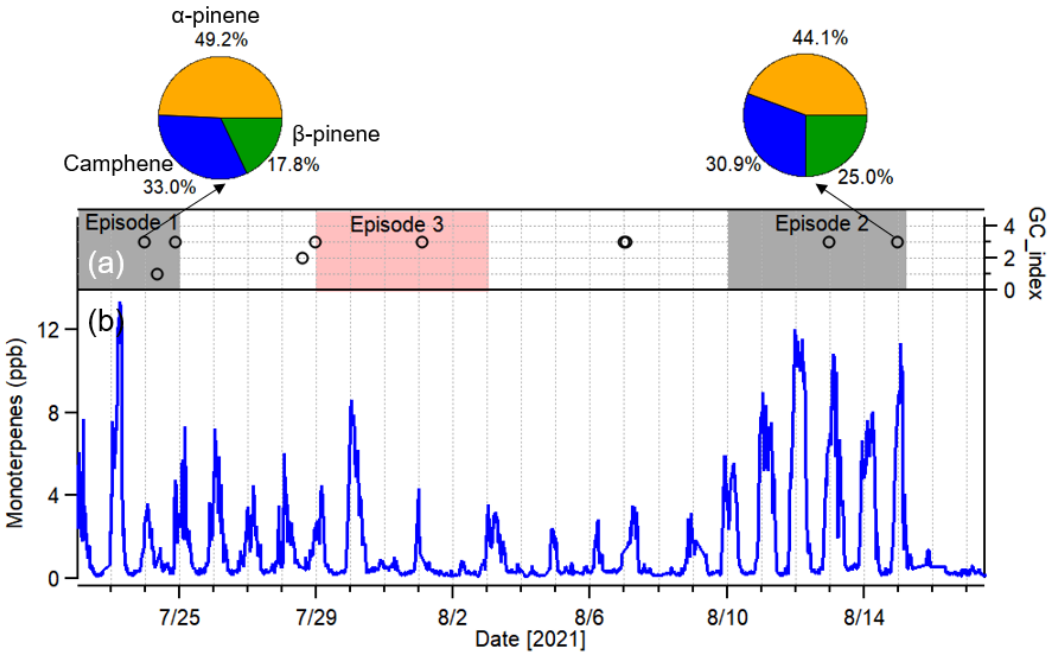

Figure 37 Time series of total monoterpenes along with the index of FastGC measurement time midpoint. (1) night, (2) midday, (3) morning. The top pie chart shows the relative contribution of three isomers to total monoterpenes for two nights of 07/23 and 08/14 2021.

3.3.3 Source analysis of OA

The source factors resolved by PMF analysis of OA measured by the AMS are shown in Figure 38 and Figure S19. The correlation coefficients of OA factors with external tracers were given in appendix Table S3. In total, five OA factors were identified including one hydrocarbon-like OA (HOA), two semi-volatile oxygenated OA (SV-OOA1 and SV-OOA2), and two low-volatility oxygenated OA (LV-OOA1 and LV-OOA2). The mass spectrum of HOA was characterized by high contributions of alkyl fragments mainly including *m/z*41 ($C_3H_5^+$), *m/z*43 ($C_3H_7^+$), *mz*55 ($C_4H_7^+$) and *m/z*57 ($C_4H_9^+$). Consistent with the results of previous studies (Crippa et al., 2013b), HOA showed a high H:C ratio (1.96) and low O/C ratio (0.26). Furthermore, HOA showed a similar temporal variation as BC, and thus HOA was considered to be mainly related to primary traffic emissions. The diurnal pattern of HOA showed a broad peak in the morning hours (7:00-9:00), which was corresponding to the morning rush hours. However, this peak was less pronounced than that observed in downtown Karlsruhe (Song et al., 2022), which is likely attributed to less traffic on the campus. During the entire measurement period, the contribution of HOA to total OA was 6 ± 5%, indicating that minor influence of primary traffic emissions on OA at this location.

Two SV-OOAs were resolved with comparable O/C ratios of 0.45 for SV-OOA1 and 0.51 for SV-OOA2 respectively, which are within the typical range of 0.3-0.60 reported for SV-OOA factors previously reported at different environments (Ng et al., 2011). The mass spectrum of SV-OOA1 showed a predominant ion of *m/z*43 ($C_2H_3O^+$), which was similar to that of SV-OOA in previous studies (Crippa et al., 2013b). In contrast, the mass spectrum of SV-OOA2 showed less contribution from $C_2H_3O^+$ but with higher abundances of *m/z*44 (CO_2^+). Generally, higher abundances of *m/z*44 (CO_2^+) than *m/z*43 ($C_2H_3O^+$) were expected in LV-OOA compared to that in SV-OOA, consequently the O/C in SV-OOA was significantly lower than in LV-OOA (Ng et al., 2011). However, SV-OOA2 showed lower O/C ratios compared to the range of LV-OOA factor (0.70-1.10) reported in many previous studies (Ng et al., 2011). Note that the O/C ratio depends not only on the relative abundance of the *m/z*44 (f_{44}) but also on hundreds of other ions containing carbon and oxygen. Thus, f_{44} alone is unable to predict the O/C value accurately if ions other than CO_2^+ also contribute significantly to overall O/C (Chhabra et al., 2010). In the SV-OOA2 spectrum, *m/z*29 (CHO^+) accounts for 6.3% of the total signals, compared to *m/z*44, contributing to the O/C of SV-OOA2. In addition, both SV-OOA1 and SV-OOA2 mass spectra were also characterized with important contributions from the ion *m/z*91 ($C_7H_7^+$). $C_7H_7^+$ was considered to be highly associated with biogenic SOA in previous studies at forest sites (Lee et al., 2016; Liu et al., 2017; Zhang et al., 2020), while it can also arise from the fragmentation of aromatic compounds from anthropogenic sources (Poulain et al., 2021). In this study, HOA, SV-OOA1 and SV-OOA2 all showed significant contributions of $C_7H_7^+$, thus $C_7H_7^+$ cannot be regarded as a good tracer for specific sources. In addition, we also observed higher abundance of a series of alkyl ions such as *mz*77 ($C_6H_5^+$), *m/z*78 ($C_6H_6^+$), *mz*79 ($C_6H_7^+$), *mz*($C_7H_7^+$), *m/z*105 ($C_8H_9^+$), *mz*115 ($C_9H_7^+$) in mass spectrum of SV-OOA2 compared to SV-OOA1. These ions could be related to the fragmentation of aromatic hydrocarbons (Chhabra et al., 2010). A good correlation between SV-OOA1 and organic nitrate indicated that they are of semi-volatile nature (R = 0.92, Fig. S18). Furthermore, SV-OOA1 showed good correlations with the monoterpene oxidation product pinonaldehyde measured by the PTR-MS. The diurnal variation of SV-OOA1 showed significant increases during nighttime, therefore SV-OOA1 is related to nighttime chemistry including the oxidation of biogenic VOCs by O_3 and nitrate radicals. In contrast, SV-OOA2 showed weak correlation with nitrate but a better correlation with cresol, a product of aromatic hydrocarbon oxidation. In addition, a significant increase of SV-OOA2 mass concentrations was observed during the days with the air

masses from the Karlsruhe urban area (episode 2). Therefore, SV-OOA2 was mainly attributed to the anthropogenic sources in this study. During the entire measurement period, the contributions of SV-OOA1 and SV-OOA2 were 20 ± 12% and 17 ± 9% to total OA, respectively.

Two LV-OOAs were identified with higher O/C ratios of 0.86 for LV-OOA1 and 1.00 for LV-OOA2 respectively, which are within the range of 0.70-1.10 for LV-OOA factors reported in previous studies (Ng et al., 2011). The mass spectra of both LV-OOA1 and LV-OOA2 were distinguished by the predominant ions of *m/z*44 (CO_2^+) and *m/z*28 (CO^+). LV-OOA1 showed a strong correlation with CO_2^+, but no correlation was found between LV-OOA2 and CO_2^+. In contrast, LV-OOA2 showed a good correlation (R = 0.84) with *m/z*79 ($CH_3SO_2^+$), an ion derived from the fragmentation of methanesulfonic acid (MSA) regarded as a marker of marine sources (Crippa et al., 2013b; Huang et al., 2018a). A significant increase of LV-OOA1 mass concentrations was found during daytime, which was similar to the diurnal pattern of odd oxygen ($O_x = O_3 + NO_2$), a tracer for photochemical processes. This suggests that LV-OOA1 was strongly contributed by the photochemical formation. LV-OOA2 showed less pronounced diurnal variations compared to LV-OOA1. Based on the back-trajectory analysis, significant increase of LV-OOA1 mass concentrations were found under the influence of air mass clusters (C1, C2 and C3). However, lower mass concentrations of LV-OOA1 were found during the periods with the influence of marine air mass clusters (C4 and C5). This was also caused by wet deposition of aerosol particles by rainfall events under the influence of marine air masses as discussed above. On the contrary, significantly increases of LV-OOA2 mass concentrations were observed at dry days when the sampling site was mainly influenced by the marine air mass clusters (C4 and C5). Therefore, we suggest that LV-OOA2 was associated with the long-range transport of marine sources. Crippa et al. (Crippa et al., 2013b), also identified a marine OOA measured in Paris, France in summer 2009 and found a significant increase of marine OOA mass under the influence of the Atlantic Ocean air masses. In this study, LV-OOA2 showed higher O:C value (1.0) compared to that in marine OOA (0.57) in Paris in summer (Crippa et al., 2013b). This suggests that LV-OOA2 was attributed to aged marine OOA after long-range transport. During the entire measurement period, the contribution of LV-OOA1 and LV-OOA2 were 35 ± 17% and 22 ± 16% to total OA, respectively.

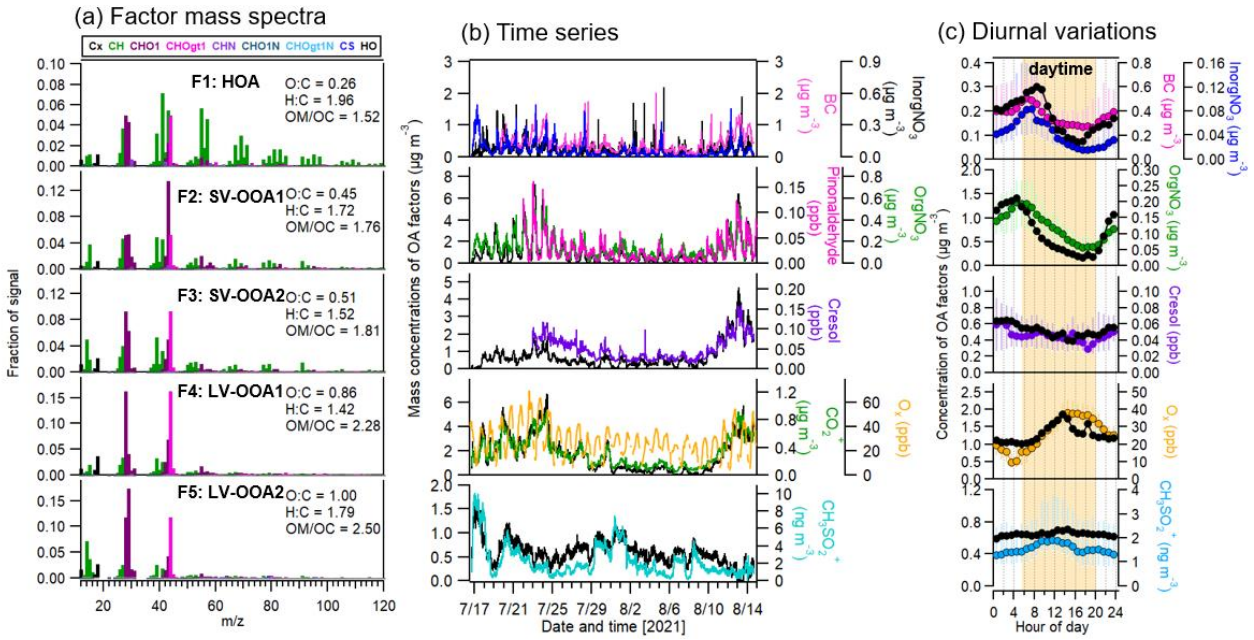

Figure 38. Source apportionment of organic aerosol by the PMF analysis on the OA mass spectra measured by the AMS. (a) Mass spectra of OA factors for hydrocarbon-like OA (HOA), semi-volatile oxygenated OA (SV-OOA1 and SV-OOA2) and low-volatility oxygenated OA (LV-OOA1 and LV-OOA2). (b) time series of OA factors and external tracer species i.e., BC, inorganic and organic nitrate ($InorgNO_3$ and $OrgNO_3$), CO_2^+ and $CH_3SO_2^+$ measured by the AMS, pinonaldehyde and cresol measured by the PTR and odd oxygen (O_3+NO_2). (c) medians of diurnal variations of OA factors, and external tracers with the whiskers (the 25th and 75th percentile values).

3.3.4 Source apportionment of VOCs

Five factors were characterized by the PMF analysis of the VOCs measured by the PTR-MS are shown in Figure 39 and Figure S20. The correlation coefficients of VOC factors with external tracers were given in Table S3. The first factor was identified as primary traffic VOCs (traffic VOCs) with the dominant contributions by the ions of *mz*47.05 ($C_2H_7O^+$), *m/z*79.05 ($C_6H_7^+$), *m/z*93.07 ($C_7H_9^+$), *m/z*107.09 ($C_8H_{11}^+$), *m/z*121.10 ($C_9H_{13}^+$) and *m/z*135.12 ($C_{10}H_{15}^+$), These ions can be assigned to ethanol, benzene, toluene, C_8-aromatics, C_9-aromatics and C_{10}-aromatics. In particular, ethanol almost completely came from VOC factor 1. As discussed above, ethanol was mainly emitted from traffic in this study. Aromatic hydrocarbons are widely reported as tracers for traffic emissions (Baudic et al., 2016; Gkatzelis et al., 2021). As expected, these aromatic compounds showed good correlations with traffic-VOCs factor (R = 0.7-0.9, Table S3). Besides, a similar trend of the traffic-VOC factor was observed with that of HOA and BC during the measurement period, indicating that they came from traffic emissions. The diurnal variation of the traffic VOC factor showed a clear peak value with ~5.4 ppb at morning rush hours (8:00-9:00).

After this peak, the concentration of traffic VOC factors dropped down rapidly to very low levels (< 0.1 ppb) during daytime hours (13:00-20:00). This is likely caused by the increased boundary layer height and rapid photochemical consumptions of VOCs by OH· radicals. The traffic-VOCs factor also showed an increase after 20:00 and reached a plateau at around 02:00 during nighttime, which was associated with the shrinking boundary layer height and less photochemical oxidation. During the entire measurement period, the average contribution by the traffic VOC factor to TVOCs was 12 ± 13% (± 1σ).

The second factor was characterized as nighttime VOCs since it showed significantly higher concentrations during nighttime. The factor profile was characterized with largest contributions by the monoterpenes (*m/z*137.13, $C_{10}H_{17}^+$) and its fragmentation ions (*m/z*81.07 $C_6H_9^+$ and *m/z*95.08 $C_7H_{13}^+$). High contributions of *m/z*67.06 ($C_5H_7^+$), *m/z*79.05 ($C_6H_7^+$) and *m/z*93.07 ($C_7H_9^+$) were also found in this factor, which were also attributed by the minor fragmentation ions of various monoterpenes inside the PTR instrument as reported by previous studies (Kari et al., 2018; Materić et al., 2017; Tani et al., 2003). Besides, high loadings of sesquiterpene-related ions (*m/z*205.20 $C_{15}H_{25}^+$ and *m/z*149.13 $C_{11}H_{17}^+$) were also found in this factor (Kari et al., 2018; Kim et al., 2009). The time series of the nighttime VOC factor correlated well with concentrations of monoterpenes and sesquiterpenes. Furthermore, a good correlation was observed between the nighttime-VOCs factor and SV-OOA1 (R = 0.7), suggesting that they were involved in similar chemical processes. The nighttime-VOC factor showed a continuous decrease with increasing boundary layer height from 6:00-10:00 and kept at low levels (< 1 ppb) during daytime. Subsequently, a fast increase was observed with decreasing boundary layer height from 20:00 to 02:00 during the night. A further decrease of the nighttime-VOC factor was found during late nighttime (2:00-6:00), which was opposite to the continuous increase of SV-OOA1. In fact, we also found a further decrease of O_3 and NO_2 concentrations at 2:00-6:00. Therefore, the nighttime oxidation of the nighttime VOC factor (mainly monoterpenes and sesquiterpenes) by O_3 or NO_3· radicals could lead to the formation of SV-OOA1 and organic nitrates. The diurnal variation of the nighttime VOC factor resembled to a previous study with the PMF analysis on PTR-MS mass measurements at a pine forests showing a significant increase of monoterpene- or sesquiterpene-related factors during nighttime (Li et al., 2021a). In the present study, although the nighttime-VOC factors accounted for 11 ± 16% of TVOCs, it may play an important role in nighttime chemistry and corresponding SOA formation.

The third factor contained abundant oxygenated VOCs (OVOCs) such as $C_7H_8O_{1-3}$, $C_8H_{10}O_{2-3}$, $C_9H_{10}O_{1-3}$ and $C_9H_{12}O_3$, thus was identified as a second oxygenated VOC factor (SecVOC1). These OVOCs ions could be further attributed to the oxidation products of aromatic hydrocarbons. For example, C_7H_8O, $C_7H_8O_2$, $C_7H_8O_3$ can be assigned as cresol, dihydroxy toluene and dicarbonyl epoxide, which were reported as the oxidation products of toluene (Li et al., 2021b; Zaytsev et al., 2019). $C_9H_{10}O$ and $C_9H_{12}O_3$ can be characterized as dimethylbenzaldehyde and dicarbonyl epoxide respectively, which were found as major products of trimethylbenzene oxidation (Zaytsev et al., 2019). The time series of SecVOC1 was well correlated with these OVOC species (e.g., C_7H_8O and $C_7H_8O_2$, Table S3). A similar trend of SecVOC1 was found with the SV-OOA2 factor. Particularly, both SecVOC1 and SV-OOA2 showed significantly increase during episode 2 when the sampling site was influenced by air masses from the Karlsruhe urban area. The diurnal variation of SecVOC1 showed a minor peak at morning hours (7:00-8:00) like traffic-VOCs. These OVOCs were expected to increase under air masses with high wind speeds from urban Karlsruhe during daytime. In fact, it started to decrease after the morning peak and reached lower levels (~1 ppb) at 14:00-15:00 during daytime. These OVOCs are highly reactive and subsequently oxidized by OH radicals, which can produce low-molecular-weight VOCs (e.g., methylglyoxal) or low-volatility compounds to from SOA particles during daytime. During the entire study, the SecVOC1 factor accounted for 11 ± 9% of TVOCs.

The fourth factor was characterized by high contributions of low-molecular weight ion peaks (m/z<120). These predominant peak ions can be assigned as OVOCs including formic acid (CH_2O_2), acetone (C_3H_6O), acetic acid ($C_2H_4O_2$) and hydroxyacetone ($C_3H_6O_2$). Therefore, this factor can be assigned as another second oxygenated VOCs (SecVOC2). Previous studies reported that these small OVOCs were the oxidation products from photochemical processes (Gkatzelis et al., 2021). The time series of SecVOC2 and formic acid strongly correlated with O_x (R = 0.9), confirming that SecVOC2 was caused by photochemical oxidation. The diurnal variations of SecVOC2 showed clear peak values at 14:00-16:00 during daytime as O_x. The SecVOC2 was the largest contributor to TVOCs (37 ± 29%) during the entire measurement study. This was due to the fact that these small molecular weight OVOCs are formed by strong photochemical processing during hot summer days. In addition, these compounds have relative long atmospheric lifetimes e.g., 15 days for acetone (Jacob et al., 2002) and 2-4 days for formic acid (Chebbi and Carlier, 1996).

The fifth factor had high contributions of more oxidized VOCs such as $C_3H_4O_2$, $C_2H_4O_3$, $C_3H_4O_3$, $C_5H_2O_2$, $C_4H_2O_3$, $C_6H_4O_2$ and nitrogen-containing compounds (C_2H_3N and C_2H_5N). Note that these species typically showed low concentrations over the entire measurement period. This factor exhibited insignificant temporal variation compared to other VOC factors, but showed a similar trend as the variation of wind directions. On 27th July, a significant increase of this factor concentration was found along with the shift from continental air mass origins (C3) to marine ones (C4-C5). Furthermore, the concentration of this factor exhibited a slight decrease after the air mass origins changed back to continental air masses after 12th August. Based on these results, the fifth factor can be attributed to regional background associated with the advection of aged air masses. The diurnal variations show slight increases at morning and evening hours (10:00-12:00 and 20:00-22:00). During the entire measurement period, the contribution of regional background VOCs to TVOCs was 28 ± 21%.

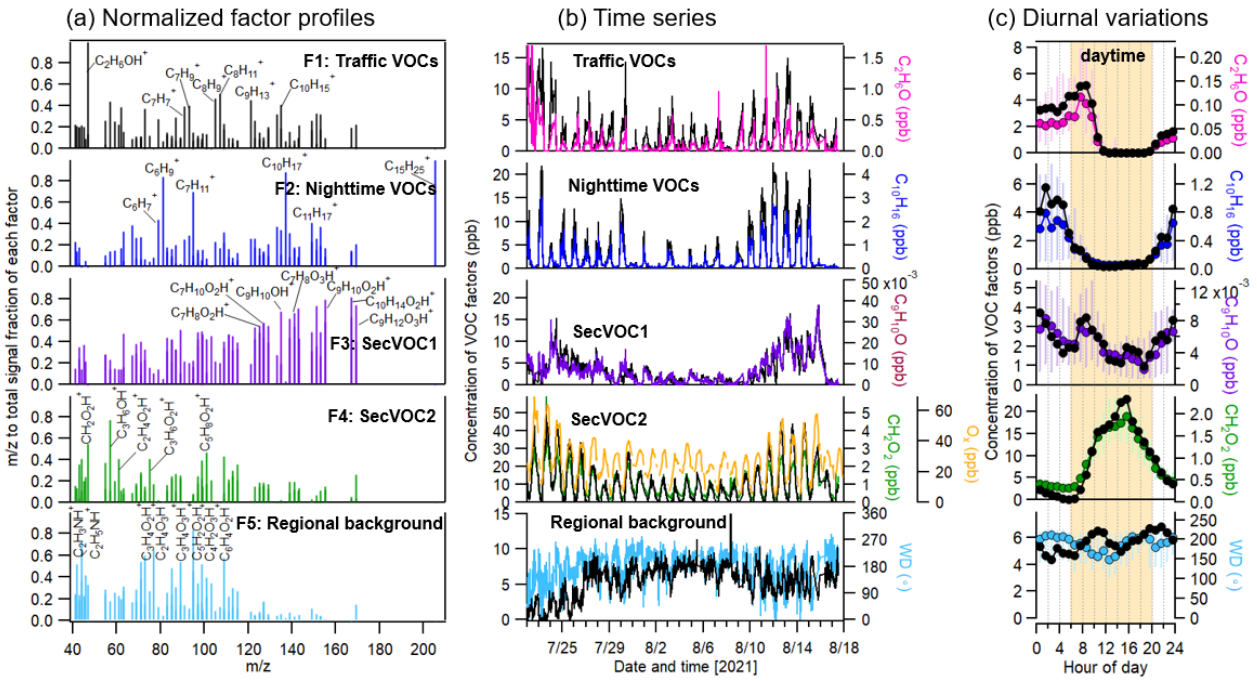

Figure 39. (a) Normalized VOC factor profiles by the PMF analysis on the m/z peaks measured by the PTR-MS: traffic VOCs, nighttime VOCs, secondary oxygenated VOCs (SecVOC1 and SecVOC2) and regional background (b) time series of VOC factors and external tracer species i.e., C_2H_6O (ethanol), $C_{10}H_{16}$, $C_9H_{10}O$, CH_2O_2 measured by the PTR-MS, O_x (O_3+NO_2) and wind direction. (c) medians of diurnal variations of VOC factors and external tracers with the whiskers (the 25th and 75th percentile values).

3.3.5 Controlling factors for nighttime particle mass increase and growth

In this study, nighttime particle growth events were frequently observed especially during two heatwave episodes EP1 and EP2. Limited by the minimum SMPS size cutoff (13.6 nm), it was not possible to see the occurring of very fresh new particle formation directly before the nighttime growth. Therefore, the particle growth stage from a few nanometers to tens of nanometers was investigated during these nighttimes. The nighttime particle growth phenomenon has been previously reported for the same location and the same season (Huang et al., 2019a). The particle growth was found to be associated with organic nitrate formation from the reaction of BVOCs and nitrate radicals ($NO_{3\cdot}$) with an estimated contribution of 18-25% of mass increase. In this study, I investigated how the anthropogenic and biogenic VOC oxidation control the nighttime particle mass and size evolution. The diurnal variations of fractions of OA and nitrate as well as atmospheric oxidants (O_3 and $NO_{3\cdot}$ radicals) during EP1 and EP2 compared to EP3 are shown in Figure 40. The diurnal variations of meteorological parameters (temperature, RH, boundary layer height, radiation), VOC and OA factors during these three episodes are given in Figure 40. The fraction of OA reached up 0.7-0.8 during nighttime of heatwave episodes (EP1 and EP2). The fraction of nitrate also showed an increase during nighttime from 0.02 at 21:00 to 0.04 at 6:00 the next day during EP1 and EP2. The median size of particles exhibited a strong increase during nighttime of heatwave episodes (EP1 and EP2) with the average growth rate of 3.5 ± 0.7 and 4.0 ± 0.7 nm h^{-1}, which were close to results of a previous study (range: 2.2-10.3 nm h^{-1}, average: 5.3 ± 3.1 nm h^{-1}) at the same location (Huang et al., 2019a). However, no significant nighttime particle growths were found during the relatively clean episode (EP3).

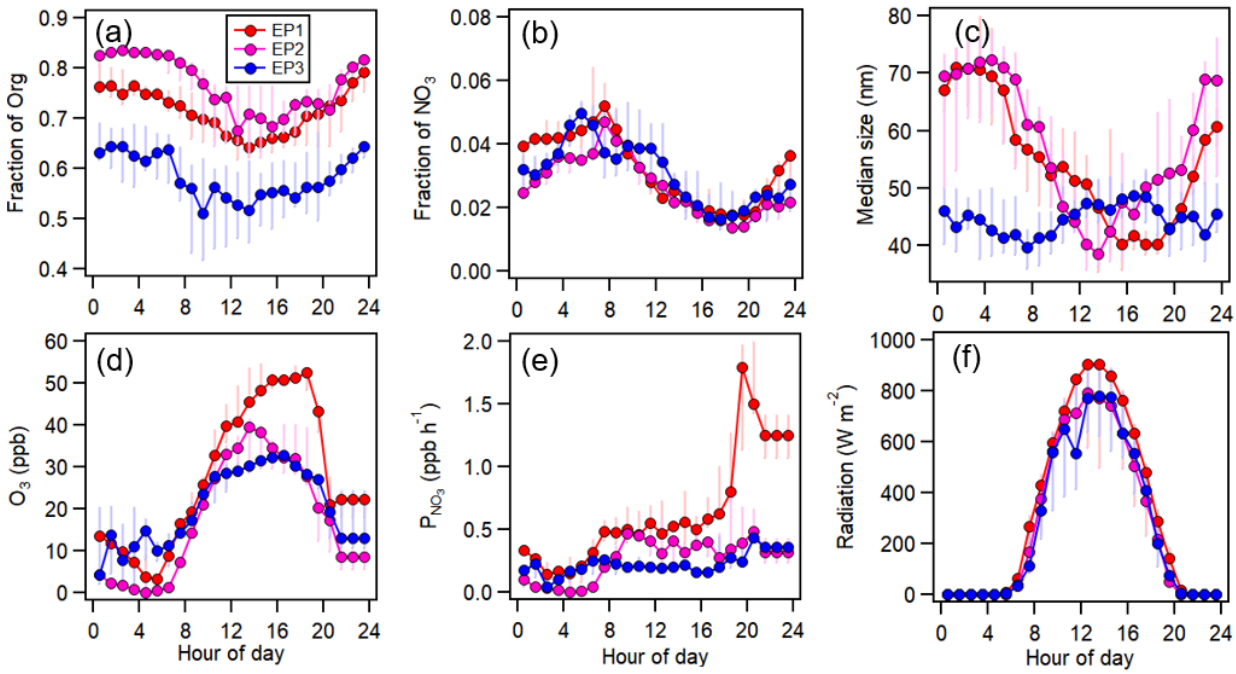

Figure 40 Diurnal variations of (a-b) mass fraction of organics and nitrate measured by the AMS, (c) median particle size measured by the SMPS, (d) O^3 concentrations (e) production rate of nitrate radical (P_{NO_3} = $[NO_2]$*O_3) and (f) radiation during three episodes (EP1&2; moderately polluted; EP3: relatively clean).

In fact, there were no significant changes of meteorological conditions (temperature, RH, boundary layer height, radiation) among these three episodes except for air mass origins (Figure 41). For VOC and OA factors, traffic VOCs and HOA showed a rapid increase as the boundary layer height decreased during nighttime. Note that there were no significant traffic emissions expected on the KIT campus. It is therefore reasonable to exclude the traffic emissions for the particle mass increase and growth. Nighttime VOC and SV-OOA1 also showed fast increase especially during heatwave episodes (EP1 and EP2), indicating the importance of semi-volatile organic aerosol formed from the biogenic VOC oxidation to the nighttime particle mass increase. In particular, high relative humidities and lower temperatures during nighttime could facilitate the partitioning of semi-volatile organic compounds. In addition, the diurnal variation of SecVOC1 showed two peaks at 10:00-11:00 and 21:00 during EP2 with the influence of air masses from urban Karlsruhe, while that only had one peak at 21:00 during EP3 with the influence of local air. Note that the morning peak of SecVOC1 was later than the peak time for local traffic emissions (7:00-9:00), which could be related to the transport of urban emissions from downtown Karlsruhe. Given the transport time as 1.5 h with the average wind speeds of 1.5-2 m s^{-1}, the transport distance can

be estimated to be 8-11 km. Thus, the morning peak of SecVOC1 was caused by the transport of Karlsruhe urban emissions. The evening peak of SecVOC1 during EP1 and EP2 were mainly caused by the reduced boundary layer height. During EP2, after the evening peak of SecVOC1, SV-OOA2 showed a fast increase correspondingly. SecVOC2 showed higher concentrations during daytime in all episodes due to strong photochemistry. However, LV-OOA1 showed a relatively flat variation especially during nighttime, suggesting that the role of LV-OOA1 in nighttime particle mass increase and growth was negligible.

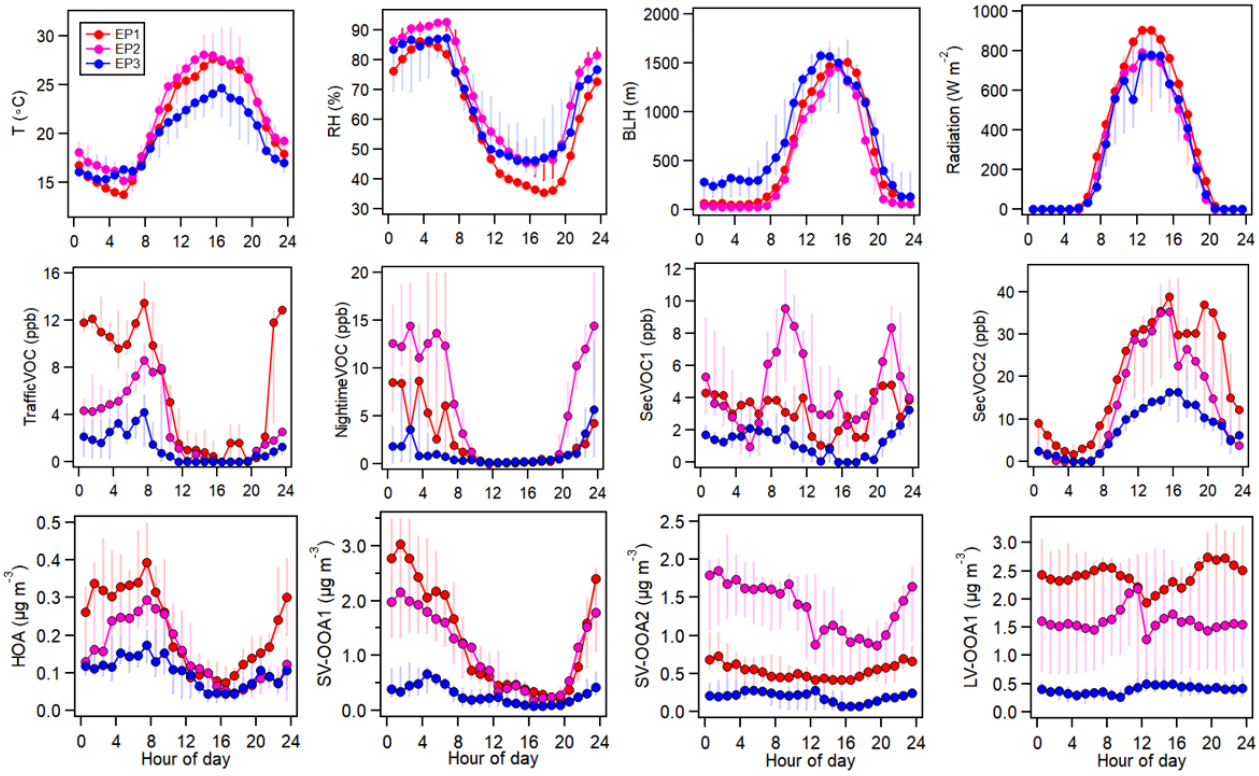

Figure 41 Diurnal variations of meteorological parameters (top), PMF derived VOC (middle) and OA factors (bottom) during three episodes (EP1&2; moderately polluted; EP3: relatively clean).

Then one representative nights of 12-13 August during EP2 was selected to demonstrate the roles of VOC and OA factors in nighttime particle growth events. This nighttime particle growth event was characterized with the increase of geometric mean size from ~57 nm at 21:00 12th August to ~84 nm at 0:00 13th August. Correspondingly, the particle growth rate was estimated as 9.0 ± 0.6 nm h^{-1}. The nighttime increase of aerosol mass could be related to a reduced PBL in addition to nighttime chemical processes. To remove the effect of PBL evolution, the mass concentrations of organics and sulfate were normalized to BC (OA/BC and SO_4/BC). The normalized OA/BC

concentrations showed a clearly increase compared to relatively stable SO_4/BC during this night. This means that the mass increase of OA was associated with additional sources and/or chemical processes rather than the shrinking PBL height. By linking to the OA factors, it was found that the OA increase can be mainly attributed to the increase of SV-OOA1. As discussed above, SV-OOA1 was strongly related to monoterpene oxidation, which accounted for 78% of the mass increase of OA at this night.

During nighttime, the oxidation of BVOCs was mainly caused by ozonolysis and nitrate radical (NO_3·)-initialized reactions. The concentration of O_3 and the production rate of NO_3· radicals showed significant decreases at this night (Figure 42). The decrease of O_3 was likely associated with the direct ozonolysis reaction of BVOCs (e.g., monoterpenes and sesquiterpenes), which can lead to the formation of SV-OOA. Furthermore, the decrease of production rate of NO_3· radicals could result in the formation of organic nitrate via the reaction of BVOCs and NO_3· radicals. Note that the concentrations of N_2O_5 measured by the CIMS were much lower than the NO_2 concentrations, suggesting the main sink of the NO_3· radical was to react with BVOCs rather than the reaction of NO_3· radicals with NO_2. Unexpectedly, significant increases of mass fraction of nighttime VOCs were observed during the nighttime. This could be explained by the competition among the evolution of PBL height, emissions and the removal of BVOCs (monoterpenes and sesquiterpenes) by chemical reactions. Firstly, the shrinking PBL height could lead to an accumulation of VOC concentrations, which explained the increased fraction of traffic VOC factor during nighttime. Secondly, as the temperature showed a decrease over the nighttime (Figure 42), it can be expected that the emissions of BVOCs from trees were also decreasing (Hakola et al., 2012). Thirdly, the concentrations of O_3 and NO_3 radicals (~$[NO_2]$*$[O_3]$) decreased also over nighttime (Figure 42), which could slow down the removal of BVOCs by oxidation reactions. In particular, the highest fraction of nighttime VOC factor was observed along with very low concentrations of O_3 and NO_3 radicals at nighttime (3:00-4:00) of 13th August when there were no changes in temperature and PBL height. At this night, the corresponding factions of secondary anthropogenic factors (SecVOC1 and SV-OOA2) and regional background factors (regional background VOC and LV-OOA2) showed negligible changes. Besides, both SecVOC2 and LV-OOA1 showed the rapid decrease from daytime to nighttime, which was caused by the reduced photochemical oxidation processes. Overall, this characteristic nighttime particle growth and mass

increase were caused by the formation of SV-OOA resulting from the oxidation of BVOCs especially monoterpenes.

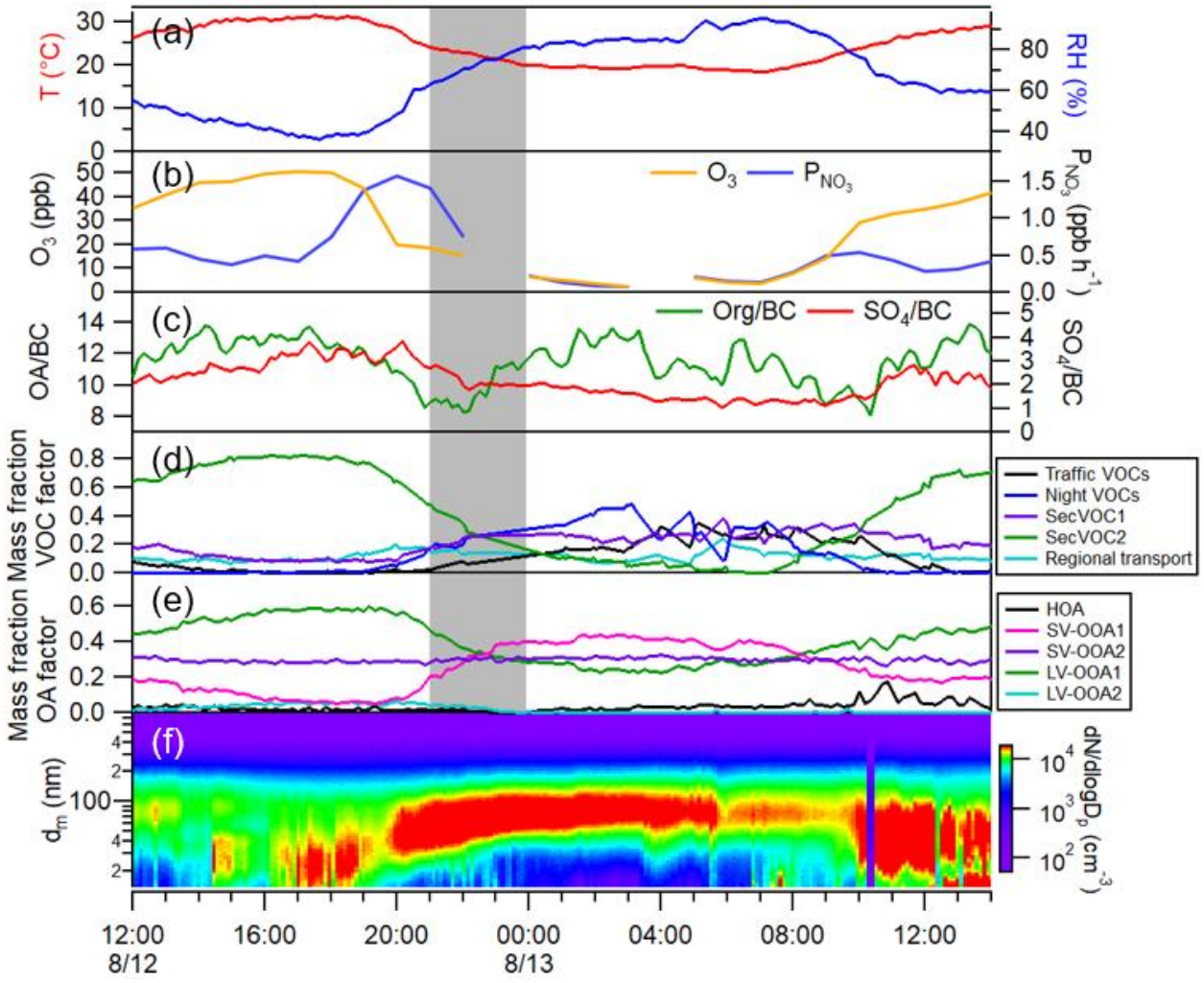

Figure 42. Evolution of a characteristic nighttime particle growth at night of 12-13 August. (a) temperature and relative humidity, (b) O_3 concentration and production rate of nitrate radical ($P_{NO_3} = [NO_2]*O_3$), (c) ratio of organics and sulfate to BC (Org/BC and SO_4/BC) (d-e) mass fraction of VOC factors and OA factors (f) particle number size distribution. The period of nighttime particle growth (21:00-0:00) is marked in shadow grey area.

3.3.6 Summary

In this chapter, aerosol particles and trace gases were comprehensively characterized using a HR-ToF-AMS and a PTR-ToF-MS as well as a suite of supplementary instruments during summertime in 2021 at a rural site of southwest Germany. During the entire measurement period, the average concentration of NR-$PM_{2.5}$ by the AMS was 6.2 ± 3.5 µg m^{-3} with OA being the predominant contributor with 67 ± 12% followed by sulfate with 23 ± 10%. The PTR-MS

measurements show that higher concentrations of isoprene (1.61 ± 0.96 ppb) and monoterpenes (1.71 ± 2.48 ppb) than benzene (0.30 ± 0.22 ppb) and toluene (0.28 ± 0.22 ppb). PMF analyses were used to investigate the sources of OA particles and VOCs. The PMF results showed minor contribution of traffic-related HOA to total OA mass (6 ± 5%), while oxygenated OA factors contributed most to the OA mass (94 ± 5%). Similarly, VOC factors resolved from the PMF analysis were related to secondary oxidation processes contributing 78 ± 29% to total VOC concentrations. These results demonstrate the importance of chemical processing for the variations in organic aerosol composition. Furthermore, two heatwave episodes were characterized with high aerosol mass concentrations. During these two heatwave episodes, the mass concentrations of OA showed significant nighttime increases compared to relative stable sulfate concentrations. Correspondingly, the particle size showed the growth rate of 3.5-4.0 nm h^{-1} during nighttime of two heatwave episodes. By link to the OA factors, SV-OOA associated with monoterpene oxidation showed more pronounced increases, which was responsible for the nighttime organic mass increase and particle growth. Furthermore, the nighttime aerosol mass increase and particle growth were characterized with stagnant conditions with lower temperature and high relative humidity during nighttime, which facilitated the gas-to-particle partitioning of SV-OOA.

3.4 Characteristics of VOCs and SOA formation in a stressed pine forest

Figure 43 shows the location of the sampling site at the Eifel forest (50.43 °N, 6.24 °E) in North Rhine-Westphalia, western Germany. The forest is largely composed of Norway spruce and European beech trees (Sirocko et al., 2013), which are important contributors to terpene emissions. These trees are currently suffering from the abiotic (drought and heatwave) and biotic (bark beetle attacks) stresses (Phuntsho, 2020), which may have impacts on the variations of plant VOC emissions and subsequent aerosol particle formation by VOC oxidation. In addition to plant emissions, some anthropogenic activities near the forest like a biogas power plant may also release VOCs and aerosol particles (Salazar Gómez et al., 2016). Therefore, I performed this field campaign at the Eifel forest in June 2020 and provided insights into the variations of VOCs and aerosol particles based on state-of-the-art PTR-MS measurements. These results shall be helpful to better understand the sources and chemical processing of VOCs leading to potential aerosol particle formation for those stressed forest environments even nearby anthropogenic emissions sources.

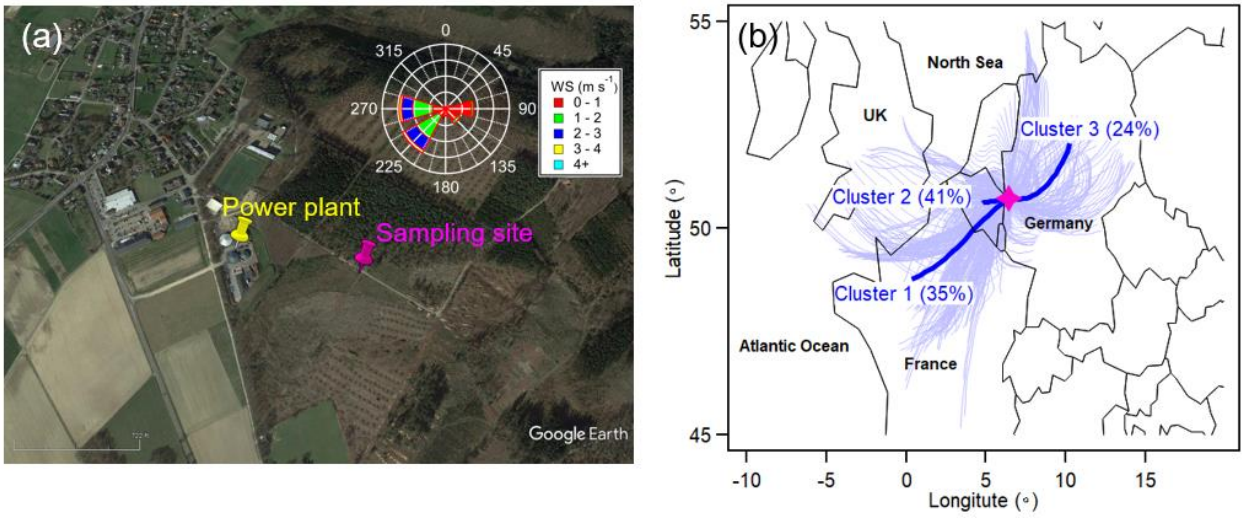

Figure 43. (a) Location of the sampling site and a nearby biogas power plant with inserted wind rose plot. (b) Three clusters of air mass back-trajectories during the entire measurement periods. The numbers indicate the percentage contribution of each cluster to all back-trajectories.

3.4.1 Meteorological conditions and greenhouse gases

Figure 44 shows the time series of meteorological parameters during the entire observation period. The temperature ranged from 6.8 to 30.8 °C with an average of 16.6 ± 4.7 °C (± 1σ). The average RH was 71% ± 16% during the entire measurement period. Note that the meteorological data were missing from 12th-15th June due to a sensor failure. In addition, hourly meteorological

data including temperature, relative humidity, boundary layer height and precipitation were retrieved from the ERA5 reanalysis data. Good agreements were found for these meteorological parameters from the measurements and ERA5 data (Fig. S21). Solar radiation and boundary layer height showed maximum values at midday. The wind conditions varied among westerly, southwesterly and easterly winds. The southwesterly and easterly winds were from the forest regions. In contrast, the westerly winds had higher wind speeds (> 1 m s^{-1}), which could bring emissions from a biogas power plant to the sampling site. The variations of wind conditions were consistent with the air mass origins. Based on HYSPLIT analysis, all air mass back-trajectories were grouped into three clusters. Clusters C1 (southwest) and C3 (northeast) correspond to two long-range transport air masses, while C2 (west) represents relatively local air masses. Several heavy rainfall events (>10 mm h^{-1}) occurred along with long-range transport air masses. Two sunny periods were influenced by the air mass cluster 2, but characterized with different temperature and RH. Period 1 (9^{th} to13^{th} June) was characterized as lower-temperature (Low-T) period with an average temperature (12.9 ± 1.7 °C) and RH (71% ± 9%), while period 2 (24^{th} to 27^{th} June) was defined as higher-temperature (High-T) period with an average temperature (23.0 ± 4.2 °C) and RH (47% ± 11%). The meteorological conditions play important roles in the variations of trace gases and aerosol particles, which will be discussed in the following sections.

In this study, the mixing ratios of CH_4 varied from 1.90 to 2.56 ppm with an average of 1.98 ± 0.05 ppm. The mixing ratios of CO_2 ranged from 383 to 567 ppm with an average of 406 ± 11 ppm. CH_4 and CO_2 are significant greenhouse gases, which can be largely contributed by natural sources globally (Tian et al., 2016). On a regional scale, anthropogenic sources like power plants for the energy production (Olivier et al., 2005; Sanz-Bobi et al., 2012; Ullah Khan et al., 2017) can lead to enhanced CH_4 mixing ratios. Many CH_4 spikes were observed during the measurement periods e.g., 11^{th}, 17^{th}, 20^{th} -23^{nd} and 27^{th} June. These CH_4 spikes occurred mostly during nighttime along with the shift of easterly to westerly wind directions. The westerly winds can bring the CH_4 from the nearby biogas power plant to the sampling site. No concurrent spikes were observed for CO_2, suggesting that the impact of the biogas power plant on CO_2 variations was negligible. CO is commonly used as a tracer of combustion emissions with long lifetime (several months) and weak chemical reactivity (Warneke et al., 2006). In this study, the average mixing ratios was 106 ± 19 ppb. No correlation was found between CO and CH_4, indicating that they have different sources. Unlike CH_4, CO showed occasional spikes during daytime (e.g., 10^{th},14^{th} and 27^{th} June), which

were likely caused by cars which occasionally passed by the sampling site. The average mixing ratio of O_3 was 36.2 ± 12.9 ppb during the entire measurement period. The average mixing ratios of O_3 during the higher temperature period (51.3 ± 8.1 ppb) was significantly higher than during the lower-temperature period (31.8 ± 12.9 ppb), indicating stronger photochemical oxidation processes during associated with higher temperatures.

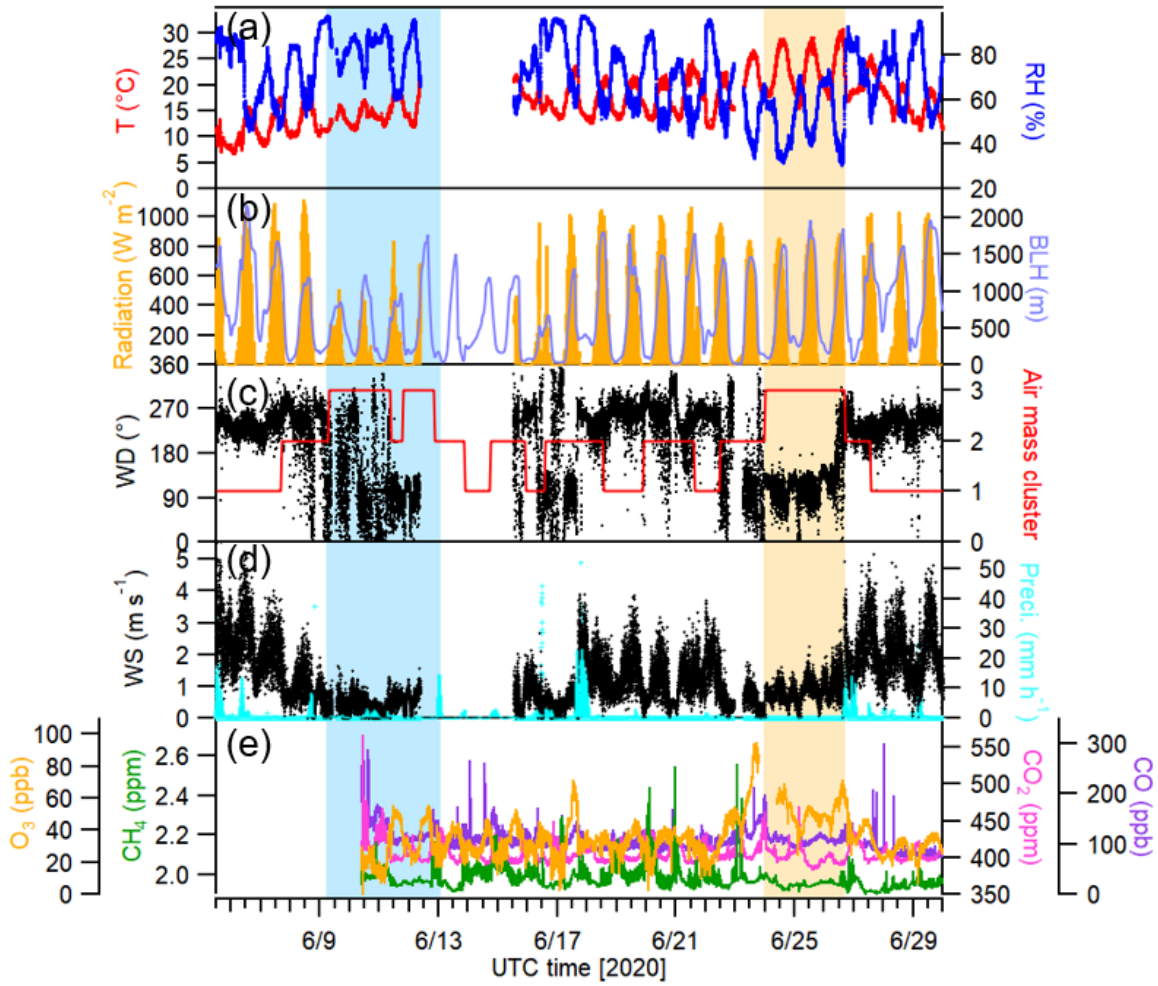

Figure 44. Time series of meteorological parameters (a) temperature and relative humidity. (b) radiation and boundary layer height. (c) wind direction and air mass origins. (e) wind speed and precipitation (f) concentrations of O_3, CH_4, CO, CO_2. The blue and yellow shaded areas show the period air from forest with low and high temperature, respectively.

3.4.2 Variations of selected VOCs and aerosol particles

The time series of selected VOCs including isoprene, monoterpenes, sesquiterpenes, green leaf volatiles and aromatic hydrocarbons are shown in Figure 45. The diurnal variations of isoprene, monoterpenes, sesquiterpenes, benzene, toluene and hexenals are shown in Figure 46. These VOCs

are usually considered to be significant precursors of SOA formation. Based on the results in section 3.1, there were good agreements of most VOCs measured by the PTR-MS-4000 and Vocus-PTR-MS. The data of sesquiterpenes were not available for 5-22 June due to a transmission loss for the higher mass range (> *m/z*200) in PTR-MS-4000. A good agreement of sesquiterpenes detected by PTR-MS-4000 and Vocus-PTR-MS was found for 22-30 June. Compared to PTR-MS-4000, Vocus-PTR-MS can well detect various VOC oxidation products and intermediates with higher molecular weight in the gas phase (Li et al., 2021a). However, PTR-MS-4000 with a CHARON inlet can also measure the chemical composition of organic aerosol in the particle phase (Gkatzelis et al., 2018b). Therefore, the combination of CHARON-PTR-MS and Vocus-PTR-MS data provides a good opportunity for investigating the chemical processes of VOCs and organic aerosol in this study.

The average mixing ratio of isoprene was 0.71 ± 0.58 ppb, consistent with that observed in the a Norway spruce-dominated forest in central Germany (0.34 ± 0.16 ppb) (Bourtsoukidis et al., 2014) and a pine tree-dominated Landes forest in France (~0.6 ppb) in summer seasons (Li et al., 2020; Mermet et al., 2021). These values were higher than that reported in boreal forests (0.01-0.2 ppb) during summertime (Hellén et al., 2018; Lappalainen et al., 2009), but much lower than in tropical forest as in Amazonia (2.2-7.8 ppb) (Yáñez-Serrano et al., 2015). The difference of isoprene among these forests could be attributed to the different tree types with higher isoprene emissions from deciduous trees like in tropical forests than by conifer trees like in boreal forests but of course also due to different prevailing meteorological conditions. The diurnal variation of isoprene showed higher concentration during daytime with high temperature and intensive radiation for the entire measurement period (Figure 46). Compared to low-T period, the diurnal variation of isoprene showed significantly increase during the daytime of high-T period, which was in line with the fact that high temperature and intensive radiation facilitate the emissions of pine trees (Guenther et al., 1993; Kuhn et al., 2002).

The mixing ratios of monoterpenes varied from 0.02 to 53.5 ppb with an average of 2.1 ppb during the entire measurement period. The average monoterpene level in this study was higher than that in a forest site in central Germany (0.5 ± 0.21 ppb) (Bourtsoukidis et al., 2014) but lower than those observed in the French Landes forest (~6 ppb) (Li et al., 2020; Mermet et al., 2021). The variations of monoterpenes can be driven by many factors including tree types, emissions induced by meteorological conditions and chemical processes. In this study, there were occasional spikes

of monoterpenes (>10 ppb) along with the shift of wind directions at early nights of e.g., 7-11 June and 22-23 June. In particular, the highest mixing ratios of monoterpenes (53.5 ppb) were observed at the night of 8-9 June when the easterly winds changed to westerly winds. As mentioned above, the westerly winds did bring emissions of a biogas power plant to the sampling site. Therefore, the occurrence of these spikes indicate that biogas power plant was an important point source of monoterpenes. The diurnal variation of monoterpenes showed a peak concentration at 22:00 during nighttime of the entire measurement period. This peak was more pronounced at 22:00 with the highest concentration (~9 ppb) during nighttime of low-T period, which was mainly caused by the biogas power plant emissions during nighttime. Besides, monoterpene showed the increase during daytime of high-T period, while no peak was observed during nighttime of high-T period when the sampling site was mainly influenced by the forest air. The daytime increase of monoterpene indicated that high temperature can facilitate the plant emissions again.

The average mixing ratios of sesquiterpenes ranged from below detection limit to 24.5 ppt with an average of 3.8 ± 3.8 ppt. The average sesquiterpene level was much lower than those observed at a forest site in central Germany (90 ± 80 ppt) and in the French Landes forest (64.5 ppt) in summer (Li et al., 2020). Recently, Fischer et al., (2021) reported the concentrations of sesquiterpenes ranging from 1 to 10 ppt measured by the PTR3-TOF-MS s above a boreal forest in spring 2016. Note that the quantification of sesquiterpenes by the PTR was based on the signal of parent ion $C_{15}H_{25}^{+}$. One common issue is significant fragmentation of sesquiterpenes to produce fragment ions inside all PTR instruments (Kari et al., 2018; Kim et al., 2009) as discussed in section 3.1. Therefore, no correction of fragmentation will lead to the underestimation of sesquiterpene quantification by the PTR. In this study, without the correction of sesquiterpene fragmentation, the mixing ratios of sesquiterpenes can be regarded as a lower limit. Similar to monoterpenes, sesquiterpenes showed a pronounced peak during daytime of high-T period compared to low-T period. It should be noted that monoterpenes and sesquiterpenes are highly reactive towards OH radicals and O_3, which could be chemically removed during daytime. Therefore, the increase of monoterpenes and sesquiterpenes showed the emissions of terpeniods were higher than the removal by the photochemical oxidation during high-T period.

Green leaf volatiles (GLVs) represent another important group of plant volatile, mostly consisting of C_5 and C_6 alcohols, aldehydes and esters (e.g., pentanone, pentanone, hexenals). The releases of GLVs are often associated with the stress (high temperature and insect herbivory) on

the plants. The average mixing ratios of pentanones ($C_5H_{10}O$) and hexenals ($C_6H_{10}O$) were 11.3 ± 5.9 ppt and 9.4 ± 5.3 ppt, respectively. Previous studies investigated the emissions of GLVs mostly based on branch enclosure measurements (Brilli et al., 2011; Schaub et al., 2010), and only few data are available on ambient concentrations of GLVs (Fall et al., 2001; Hellén et al., 2018; Jardine et al., 2015b). The average mixing ratios of hexenals were slightly higher than the average level of trans-2-hexenal (4.6 ppt) measured by a GC-MS at a boreal forest site in summer 2015 (Hellén et al., 2018). Note that the PTR-MS cannot separate the isomers of VOCs, therefore it measures the total hexenals. Furthermore, fragmentation of GLV species inside the PTR-MS instrument (Pang, 2015) can lead to a underestimation of these species. Therefore, the mixing ratios of pentanones and hexenals were regarded as lower limits. The diurnal variation of hexenals showed increases during daytime of entire measurement period. There was no significant change in hexenal diurnal variations between low-T and high-T periods, suggesting that temperature may play a minor role in the emissions of hexenals.

The mixing ratios of aromatic hydrocarbons were very low with average values of 0.11 ± 0.14 ppb, 0.16 ± 0.19 ppb and 0.03 ± 0.04 ppb for benzene, toluene and xylenes respectively. These aromatic hydrocarbons are widely considered as tracers for fossil fuel/biomass burning (Gkatzelis et al., 2021; Wang et al., 2020), whereas other anthropogenic sources such as a biogas power plant can also release significant amounts of aromatic hydrocarbons (Salazar Gómez et al., 2016; Sanz-Bobi et al., 2012). In fact, some aromatic spikes were observed (> 0.5 ppb) along with the shift of wind directions from the easterly to westerly. Therefore, the westerly winds may bring biogas power plant emissions including aromatics as well. The diurnal variations of benzene and toluene showed slightly increases during nighttime of entire measurement period, while they had a similar peak at 22:00 as monoterpenes. These concurrent peaks of monoterpenes and aromatic hydrocarbons indicated the importance of biogas power plant emissions again.

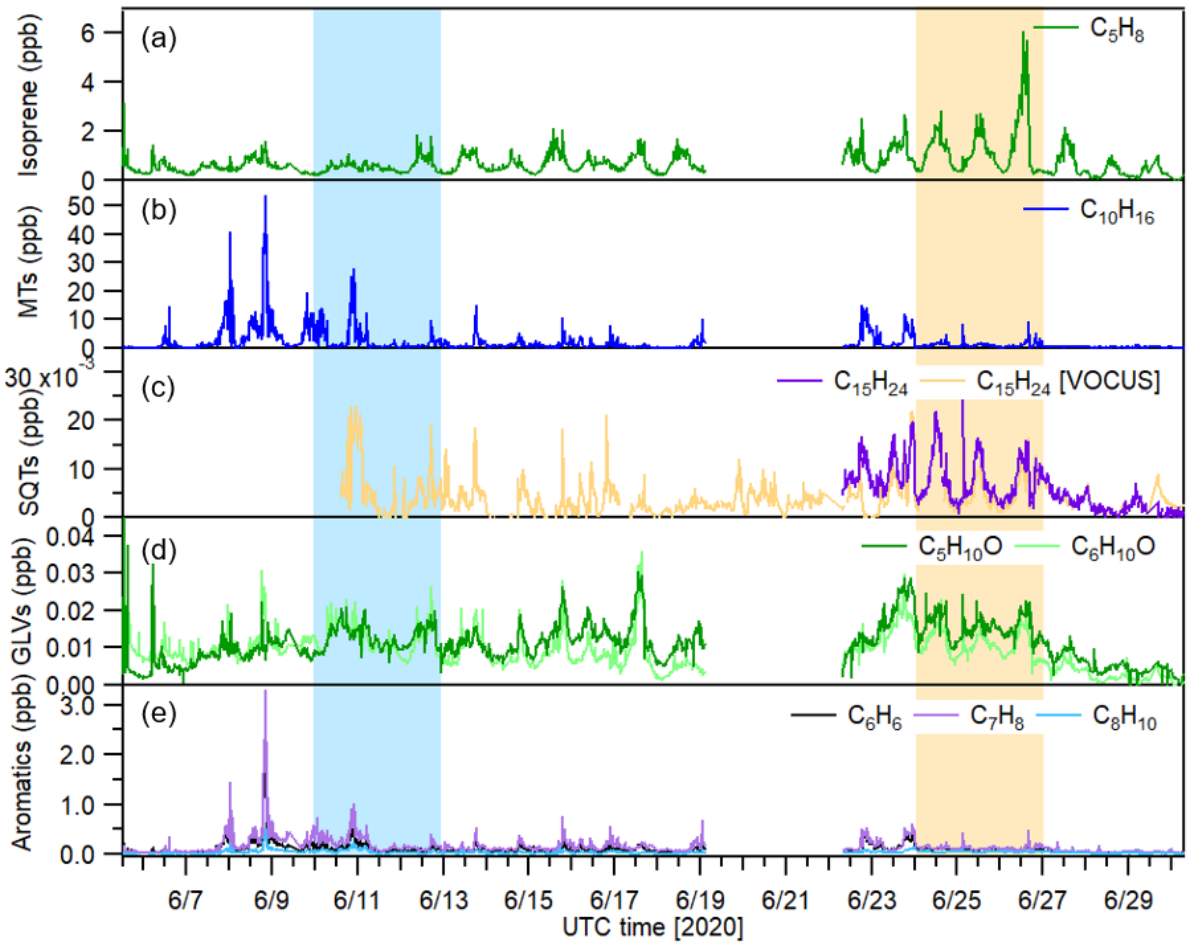

Figure 45. Time series of VOC mixing ratios (a) isoprene (C_5H_8); (b) monoterpenes ($C_{10}H_{16}$); (c) sesquiterpenes ($C15_5H_{24}$), (d) green leaf volatiles ($C_5H_{10}O$ and $C_6H_{10}O$), (e) benzene (C_6H_6), toluene (C_7H_8) and xylenes (C_8H_{10}). The sesquiterpene data were not available for 5th to 22nd June due to the transmission loss of the PTR-MS-4000, which are complemented by measurement by the Vocus-PTR-MS. The blue and yellow shaded areas show the period air from forest with low and high temperature, respectively.

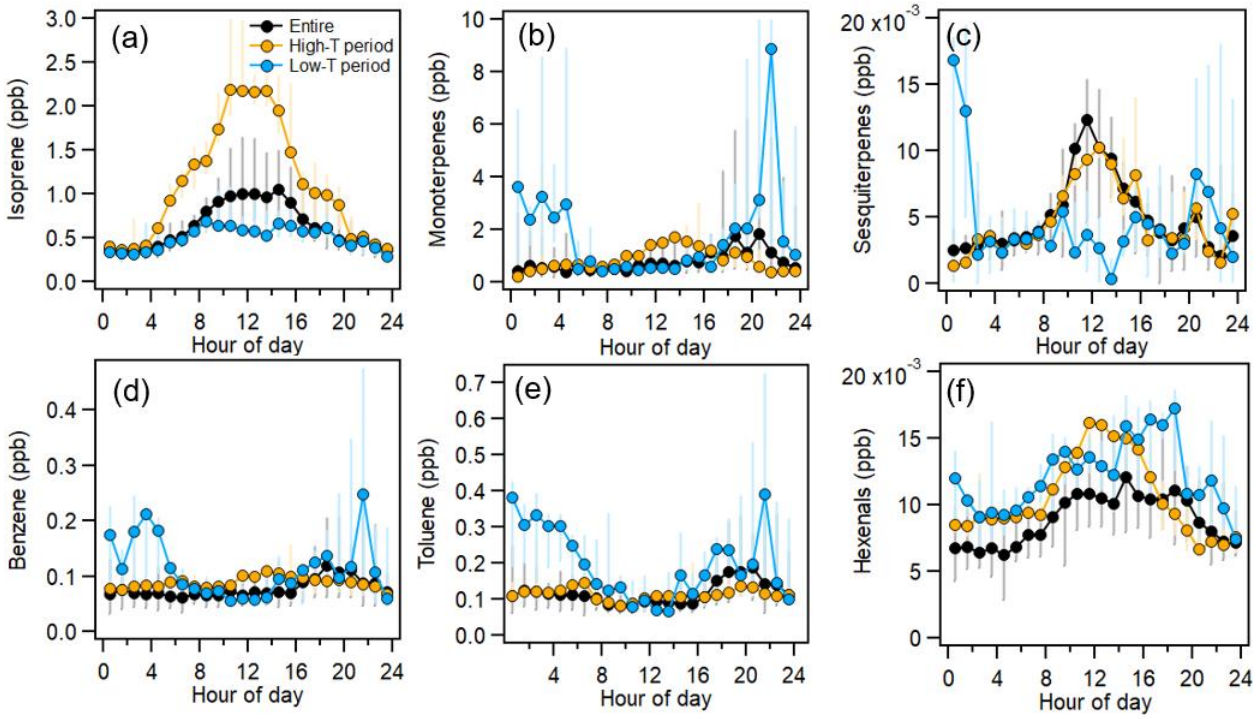

Figure 46 Diurnal variations of (a) isoprene, (b) monoterpenes, (c) sesquiterpenes, (d) benzene, (e) toluene and (f) hexenals for the entire measurement period (black), high-temperature (yellow) and low-temperature periods (blue).

During the entire measurement period, the average mass concentrations of $PM_{2.5}$ and PM_1 measured by the OPC were 5.5 ± 4.7 μg m^{-3} and 5.0 ± 4.5 μg m^{-3} respectively, indicating that PM_1 comprises the majority of $PM_{2.5}$ mass. The average mass concentrations of nitrate and organic aerosol particles measured by the CHARON-PTR-MS were 1.02 ± 2.23 μg m^{-3} and 0.87 ± 0.41 μg m^{-3} respectively. Besides, the average mass concentration of BC measured by the aethalometer was 0.17 ± 0.11 μg m^{-3}. The mass concentrations of aerosol components varied significantly over the entire measurement period. Nitrate showed occasional peaks during the periods of e.g., 7^{th}-11^{th}, 14^{th}, 17^{th}, 22^{nd} June when higher mass concentrations of PM_1 (>10 μg m^{-3}) were observed. The contribution of nitrate to PM_1 mass can reach up to > 45%, indicating that the importance of nitrate in the occurrence of these aerosol particle peaks. There were no concurrent peaks found for BC at the same time. To estimate the relative influences of traffic and biomass burning on BC, the Absorption Ångström exponents (AAE) were calculated by using two wavelengths (470 and 880 nm) from the aethalometer (Sandradewi et al., 2008a). The average value of AAE was 1.23 ± 0.68, which was close to that for the traffic-related BC (0.8~1.1) (Blanco-Donado et al., 2022). Therefore, PM_1 and nitrate peaks without concurrent BC peaks suggest that the peaks of PM_1 and nitrate may

come from non-traffic sources and/or secondary formation processes. Comparing two periods with different temperatures, it can be found that significantly higher mass concentration of PM_1 and nitrate were observed during the lower-temperature period. As mentioned above, the lower-temperature period had the shift of wind directions occasionally from the biogas power plant to the forest, which may lead to the accumulation of aerosol particles. Furthermore, lower temperatures corresponded to higher relative humidities, which favor portioning of semi-volatile aerosol components like nitrate. In contrast, there were constant winds from the local forest during the higher temperature period along with constant low concentrations of BC and CO. Therefore, less biogas power plant emissions during this period. In fact, high concentrations of BVOCs were observed during the higher temperature period. High concentrations of organics (> 1 µg m^{-3}) were found, which might be related to the oxidation of BVOCs. Nitrate showed low concentrations (< 0.5 µg m^{-3}) during the higher temperature period, which may be caused by the evaporation of semi-volatile aerosol components. It should be noted that nitrate includes inorganic nitrate like ammonium nitrate and organic nitrate. The separation of inorganic and organic nitrates is not possible by the CHARON-PTR-MS or other instruments in this study. Based on the wind conditions, air mass origins and variation of BC, it was reasonable to speculate that nitrate was mainly contributed by organic nitrate during the higher temperature period. In the following section, the link between BVOC oxidation and SOA formation will be discussed in depth especially for the high-temperature period.

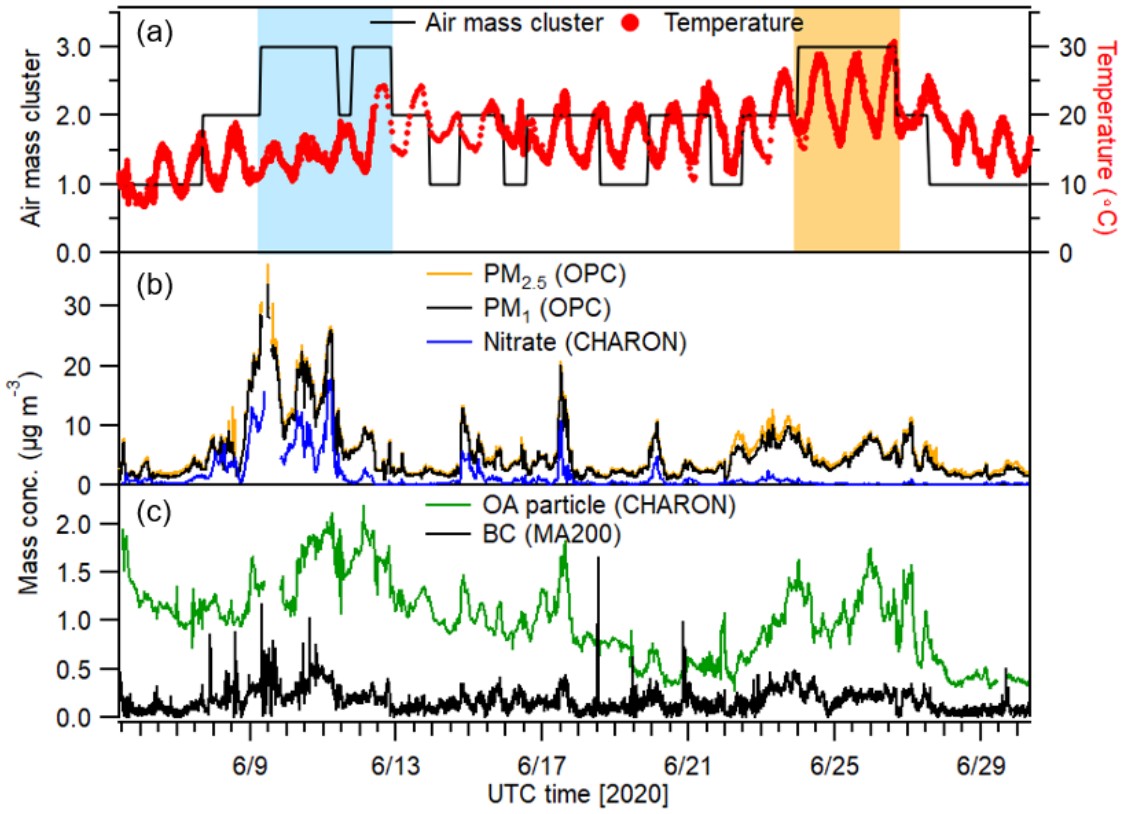

Figure 47. Time series of (a) air mass cluster and temperature, (b) mass concentrations of PM_1, $PM_{2.5}$ and nitrate. (c) concentrations of organic aerosol particles and BC. The shaded areas show two periods with local air masses but different temperature.

3.4.3 Wind dependence of trace gases

As mentioned above, the variations of trace gases were strongly associated with the wind directions. Figure 48 shows the wind-direction dependence of other meteorological parameters (WS, radiation, RH and T) and the concentrations of CH_4, CO and CO_2. Here I further divided the wind conditions into four different groups according to other meteorological parameters. Group 1 (G1) represents the northerly to easterly winds (0° < WD < 90°) from the forest with very low wind speeds (< 0.5 m s^{-1}) for stagnant conditions. Group 2 (G2) represents the easterly to southerly winds (90° < WD < 180°) from the forest with higher temperature and low RH. Group 3 (G3) represents the southerly to westerly winds (180° < WD < 270°) from the forest but with higher wind speeds (> 1 m s^{-1}), which can lead to long-range transport and/or dilution. Group 4 (G4) represents the westerly to northerly winds (270° < WD < 360°) during nighttime without radiation, coming from the biogas power plant and the Kleinhau village.

The concentrations of CH_4 were significantly elevated in G4 when the wind was coming from the biogas power plant direction, strongly pointing to the biogas power plant as an emission source for CH_4. CO_2 also showed slight increase in G4, while CO showed no changes. Therefore, elevation of CH_4 and CO_2 concentrations in G4 can be attributed by the biogas power plant emissions rather than other anthropogenic emissions like traffic or biomass burning from the small village Kleinhau. The highest concentrations of CO_2 and CO were observed in G1, which may be associated with the accumulation of air pollutants under stagnant condition. In contrast, lowest concentration of CO was observed in G3 with the dilution due to higher wind speeds.

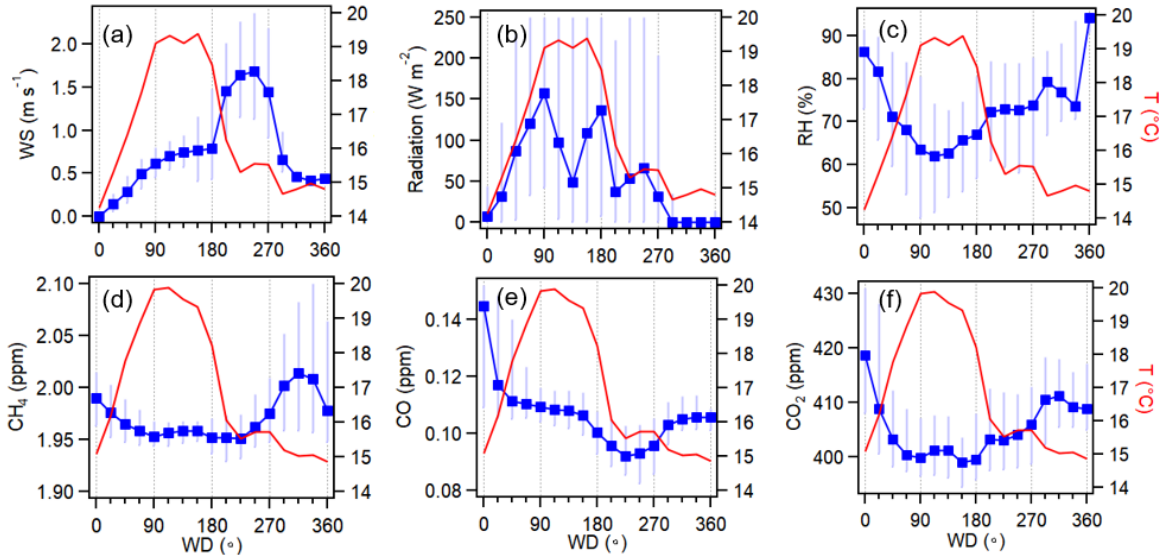

Figure 48. Bin plots with the wind directions for (a) wind speed, (b) radiation, (c) relative humidity, (d-f) concentration of CH_4, CO, CO_2 along with temperature (red lines). Solid dots denote the median value in each bin. The bottom and top of sticks represent the 25th and 75th percentiles.

In a same way, the wind-direction dependence of VOC concentrations of isoprene, monoterpene, sesquiterpenes, green leaf volatiles, benzene, toluene and xylenes along with the temperature was investigated and plotted in Figure 49. In G1, the mixing ratios of isoprene showed an enhancement as temperature increased, which was consistent with that higher temperature can facilitate isoprene emissions. In G2, a clear drop was found for isoprene mixing ratios at the WD of 135°, which was similar with a drop of solar radiation. This can be explained by the fact that isoprene emissions are controlled by both temperature and radiation (Guenther et al., 1993; Kuhn et al., 2002). Besides, low mixing ratios of isoprene were observed in G3 and G4 with lower temperatures. Monoterpenes, benzene, toluene and hexenals showed a clear peak concentration in G4, especially when the wind

was coming from the biogas power plant direction (WD = 295°). This suggests that the biogas power plant is an important source of monoterpenes and aromatic hydrocarbons as well. A previous study has reported VOC emissions from three different biogas power plants in Germany based on GC-MS measurement (Salazar Gómez et al., 2016). Terpenes are among the predominant non-methane VOCs in the emissions of biogas power plants, especially α-pinene and limonene.

Considering the data when the winds were coming from the forest regions in G1-G3 (0° < WD < 270°), monoterpenes and sesquiterpenes show the decrease as temperature increased in G1 and G2. Higher concentrations of atmospheric oxidants (O_3 and OH radicals) were expected during daytime in G1 and G2, which could lead to the chemical removal of monoterpenes and sesquiterpenes. In contrast, higher mixing ratios of monoterpenes and sesquiterpenes were found in G1, which were related to lower wind speeds and weaker chemical removal. For green leaf volatiles, pentanone and pentanone showed a positive relationship with temperature in G2 and G3 (90° < WD < 270°), suggesting that higher temperatures may enhance the emissions of pentanone and pentanone. Even though the temperature was low in G1 (especially 0° < WD < 45°), constantly higher mixing ratios of green leaf volatiles were found. Similarly, higher mixing ratios of aromatic hydrocarbons were found in G1 with 0° < WD < 45°. These results were mainly associated with lower wind speeds and weak chemical removal as explained for the variations of monoterpenes and sesquiterpenes.

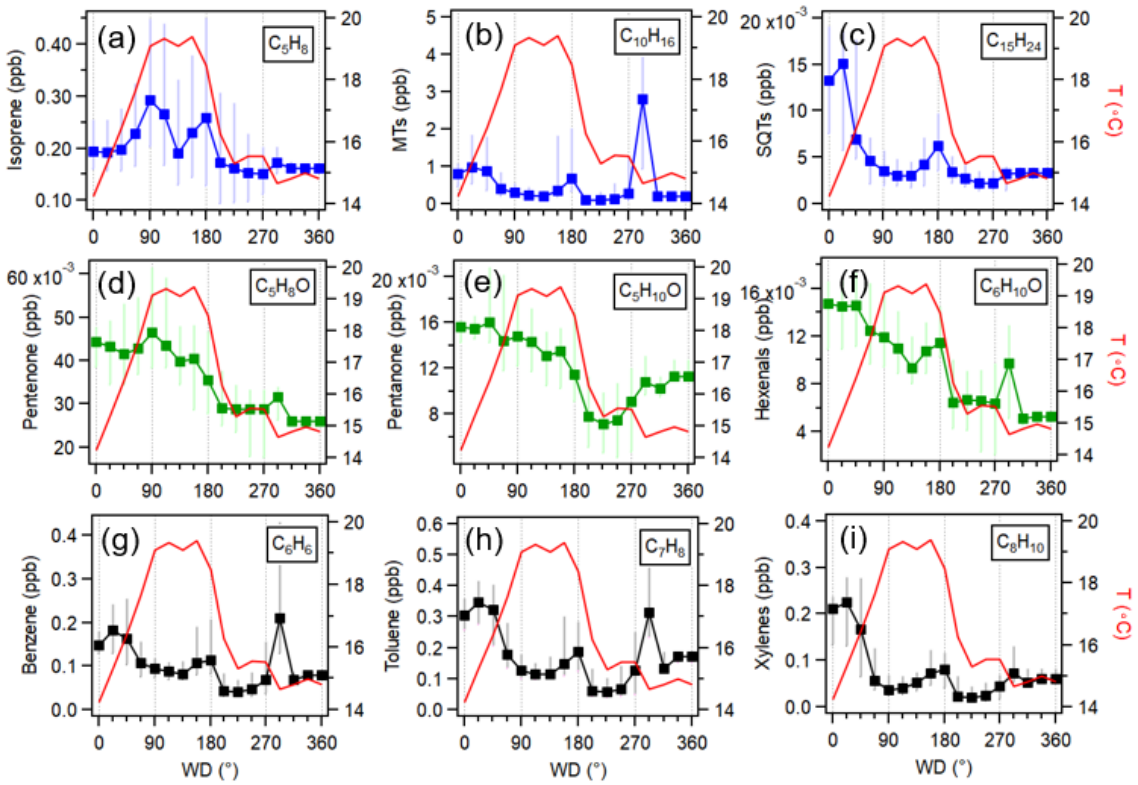

Figure 49. Concentration plots binned by wind directions for (a) isoprene, (b) monoterpenes, (c) sesquiterpenes, (d) pentanone, (e) pentanone, (f) hexenals, (g) benzene, (h) toluene, (i) xylenes along with temperature (red lines). Solid dots denote the median value in each bin. The bottom and top of sticks represent the 25th and 75th percentiles.

3.4.4 Insights into BVOC oxidation and SOA chemistry

Figure 50 shows the temporal evolution of temperature, relative humidity, concentrations of monoterpenes, O_3, CO and aerosol components as well as bulk O:C and H:C ratios from 22nd to 30th June. This case can provide a good opportunity to investigate the impact of meteorological parameters on the variations of VOCs and SOA formation processes by state-of-the-art PTR-MS instrument. This case was selected mainly due to the following reasons. Firstly, organic compounds in both gas and particle phase were well detected for the CHARON-PTR-MS without transmission loss issue and Vocus-PTR-MS during this case. Secondly, low concentrations of BC (< 0.5 μg m^{-3}) were observed during this case, thus the impacts of primary anthropogenic emissions on aerosol particles should be minor during this case. Thirdly, this case covers the higher temperature period from 24th-27th June (max. ~30 °C) with higher O_3 levels (max. ~92 ppb), which could facilitate increased emissions of BVOCs and their oxidation to SOA formation. During this case, there were some spikes of monoterpenes (> 5 ppb) observed, which were associated with the fluctuation of

wind direction bringing the biogas power plant emissions to the sampling site. The average mass concentration of organics was 0.86 ± 0.36 μg m^{-3}, which comprises of on average 19 ± 8% to total PM_1 mass during this case. Note that a large fraction of PM_1 mass (~71%) were not defined here. This undefined PM_1 fraction could be attributed to low-volatility aerosol species like ammonium sulfate or low-volatility organic compounds, which cannot be measured by the CHARON-PTR-MS. The nitrate fraction in PM_1 was on average 5.7 ± 7.9%, close to the values reported for PM_1 measured by the AMS (3-10%) in urban/rural areas during summertime previously (Huang et al., 2019a; Song et al., 2022). Here the CHARON-PTR-MS-measured nitrate can be regarded as the upper limit of organic nitrate especially during this case with minor impact of anthropogenic emissions. The O:C and H:C of bulk organics were 0.32 ± 0.03 and 1.56 ± 0.10 respectively, which were within the range of SV-OOA (O:C: 0.35 ± 0.14 and H:C: 1.55 ± 0.10) resolved from the factor analysis of organics measured by the AMS in previous studies (Ng et al., 2011; Ng et al., 2010). This suggests that CHARON-PTR-MS measured the majority of semi-volatile organic compounds. If considering the CHARON-PTR-MS-measured organics as SV-OOA, its mass fraction to PM_1 was close to the values (20 ± 5%) in previous studies (Huang et al., 2019a; Song et al., 2022). Therefore, CHARON-PTR-MS can well quantify semi-volatile aerosol species including organics and nitrate, while the low-volatile aerosol species were not determined in this study.

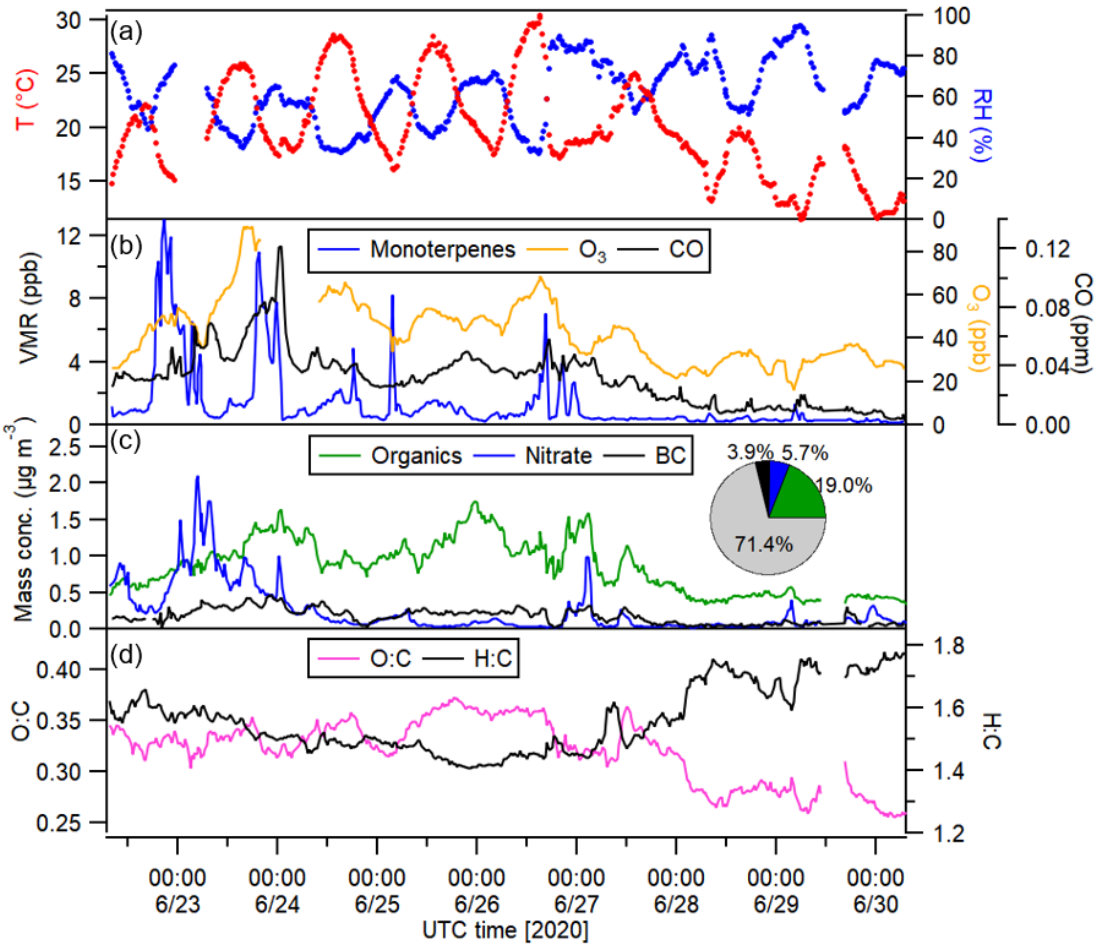

Figure 50 Time series of (a) temperature (T) and relative humidity (RH); (b) mixing ratios of monoterpene, O_3 and CO; (c) mass concentrations of organics, nitrate measured by the CHARON and BC. The insert pie chart shows the relative contribution of organics, nitrate and BC to total PM_1 mass (71.4% as undefined PM_1 fraction). (d) bulk oxygen to carbon and hydrogen to carbon ratios (O:C and H:C).

During this case, the diurnal variations of temperature and relative humidity showed an opposite trend (Figure 51). Total particle organic and nitrate mass concentrations showed increases during nighttime, which can be attributed to the evolution of the boundary layer and nighttime chemistry. According to the ERA5 reanalysis data, the boundary layer height showed the decrease during nighttime. It should be noted that the ERA5 only provides the hourly data and may not resolve the boundary layer height accurately for the transition from day to night as reported by a recent study (Sinclair et al., 2021). Given the limitation of ERA5 BLH data, another method was adapted to remove the effect of BLH evolution by the normalization of data to ΔCO, where ΔCO is the total CO concentration subtracted the background concentration (minimum value for the entire measurement period). In this study, CO generally showed a negative relationship with the BLH

(Fig. S23). The diurnal variations of monoterpene/ΔCO showed two peaks at 4:00 in the morning and 21:00 in the evening respectively, which could correspond to the time point with high plant emissions and low atmospheric oxidation capacity. The value of monoterpene/ΔCO showed a rapid decrease after the morning peak. Note that the reactions of monoterpenes with OH· radicals is approximately 2 times faster than that of monoterpenes with O_3 (Atkinson et al., 1990). This may explain the rapid decrease of monoterpene/ΔCO after the morning peak during daytime. However, during the nighttime, a simultaneously decrease of O_3 and monoterpene/ΔCO is observed, leading to the oxidation of monoterpenes. Correspondingly, there is a clear increase of organics/ΔCO and nitrate/ΔCO during nighttime especially for late evening (0:00-3:00). Therefore, it is reasonable to conclude that the nighttime increases of organic mass were caused by the oxidation of monoterpenes by O_3. Currently, the data of NO_2 were not well quantified and many extremely high and unexpected values (> 100 ppb) were observed in this campaign (Fig. S24). The median diurnal variation of NO_2 showed a simultaneously decrease as O_3 during nighttime, implying the production of NO_3· radicals by the reaction of NO_2 and O_3. The nighttime increase of particle nitrate (or organic nitrate) measured by the CHARON could be related to the reaction of monoterpenes and NO_3· radicals. The diurnal variation of O:C shows an increase during daytime as the concentration of O_3 increases, while H:C shows an opposite trend. This indicates the photochemical oxidation processes during daytime.

During this case, the CHARON-PTR-MS and Vocus-PTR-MS can detect many oxygenated organic molecules such as $C_{10}H_{14,16}O_{1\text{-}5}$, $C_9H_{13,15}O_{1\text{-}5}$, $C_8H_{12,14}O_{1\text{-}5}$ and $C_7H_{10,12}O_{3\text{-}6}$. These organic molecules were widely regarded as the products of monoterpene oxidation in simulation chamber studies (Gkatzelis et al., 2018b; Riva et al., 2019), and also recently reported in field studies by the high sensitivity Vocus-PTR-MS (Li et al., 2020). Specifically, $C_{10}H_{16}O_3$ can be assigned as *cis*-pinonic acid, widely regarded as one of α-pinene-derived SOA tracers (Claeys et al., 2007; Zhang et al., 2015). The CHARON-PTR-MS can detect the less-oxygenated monoterpene-derived organic molecules ($C_{10}H_{16}O_{1\text{-}3}$) in both gas and particle phases. In addition to less-oxygenated monoterpene-derived organic molecules, the Vocus-PTR-MS can also detect more-oxygenated ones ($C_{10}H_{16}O_{4\text{-}5}$) in the gas phase. In order to investigate the evolution of monoterpene oxidation, the diurnal variations of monoterpene oxidation products (e.g., $C_{10}H_{16}O_x$) in both gas and particle phases were calculated. The diurnal variations of $C_{10}H_{16}O_{1\text{-}3}$ signals in both gas and particle phases showed significant increases during nighttime. Given the rapid decrease of monoterpene and O_3

during nighttime, it can be concluded that the ozonolysis of monoterpenes can lead to the formation of less oxygenated organic compounds and mostly of semi-volatile nature. In contrast, the diurnal variations of more-oxygenated organic molecules $C_{10}H_{16}O_{4\text{-}5}$ in the gas phase showed significant increases during daytime, which was caused by the photochemical oxidation (including autooxidation) of monoterpenes during daytime.

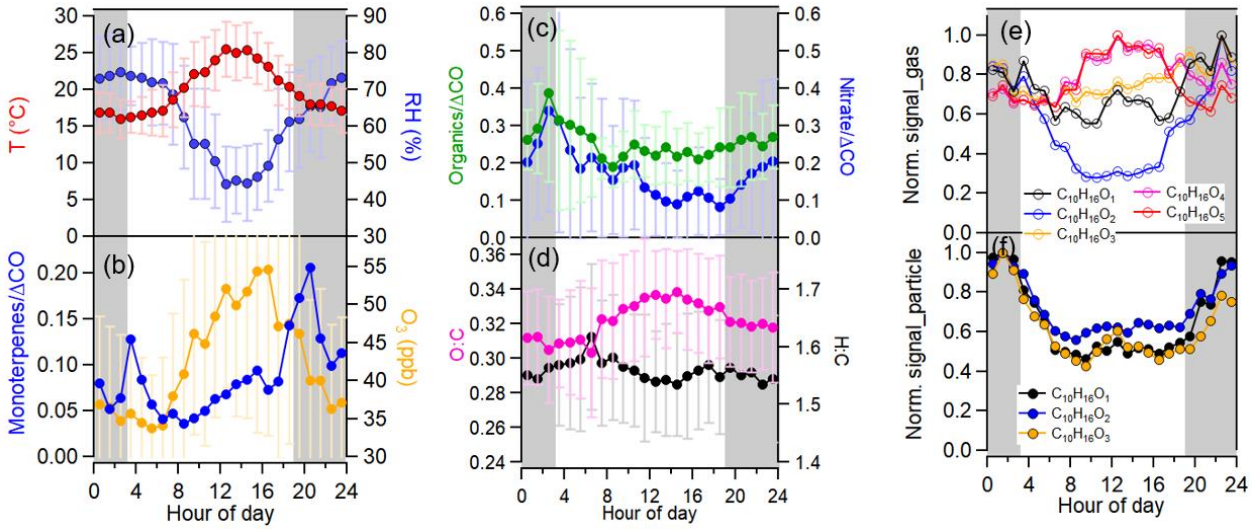

Figure 51 The mean diurnal variations of (a) temperature and relative humidity, (b) O_3 mixing ratios and monoterpenes/ΔCO, (c) organics/ΔCO and nitrate/ΔCO, (d) O:C and H:C ratios, (e-f) mean normalized signal of monoterpene oxidation products ($C_{10}H_{16}O_{1\text{-}5}$) in gas and particle phases. Signals were normalized to their maximum values.

Furthermore, I calculated the relative fraction of semi-volatile organic molecules in particle to that in gas phase based on the CHARON-PTR-MS measurement. Generally, the partition coefficient (K_i) can be calculated as following equation (Pankow, 1994):

$$\boldsymbol{K_i} = \frac{[i]_{particle}}{[i]_{gas} * \boldsymbol{M_{org}}} \quad (3)$$

Where M_{org} is the aerosol organic mass concentration, $[i]_{particle}$ and $[i]_{gas}$ are the concentrations of compound i in the particle and gas phases, respectively. Therefore, the relative fraction of semi-volatile organic molecules in particle to that in gas phase can be used as a proxy for the partition coefficient. Although the partition coefficient can also be directly calculated for each molecules, it may suffer large uncertainties due to the fragmentation inside PTR (Gkatzelis et al., 2018a) especially for complex ambient air. As shown in Figure 52, the relationship between particle to gas

fraction of $C_{10}H_{16}O_{1-3}$ and relative humidity were investigated. The particle to gas fraction of $C_{10}H_{16}O$ and $C_{10}H_{16}O_3$ positively correlated with the increase of RH. The increased fractions of $C_{10}H_{16}O$ and $C_{10}H_{16}O_3$ were estimated as 0.006 and 0.005 for an increase of 1% in RH. The particle to gas fraction of $C_{10}H_{16}O_2$ also showed a positive correlation with RH when the RH was above 65%. However, no significant change for particle to gas fraction of $C_{10}H_{16}O_2$ was found with RH when it was below 65%, which cannot be explicitly explained now. Furthermore, RH showed a negative correlation with temperature (R = 0.82). Therefore, high RH and low temperature can efficiently facilitate the partitioning of monoterpene-derived semi-volatile organic compounds. During this case, the decrease of temperature and increase of RH from day to night were very pronounced during higher temperature periods (24^{th}-27^{th} June, Figure 50). Therefore, these results indicate that monoterpene oxidation and subsequent gas-to-particle partitioning dominate SOA formation and mass increase during nighttime.

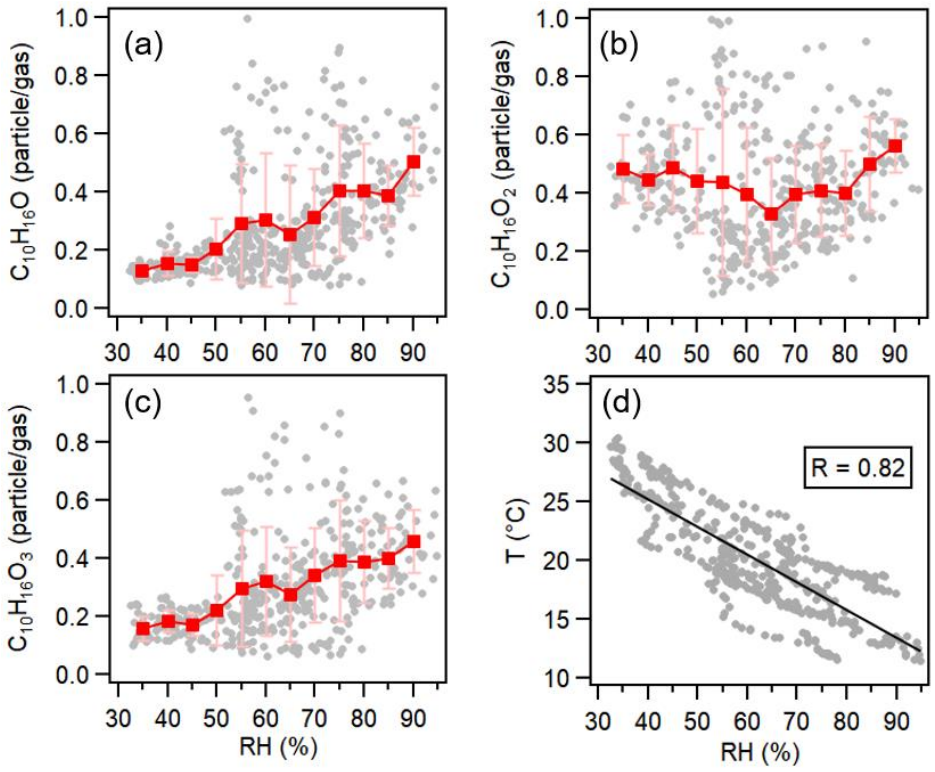

Figure 52 (a-c) Scatter plot of particle to gas phase fractionation of $C_{10}H_{16}O$, $C_{10}H_{16}O_2$ and $C_{10}H_{16}O_3$ vs. relative humidity (RH). The data are binned with RH increments of 5%; mean values (red squares) and standard deviations are displayed for data in each bin. (d) linear fitting plots between RH and temperature (T).

3.4.5 Summary

In this study, two new state-of-the-art CHARON-PTR-MS and Vocus-PTR-MS were deployed in a stressed pine forest in western Germany for characterizing the variations and sources of VOCs and their contributions to SOA formation. A nearby biogas power plant was identified as an important source for methane, monoterpenes and aromatics. Two periods were characterized with the influence mostly by air masses from the forest but with lower- and higher-temperatures. Higher concentrations of isoprene, monoterpenes and sesquiterpenes were observed for higher temperature period with intensive radiation. In contrast, monoterpenes and sesquiterpenes showed higher concentrations during nighttime of lower temperature period, which were caused by the biogas power plant emissions. High concentrations of semi-volatile OA measured by the CHARON-PTR-MS were found at nights with relatively high temperatures. The diurnal variations of less oxygenated and semi-volatile monoterpene derived organic products ($C_{10}H_{16}O_{1\text{-}3}$) showed increasing concentrations during nighttime. However, more-oxygenated and low-volatility organic products ($C_{10}H_{16}O_{4\text{-}5}$) showed opposite diurnal variations with increases during daytime, which can explain the chemical removal of monoterpenes during daytime. However, lower temperatures and increased RH during nighttime facilitates the gas-to-particle partitioning of semi-volatile monoterpene-derived organic molecules. In this study, the relative fraction of $C_{10}H_{16}O_{1\text{-}3}$ in particle phase can be increase of 0.005-0.006 by the RH increase of 1%. These results provide insights in the chemical evolution of organic compounds from the major atmospheric VOC source based on the state-of-the-art PTR-MS instruments.

4. Conclusions and outlook

4.1 Conclusions and atmospheric implications

Atmospheric organic compounds play important roles in air quality and climate change. Quantification of the composition of VOCs and OA particles and determining their source contributions and evolution processes are crucial to assess their environmental impacts.

In this work, I have characterized the performance of a new PTR-MS coupled with a CHARON inlet and a FastGC for measuring the VOCs and their isomers as well volatile aerosol components with intermittent measurement in one instrument. Good linear correlations were found for the CHARON-measured volatile organic aerosol with the AMS-measured organics as well as for the VOCs measured by the PTR-MS with the Vocus-PTR-MS. The O:C ratios of bulk OA measured the CHARON varied from 0.25-0.40 in chamber and field measurements, which were close to that for semi-volatile organic aerosol derived from the AMS. The CHARON can detect less-oxygenated organic compounds typically with up to 1-5 oxygen atoms per molecule. The FastGC was characterized for the kinetic studies in chamber experiments and for the ambient air to separate monoterpene isomers from pine tree emissions. These results show the strength of CHARON/FastGC-PTR-MS for quantitatively tracing the levels of VOC precursors and their oxidation products with intermittent measurements compared to other instruments e.g., AMS.

Based on two field measurements conducted at an urban kerbsite of downtown Karlsruhe, I have determined that $PM_{2.5}$ mostly consists of OA in both summer (60 ± 12%) and winter (44 ± 10%). Source analysis results indicated that the OA was dominated by SOA with 82 ± 26% in summer and 48 ± 22% in winter. I have demonstrated the controlling factors for two pollution episodes in summer and winter. A summer heatwave can lead to the increase of biogenic VOC emissions and thus SOA formation for the pollution episode. In winter, the pollution episode was caused by various sources including local industrial emissions, Saharan dust and anthropogenic emissions in central Europe via regional transport. These results highlight the complexity of $PM_{2.5}$ sources in context of seasonality and meteorology in urban environments and provide implications for the establishment of new strategies to improve urban air quality in Karlsruhe and similar cities in Europe.

During a field measurement at a rural site in the north of Karlsruhe in summer, I estimated the source contributions of OA particles and VOCs. The results revealed that SOA totally accounted

for 94 ± 5% of total OA and the secondary oxidation VOC factor totally contributed to 78 ± 29% of total VOCs. Furthermore, I characterized two heatwave episodes with nighttime OA mass increases and particle growth rates (3.5-4.0 nm h^{-1}). This efficient particle growth was correlated with stagnant conditions with relatively lower temperatures and high relative humidity, and can be attributed to gas-to-particle partitioning of semi-volatile oxygenated organic aerosol (SV-OOA) formed from the oxidation of monoterpenes. These results are in line with the findings with a previous study at this region (Huang et al., 2019a), but can improve our understanding on the evolution processes of organic compounds from source emissions to the formation of SOA and thus nighttime pollution during heat waves. This works could also provide implications for explaining the discrepancy between the measured and air quality model results, e.g., missing emission sources or formation mechanisms (Shen et al., 2019).

During a field campaign in a stressed pine forest in the Eifel in western Germany, I identified that a nearby biogas power plant was an important source for methane, monoterpenes and aromatic compounds. I quantified the concentration levels of biogenic and anthropogenic VOCs with two state-of-the-art PTR-MS. Consistent with previous studies at European pine tree forests (Hakola et al., 2012; Li et al., 2020), the diurnal variation of isoprene showed high concentrations during daytime. Although monoterpenes and sesquiterpenes showed high concentrations during nighttime of entire measurement period, which was in line with previous studies as well. However, I found that monoterpenes and sesquiterpenes exhibited a daytime increase during a heatwave episode even with high O_3 concentration, indicating that high temperature can facilitate the emissions of monoterpenes and sesquiterpenes. The diurnal variations of less-oxygenated monoterpene-derived organic products (e.g., $C_{10}H_{16}O_{1\text{-}3}$) in both gas and particle phases showed significant increases at nights of heat wave episode. However, more-oxygenated organic products ($C_{10}H_{16}O_{4\text{-}5}$) increased during daytime, indicating strong photochemical removal of monoterpenes. In contrast, lower temperature and higher RH at nights favor the partitioning of semi-volatile organic components; e.g., fractionation of $C_{10}H_{16}O_{1\text{-}3}$ to particle phase increases with 0.005-0.006 per % increase in RH. Therefore, temperature and RH not only influence the biogenic VOC emissions but also their conversion processes to SOA formation. It should be further studied if the evolution of BVOCs and their atmospheric oxidation processes could be similar for other European forest environment in response to the hot weather (e.g., heat wave).

To conclude, this dissertation contributes to our fundamental understanding on relative influence of biogenic and anthropogenic emissions on atmospheric organic compounds, which improves our understanding for their impacts on air quality. The major findings and/or knowledge gaps this dissertation emphasizes or contributes to fill in are summarized in a simplified concept in Figure 53.

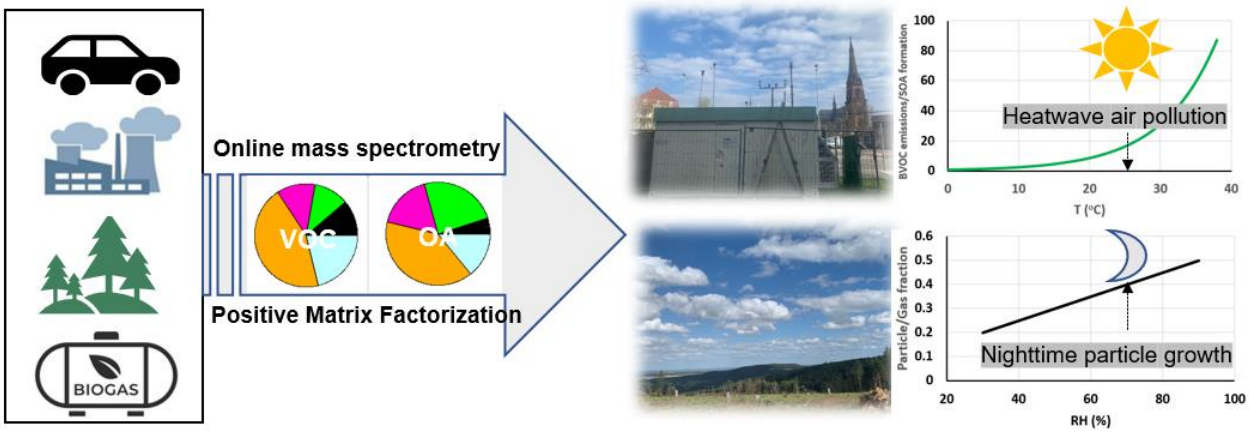

Figure 53 Concept figure of the results about the sources of VOC and OA particles resolved by the mass spectrometry and PMF analysis. The heat wave with high temperature can facilitate the BVOC emissions and SOA formation, and high relative humidity (RH) during nighttime can facilitate the partitioning of gas-to-particle for the particle growth.

4.2 Outlook

This dissertation illustrated the composition, sources and evolution processes of atmospheric organic compounds at different environment (urban, rural and forest) in different seasons (summer and winter). The roles of atmospheric organic compounds in short-term pollution episodes were demonstrated based on these field observations. In addition, this dissertation also initiates several new technical and scientific questions, which could be the research topics for future studies:

- Would it be feasible to combine the datasets of VOC and aerosol particles measured by the CHARON-PTR-MS for a PMF analysis from the field measurements? Can we get more information for a better understanding on VOC oxidation processes compared to PMF analysis with a single dataset of VOC or OA?
- Intercomparison measurements with more specific analytical techniques both in the laboratory and in the field are needed to better interpret the CHARON-PTR-MS mass spectra and fully explore the chemical evolution of organic compounds.

- In this dissertation, a large contribution of residential wood combustion (25%) to total OA was found in downtown Karlsruhe during wintertime. Future work should focus on the molecular characterization of OA and VOCs from CHARON-PTR-MS and FIGEARO-CIMS to improve the understanding of biomass burning emissions and evolution.
- In forest areas, frequent heat waves may lead to drought and bark beetle attacks, which might change the plant emissions and thus SOA chemical composition. The impact of these biotic factors on the variations of VOCs and SOA formation needs more comprehensive field measurement at specific locations and periods in the future.
- The emission ratios of biogas power plant could be estimated in comparison to the emission inventory. Would it will be valuable for the modelling studies with better constraints of emission sources? In addition, the impact of biogas power plant emissions on regional air quality should be investigated as the increased biogas power plants distributed widely in the rural and forested areas in European countries.

References

Alas, H.D.C., Müller, T., Weinhold, K., Pfeifer, S., Glojek, K., Gregorič, A., Močnik, G., Drinovec, L., Costabile, F., Ristorini, M., Wiedensohler, A., 2020. Performance of microAethalometers: Real-world Field Intercomparisons from Multiple Mobile Measurement Campaigns in Different Atmospheric Environments. Aerosol and Air Quality Research 20, 2640-2653.

Ameye, M., Allmann, S., Verwaeren, J., Smagghe, G., Haesaert, G., Schuurink, R.C., Audenaert, K., 2018. Green leaf volatile production by plants: a meta-analysis. New Phytologist 220, 666-683.

Amin, H., Atkins, P.T., Russo, R.S., Brown, A.W., Sive, B., Hallar, A.G., Huff Hartz, K.E., 2012. Effect of Bark Beetle Infestation on Secondary Organic Aerosol Precursor Emissions. Environ. Sci. Technol. 46, 5696-5703.

Artíñano, B., Pujadas, M., Alonso-Blanco, E., Becerril-Valle, M., Coz, E., Gómez-Moreno, F.J., Salvador, P., Nuñez, L., Palacios, M., Diaz, E., 2018. Real-time monitoring of atmospheric ammonia during a pollution episode in Madrid (Spain). Atmos. Environ. 189, 80-88.

Atkinson, R., Hasegawa, D., Aschmann, S.M., 1990. Rate constants for the gas-phase reactions of O3 with a series of monoterpenes and related compounds at 296 ± 2 K. International Journal of Chemical Kinetics 22, 871-887.

Bäck, J., Aalto, J., Henriksson, M., Hakola, H., He, Q., Boy, M., 2012. Chemodiversity of a Scots pine stand and implications for terpene air concentrations. Biogeosciences 9, 689-702.

Baker, J., Walker, H.L., Cai, X., 2004. A study of the dispersion and transport of reactive pollutants in and above street canyons—a large eddy simulation. Atmos. Environ. 38, 6883-6892.

Barber, S., Blake, R.S., White, I.R., Monks, P.S., Reich, F., Mullock, S., Ellis, A.M., 2012. Increased Sensitivity in Proton Transfer Reaction Mass Spectrometry by Incorporation of a Radio Frequency Ion Funnel. Analytical Chemistry 84, 5387-5391.

Barreira, L.M.F., Ylisirniö, A., Pullinen, I., Buchholz, A., Li, Z., Lipp, H., Junninen, H., Hõrrak, U., Noe, S.M., Krasnova, A., Krasnov, D., Kask, K., Talts, E., Niinemets, Ü., Ruiz-Jimenez, J., Schobesberger, S., 2021. The importance of sesquiterpene oxidation products for secondary organic aerosol formation in a springtime hemiboreal forest. Atmos. Chem. Phys. 21, 11781-11800.

Baudic, A., Gros, V., Sauvage, S., Locoge, N., Sanchez, O., Sarda-Estève, R., Kalogridis, C., Petit, J.E., Bonnaire, N., Baisnée, D., Favez, O., Albinet, A., Sciare, J., Bonsang, B., 2016. Seasonal variability and source apportionment of volatile organic compounds (VOCs) in the Paris megacity (France). Atmos. Chem. Phys. 16, 11961-11989.

Bertozzi, B., Wagner, R., Song, J., Höhler, K., Pfeifer, J., Saathoff, H., Leisner, T., Möhler, O., 2021. Ice nucleation ability of ammonium sulfate aerosol particles internally mixed with secondary organics. Atmos. Chem. Phys. 21, 10779-10798.

Bi, C., Krechmer, J.E., Canagaratna, M.R., Isaacman-VanWertz, G., 2021a. Correcting bias in log-linear instrument calibrations in the context of chemical ionization mass spectrometry. Atmos. Meas. Tech. 14, 6551-6560.

Bi, C., Krechmer, J.E., Frazier, G.O., Xu, W., Lambe, A.T., Claflin, M.S., Lerner, B.M., Jayne, J.T., Worsnop, D.R., Canagaratna, M.R., Isaacman-VanWertz, G., 2021b. Coupling a gas chromatograph simultaneously to a flame ionization detector and chemical ionization mass spectrometer for isomer-resolved measurements of particle-phase organic compounds. Atmos. Meas. Tech. 14, 3895-3907.

Blake, R.S., Monks, P.S., Ellis, A.M., 2009. Proton-Transfer Reaction Mass Spectrometry. Chem Rev 109, 861-896.

Blanco-Donado, E.P., Schneider, I.L., Artaxo, P., Lozano-Osorio, J., Portz, L., Oliveira, M.L.S., 2022. Source identification and global implications of black carbon. Geoscience Frontiers 13, 101149.

Bourtsoukidis, E., Williams, J., Kesselmeier, J., Jacobi, S., Bonn, B., 2014. From emissions to ambient mixing ratios: online seasonal field measurements of volatile organic compounds over a Norway spruce-dominated forest in central Germany. Atmos. Chem. Phys. 14, 6495-6510.

Brilli, F., Ruuskanen, T.M., Schnitzhofer, R., Müller, M., Breitenlechner, M., Bittner, V., Wohlfahrt, G., Loreto, F., Hansel, A., 2011. Detection of Plant Volatiles after Leaf Wounding and Darkening by Proton Transfer Reaction "Time-of-Flight" Mass Spectrometry (PTR-TOF). PLOS ONE 6, e20419.

Bruns, E.A., El Haddad, I., Slowik, J.G., Kilic, D., Klein, F., Baltensperger, U., Prévôt, A.S.H., 2016. Identification of significant precursor gases of secondary organic aerosols from residential wood combustion. Scientific Reports 6, 27881.

Bruns, E.A., Slowik, J.G., El Haddad, I., Kilic, D., Klein, F., Dommen, J., Temime-Roussel, B., Marchand, N., Baltensperger, U., Prevot, A.S.H., 2017. Characterization of gas-phase organics using proton transfer reaction time-of-flight mass spectrometry: fresh and aged residential wood combustion emissions. Atmos. Chem. Phys. 17, 705-720.

Bsaibes, S., Piel, F., Gros, V., Truong, F., Lafouge, F., Ciuraru, R., Buysse, P., Kammer, J., Loubet, B., Staudt, M., 2020. Monoterpene Chemical Speciation with High Time Resolution Using a FastGC/PTR-MS: Results from the COV3ER Experiment on Quercus ilex. Atmosphere-Basel 11, 690.

Burnett, R.T., Pope, C.A., Ezzati, M., Olives, C., Lim, S.S., Mehta, S., Shin, H.H., Singh, G., Hubbell, B., Brauer, M., Anderson, H.R., Smith, K.R., Balmes, J.R., Bruce, N.G., Kan, H., Laden, F., Prüss-Ustün, A., Turner, M.C., Gapstur, S.M., Diver, W.R., Cohen, A., 2014. An Integrated Risk Function for Estimating the Global Burden of Disease Attributable to Ambient Fine Particulate Matter Exposure. Environmental Health Perspectives 122, 397-403.

Canagaratna, M.R., Jayne, J.T., Jimenez, J.L., Allan, J.D., Alfarra, M.R., Zhang, Q., Onasch, T.B., Drewnick, F., Coe, H., Middlebrook, A., Delia, A., Williams, L.R., Trimborn, A.M., Northway, M.J., DeCarlo, P.F., Kolb, C.E., Davidovits, P., Worsnop, D.R., 2007. Chemical and microphysical characterization of ambient aerosols with the aerodyne aerosol mass spectrometer. Mas.s Spectrom. Rev. 26, 185-222.

Canagaratna, M.R., Jimenez, J.L., Kroll, J.H., Chen, Q., Kessler, S.H., Massoli, P., Hildebrandt Ruiz, L., Fortner, E., Williams, L.R., Wilson, K.R., Surratt, J.D., Donahue, N.M., Jayne, J.T., Worsnop, D.R., 2015. Elemental ratio measurements of organic compounds using aerosol mass spectrometry: characterization, improved calibration, and implications. Atmos. Chem. Phys. 15, 253-272.

Canagaratna, M.R., Onasch, T.B., Wood, E.C., Herndon, S.C., Jayne, J.T., Cross, E.S., Miake-Lye, R.C., Kolb, C.E., Worsnop, D.R., 2010. Evolution of Vehicle Exhaust Particles in the Atmosphere. J Air Waste Manage 60, 1192-1203.

Canonaco, F., Crippa, M., Slowik, J.G., Baltensperger, U., Prévôt, A.S.H., 2013. SoFi, an IGOR-based interface for the efficient use of the generalized multilinear engine (ME-2) for the source apportionment: ME-2 application to aerosol mass spectrometer data. Atmos. Meas. Tech. 6, 3649-3661.

Canonaco, F., Slowik, J.G., Baltensperger, U., Prevot, A.S.H., 2015. Seasonal differences in oxygenated organic aerosol composition: implications for emissions sources and factor analysis. Atmos. Chem. Phys. 15, 6993-7002.

Cappellin, L., Karl, T., Probst, M., Ismailova, O., Winkler, P.M., Soukoulis, C., Aprea, E., Märk, T.D., Gasperi, F., Biasioli, F., 2012. On Quantitative Determination of Volatile Organic Compound Concentrations Using Proton Transfer Reaction Time-of-Flight Mass Spectrometry. Environ. Sci. Technol. 46, 2283-2290.

Chebbi, A., Carlier, P., 1996. Carboxylic acids in the troposphere, occurrence, sources, and sinks: A review. Atmos. Environ. 30, 4233-4249.

Chhabra, P.S., Flagan, R.C., Seinfeld, J.H., 2010. Elemental analysis of chamber organic aerosol using an aerodyne high-resolution aerosol mass spectrometer. Atmos. Chem. Phys. 10, 4111-4131.

Claeys, M., Iinuma, Y., Szmigielski, R., Surratt, J.D., Blockhuys, F., Van Alsenoy, C., Böge, O., Sierau, B., Gómez-González, Y., Vermeylen, R., Van der Veken, P., Shahgholi, M., Chan, A.W.H., Herrmann, H., Seinfeld, J.H., Maenhaut, W., 2009. Terpenylic Acid and Related Compounds from the Oxidation of α-Pinene: Implications for New Particle Formation and Growth above Forests. Environ. Sci. Technol. 43, 6976-6982.

Claeys, M., Szmigielski, R., Kourtchev, I., Van der Veken, P., Vermeylen, R., Maenhaut, W., Jaoui, M., Kleindienst, T.E., Lewandowski, M., Offenberg, J.H., Edney, E.O., 2007. Hydroxydicarboxylic Acids:

Markers for Secondary Organic Aerosol from the Photooxidation of α-Pinene. Environ. Sci. Technol. 41, 1628-1634.

Claflin, M.S., Pagonis, D., Finewax, Z., Handschy, A.V., Day, D.A., Brown, W.L., Jayne, J.T., Worsnop, D.R., Jimenez, J.L., Ziemann, P.J., de Gouw, J., Lerner, B.M., 2021. An in situ gas chromatograph with automatic detector switching between PTR- and EI-TOF-MS: isomer-resolved measurements of indoor air. Atmos. Meas. Tech. 14, 133-152.

Coggon, M.M., Veres, P.R., Yuan, B., Koss, A., Warneke, C., Gilman, J.B., Lerner, B.M., Peischl, J., Aikin, K.C., Stockwell, C.E., Hatch, L.E., Ryerson, T.B., Roberts, J.M., Yokelson, R.J., de Gouw, J.A., 2016. Emissions of nitrogen-containing organic compounds from the burning of herbaceous and arboraceous biomass: Fuel composition dependence and the variability of commonly used nitrile tracers. Geophys. Res. Lett. 43, 9903-9912.

Crippa, M., Canonaco, F., Lanz, V.A., Äijälä, M., Allan, J.D., Carbone, S., Capes, G., Ceburnis, D., Dall'Osto, M., Day, D.A., DeCarlo, P.F., Ehn, M., Eriksson, A., Freney, E., Hildebrandt Ruiz, L., Hillamo, R., Jimenez, J.L., Junninen, H., Kiendler-Scharr, A., Kortelainen, A.M., Kulmala, M., Laaksonen, A., Mensah, A.A., Mohr, C., Nemitz, E., O'Dowd, C., Ovadnevaite, J., Pandis, S.N., Petäjä, T., Poulain, L., Saarikoski, S., Sellegri, K., Swietlicki, E., Tiitta, P., Worsnop, D.R., Baltensperger, U., Prévôt, A.S.H., 2014. Organic aerosol components derived from 25 AMS data sets across Europe using a consistent ME-2 based source apportionment approach. Atmos. Chem. Phys. 14, 6159-6176.

Crippa, M., DeCarlo, P.F., Slowik, J.G., Mohr, C., Heringa, M.F., Chirico, R., Poulain, L., Freutel, F., Sciare, J., Cozic, J., Di Marco, C.F., Elsasser, M., Nicolas, J.B., Marchand, N., Abidi, E., Wiedensohler, A., Drewnick, F., Schneider, J., Borrmann, S., Nemitz, E., Zimmermann, R., Jaffrezo, J.L., Prevot, A.S.H., Baltensperger, U., 2013a. Wintertime aerosol chemical composition and source apportionment of the organic fraction in the metropolitan area of Paris. Atmos. Chem. Phys. 13, 961-981.

Crippa, M., El Haddad, I., Slowik, J.G., DeCarlo, P.F., Mohr, C., Heringa, M.F., Chirico, R., Marchand, N., Sciare, J., Baltensperger, U., Prevot, A.S.H., 2013b. Identification of marine and continental aerosol sources in Paris using high resolution aerosol mass spectrometry. J Geophys Res-Atmos 118, 1950-1963.

Cubison, M.J., Ortega, A.M., Hayes, P.L., Farmer, D.K., Day, D., Lechner, M.J., Brune, W.H., Apel, E., Diskin, G.S., Fisher, J.A., Fuelberg, H.E., Hecobian, A., Knapp, D.J., Mikoviny, T., Riemer, D., Sachse, G.W., Sessions, W., Weber, R.J., Weinheimer, A.J., Wisthaler, A., Jimenez, J.L., 2011. Effects of aging on organic aerosol from open biomass burning smoke in aircraft and laboratory studies. Atmos. Chem. Phys. 11, 12049-12064.

DeCarlo, P.F., Dunlea, E.J., Kimmel, J.R., Aiken, A.C., Sueper, D., Crounse, J., Wennberg, P.O., Emmons, L., Shinozuka, Y., Clarke, A., Zhou, J., Tomlinson, J., Collins, D.R., Knapp, D., Weinheimer, A.J., Montzka, D.D., Campos, T., Jimenez, J.L., 2008. Fast airborne aerosol size and chemistry measurements above Mexico City and Central Mexico during the MILAGRO campaign. Atmos. Chem. Phys. 8, 4027-4048.

DeCarlo, P.F., Kimmel, J.R., Trimborn, A., Northway, M.J., Jayne, J.T., Aiken, A.C., Gonin, M., Fuhrer, K., Horvath, T., Docherty, K.S., Worsnop, D.R., Jimenez, J.L., 2006. Field-deployable, high-resolution, time-of-flight aerosol mass spectrometer. Analytical Chemistry 78, 8281-8289.

DeWitt, H.L., Hellebust, S., Temime-Roussel, B., Ravier, S., Polo, L., Jacob, V., Buisson, C., Charron, A., André, M., Pasquier, A., Besombes, J.L., Jaffrezo, J.L., Wortham, H., Marchand, N., 2015. Near-highway aerosol and gas-phase measurements in a high-diesel environment. Atmos. Chem. Phys. 15, 4373-4387.

Docherty, K.S., Wu, W., Lim, Y.B., Ziemann, P.J., 2005. Contributions of Organic Peroxides to Secondary Aerosol Formed from Reactions of Monoterpenes with O3. Environ. Sci. Technol. 39, 4049-4059.

Duan, J., Huang, R.J., Li, Y.J., Chen, Q., Zheng, Y., Chen, Y., Lin, C.S., Ni, H.Y., Wang, M., Ovadnevaite, J., Ceburnis, D., Chen, C.Y., Worsnop, D.R., Hoffmann, T., O'Dowd, C., Cao, J.J., 2020. Summertime and wintertime atmospheric processes of secondary aerosol in Beijing. Atmos. Chem. Phys. 20, 3793-3807.

Ehn, M., Thornton, J.A., Kleist, E., Sipilä, M., Junninen, H., Pullinen, I., Springer, M., Rubach, F., Tillmann, R., Lee, B., Lopez-Hilfiker, F., Andres, S., Acir, I.-H., Rissanen, M., Jokinen, T., Schobesberger, S., Kangasluoma, J., Kontkanen, J., Nieminen, T., Kurtén, T., Nielsen, L.B., Jørgensen, S., Kjaergaard, H.G., Canagaratna, M., Maso, M.D., Berndt, T., Petäjä, T., Wahner, A., Kerminen, V.-M., Kulmala, M., Worsnop, D.R., Wildt, J., Mentel, T.F., 2014. A large source of low-volatility secondary organic aerosol. Nature 506, 476-479.

Eichler, P., Muller, M., D'Anna, B., Wisthaler, A., 2015. A novel inlet system for online chemical analysis of semi-volatile submicron particulate matter. Atmos. Meas. Tech. 8, 1353-1360.

Fall, R., Karl, T., Hansel, A., Jordan, A., Lindinger, W., 1999. Volatile organic compounds emitted after leaf wounding: On-line analysis by proton-transfer-reaction mass spectrometry. J. Geophys. Res.-Atmos. 104, 15963-15974.

Fall, R., Karl, T., Jordan, A., Lindinger, W., 2001. Biogenic C5 VOCs: release from leaves after freeze–thaw wounding and occurrence in air at a high mountain observatory. Atmos. Environ. 35, 3905-3916.

Fischer, L., Breitenlechner, M., Canaval, E., Scholz, W., Striednig, M., Graus, M., Karl, T.G., Petäjä, T., Kulmala, M., Hansel, A., 2021. First eddy covariance flux measurements of semi-volatile organic compounds with the PTR3-TOF-MS. Atmos. Meas. Tech. 14, 8019-8039.

Freutel, F., Schneider, J., Drewnick, F., von der Weiden-Reinmüller, S.L., Crippa, M., Prévôt, A.S.H., Baltensperger, U., Poulain, L., Wiedensohler, A., Sciare, J., Sarda-Estève, R., Burkhart, J.F., Eckhardt, S., Stohl, A., Gros, V., Colomb, A., Michoud, V., Doussin, J.F., Borbon, A., Haeffelin, M., Morille, Y., Beekmann, M., Borrmann, S., 2013. Aerosol particle measurements at three stationary sites in the megacity of Paris during summer 2009: meteorology and air mass origin dominate aerosol particle composition and size distribution. Atmos. Chem. Phys. 13, 933-959.

Gao, L., Song, J., Mohr, C., Huang, W., Vallon, M., Jiang, F., Leisner, T., Saathoff, H., 2022. Kinetics, SOA yields and chemical composition of secondary organic aerosol from β-caryophyllene ozonolysis with and without nitrogen oxides between 213 and 313 K. Atmos. Chem. Phys. Discuss. 2022, 1-44.

Ghimire, R.P., Kivimäenpää, M., Blomqvist, M., Holopainen, T., Lyytikäinen-Saarenmaa, P., Holopainen, J.K., 2016. Effect of bark beetle (Ips typographus L.) attack on bark VOC emissions of Norway spruce (Picea abies Karst.) trees. Atmos. Environ. 126, 145-152.

Gilardoni, S., Massoli, P., Paglione, M., Giulianelli, L., Carbone, C., Rinaldi, M., Decesari, S., Sandrini, S., Costabile, F., Gobbi, G.P., Pietrogrande, M.C., Visentin, M., Scotto, F., Fuzzi, S., Facchini, M.C., 2016. Direct observation of aqueous secondary organic aerosol from biomass-burning emissions. P. Natl. Acad. Sci. USA 113, 10013-10018.

Gkatzelis, G.I., Coggon, M.M., McDonald, B.C., Peischl, J., Gilman, J.B., Aikin, K.C., Robinson, M.A., Canonaco, F., Prevot, A.S.H., Trainer, M., Warneke, C., 2021. Observations Confirm that Volatile Chemical Products Are a Major Source of Petrochemical Emissions in U.S. Cities. Environ. Sci. Technol. 55, 4332-4343.

Gkatzelis, G.I., Hohaus, T., Tillmann, R., Gensch, I., Müller, M., Eichler, P., Xu, K.M., Schlag, P., Schmitt, S.H., Yu, Z., Wegener, R., Kaminski, M., Holzinger, R., Wisthaler, A., Kiendler-Scharr, A., 2018a. Gas-to-particle partitioning of major biogenic oxidation products: a study on freshly formed and aged biogenic SOA. Atmos. Chem. Phys. 18, 12969-12989.

Gkatzelis, G.I., Tillmann, R., Hohaus, T., Müller, M., Eichler, P., Xu, K.M., Schlag, P., Schmitt, S.H., Wegener, R., Kaminski, M., Holzinger, R., Wisthaler, A., Kiendler-Scharr, A., 2018b. Comparison of three aerosol chemical characterization techniques utilizing PTR-ToF-MS: a study on freshly formed and aged biogenic SOA. Atmos. Meas. Tech. 11, 1481-1500.

Griffin, R.J., Cocker III, D.R., Flagan, R.C., Seinfeld, J.H., 1999. Organic aerosol formation from the oxidation of biogenic hydrocarbons. J. Geophys. Res.-Atmos. 104, 3555-3567.

Guenther, A.B., Jiang, X., Heald, C.L., Sakulyanontvittaya, T., Duhl, T., Emmons, L.K., Wang, X., 2012. The Model of Emissions of Gases and Aerosols from Nature version 2.1 (MEGAN2.1): an extended and updated framework for modeling biogenic emissions. Geosci. Model Dev. 5, 1471-1492.

Guenther, A.B., Zimmerman, P.R., Harley, P.C., Monson, R.K., Fall, R., 1993. Isoprene and Monoterpene Emission Rate Variability - Model Evaluations and Sensitivity Analyses. J Geophys Res-Atmos 98, 12609-12617.

Hakola, H., Hellén, H., Hemmilä, M., Rinne, J., Kulmala, M., 2012. In situ measurements of volatile organic compounds in a boreal forest. Atmos. Chem. Phys. 12, 11665-11678.

Hakola, H., Tarvainen, V., Bäck, J., Ranta, H., Bonn, B., Rinne, J., Kulmala, M., 2006. Seasonal variation of mono- and sesquiterpene emission rates of Scots pine. Biogeosciences 3, 93-101.

Hallquist, M., Wenger, J.C., Baltensperger, U., Rudich, Y., Simpson, D., Claeys, M., Dommen, J., Donahue, N.M., George, C., Goldstein, A.H., Hamilton, J.F., Herrmann, H., Hoffmann, T., Iinuma, Y., Jang, M., Jenkin, M.E., Jimenez, J.L., Kiendler-Scharr, A., Maenhaut, W., McFiggans, G., Mentel, T.F., Monod, A., Prévôt, A.S.H., Seinfeld, J.H., Surratt, J.D., Szmigielski, R., Wildt, J., 2009. The formation, properties and impact of secondary organic aerosol: current and emerging issues. Atmos. Chem. Phys. 9, 5155-5236.

Hamilton, J.F., Lewis, A.C., Carey, T.J., Wenger, J.C., Borrás i Garcia, E., Muñoz, A., 2009. Reactive oxidation products promote secondary organic aerosol formation from green leaf volatiles. Atmos. Chem. Phys. 9, 3815-3823.

Hellén, H., Praplan, A.P., Tykkä, T., Helin, A., Schallhart, S., Schiestl-Aalto, P.P., Bäck, J., Hakola, H., 2021. Sesquiterpenes and oxygenated sesquiterpenes dominate the VOC (C5–C20) emissions of downy birches. Atmos. Chem. Phys. 21, 8045-8066.

Hellén, H., Praplan, A.P., Tykkä, T., Ylivinkka, I., Vakkari, V., Bäck, J., Petäjä, T., Kulmala, M., Hakola, H., 2018. Long-term measurements of volatile organic compounds highlight the importance of sesquiterpenes for the atmospheric chemistry of a boreal forest. Atmos. Chem. Phys. 18, 13839-13863.

Hellén, H., Schallhart, S., Praplan, A.P., Tykkä, T., Aurela, M., Lohila, A., Hakola, H., 2020. Sesquiterpenes dominate monoterpenes in northern wetland emissions. Atmos. Chem. Phys. 20, 7021-7034.

Henze, D.K., Seinfeld, J.H., Ng, N.L., Kroll, J.H., Fu, T.M., Jacob, D.J., Heald, C.L., 2008. Global modeling of secondary organic aerosol formation from aromatic hydrocarbons: high- vs. low-yield pathways. Atmos. Chem. Phys. 8, 2405-2420.

Hersbach, H., Bell, B., Berrisford, P., Hirahara, S., Horányi, A., Muñoz-Sabater, J., Nicolas, J., Peubey, C., Radu, R., Schepers, D., Simmons, A., Soci, C., Abdalla, S., Abellan, X., Balsamo, G., Bechtold, P., Biavati, G., Bidlot, J., Bonavita, M., De Chiara, G., Dahlgren, P., Dee, D., Diamantakis, M., Dragani, R., Flemming, J., Forbes, R., Fuentes, M., Geer, A., Haimberger, L., Healy, S., Hogan, R.J., Hólm, E., Janisková, M., Keeley, S., Laloyaux, P., Lopez, P., Lupu, C., Radnoti, G., de Rosnay, P., Rozum, I., Vamborg, F., Villaume, S., Thépaut, J.-N., 2020. The ERA5 global reanalysis. Quarterly Journal of the Royal Meteorological Society 146, 1999-2049.

Hlásny, T., König, L., Krokene, P., Lindner, M., Montagné-Huck, C., Müller, J., Qin, H., Raffa, K.F., Schelhaas, M.-J., Svoboda, M., Viiri, H., Seidl, R., 2021. Bark Beetle Outbreaks in Europe: State of Knowledge and Ways Forward for Management. Current Forestry Reports 7, 138-165.

Hofman, J., Staelens, J., Cordell, R., Stroobants, C., Zikova, N., Hama, S.M.L., Wyche, K.P., Kos, G.P.A., Van der Zee, S., Smallbone, K.L., Weijers, E.P., Monks, P.S., Roekens, E., 2016. Ultrafine particles in four European urban environments: Results from a new continuous long-term monitoring network. Atmos. Environ. 136, 68-81.

Holopainen, J.K., Gershenzon, J., 2010. Multiple stress factors and the emission of plant VOCs. Trends in Plant Science 15, 176-184.

Holzinger, R., Acton, W.J.F., Bloss, W.J., Breitenlechner, M., Crilley, L.R., Dusanter, S., Gonin, M., Gros, V., Keutsch, F.N., Kiendler-Scharr, A., Kramer, L.J., Krechmer, J.E., Languille, B., Locoge, N., Lopez-Hilfiker, F., Materić, D., Moreno, S., Nemitz, E., Quéléver, L.L.J., Sarda Esteve, R., Sauvage, S., Schallhart, S., Sommariva, R., Tillmann, R., Wedel, S., Worton, D.R., Xu, K., Zaytsev, A., 2019. Validity and limitations of simple reaction kinetics to calculate concentrations of organic compounds from ion counts in PTR-MS. Atmos. Meas. Tech. 12, 6193-6208.

Huang, R.J., He, Y., Duan, J., Li, Y., Chen, Q., Zheng, Y., Chen, Y., Hu, W., Lin, C., Ni, H., Dai, W., Cao, J., Wu, Y., Zhang, R., Xu, W., Ovadnevaite, J., Ceburnis, D., Hoffmann, T., O'Dowd, C.D., 2020.

Contrasting sources and processes of particulate species in haze days with low and high relative humidity in wintertime Beijing. Atmos. Chem. Phys. 20, 9101-9114.

Huang, S., Wu, Z., Poulain, L., van Pinxteren, M., Merkel, M., Assmann, D., Herrmann, H., Wiedensohler, A., 2018a. Source apportionment of the organic aerosol over the Atlantic Ocean from 53° N to 53° S: significant contributions from marine emissions and long-range transport. Atmos. Chem. Phys. 18, 18043-18062.

Huang, W., Saathoff, H., Pajunoja, A., Shen, X., Naumann, K.H., Wagner, R., Virtanen, A., Leisner, T., Mohr, C., 2018b. α-Pinene secondary organic aerosol at low temperature: chemical composition and implications for particle viscosity. Atmos. Chem. Phys. 18, 2883-2898.

Huang, W., Saathoff, H., Shen, X., Ramisetty, R., Leisner, T., Mohr, C., 2019a. Chemical Characterization of Highly Functionalized Organonitrates Contributing to Night-Time Organic Aerosol Mass Loadings and Particle Growth. Environ. Sci. Technol. 53, 1165-1174.

Huang, W., Saathoff, H., Shen, X., Ramisetty, R., Leisner, T., Mohr, C., 2019b. Seasonal characteristics of organic aerosol chemical composition and volatility in Stuttgart, Germany. Atmos. Chem. Phys. 19, 11687-11700.

Huangfu, Y., Yuan, B., Wang, S., Wu, C., He, X., Qi, J., de Gouw, J., Warneke, C., Gilman, J.B., Wisthaler, A., Karl, T., Graus, M., Jobson, B.T., Shao, M., 2021. Revisiting Acetonitrile as Tracer of Biomass Burning in Anthropogenic-Influenced Environments. Geophys. Res. Lett. 48, e2020GL092322.

IPCC, 2021. Climate Change 2021: The Physical Science Basis. Contribution of Working Group I to the Sixth Assessment Report of the Intergovernmental Panel on Climate Change. Cambridge University Press, Cambridge, United Kingdom and New York, NY, USA.

Iyer, S., Lopez-Hilfiker, F., Lee, B.H., Thornton, J.A., Kurtén, T., 2016. Modeling the Detection of Organic and Inorganic Compounds Using Iodide-Based Chemical Ionization. The Journal of Physical Chemistry A 120, 576-587.

Jacob, D.J., Field, B.D., Jin, E.M., Bey, I., Li, Q., Logan, J.A., Yantosca, R.M., Singh, H.B., 2002. Atmospheric budget of acetone. J. Geophys. Res.-Atmos. 107, ACH 5-1-ACH 5-17.

Janson, R.W., 1993. Monoterpene emissions from Scots pine and Norwegian spruce. J. Geophys. Res.-Atmos. 98, 2839-2850.

Jardine, A.B., Jardine, K.J., Fuentes, J.D., Martin, S.T., Martins, G., Durgante, F., Carneiro, V., Higuchi, N., Manzi, A.O., Chambers, J.Q., 2015a. Highly reactive light-dependent monoterpenes in the Amazon. Geophys. Res. Lett. 42, 1576-1583.

Jardine, K.J., Chambers, J.Q., Holm, J., Jardine, A.B., Fontes, C.G., Zorzanelli, R.F., Meyers, K.T., De Souza, V.F., Garcia, S., Gimenez, B.O., Piva, L.R.d.O., Higuchi, N., Artaxo, P., Martin, S., Manzi, A.O., 2015b. Green Leaf Volatile Emissions during High Temperature and Drought Stress in a Central Amazon Rainforest. Plants 4, 678-690.

Jimenez, J.L., Canagaratna, M.R., Donahue, N.M., Prevot, A.S.H., Zhang, Q., Kroll, J.H., DeCarlo, P.F., Allan, J.D., Coe, H., Ng, N.L., Aiken, A.C., Docherty, K.S., Ulbrich, I.M., Grieshop, A.P., Robinson, A.L., Duplissy, J., Smith, J.D., Wilson, K.R., Lanz, V.A., Hueglin, C., Sun, Y.L., Tian, J., Laaksonen, A., Raatikainen, T., Rautiainen, J., Vaattovaara, P., Ehn, M., Kulmala, M., Tomlinson, J.M., Collins, D.R., Cubison, M.J., Dunlea, E.J., Huffman, J.A., Onasch, T.B., Alfarra, M.R., Williams, P.I., Bower, K., Kondo, Y., Schneider, J., Drewnick, F., Borrmann, S., Weimer, S., Demerjian, K., Salcedo, D., Cottrell, L., Griffin, R., Takami, A., Miyoshi, T., Hatakeyama, S., Shimono, A., Sun, J.Y., Zhang, Y.M., Dzepina, K., Kimmel, J.R., Sueper, D., Jayne, J.T., Herndon, S.C., Trimborn, A.M., Williams, L.R., Wood, E.C., Middlebrook, A.M., Kolb, C.E., Baltensperger, U., Worsnop, D.R., 2009. Evolution of Organic Aerosols in the Atmosphere. Science 326, 1525-1529.

Johnson, D., Jenkin, M.E., Wirtz, K., Martin-Reviejo, M., 2005. Simulating the Formation of Secondary Organic Aerosol from the Photooxidation of Aromatic Hydrocarbons. Environmental Chemistry 2, 35-48.

Joo, T., Rivera-Rios, J.C., Takeuchi, M., Alvarado, M.J., Ng, N.L., 2019. Secondary Organic Aerosol Formation from Reaction of 3-Methylfuran with Nitrate Radicals. Acs Earth Space Chem 3, 922-934.

Jordan, A., Haidacher, S., Hanel, G., Hartungen, E., Mark, L., Seehauser, H., Schottkowsky, R., Sulzer, P., Mark, T.D., 2009. A high resolution and high sensitivity proton-transfer-reaction time-of-flight mass spectrometer (PTR-TOF-MS). International Journal of Mass Spectrometry 286, 122-128.

Kainulainen, P., Oksanen, J., Palomäki, V., Holopainen, J.K., Holopainen, T., 1992. Effect of drought and waterlogging stress on needle monoterpenes of Picea abies. Canadian Journal of Botany 70, 1613-1616.

Kaltsonoudis, C., Kostenidou, E., Florou, K., Psichoudaki, M., Pandis, S.N., 2016. Temporal variability and sources of VOCs in urban areas of the eastern Mediterranean. Atmos. Chem. Phys. 16, 14825-14842.

Kari, E., Miettinen, P., Yli-Pirilä, P., Virtanen, A., Faiola, C.L., 2018. PTR-ToF-MS product ion distributions and humidity-dependence of biogenic volatile organic compounds. International Journal of Mass Spectrometry 430, 87-97.

Ketzel, M., Berkowicz, R., Muller, W.J., Lohmeyer, A., 2002. Dependence of street canyon concentrations on above-roof wind speed - implications for numerical modelling. International Journal of Environment and Pollution 17, 356-366.

Kiendler-Scharr, A., Mensah, A.A., Friese, E., Topping, D., Nemitz, E., Prevot, A.S.H., Aijala, M., Allan, J., Canonaco, F., Canagaratna, M., Carbone, S., Crippa, M., Dall Osto, M., Day, D.A., De Carlo, P., Di Marco, C.F., Elbern, H., Eriksson, A., Freney, E., Hao, L., Herrmann, H., Hildebrandt, L., Hillamo, R., Jimenez, J.L., Laaksonen, A., McFiggans, G., Mohr, C., O'Dowd, C., Otjes, R., Ovadnevaite, J., Pandis, S.N., Poulain, L., Schlag, P., Sellegri, K., Swietlicki, E., Tiitta, P., Vermeulen, A., Wahner, A., Worsnop, D., Wu, H.C., 2016. Ubiquity of organic nitrates from nighttime chemistry in the European submicron aerosol. Geophys. Res. Lett. 43, 7735-7744.

Kim, S., Karl, T., Helmig, D., Daly, R., Rasmussen, R., Guenther, A., 2009. Measurement of atmospheric sesquiterpenes by proton transfer reaction-mass spectrometry (PTR-MS). Atmos. Meas. Tech. 2, 99-112.

Kodros, J.K., Papanastasiou, D.K., Paglione, M., Masiol, M., Squizzato, S., Florou, K., Skyllakou, K., Kaltsonoudis, C., Nenes, A., Pandis, S.N., 2020. Rapid dark aging of biomass burning as an overlooked source of oxidized organic aerosol. P. Natl. Acad. Sci. USA 117, 33028-33033.

Kontkanen, J., Paasonen, P., Aalto, J., Bäck, J., Rantala, P., Petäjä, T., Kulmala, M., 2016. Simple proxies for estimating the concentrations of monoterpenes and their oxidation products at a boreal forest site. Atmos. Chem. Phys. 16, 13291-13307.

Krechmer, J., Lopez-Hilfiker, F., Koss, A., Hutterli, M., Stoermer, C., Deming, B., Kimmel, J., Warneke, C., Holzinger, R., Jayne, J., Worsnop, D., Fuhrer, K., Gonin, M., de Gouw, J., 2018. Evaluation of a New Reagent-Ion Source and Focusing Ion–Molecule Reactor for Use in Proton-Transfer-Reaction Mass Spectrometry. Analytical Chemistry 90, 12011-12018.

Kristensen, K., Cui, T., Zhang, H., Gold, A., Glasius, M., Surratt, J.D., 2014. Dimers in α-pinene secondary organic aerosol: effect of hydroxyl radical, ozone, relative humidity and aerosol acidity. Atmos. Chem. Phys. 14, 4201-4218.

Kuhn, U., Rottenberger, S., Biesenthal, T., Wolf, A., Schebeske, G., Ciccioli, P., Brancaleoni, E., Frattoni, M., Tavares, T.M., Kesselmeier, J., 2002. Isoprene and monoterpene emissions of Amazônian tree species during the wet season: Direct and indirect investigations on controlling environmental functions. J. Geophys. Res.-Atmos. 107, LBA 38-31-LBA 38-13.

Kumar, P., Fennell, P., Britter, R., 2008. Effect of wind direction and speed on the dispersion of nucleation and accumulation mode particles in an urban street canyon. Sci. Total Environ. 402, 82-94.

Languille, B., Gros, V., Petit, J.-E., Honoré, C., Baudic, A., Perrussel, O., Foret, G., Michoud, V., Truong, F., Bonnaire, N., Sarda-Estève, R., Delmotte, M., Feron, A., Maisonneuve, F., Gaimoz, C., Formenti, P., Kotthaus, S., Haeffelin, M., Favez, O., 2020. Wood burning: A major source of Volatile Organic Compounds during wintertime in the Paris region. Sci. Total Environ. 711, 135055.

Lanz, V.A., Prevot, A.S.H., Alfarra, M.R., Weimer, S., Mohr, C., DeCarlo, P.F., Gianini, M.F.D., Hueglin, C., Schneider, J., Favez, O., D'Anna, B., George, C., Baltensperger, U., 2010. Characterization of aerosol chemical composition with aerosol mass spectrometry in Central Europe: an overview. Atmos. Chem. Phys. 10, 10453-10471.

Lappalainen, H.K., Sevanto, S., Bäck, J., Ruuskanen, T.M., Kolari, P., Taipale, R., Rinne, J., Kulmala, M., Hari, P., 2009. Day-time concentrations of biogenic volatile organic compounds in a boreal forest canopy and their relation to environmental and biological factors. Atmos. Chem. Phys. 9, 5447-5459.

Lee, A.K.Y., Abbatt, J.P.D., Leaitch, W.R., Li, S.M., Sjostedt, S.J., Wentzell, J.J.B., Liggio, J., Macdonald, A.M., 2016. Substantial secondary organic aerosol formation in a coniferous forest: observations of both day- and nighttime chemistry. Atmos. Chem. Phys. 16, 6721-6733.

Lee, B.H., Lopez-Hilfiker, F.D., Mohr, C., Kurtén, T., Worsnop, D.R., Thornton, J.A., 2014. An Iodide-Adduct High-Resolution Time-of-Flight Chemical-Ionization Mass Spectrometer: Application to Atmospheric Inorganic and Organic Compounds. Environ. Sci. Technol. 48, 6309-6317.

Lee, B.P., Li, Y.J., Yu, J.Z., Louie, P.K.K., Chan, C.K., 2015. Characteristics of submicron particulate matter at the urban roadside in downtown Hong Kong—Overview of 4 months of continuous high-resolution aerosol mass spectrometer measurements. J. Geophys. Res.-Atmos. 120, 7040-7058.

Leglise, J., Müller, M., Piel, F., Otto, T., Wisthaler, A., 2019. Bulk Organic Aerosol Analysis by Proton-Transfer-Reaction Mass Spectrometry: An Improved Methodology for the Determination of Total Organic Mass, O:C and H:C Elemental Ratios, and the Average Molecular Formula. Analytical Chemistry 91, 12619-12624.

Li, H., Canagaratna, M.R., Riva, M., Rantala, P., Zhang, Y., Thomas, S., Heikkinen, L., Flaud, P.M., Villenave, E., Perraudin, E., Worsnop, D., Kulmala, M., Ehn, M., Bianchi, F., 2021a. Atmospheric organic vapors in two European pine forests measured by a Vocus PTR-TOF: insights into monoterpene and sesquiterpene oxidation processes. Atmos. Chem. Phys. 21, 4123-4147.

Li, H., Riva, M., Rantala, P., Heikkinen, L., Daellenbach, K., Krechmer, J.E., Flaud, P.M., Worsnop, D., Kulmala, M., Villenave, E., Perraudin, E., Ehn, M., Bianchi, F., 2020. Terpenes and their oxidation products in the French Landes forest: insights from Vocus PTR-TOF measurements. Atmos. Chem. Phys. 20, 1941-1959.

Li, Y., Zhao, J., Wang, Y., Seinfeld, J.H., Zhang, R., 2021b. Multigeneration Production of Secondary Organic Aerosol from Toluene Photooxidation. Environ. Sci. Technol. 55, 8592-8603.

Linke, C., Ibrahim, I., Schleicher, N., Hitzenberger, R., Andreae, M.O., Leisner, T., Schnaiter, M., 2016. A novel single-cavity three-wavelength photoacoustic spectrometer for atmospheric aerosol research. Atmos. Meas. Tech. 9, 5331-5346.

Liu, J., Russell, L.M., Lee, A.K.Y., McKinney, K.A., Surratt, J.D., Ziemann, P.J., 2017. Observational evidence for pollution-influenced selective uptake contributing to biogenic secondary organic aerosols in the southeastern U.S. Geophys. Res. Lett. 44, 8056-8064.

Lopes, M., Serrano, L., Ribeiro, I., Cascão, P., Pires, N., Rafael, S., Tarelho, L., Monteiro, A., Nunes, T., Evtyugina, M., Nielsen, O.J., Gameiro da Silva, M., Miranda, A.I., Borrego, C., 2014. Emissions characterization from EURO 5 diesel/biodiesel passenger car operating under the new European driving cycle. Atmos. Environ. 84, 339-348.

Lopez-Hilfiker, F.D., Iyer, S., Mohr, C., Lee, B.H., D'Ambro, E.L., Kurtén, T., Thornton, J.A., 2016. Constraining the sensitivity of iodide adduct chemical ionization mass spectrometry to multifunctional organic molecules using the collision limit and thermodynamic stability of iodide ion adducts. Atmos. Meas. Tech. 9, 1505-1512.

Ma, R., Li, K., Guo, Y., Zhang, B., Zhao, X., Linder, S., Guan, C., Chen, G., Gan, Y., Meng, J., 2021. Mitigation potential of global ammonia emissions and related health impacts in the trade network. Nature Communications 12, 6308.

Materić, D., Lanza, M., Sulzer, P., Herbig, J., Bruhn, D., Gauci, V., Mason, N., Turner, C., 2017. Selective reagent ion-time of flight-mass spectrometry study of six common monoterpenes. International Journal of Mass Spectrometry 421, 40-50.

Materic, D., Lanza, M., Sulzer, P., Herbig, J., Bruhn, D., Turner, C., Mason, N., Gauci, V., 2015. Monoterpene separation by coupling proton transfer reaction time-of-flight mass spectrometry with fastGC. Anal. Bioanal. Chem. 407, 7757-7763.

Materić, D., Lanza, M., Sulzer, P., Herbig, J., Bruhn, D., Turner, C., Mason, N., Gauci, V., 2015. Monoterpene separation by coupling proton transfer reaction time-of-flight mass spectrometry with fastGC. Anal. Bioanal. Chem. 407, 7757-7763.

McFiggans, G., Mentel, T.F., Wildt, J., Pullinen, I., Kang, S., Kleist, E., Schmitt, S., Springer, M., Tillmann, R., Wu, C., Zhao, D., Hallquist, M., Faxon, C., Le Breton, M., Hallquist, Å.M., Simpson, D., Bergström, R., Jenkin, M.E., Ehn, M., Thornton, J.A., Alfarra, M.R., Bannan, T.J., Percival, C.J., Priestley, M., Topping, D., Kiendler-Scharr, A., 2019. Secondary organic aerosol reduced by mixture of atmospheric vapours. Nature 565, 587-593.

Mentel, T.F., Kleist, E., Andres, S., Dal Maso, M., Hohaus, T., Kiendler-Scharr, A., Rudich, Y., Springer, M., Tillmann, R., Uerlings, R., Wahner, A., Wildt, J., 2013. Secondary aerosol formation from stress-induced biogenic emissions and possible climate feedbacks. Atmos. Chem. Phys. 13, 8755-8770.

Mermet, K., Perraudin, E., Dusanter, S., Sauvage, S., Léonardis, T., Flaud, P.-M., Bsaibes, S., Kammer, J., Michoud, V., Gratien, A., Cirtog, M., Al Ajami, M., Truong, F., Batut, S., Hecquet, C., Doussin, J.-F., Schoemaecker, C., Gros, V., Locoge, N., Villenave, E., 2021. Atmospheric reactivity of biogenic volatile organic compounds in a maritime pine forest during the LANDEX episode 1 field campaign. Sci. Total Environ. 756, 144129.

Middlebrook, A.M., Bahreini, R., Jimenez, J.L., Canagaratna, M.R., 2012. Evaluation of Composition-Dependent Collection Efficiencies for the Aerodyne Aerosol Mass Spectrometer using Field Data. Aerosol. Sci. Tech. 46, 258-271.

Minguillon, M.C., Perez, N., Marchand, N., Bertrand, A., Temime-Roussel, B., Agrios, K., Szidat, S., van Drooge, B., Sylvestre, A., Alastuey, A., Reche, C., Ripoll, A., Marco, E., Grimalt, J.O., Querol, X., 2016. Secondary organic aerosol origin in an urban environment: influence of biogenic and fuel combustion precursors. Faraday Discuss. 189, 337-359.

Möhler, O., Stetzer, O., Schaefers, S., Linke, C., Schnaiter, M., Tiede, R., Saathoff, H., Krämer, M., Mangold, A., Budz, P., Zink, P., Schreiner, J., Mauersberger, K., Haag, W., Kärcher, B., Schurath, U., 2003. Experimental investigation of homogeneous freezing of sulphuric acid particles in the aerosol chamber AIDA. Atmos. Chem. Phys. 3, 211-223.

Mohr, C., DeCarlo, P.F., Heringa, M.F., Chirico, R., Slowik, J.G., Richter, R., Reche, C., Alastuey, A., Querol, X., Seco, R., Penuelas, J., Jimenez, J.L., Crippa, M., Zimmermann, R., Baltensperger, U., Prevot, A.S.H., 2012. Identification and quantification of organic aerosol from cooking and other sources in Barcelona using aerosol mass spectrometer data. Atmos. Chem. Phys. 12, 1649-1665.

Mohr, C., Huffman, J.A., Cubison, M.J., Aiken, A.C., Docherty, K.S., Kimmel, J.R., Ulbrich, I.M., Hannigan, M., Jimenez, J.L., 2009. Characterization of Primary Organic Aerosol Emissions from Meat Cooking, Trash Burning, and Motor Vehicles with High-Resolution Aerosol Mass Spectrometry and Comparison with Ambient and Chamber Observations. Environ. Sci. Technol. 43, 2443-2449.

Mohr, C., Lopez-Hilfiker, F.D., Yli-Juuti, T., Heitto, A., Lutz, A., Hallquist, M., D'Ambro, E.L., Rissanen, M.P., Hao, L., Schobesberger, S., Kulmala, M., Mauldin III, R.L., Makkonen, U., Sipilä, M., Petäjä, T., Thornton, J.A., 2017. Ambient observations of dimers from terpene oxidation in the gas phase: Implications for new particle formation and growth. Geophys. Res. Lett. 44, 2958-2966.

Mohr, C., Thornton, J.A., Heitto, A., Lopez-Hilfiker, F.D., Lutz, A., Riipinen, I., Hong, J., Donahue, N.M., Hallquist, M., Petäjä, T., Kulmala, M., Yli-Juuti, T., 2019. Molecular identification of organic vapors driving atmospheric nanoparticle growth. Nature Communications 10, 4442.

Muller, M., Eicher, P., D'Anna, B., Tan, W., Wisthaler, A., 2017. Direct Sampling and Analysis of Atmospheric Particulate Organic Matter by Proton-Transfer-Reaction Mass Spectrometry. Analytical Chemistry 89, 10889-10897.

Müller, M., Mikoviny, T., Jud, W., D'Anna, B., Wisthaler, A., 2013. A new software tool for the analysis of high resolution PTR-TOF mass spectra. Chemometrics and Intelligent Laboratory Systems 127, 158-165.

Nakao, S., Clark, C., Tang, P., Sato, K., Cocker Iii, D., 2011. Secondary organic aerosol formation from phenolic compounds in the absence of NO_x. Atmos. Chem. Phys. 11, 10649-10660.

Ng, N.L., Brown, S.S., Archibald, A.T., Atlas, E., Cohen, R.C., Crowley, J.N., Day, D.A., Donahue, N.M., Fry, J.L., Fuchs, H., Griffin, R.J., Guzman, M.I., Herrmann, H., Hodzic, A., Iinuma, Y., Jimenez, J.L., Kiendler-Scharr, A., Lee, B.H., Luecken, D.J., Mao, J., McLaren, R., Mutzel, A., Osthoff, H.D., Ouyang, B., Picquet-Varrault, B., Platt, U., Pye, H.O.T., Rudich, Y., Schwantes, R.H., Shiraiwa, M., Stutz, J., Thornton, J.A., Tilgner, A., Williams, B.J., Zaveri, R.A., 2017. Nitrate radicals and biogenic volatile organic compounds: oxidation, mechanisms, and organic aerosol. Atmos. Chem. Phys. 17, 2103-2162.

Ng, N.L., Canagaratna, M.R., Jimenez, J.L., Chhabra, P.S., Seinfeld, J.H., Worsnop, D.R., 2011. Changes in organic aerosol composition with aging inferred from aerosol mass spectra. Atmos. Chem. Phys. 11, 6465-6474.

Ng, N.L., Canagaratna, M.R., Zhang, Q., Jimenez, J.L., Tian, J., Ulbrich, I.M., Kroll, J.H., Docherty, K.S., Chhabra, P.S., Bahreini, R., Murphy, S.M., Seinfeld, J.H., Hildebrandt, L., Donahue, N.M., DeCarlo, P.F., Lanz, V.A., Prevot, A.S.H., Dinar, E., Rudich, Y., Worsnop, D.R., 2010. Organic aerosol components observed in Northern Hemispheric datasets from Aerosol Mass Spectrometry. Atmos. Chem. Phys. 10, 4625-4641.

Ng, N.L., Chhabra, P.S., Chan, A.W.H., Surratt, J.D., Kroll, J.H., Kwan, A.J., McCabe, D.C., Wennberg, P.O., Sorooshian, A., Murphy, S.M., Dalleska, N.F., Flagan, R.C., Seinfeld, J.H., 2007a. Effect of NO_x level on secondary organic aerosol (SOA) formation from the photooxidation of terpenes. Atmos. Chem. Phys. 7, 5159-5174.

Ng, N.L., Kroll, J.H., Chan, A.W.H., Chhabra, P.S., Flagan, R.C., Seinfeld, J.H., 2007b. Secondary organic aerosol formation from m-xylene, toluene, and benzene. Atmos. Chem. Phys. 7, 3909-3922.

Norra, S., Stuben, D., 2004. Trace element patterns and seasonal variability of dust precipitation in a low polluted city - The example of Karlsruhe/Germany. Environ. Monit. Assess 93, 203-228.

Noziere, B., Kalberer, M., Claeys, M., Allan, J., D'Anna, B., Decesari, S., Finessi, E., Glasius, M., Grgic, I., Hamilton, J.F., Hoffmann, T., Iinuma, Y., Jaoui, M., Kahno, A., Kampf, C.J., Kourtchev, I., Maenhaut, W., Marsden, N., Saarikoski, S., Schnelle-Kreis, J., Surratt, J.D., Szidat, S., Szmigielski, R., Wisthaler, A., 2015. The Molecular Identification of Organic Compounds in the Atmosphere: State of the Art and Challenges. Chem Rev 115, 3919-3983.

Nurmatov, U.B., Tagieva, N., Semple, S., Devereux, G., Sheikh, A., 2013. Volatile organic compounds and risk of asthma and allergy: a systematic review and meta-analysis of observational and interventional studies. Primary Care Respiratory Journal 22, S9-S15.

Olivier, J.G.J., Van Aardenne, J.A., Dentener, F.J., Pagliari, V., Ganzeveld, L.N., Peters, J.A.H.W., 2005. Recent trends in global greenhouse gas emissions:regional trends 1970–2000 and spatial distributionof key sources in 2000. Environmental Sciences 2, 81-99.

Ortega, A.M., Day, D.A., Cubison, M.J., Brune, W.H., Bon, D., de Gouw, J.A., Jimenez, J.L., 2013. Secondary organic aerosol formation and primary organic aerosol oxidation from biomass-burning smoke in a flow reactor during FLAME-3. Atmos. Chem. Phys. 13, 11551-11571.

Paatero, P., Tapper, U., 1994a. Positive Matrix Factorization - a Nonnegative Factor Model with Optimal Utilization of Error-Estimates of Data Values. Environmetrics 5, 111-126.

Paatero, P., Tapper, U., 1994b. Positive matrix factorization: A non-negative factor model with optimal utilization of error estimates of data value“. Environmetrics 5, 111-126.

Pagonis, D., Sekimoto, K., de Gouw, J., 2019. A Library of Proton-Transfer Reactions of H3O+ Ions Used for Trace Gas Detection. Journal of the American Society for Mass Spectrometry 30, 1330-1335.

Pang, X., 2015. Biogenic volatile organic compound analyses by PTR-TOF-MS: Calibration, humidity effect and reduced electric field dependency. Journal of Environmental Sciences 32, 196-206.

Pankow, J.F., 1994. An absorption model of gas/particle partitioning of organic compounds in the atmosphere. Atmos. Environ. 28, 185-188.

Petit, J.E., Favez, O., Albinet, A., Canonaco, F., 2017. A user-friendly tool for comprehensive evaluation of the geographical origins of atmospheric pollution: Wind and trajectory analyses. Environ. Modell. Softw. 88, 183-187.

Phuntsho, p., 2020. Differentiating healthy and bark beetle infected spruce trees with Sentinel-1 SAR.

Piel, F., Müller, M., Winkler, K., Skytte af Sätra, J., Wisthaler, A., 2021. Introducing the extended volatility range proton-transfer-reaction mass spectrometer (EVR PTR-MS). Atmos. Meas. Tech. 14, 1355-1363.

Pirjola, L., Niemi, J.V., Saarikoski, S., Aurela, M., Enroth, J., Carbone, S., Saarnio, K., Kuuluvainen, H., Kousa, A., Ronkko, T., Hillamo, R., 2017. Physical and chemical characterization of urban winter-time aerosols by mobile measurements in Helsinki, Finland. Atmos. Environ. 158, 60-75.

Poulain, L., Fahlbusch, B., Spindler, G., Müller, K., van Pinxteren, D., Wu, Z., Iinuma, Y., Birmili, W., Wiedensohler, A., Herrmann, H., 2021. Source apportionment and impact of long-range transport on carbonaceous aerosol particles in central Germany during HCCT-2010. Atmos. Chem. Phys. 21, 3667-3684.

Räisänen, T., Ryyppö, A., Kellomäki, S., 2009. Monoterpene emission of a boreal Scots pine (Pinus sylvestris L.) forest. Agricultural and Forest Meteorology 149, 808-819.

Richards-Henderson, N.K., Pham, A.T., Kirk, B.B., Anastasio, C., 2015. Secondary Organic Aerosol from Aqueous Reactions of Green Leaf Volatiles with Organic Triplet Excited States and Singlet Molecular Oxygen. Environ. Sci. Technol. 49, 268-276.

Rieger, D., Bangert, M., Bischoff-Gauss, I., Forstner, J., Lundgren, K., Reinert, D., Schroter, J., Vogel, H., Zangl, G., Ruhnke, R., Vogel, B., 2015. ICON-ART 1.0-a new online-coupled model system from the global to regional scale. Geosci Model Dev 8, 1659-1676.

Rieger, D., Steiner, A., Bachmann, V., Gasch, P., Forstner, J., Deetz, K., Vogel, B., Vogel, H., 2017. Impact of the 4 April 2014 Saharan dust outbreak on the photovoltaic power generation in Germany. Atmos. Chem. Phys. 17, 13391-13415.

Rinne, J., Taipale, R., Markkanen, T., Ruuskanen, T.M., Hellén, H., Kajos, M.K., Vesala, T., Kulmala, M., 2007. Hydrocarbon fluxes above a Scots pine forest canopy: measurements and modeling. Atmos. Chem. Phys. 7, 3361-3372.

Riva, M., Rantala, P., Krechmer, J.E., Peräkylä, O., Zhang, Y., Heikkinen, L., Garmash, O., Yan, C., Kulmala, M., Worsnop, D., Ehn, M., 2019. Evaluating the performance of five different chemical ionization techniques for detecting gaseous oxygenated organic species. Atmos. Meas. Tech. 12, 2403-2421.

Rodelas, R.R., Chakraborty, A., Perdrix, E., Tison, E., Riffault, V., 2019. Real-time assessment of wintertime organic aerosol characteristics and sources at a suburban site in northern France. Atmos. Environ. 203, 48-61.

Romano, A., Fischer, L., Herbig, J., Campbell-Sills, H., Coulon, J., Lucas, P., Cappellin, L., Biasioli, F., 2014. Wine analysis by FastGC proton-transfer reaction-time-of-flight-mass spectrometry. International Journal of Mass Spectrometry 369, 81-86.

Ruuskanen, T.M., Müller, M., Schnitzhofer, R., Karl, T., Graus, M., Bamberger, I., Hörtnagl, L., Brilli, F., Wohlfahrt, G., Hansel, A., 2011. Eddy covariance VOC emission and deposition fluxes above grassland using PTR-TOF. Atmos. Chem. Phys. 11, 611-625.

Saathoff, H., Naumann, K.H., Möhler, O., Jonsson, Å.M., Hallquist, M., Kiendler-Scharr, A., Mentel, T.F., Tillmann, R., Schurath, U., 2009. Temperature dependence of yields of secondary organic aerosols from the ozonolysis of α-pinene and limonene. Atmos. Chem. Phys. 9, 1551-1577.

Salazar Gómez, J.I., Lohmann, H., Krassowski, J., 2016. Determination of volatile organic compounds from biowaste and co-fermentation biogas plants by single-sorbent adsorption. Chemosphere 153, 48-57.

Sandradewi, J., Prevot, A.S.H., Szidat, S., Perron, N., Alfarra, M.R., Lanz, V.A., Weingartner, E., Baltensperger, U., 2008a. Using aerosol light absorption measurements for the quantitative determination of wood burning and traffic emission contributions to particulate matter. Environ. Sci. Technol. 42, 3316-3323.

Sandradewi, J., Prévôt, A.S.H., Weingartner, E., Schmidhauser, R., Gysel, M., Baltensperger, U., 2008b. A study of wood burning and traffic aerosols in an Alpine valley using a multi-wavelength Aethalometer. Atmos. Environ. 42, 101-112.

Sanz-Bobi, M.A., Cuadra, F.d., Batlle, C., 2012. A review of key points of an industrial biogas plant. A European perspective, 2012 International Conference on Renewable Energy Research and Applications (ICRERA), pp. 1-6.

Sarang, K., Otto, T., Rudzinski, K., Schaefer, T., Grgić, I., Nestorowicz, K., Herrmann, H., Szmigielski, R., 2021. Reaction Kinetics of Green Leaf Volatiles with Sulfate, Hydroxyl, and Nitrate Radicals in Tropospheric Aqueous Phase. Environ. Sci. Technol. 55, 13666-13676.

Scala, A., Allmann, S., Mirabella, R., Haring, M.A., Schuurink, R.C., 2013. Green Leaf Volatiles: A Plant's Multifunctional Weapon against Herbivores and Pathogens. International Journal of Molecular Sciences 14, 17781-17811.

Schaub, A., Blande, J.D., Graus, M., Oksanen, E., Holopainen, J.K., Hansel, A., 2010. Real-time monitoring of herbivore induced volatile emissions in the field. Physiologia Plantarum 138, 123-133.

Seinfeld, J.H., Pandis, S.N., 2016a. Atmospheric chemistry and physics : from air pollution to climate change, Third edition. ed. John Wiley & Sons,, Hoboken, New Jersey, p. 1 online resource.

Seinfeld, J.H., Pandis, S.N., 2016b. Atmospheric chemistry and physics : from air pollution to climate change, Third edition. ed. John Wiley & Sons, Inc., Hoboken, New Jersey.

Sekimoto, K., Li, S.-M., Yuan, B., Koss, A., Coggon, M., Warneke, C., de Gouw, J., 2017. Calculation of the sensitivity of proton-transfer-reaction mass spectrometry (PTR-MS) for organic trace gases using molecular properties. International Journal of Mass Spectrometry 421, 71-94.

Shen, X.L., Vogel, H., Vogel, B., Huang, W., Mohr, C., Ramisetty, R., Leisner, T., Prevot, A.S.H., Saathoff, H., 2019. Composition and origin of PM2.5 aerosol particles in the upper Rhine valley in summer. Atmos. Chem. Phys. 19, 13189-13208.

Shi, J.P., Khan, A.A., Harrison, R.M., 1999. Measurements of ultrafine particle concentration and size distribution in the urban atmosphere. Sci. Total Environ. 235, 51-64.

Shrivastava, M., Cappa, C.D., Fan, J., Goldstein, A.H., Guenther, A.B., Jimenez, J.L., Kuang, C., Laskin, A., Martin, S.T., Ng, N.L., Petaja, T., Pierce, J.R., Rasch, P.J., Roldin, P., Seinfeld, J.H., Shilling, J., Smith, J.N., Thornton, J.A., Volkamer, R., Wang, J., Worsnop, D.R., Zaveri, R.A., Zelenyuk, A., Zhang, Q., 2017. Recent advances in understanding secondary organic aerosol: Implications for global climate forcing. Reviews of Geophysics 55, 509-559.

Sicard, P., De Marco, A., Agathokleous, E., Feng, Z., Xu, X., Paoletti, E., Rodriguez, J.J.D., Calatayud, V., 2020. Amplified ozone pollution in cities during the COVID-19 lockdown. Sci. Total Environ. 735, 139542.

Sinclair, V.A., Ritvanen, J., Urbancic, G., Statnaia, I., Batrak, Y., Moisseev, D., Kurppa, M., 2021. Boundary-layer height and surface stability at SMEAR II, Hyytiälä, Finland in ERA5 and observations. Atmos. Meas. Tech. Discuss. 2021, 1-42.

Sindelarova, K., Granier, C., Bouarar, I., Guenther, A., Tilmes, S., Stavrakou, T., Müller, J.F., Kuhn, U., Stefani, P., Knorr, W., 2014. Global data set of biogenic VOC emissions calculated by the MEGAN model over the last 30 years. Atmos. Chem. Phys. 14, 9317-9341.

Sirocko, F., Dietrich, S., Veres, D., Grootes, P.M., Schaber-Mohr, K., Seelos, K., Nadeau, M.-J., Kromer, B., Rothacker, L., Röhner, M., Krbetschek, M., Appleby, P., Hambach, U., Rolf, C., Sudo, M., Grim, S., 2013. Multi-proxy dating of Holocene maar lakes and Pleistocene dry maar sediments in the Eifel, Germany. Quaternary Science Reviews 62, 56-76.

Slowik, J.G., Vlasenko, A., McGuire, M., Evans, G.J., Abbatt, J.P.D., 2010. Simultaneous factor analysis of organic particle and gas mass spectra: AMS and PTR-MS measurements at an urban site. Atmos. Chem. Phys. 10, 1969-1988.

Smith, J.S., Laskin, A., Laskin, J., 2009. Molecular Characterization of Biomass Burning Aerosols Using High-Resolution Mass Spectrometry. Analytical Chemistry 81, 1512-1521.

Song, J., Saathoff, H., Gao, L., Gebhardt, R., Jiang, F., Vallon, M., Bauer, J., Norra, S., Leisner, T., 2022. Variations of PM2.5 sources in the context of meteorology and seasonality at an urban street canyon in Southwest Germany. Atmos. Environ., 119147.

Stadtler, S., Kühn, T., Schröder, S., Taraborrelli, D., Schultz, M.G., Kokkola, H., 2018. Isoprene-derived secondary organic aerosol in the global aerosol–chemistry–climate model ECHAM6.3.0–HAM2.3–MOZ1.0. Geosci. Model Dev. 11, 3235-3260.

Stein, A.F., Draxler, R.R., Rolph, G.D., Stunder, B.J.B., Cohen, M.D., Ngan, F., 2015. Noaa's Hysplit Atmospheric Transport and Dispersion Modeling System. B Am Meteorol Soc 96, 2059-2077.

Stevenson, D.S., Young, P.J., Naik, V., Lamarque, J.F., Shindell, D.T., Voulgarakis, A., Skeie, R.B., Dalsoren, S.B., Myhre, G., Berntsen, T.K., Folberth, G.A., Rumbold, S.T., Collins, W.J., MacKenzie, I.A., Doherty, R.M., Zeng, G., van Noije, T.P.C., Strunk, A., Bergmann, D., Cameron-Smith, P., Plummer, D.A., Strode, S.A., Horowitz, L., Lee, Y.H., Szopa, S., Sudo, K., Nagashima, T., Josse, B., Cionni, I., Righi, M., Eyring, V., Conley, A., Bowman, K.W., Wild, O., Archibald, A., 2013. Tropospheric ozone changes, radiative forcing and attribution to emissions in the Atmospheric Chemistry and Climate Model Intercomparison Project (ACCMIP). Atmos. Chem. Phys. 13, 3063-3085.

Sun, Y.L., Zhang, Q., Schwab, J.J., Chen, W.N., Bae, M.S., Lin, Y.C., Hung, H.M., Demerjian, K.L., 2011. A case study of aerosol processing and evolution in summer in New York City. Atmos. Chem. Phys. 11, 12737-12750.

Surratt, J.D., Chan, A.W.H., Eddingsaas, N.C., Chan, M., Loza, C.L., Kwan, A.J., Hersey, S.P., Flagan, R.C., Wennberg, P.O., Seinfeld, J.H., 2010. Reactive intermediates revealed in secondary organic aerosol formation from isoprene. Proceedings of the National Academy of Sciences 107, 6640-6645.

Taipale, R., Kajos, M.K., Patokoski, J., Rantala, P., Ruuskanen, T.M., Rinne, J., 2011. Role of de novo biosynthesis in ecosystem scale monoterpene emissions from a boreal Scots pine forest. Biogeosciences 8, 2247-2255.

Tani, A., Hayward, S., Hewitt, C.N., 2003. Measurement of monoterpenes and related compounds by proton transfer reaction-mass spectrometry (PTR-MS). International Journal of Mass Spectrometry 223-224, 561-578.

Thornton, J.A., Mohr, C., Schobesberger, S., D'Ambro, E.L., Lee, B., Lopez-Hilfiker, F.D., 2020. Evaluating Organic Aerosol Sources and Evolution with a Combined Molecular Composition and Volatility Framework Using the Filter Inlet for Gases and Aerosols (FIGAERO). Accounts Chem Res 53, 1415-1426.

Tian, H., Lu, C., Ciais, P., Michalak, A.M., Canadell, J.G., Saikawa, E., Huntzinger, D.N., Gurney, K.R., Sitch, S., Zhang, B., Yang, J., Bousquet, P., Bruhwiler, L., Chen, G., Dlugokencky, E., Friedlingstein, P., Melillo, J., Pan, S., Poulter, B., Prinn, R., Saunois, M., Schwalm, C.R., Wofsy, S.C., 2016. The terrestrial biosphere as a net source of greenhouse gases to the atmosphere. Nature 531, 225-228.

Titzmann, T., Graus, M., Müller, M., Hansel, A., Ostermann, A., 2010. Improved peak analysis of signals based on counting systems: Illustrated for proton-transfer-reaction time-of-flight mass spectrometry. International Journal of Mass Spectrometry 295, 72-77.

Tsigaridis, K., Kanakidou, M., 2007. Secondary organic aerosol importance in the future atmosphere. Atmos. Environ. 41, 4682-4692.

Ulbrich, I.M., Canagaratna, M.R., Zhang, Q., Worsnop, D.R., Jimenez, J.L., 2009. Interpretation of organic components from Positive Matrix Factorization of aerosol mass spectrometric data. Atmos. Chem. Phys. 9, 2891-2918.

Ullah Khan, I., Hafiz Dzarfan Othman, M., Hashim, H., Matsuura, T., Ismail, A.F., Rezaei-DashtArzhandi, M., Wan Azelee, I., 2017. Biogas as a renewable energy fuel – A review of biogas upgrading, utilisation and storage. Energy Conversion and Management 150, 277-294.

Vallon, M., Gao, L., Jiang, F., Krumm, B., Nadolny, J., Song, J., Leisner, T., Saathoff, H., 2022. LED-based solar simulator to study photochemistry over a wide temperature range in the large simulation chamber AIDA. Atmos. Meas. Tech. 15, 1795-1810.

Vestenius, M., Hopke, P.K., Lehtipalo, K., Petäjä, T., Hakola, H., Hellén, H., 2021. Assessing volatile organic compound sources in a boreal forest using positive matrix factorization (PMF). Atmos. Environ. 259, 118503.

Vlasenko, A., Slowik, J.G., Bottenheim, J.W., Brickell, P.C., Chang, R.Y.-W., Macdonald, A.M., Shantz, N.C., Sjostedt, S.J., Wiebe, H.A., Leaitch, W.R., Abbatt, J.P.D., 2009. Measurements of VOCs by proton transfer reaction mass spectrometry at a rural Ontario site: Sources and correlation to aerosol composition. J. Geophys. Res.-Atmos. 114.

Volkamer, R., Jimenez, J.L., San Martini, F., Dzepina, K., Zhang, Q., Salcedo, D., Molina, L.T., Worsnop, D.R., Molina, M.J., 2006. Secondary organic aerosol formation from anthropogenic air pollution: Rapid and higher than expected. Geophys. Res. Lett. 33.

Wagner, R., Bunz, H., Linke, C., Möhler, O., Naumann, K.-H., Saathoff, H., Schnaiter, M., Schurath, U., 2006. Chamber Simulations of Cloud Chemistry: The AIDA Chamber, in: Barnes, I., Rudzinski, K.J. (Eds.), Environmental Simulation Chambers: Application to Atmospheric Chemical Processes. Springer Netherlands, Dordrecht, pp. 67-82.

Wang, L., Slowik, J.G., Tong, Y., Duan, J., Gu, Y., Rai, P., Qi, L., Stefenelli, G., Baltensperger, U., Huang, R.-J., Cao, J., Prévôt, A.S.H., 2021. Characteristics of wintertime VOCs in urban Beijing: Composition and source apportionment. Atmospheric Environment: X 9, 100100.

Wang, L., Slowik, J.G., Tripathi, N., Bhattu, D., Rai, P., Kumar, V., Vats, P., Satish, R., Baltensperger, U., Ganguly, D., Rastogi, N., Sahu, L.K., Tripathi, S.N., Prévôt, A.S.H., 2020. Source characterization of volatile organic compounds measured by proton-transfer-reaction time-of-flight mass spectrometers in Delhi, India. Atmos. Chem. Phys. 20, 9753-9770.

Warneke, C., de Gouw, J.A., Stohl, A., Cooper, O.R., Goldan, P.D., Kuster, W.C., Holloway, J.S., Williams, E.J., Lerner, B.M., McKeen, S.A., Trainer, M., Fehsenfeld, F.C., Atlas, E.L., Donnelly, S.G., Stroud, V., Lueb, A., Kato, S., 2006. Biomass burning and anthropogenic sources of CO over New England in the summer 2004. J. Geophys. Res.-Atmos. 111.

Xu, L., Guo, H., Boyd, C.M., Klein, M., Bougiatioti, A., Cerully, K.M., Hite, J.R., Isaacman-VanWertz, G., Kreisberg, N.M., Knote, C., Olson, K., Koss, A., Goldstein, A.H., Hering, S.V., Gouw, J.d., Baumann, K., Lee, S.-H., Nenes, A., Weber, R.J., Ng, N.L., 2015. Effects of anthropogenic emissions on aerosol formation from isoprene and monoterpenes in the southeastern United States. Proceedings of the National Academy of Sciences 112, 37-42.

Yáñez-Serrano, A.M., Filella, I., Llusià, J., Gargallo-Garriga, A., Granda, V., Bourtsoukidis, E., Williams, J., Seco, R., Cappellin, L., Werner, C., de Gouw, J., Peñuelas, J., 2021. GLOVOCS - Master compound assignment guide for proton transfer reaction mass spectrometry users. Atmos. Environ. 244, 117929.

Yáñez-Serrano, A.M., Nölscher, A.C., Bourtsoukidis, E., Gomes Alves, E., Ganzeveld, L., Bonn, B., Wolff, S., Sa, M., Yamasoe, M., Williams, J., Andreae, M.O., Kesselmeier, J., 2018. Monoterpene chemical speciation in a tropical rainforest:variation with season, height, and time of dayat the Amazon Tall Tower Observatory (ATTO). Atmos. Chem. Phys. 18, 3403-3418.

Yáñez-Serrano, A.M., Nölscher, A.C., Williams, J., Wolff, S., Alves, E., Martins, G.A., Bourtsoukidis, E., Brito, J., Jardine, K., Artaxo, P., Kesselmeier, J., 2015. Diel and seasonal changes of biogenic volatile organic compounds within and above an Amazonian rainforest. Atmos. Chem. Phys. 15, 3359-3378.

Yao, D., Lyu, X., Lu, H., Zeng, L., Liu, T., Chan, C.K., Guo, H., 2021. Characteristics, sources and evolution processes of atmospheric organic aerosols at a roadside site in Hong Kong. Atmos. Environ. 252, 118298.

Yu, J., Cocker, D.R., Griffin, R.J., Flagan, R.C., Seinfeld, J.H., 1999a. Gas-Phase Ozone Oxidation of Monoterpenes: Gaseous and Particulate Products. Journal of Atmospheric Chemistry 34, 207-258.

Yu, J., Griffin, R.J., Cocker III, D.R., Flagan, R.C., Seinfeld, J.H., Blanchard, P., 1999b. Observation of gaseous and particulate products of monoterpene oxidation in forest atmospheres. Geophys. Res. Lett. 26, 1145-1148.

Yuan, B., Koss, A.R., Warneke, C., Coggon, M., Sekimoto, K., de Gouw, J.A., 2017. Proton-Transfer-Reaction Mass Spectrometry: Applications in Atmospheric Sciences. Chem Rev 117, 13187-13229.

Yuan, B., Shao, M., de Gouw, J., Parrish, D.D., Lu, S., Wang, M., Zeng, L., Zhang, Q., Song, Y., Zhang, J., Hu, M., 2012. Volatile organic compounds (VOCs) in urban air: How chemistry affects the interpretation of positive matrix factorization (PMF) analysis. J. Geophys. Res.-Atmos. 117.

Zaytsev, A., Koss, A.R., Breitenlechner, M., Krechmer, J.E., Nihill, K.J., Lim, C.Y., Rowe, J.C., Cox, J.L., Moss, J., Roscioli, J.R., Canagaratna, M.R., Worsnop, D.R., Kroll, J.H., Keutsch, F.N., 2019. Mechanistic study of the formation of ring-retaining and ring-opening products from the oxidation of aromatic compounds under urban atmospheric conditions. Atmos. Chem. Phys. 19, 15117-15129.

Zhang, H., Wagner, F., Saathoff, H., Vogel, H., Hoshyaripour, G.A., Bachmann, V., Förstner, J., Leisner, T., 2021. Investigation of a Saharan dust plume in Western Europe by remote sensing and transport modelling. Atmos. Meas. Tech. Discuss. 2021, 1-19.

Zhang, H., Yee, L.D., Lee, B.H., Curtis, M.P., Worton, D.R., Isaacman-VanWertz, G., Offenberg, J.H., Lewandowski, M., Kleindienst, T.E., Beaver, M.R., Holder, A.L., Lonneman, W.A., Docherty, K.S., Jaoui, M., Pye, H.O.T., Hu, W., Day, D.A., Campuzano-Jost, P., Jimenez, J.L., Guo, H., Weber, R.J., Gouw, J.d., Koss, A.R., Edgerton, E.S., Brune, W., Mohr, C., Lopez-Hilfiker, F.D., Lutz, A., Kreisberg, N.M., Spielman, S.R., Hering, S.V., Wilson, K.R., Thornton, J.A., Goldstein, A.H., 2018. Monoterpenes are the largest source of summertime organic aerosol in the southeastern United States. Proceedings of the National Academy of Sciences 115, 2038-2043.

Zhang, J., Lance, S., Marto, J., Sun, Y., Ninneman, M., Crandall, B.A., Wang, J., Zhang, Q., Schwab, J.J., 2020. Evolution of Aerosol Under Moist and Fog Conditions in a Rural Forest Environment: Insights From High-Resolution Aerosol Mass Spectrometry. Geophys. Res. Lett. 47, e2020GL089714.

Zhang, Q., Jimenez, J.L., Canagaratna, M.R., Ulbrich, I.M., Ng, N.L., Worsnop, D.R., Sun, Y.L., 2011. Understanding atmospheric organic aerosols via factor analysis of aerosol mass spectrometry: a review. Anal. Bioanal. Chem. 401, 3045-3067.

Zhang, X., McVay, R.C., Huang, D.D., Dalleska, N.F., Aumont, B., Flagan, R.C., Seinfeld, J.H., 2015. Formation and evolution of molecular products in α-pinene secondary organic aerosol. Proceedings of the National Academy of Sciences 112, 14168-14173.

Zhou, W., Xu, W.Q., Kim, H., Zhang, Q., Fu, P.Q., Worsnop, D.R., Sun, Y.L., 2020. A review of aerosol chemistry in Asia: insights from aerosol mass spectrometer measurements. Environ Sci-Proc Imp 22, 1616-1653.

Zhu, Q., Huang, X.F., Cao, L.M., Wei, L.T., Zhang, B., He, L.Y., Elser, M., Canonaco, F., Slowik, J.G., Bozzetti, C., El-Haddad, I., Prévôt, A.S.H., 2018. Improved source apportionment of organic aerosols in complex urban air pollution using the multilinear engine (ME-2). Atmos. Meas. Tech. 11, 1049-1060.

Appendix A-Supplement for the results and discussion in the dissertation

Table S1 Correlation coefficients (Pearson's R) between the time series of the OA factors with various external tracers for summer 2019DT and winter 2020DT.

	Summer data					Winter data				
OA factor	HOA	COA	SV-OOA	LV-OOA1	LV-OOA2	HOA	COA	BBOA	SV-OOA	LV-OOA
$C_4H_9^+$	**0.90**	**0.58**	0.36	-0.28	0.27	**0.97**	**0.50**	0.40	0.47	0.14
$C_6H_{10}O^+$	0.39	**0.94**	**0.51**	-0.41	0.46	**0.75**	**0.77**	**0.53**	0.47	0.11
$C_2H_4O_2^+$						0.32	**0.52**	**0.92**	**0.71**	0.43
$C_2H_3O^+$	0.23	**0.52**	**0.92**	-0.48	**0.89**	0.34	0.35	**0.66**	**0.94**	**0.68**
CO_2^+	0.19	0.46	**0.74**	-0.48	**0.98**	0.26	0.34	**0.57**	**0.79**	**0.85**
NO_3 (nitrate)	0.16	0.04	0.24	0.37	-0.05	0.1	0.09	0.18	0.47	**0.83**
SO_4 (sulfate)	0.1	-0.02	0.05	**0.53**	0.02	0.01	0.02	0.13	0.45	**0.77**
BC	0.43	**0.54**	0.7	-0.28	**0.56**	0.41	**0.58**	**0.77**	**0.59**	0.36
O_x	-0.03	0.13	-0.02	-0.3	**0.57**	-0.09	0.02	-0.44	-0.37	0.08
NO_2	0.16	0.43	**0.83**	-0.4	**0.96**	0.43	0.49	**0.55**	0.33	0.02

The values of R > 0.5 are in bold.

Table S2 Correlation coefficients (Pearson's R) between the time series of the OA factors with various external tracers for summer 2021KITcn.

External tracers	HOA	SVOOA1	SVOOA2	LVOOA1	LVOOA2
AMS_$CH_3SO_2^+$					0.84
AMS_$C_5H_6O^+$		0.85	0.84	0.82	
AMS_$C_7H_7^+$		0.93	0.87	0.66	
AMS_$C_2H_3O^+$		0.92	0.76	0.78	
AMS_CO_2^+		0.68	0.72	0.96	
AMS_$C_4H_9^+$	0.68	0.93	0.71	0.64	
SO_4 (sulfate)					
NH_4 (ammonium)					
NO_3 (nitrate)	0.50	0.63		0.50	
BC	0.50	0.70	0.67	0.74	
O_3					
NO_2		0.50			
O_x				0.50	
Temperature (T)				0.50	
Relative humidity (RH)					
Wind direction (WD)		-0.61*			
Wind speed (WS)		-0.54			
Radiation					

The values of only |R|> 0.5 are showed. * The negative values mean a negative correlation.

Table S3 Correlation coefficients (Pearson's R) between the time series of the VOC factors with various external tracers for summer 2021 KITcn.

External tracers	Traffic VOCs	Nighttime VOCs	SecVOC1	SecVOC2	Regional transport
PTR_C_7H_8O		0.55	0.84		
PTR_$C_7H_8O_2$			0.78	0.74	
PTR_$C_{10}H_{16}O_2$	0.65	0.64	0.79		
PTR_$C_{10}H_{16}O$	0.75	0.83	0.53		
PTR_$C_{10}H_{14}O$	0.79	0.65	0.57		
PTR_C_5H_8			0.68	0.50	
PTR_$C_{10}H_{16}$		1.00			
PTR_$C_{15}H_{24}$		0.88			
PTR_C_6H_6	0.67	0.92			
PTR_C_7H_8	0.82	0.80			
PTR_C_8H_{10}	0.90	0.65			
PTR_C_9H_{12}	0.84	0.73			
PTR_C_3H_6O			0.52	0.69	
PTR_CH_2O_2				0.96	
PTR_C_2H_6O	0.82				
PTR_C_4H_6O			0.60	0.81	
PTR_C_5H_8O			0.60	0.81	
O_3	-0.50*	-0.59		0.87	
NO_2	0.55				
O_x		-0.52		0.90	
Temperature				0.92	
Relative humidity				-0.84	
Wind direction	-0.60	-0.54			0.56
Wind speed		-0.59			
Radiation				0.75	

The values of |R|> 0.5 are showed. * The negative value means a negative correlation.

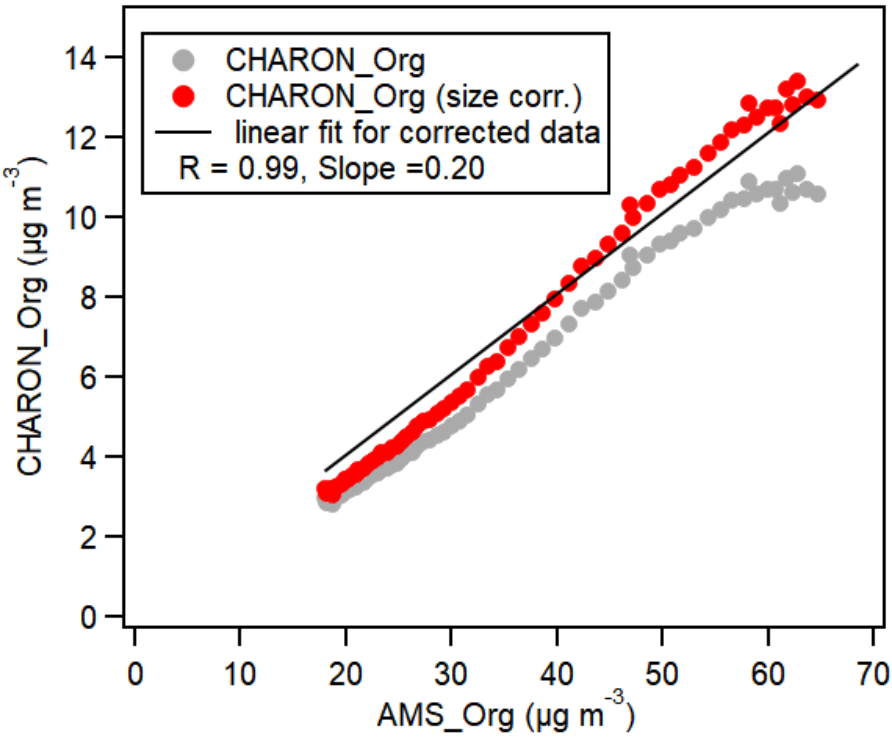

Figure S1. Comparison of organic mass measured by the AMS and CHARON with and without the correction of size effect in the chamber experiment on 5th December 2019.

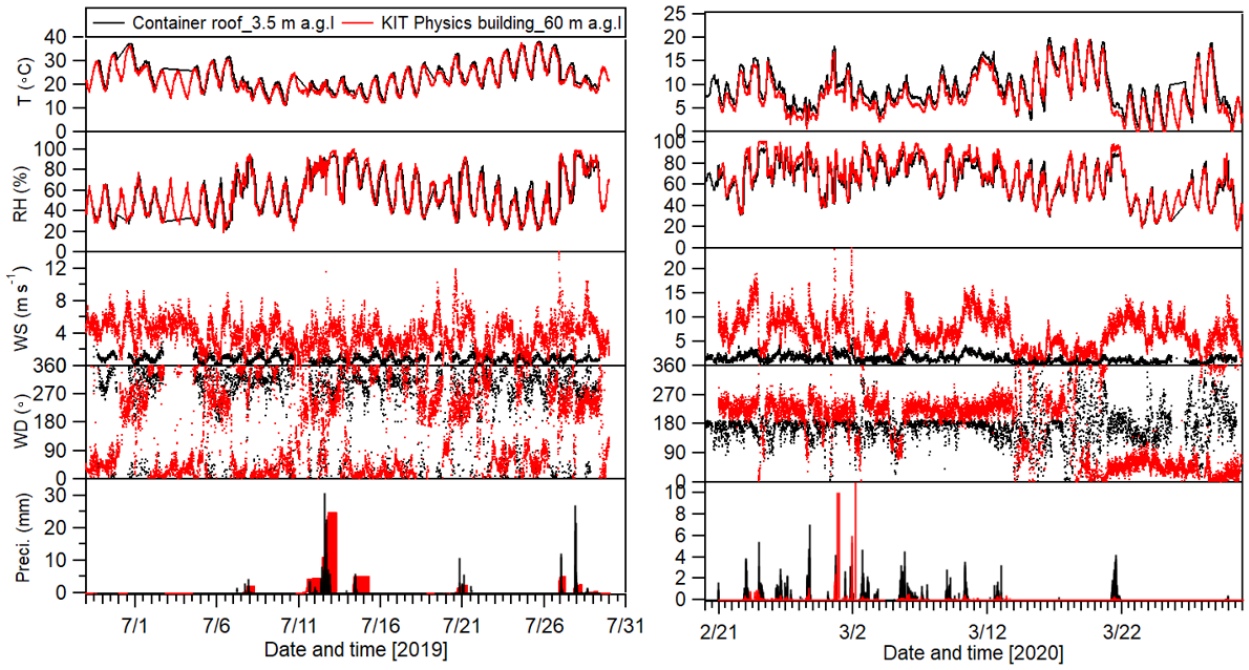

Figure S2. Overview of meteorological parameters including temperature (T), relative humidity (RH), wind speed (WS) and direction (WD) and precipitation (Preci.) measured at the container roof (3.5 m a.g.l, black) and the KIT Physics building (60 m a.g.l, red) in summer 2019 (left) and winter 2020 (right).

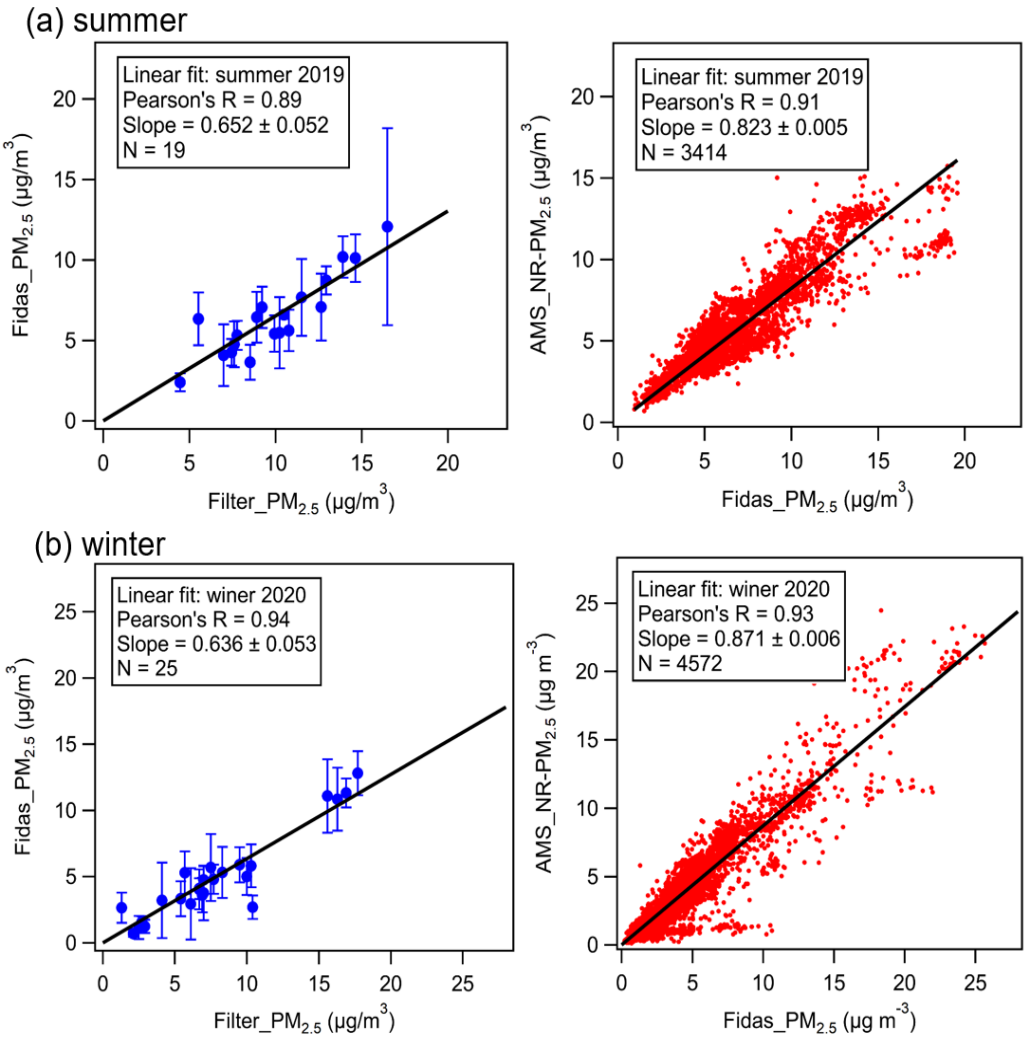

Figure S3. Linear relationships of $PM_{2.5}$ mass concentrations from gravimetric analysis of daily filters, Fidas-OPC and AMS in summer 2019 (a) and winter 2020 (b).

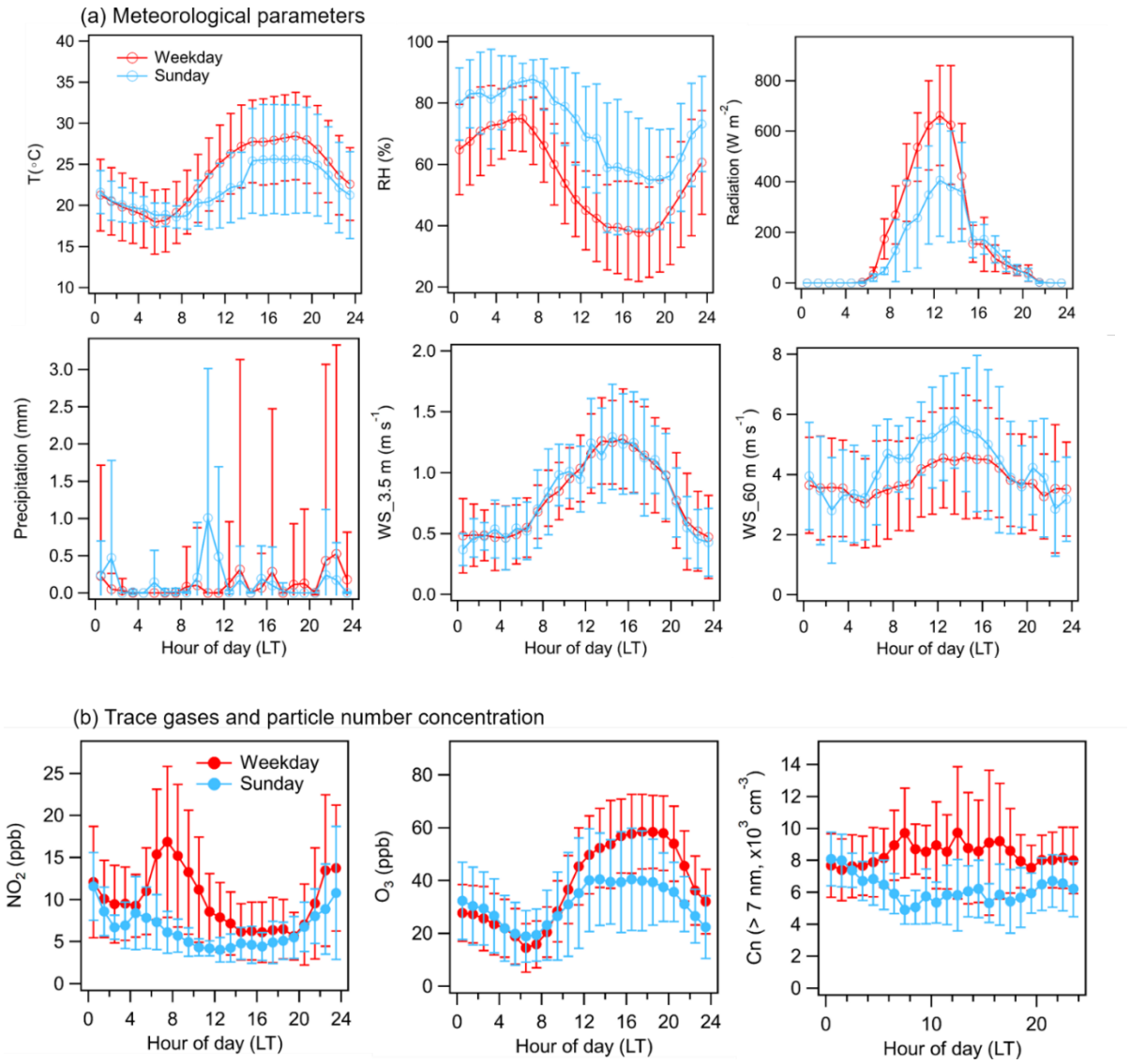

Figure S4. Diurnal variations of (a) meteorological parameters including temperature (T), relative humidity (RH), radiation, precipitation and wind speeds at the heights of 3.5 m and 60 m a.g.l; and (b) trace gas concentrations (NO_2 and O_3) and particle number concentrations for particle sizes C_n > 7 nm over the entire campaign period in summer 2019. The red and blue cycles showed the hourly data averaged over the weekdays (Monday-Saturday) and Sunday, respectively. The error bars represent ±1 standard deviation.

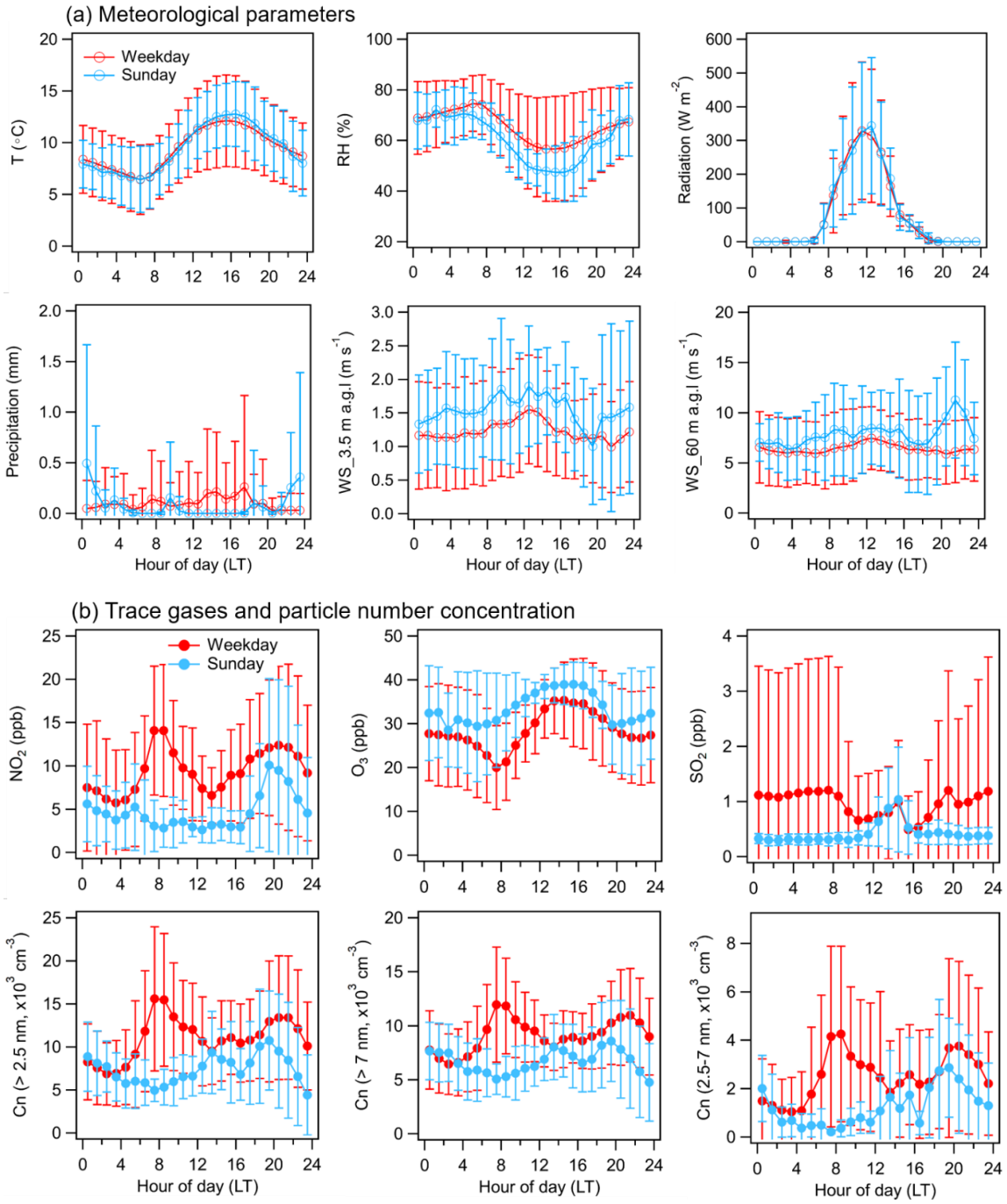

Figure S5. Diurnal variations of (a) meteorological parameters and (b) trace gas concentrations (NO_2, O_3 and SO_2) and particle number concentrations with the sizes (C_n, >2.5 nm, > 7 nm and 2.5-7 nm) over the entire winter campaign period in 2020. The red and blue cycles showed the hourly data averaged over the weekdays (Monday-Saturday) and Sunday, respectively (refer to Fig. S4).

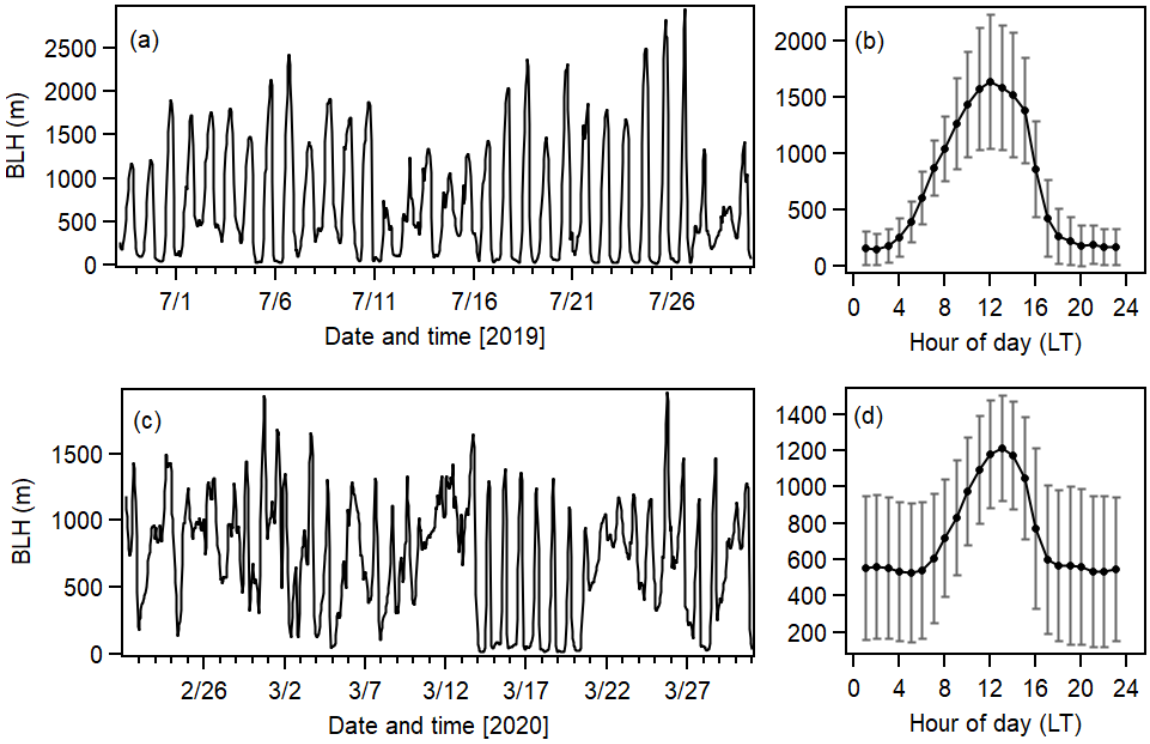

Figure S6. ERA5 boundary layer height (BLH) for Karlsruhe for (a) summer 2019 and (c) winter 2020 and average diurnal variations are shown on the right (b, d). Hourly 0.25×0.25 latitude/longitude data are averaged within 48.75°-49.25° N and 8.25°-8.50° E.

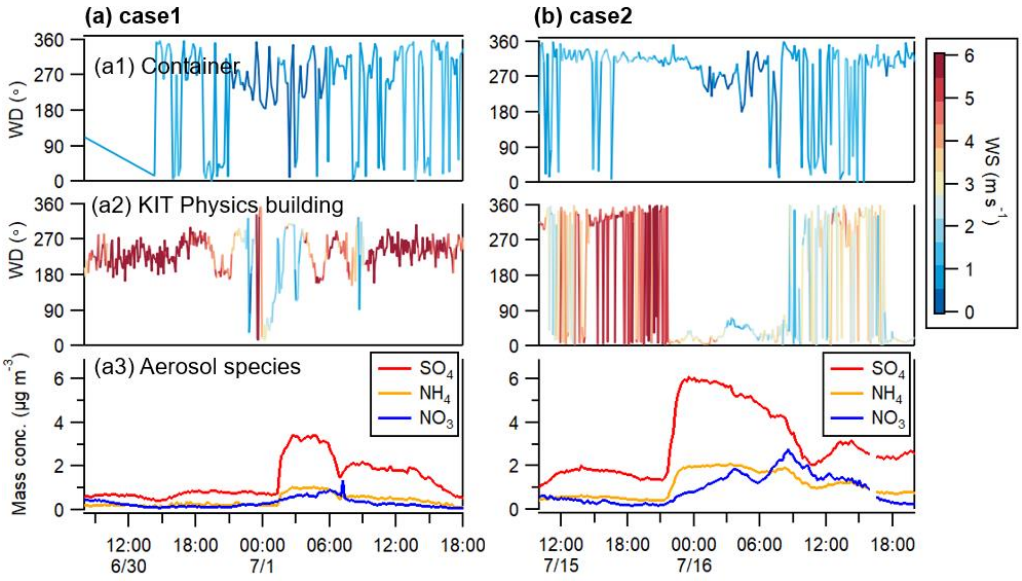

Figure S7. Evolution of wind directions colored by wind speeds at two positions, on the container roof and on top of the KIT Physics building, and aerosol species (sulfate, ammonium and nitrate) mass concentrations during two cases: (a) case 1 (30th June-1st July) and (b) case 2 (15th-16th July).

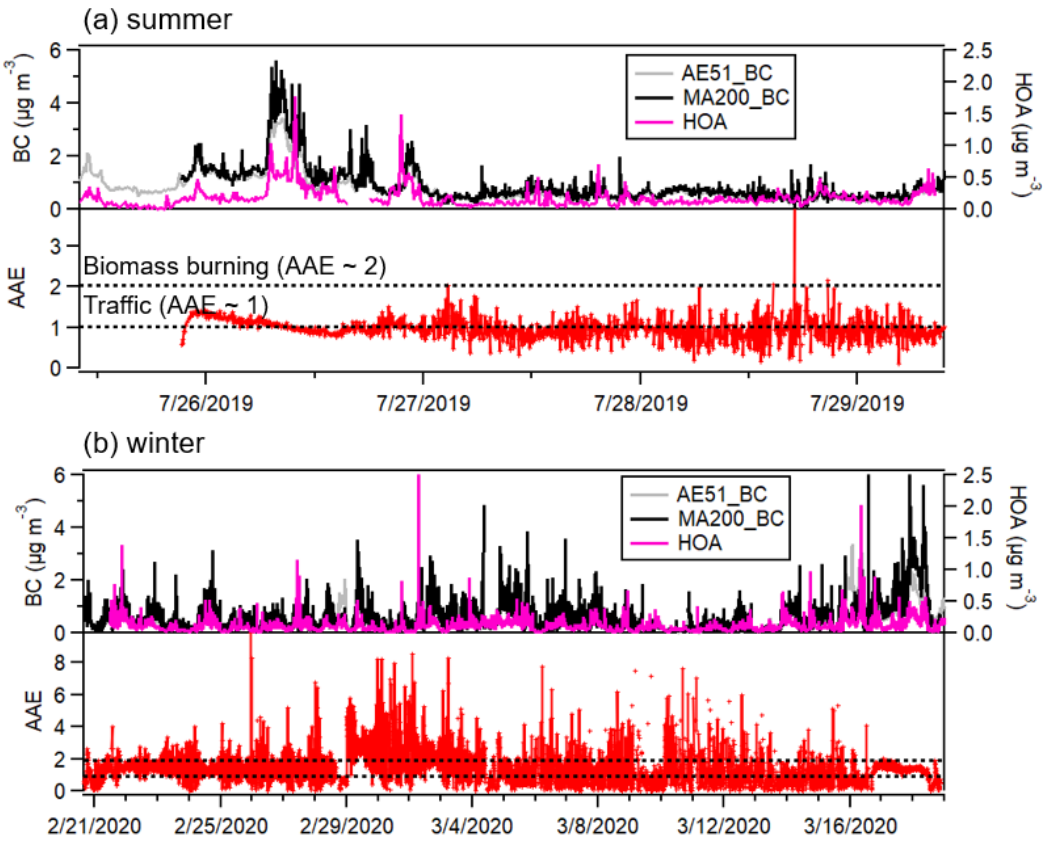

Figure S8. Time series of BC measured by two aethalometers (AE51 and MA200), HOA concentrations resolved from AMS-PMF and absorption Ångström exponent (AAE) calculated from the MA200 data during the intensive measurement periods in summer (a) and winter (b). The dash lines show the typical AAE values for traffic-dominated (~1) and biomass burning-dominated (~2) environments, respectively.

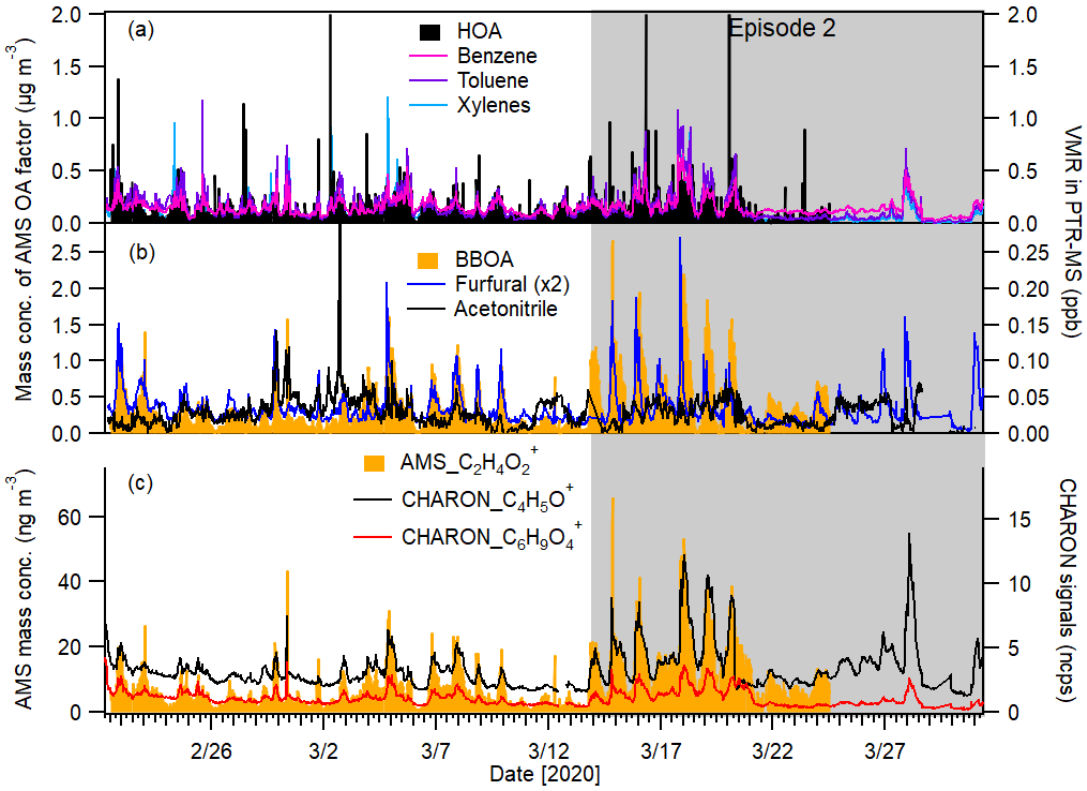

Figure S9. (a-b) Time series of AMS PMF-resolved HOA and BBOA factors compared to typical VOC species (benzene, toluene, xylenes, acetonitrile, furfural) measured by the PTR-MS in winter 2020. (c) Time series of ions related to levoglucosan fragmentation measured by AMS and CHARON-PTR-MS are shown for comparison.

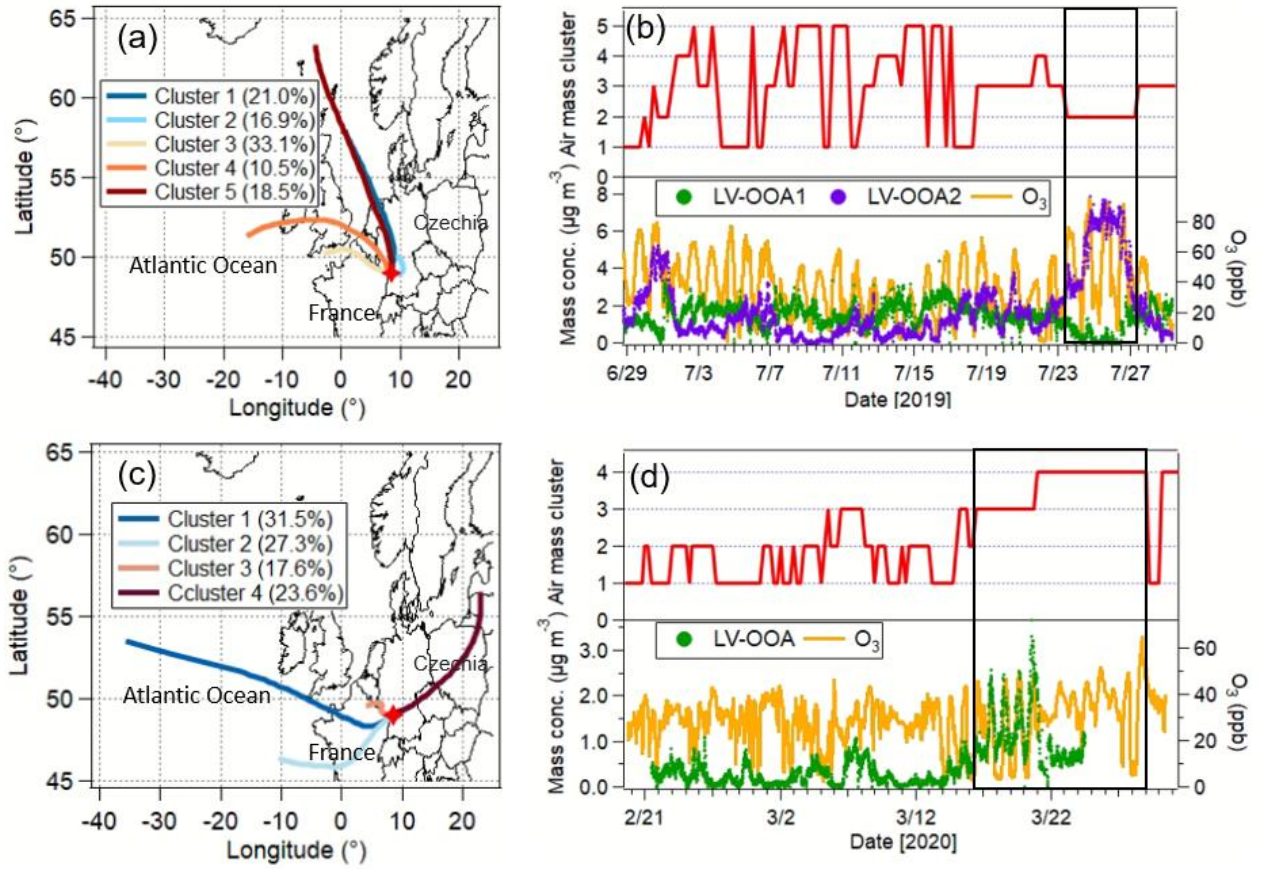

Figure S10. Cluster results of 72 h backward air mass trajectories calculated for the entire periods of (a) summer 2019 and (c) winter 2020. The percentages show the fraction of each cluster to total air mass trajectories. The variations of LV-OOA and O_3 concentrations associated with air mass clusters are shown in (b) and (d). The two episodes marked by black box are discussed in more detail in the main text.

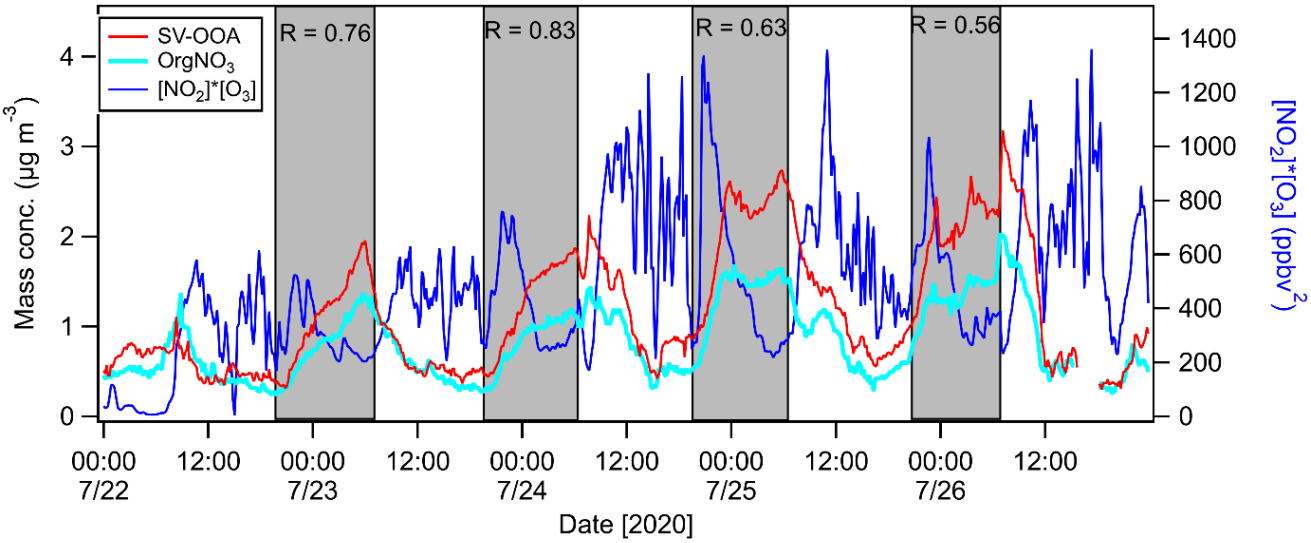

Figure S11. Time series of SV-OOA and organic nitrate measured by the AMS and the indicator of potential nitrate radicals (NO_3·~ $[NO_2]$*$[O_3]$) during the summer heatwave episode 2019 . The correlation coefficients between organic nitrate concentrations and the levels of $[NO_2]$*$[O_3]$ during nights are shown in the grey areas.

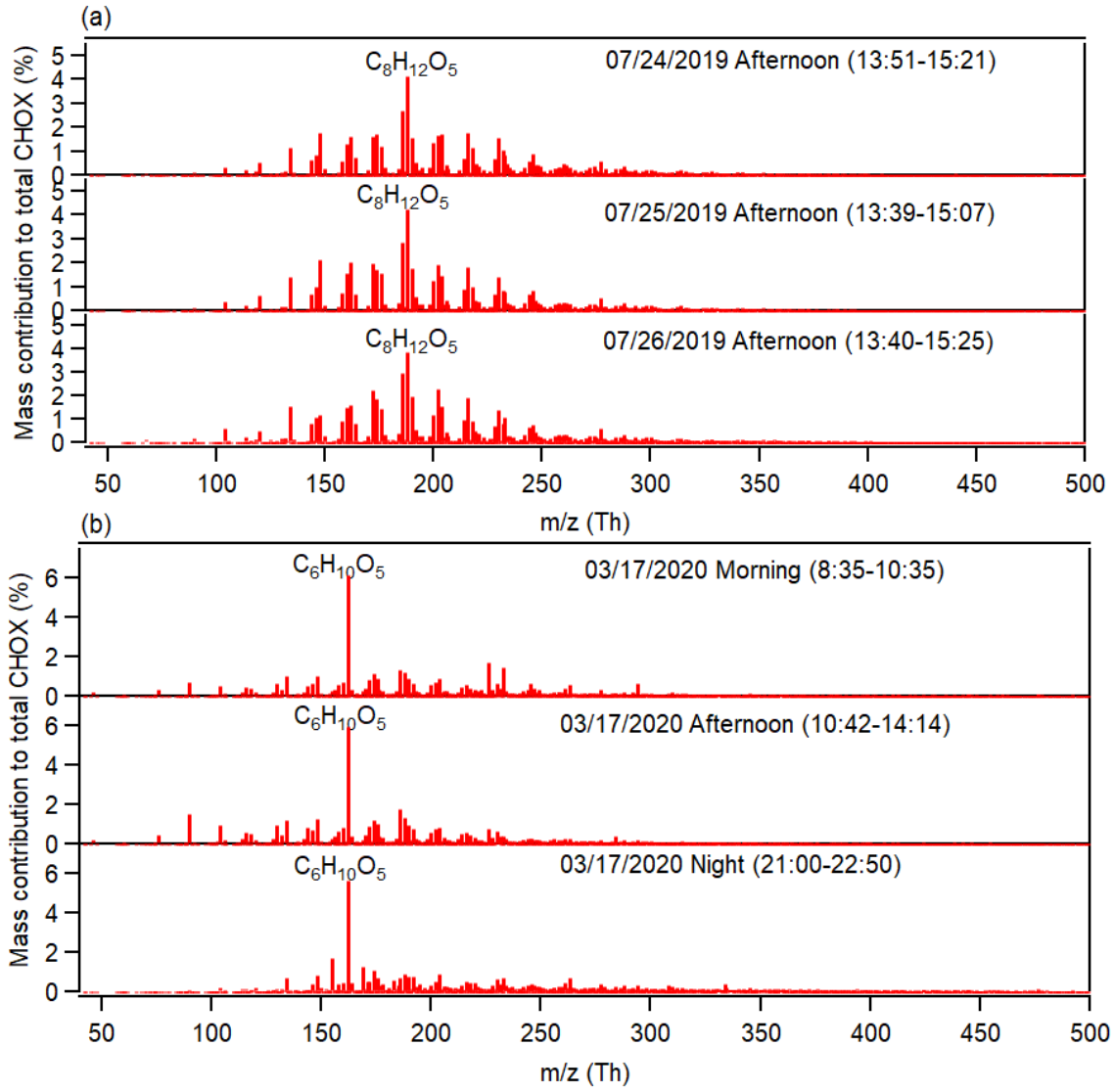

Figure S12. CIMS mass spectra of CHOX compounds including CHO and CHON in selected filter samples collected during summer heatwave episode (a) and winter transitional episodes (b) as a function of m/z (exclude mass of I- ion at m/z 126.9050 Th). Mass contributions of each compound are normalized to the sum of the mass of all detected CHOX compounds. The most abundant compounds are marked.

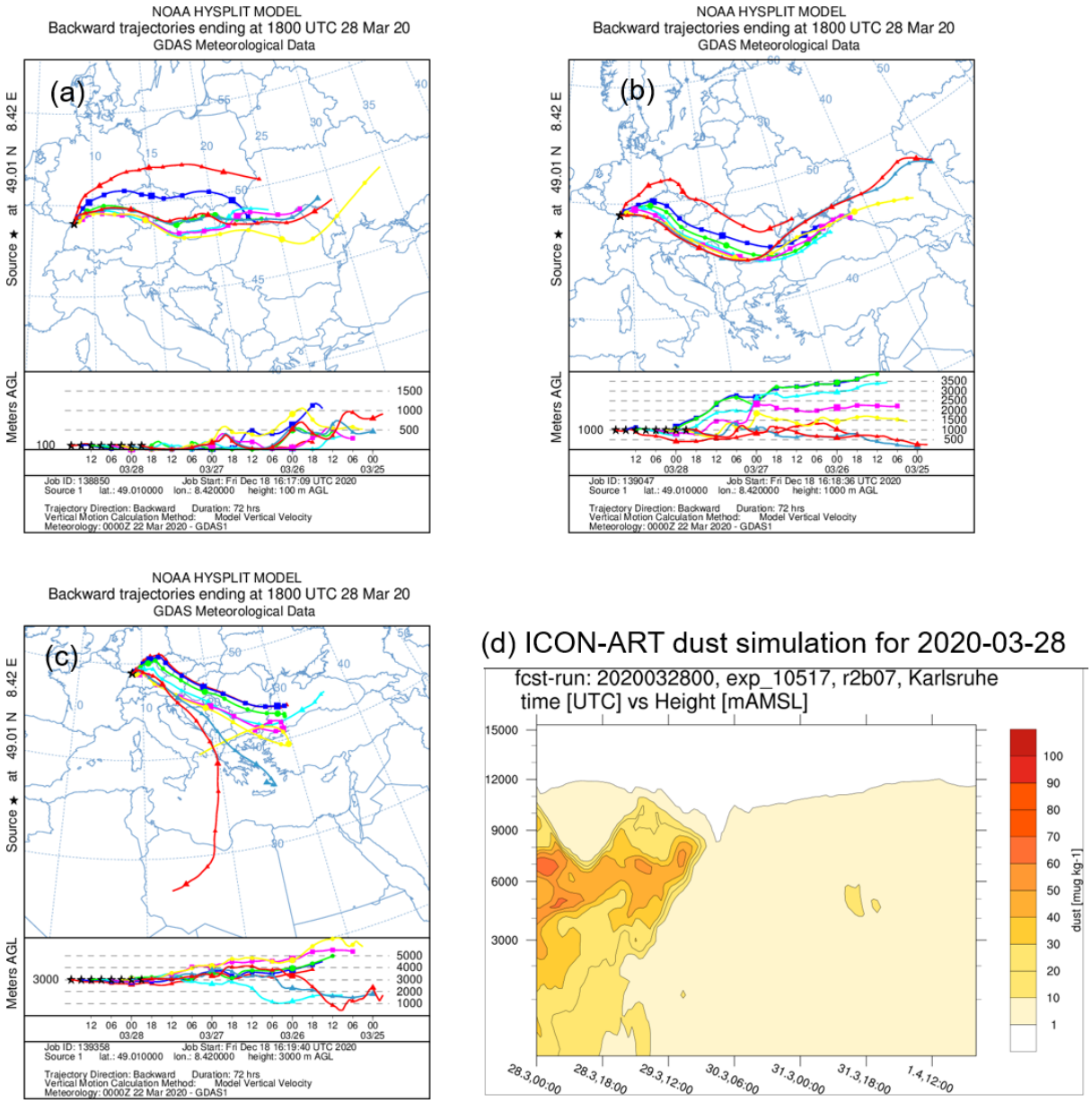

Figure S13. Three-day air mass back-trajectories at different arrival heights of (a) 100 m, (b) 1000 m and (c) 3000 m for the measurement site on March 28th, 2020. (d) Image of an ICON-ART simulation (Rieger et al., 2017) predicting Saharan dust over Karlsruhe provided by Heike Vogel, personal communication.

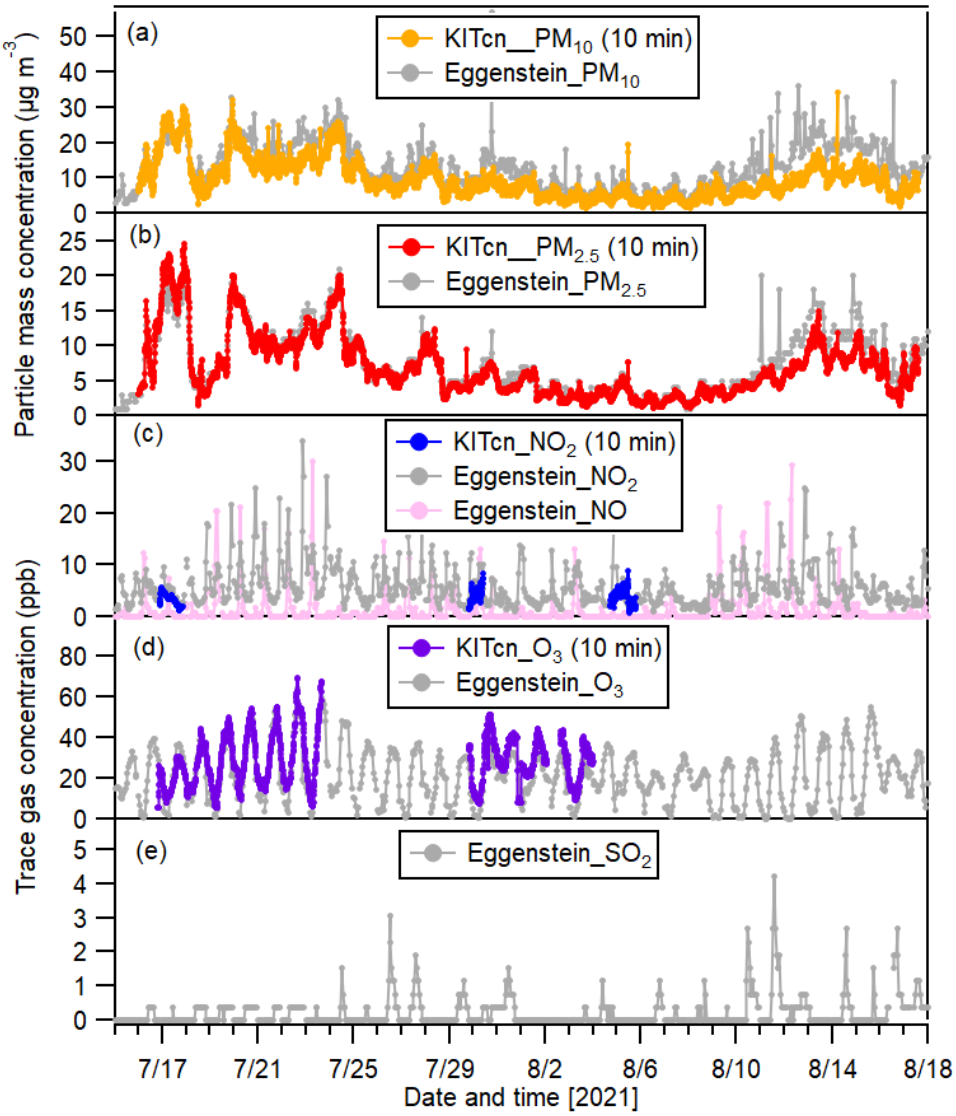

Figure S14. Time series of (a) PM_{10}, (b) $PM_{2.5}$, (c) NO_2 and NO, (d) O_3 and (e) SO_2 observed at the sampling site (KITcn) and Eggenstein air quality monitor station during the measurement period. The trace gas data of NO_2 and O_3 are only available for few days due to the multifunction

of instrument acquisition software.

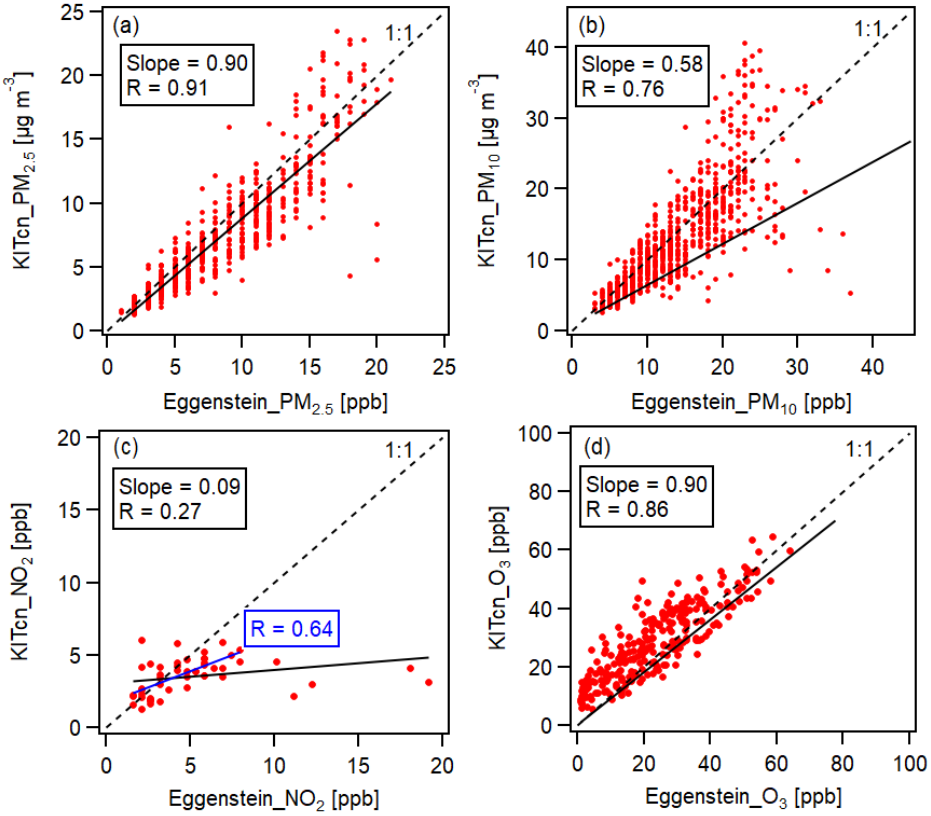

Figure S15. Scatter plots for (a) $PM_{2.5}$, (b) PM_{10}, (c) NO_2 and (d) O_3 measured at the sampling site (KITcn) and Eggenstein air quality monitor station during the measurement period. The black solid and dash lines represent the linear fit curve and 1:1 line respectively, and the blue solid line in (c) shows the linear fit curve after removing high NO_2 values (>10 ppb) observed at Eggenstein monitor station.

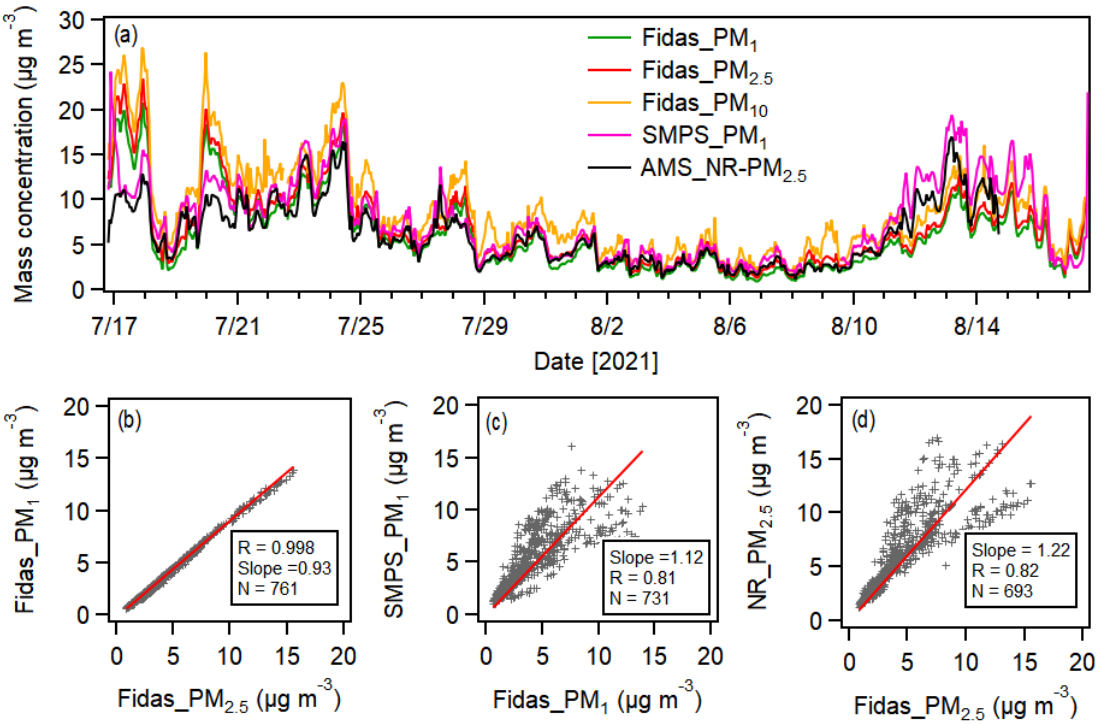

Figure S16. (a) Time series of PM_1, $PM_{2.5}$, PM_{10} measured by the Fidas200 along with the PM_1 calculated from SMPS measurement (density of 1.4 g cm-3) and the NR-$PM_{2.5}$ measured by the AMS. (c-d) scatter plots between Fidas_PM_1 vs. Fidas_$PM_{2.5}$, Fidas_PM_1 vs. SMPS_PM_1 and Fidas_$PM_{2.5}$ vs. AMS_NR-$PM_{2.5}$ during the entire measurement period.

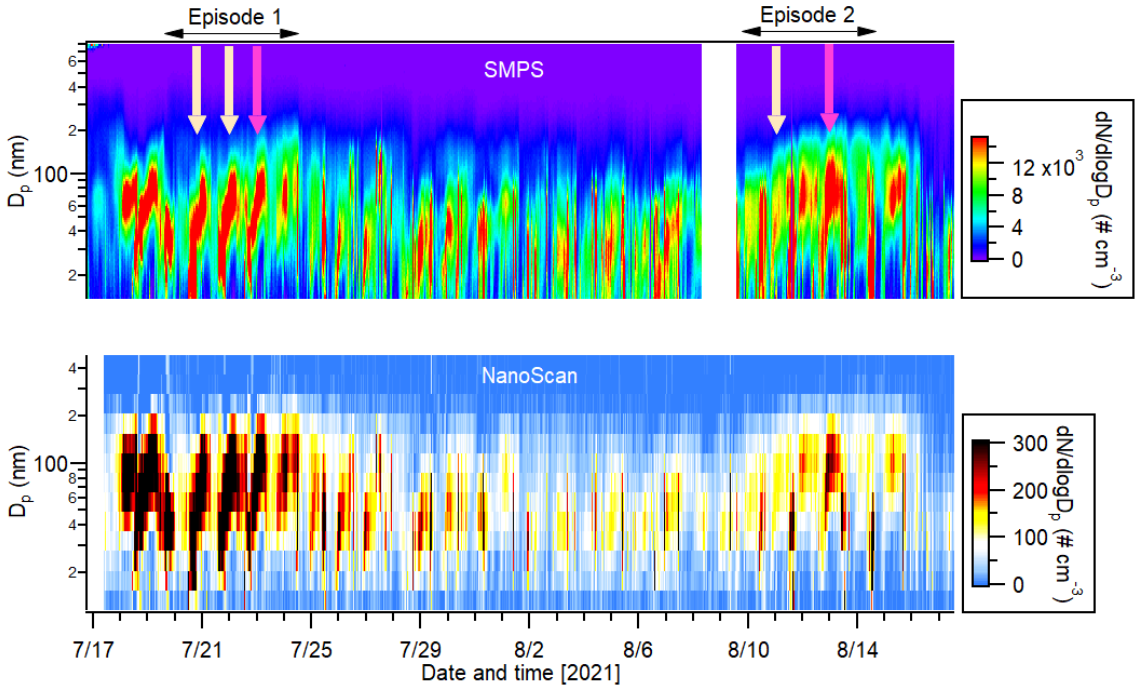

Figure S17. Particle size distribution obtained from SMPS (top panel) and NanoScan (bottom panel) during three periods. The arrows show the particle growth events during nighttime.

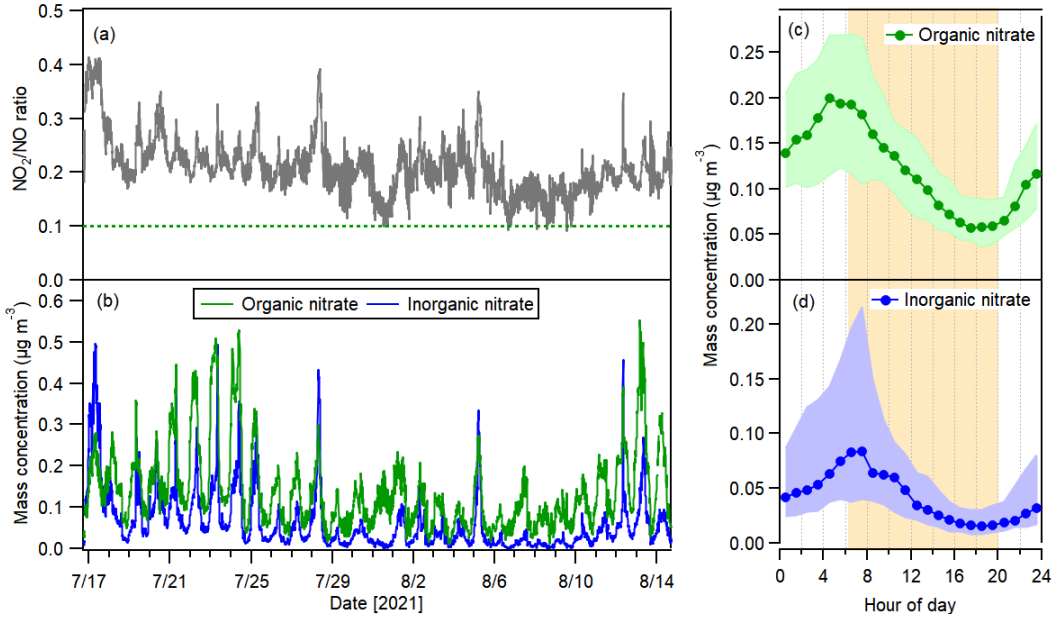

Figure S18. (a) Time series of NO_2^+/NO^+ ratios for total nitrate (green dash line represents a threshold value of 0.1 indicating the organic nitrate fragmentation by the AMS); (b) Time series of the resolved organic and inorganic nitrate. (c-d) diurnal variations of organic nitrate and inorganic nitrate.

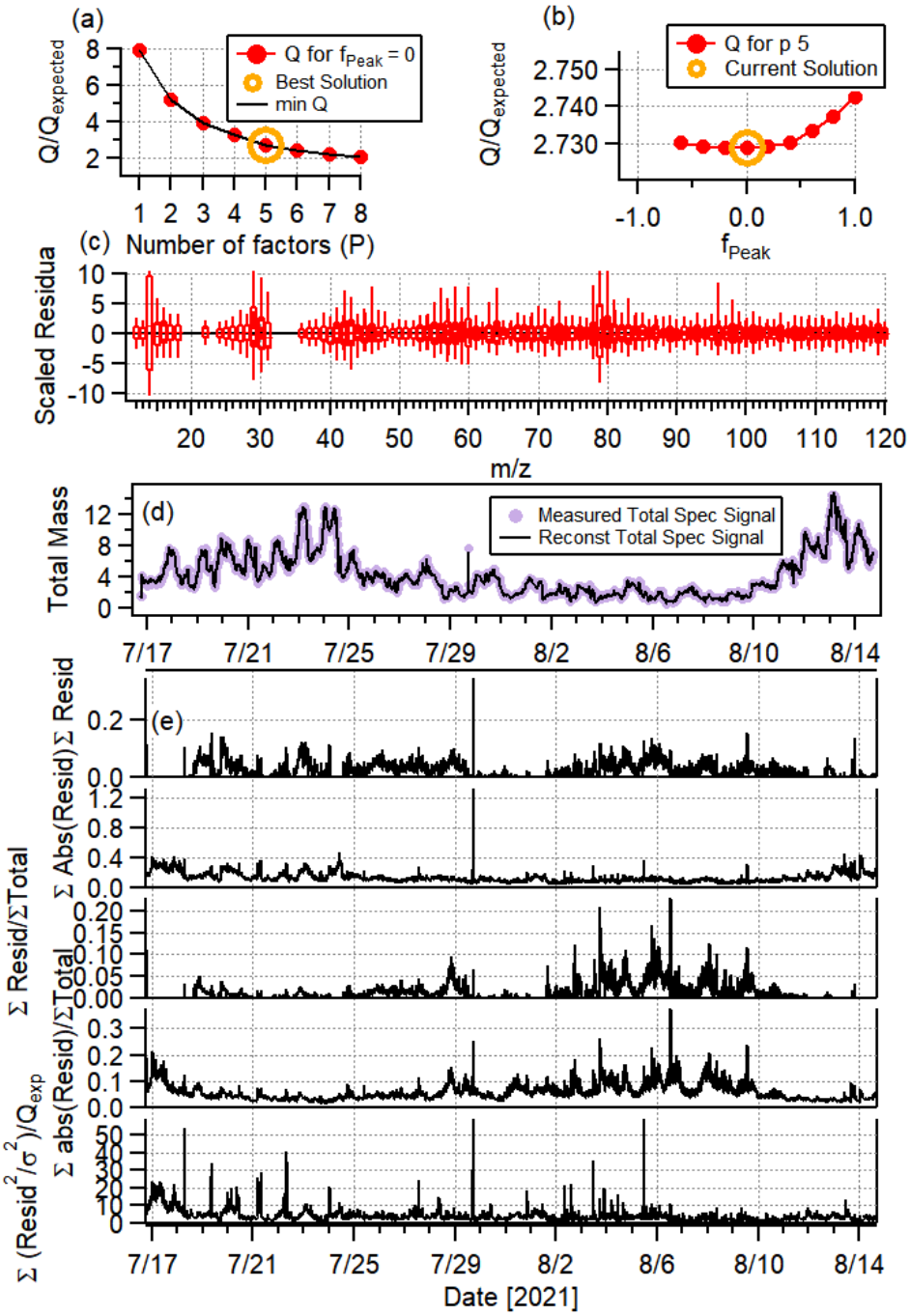

Figure S19. Key diagnostic plots for 5-factor PMF solution of organic aerosol: (a) $Q/Q_{expected}$ as a function of number of factors (P); (b) $Q/Q_{expected}$ as a function of f_{Peak};(c)) the box and whiskers plot showing the distributions of scaled residuals for each m/z; (d) time series of the measured organic mass and the reconstructed organic mass and (e) time series of variations of the residual values (= measured-reconstructed) of the fit.

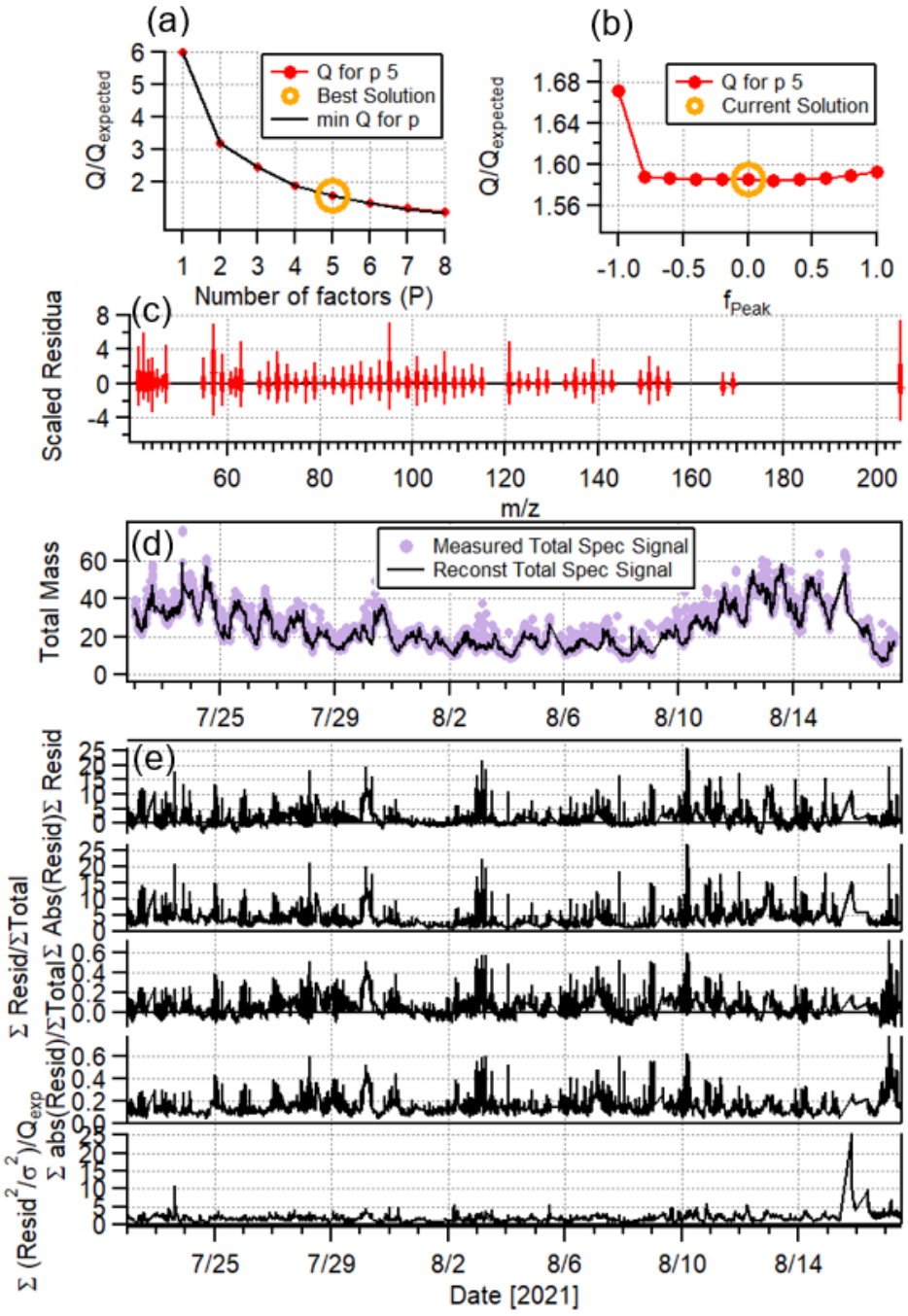

Figure S20. Key diagnostic plots for 5-factor PMF solution of VOCs: (a) $Q/Q_{expected}$ as a function of number of factors (P); (b) $Q/Q_{expected}$ as a function of f_{Peak};(c)) the box and whiskers plot showing the distributions of scaled residuals for each m/z; (d) time series of the measured organic mass and the reconstructed organic mass and (e) time series of variations of the residual values (= measured-reconstructed) of the fit.

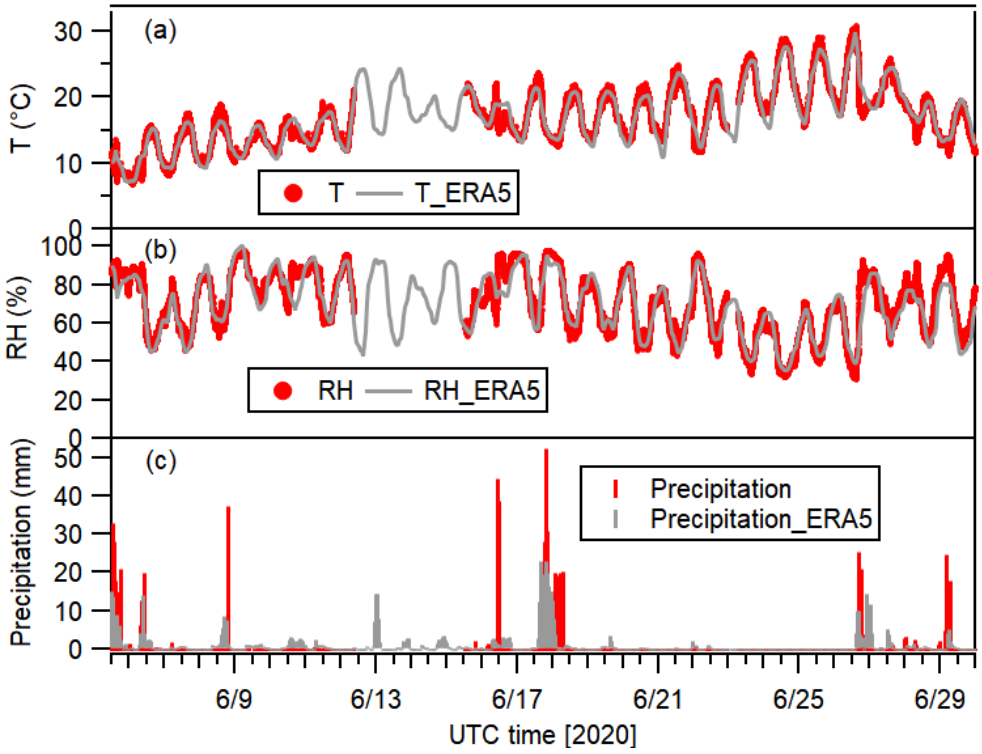

Figure S21. Comparison of meteorological parameters obtained from the meteorological sensor measurement and the ERA5 reanalysis data. (a) temperature, (b) relative humidity and (c) precipitation.

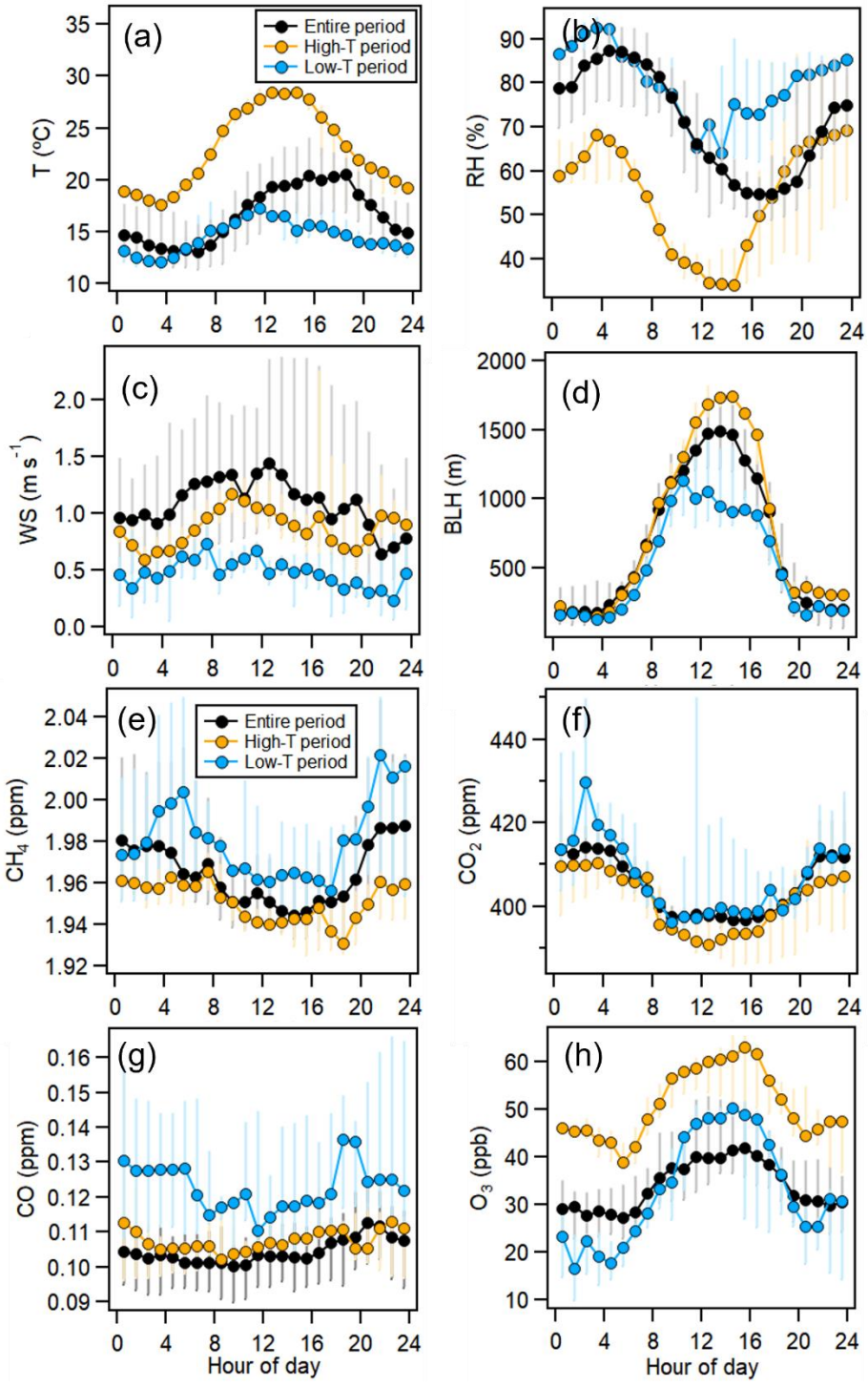

Figure S22. Median diurnal variations of T, RH, WS and boundary layer height, CH_4, CO_2, CO and O_3 during the entire, low- and high-temperature periods.

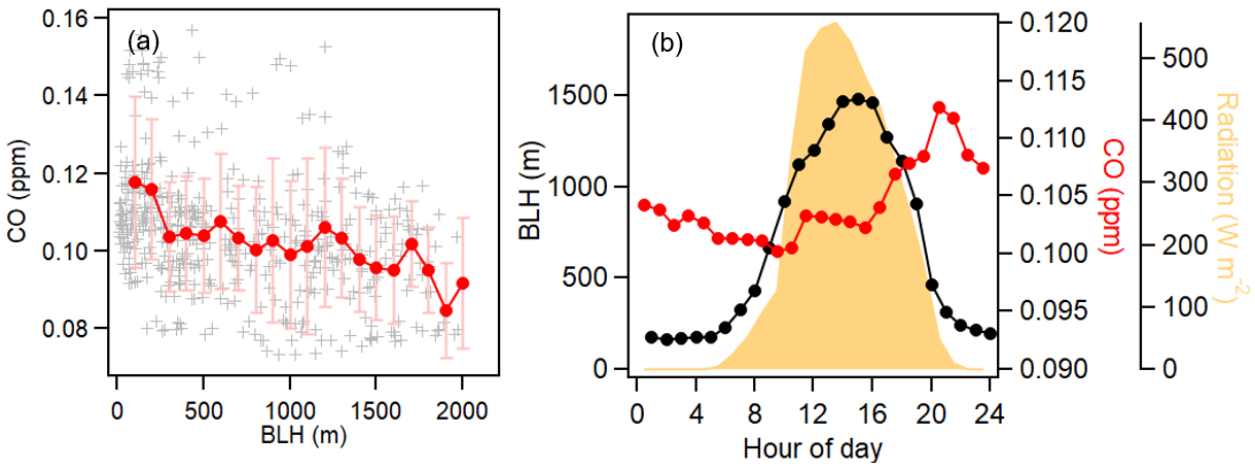

Figure S23. (a) Scatter plot of boundary layer height and CO concentrations. The data were binned with a BLH of 100 m, showing the mean ± 1σ in each bin (red) and (b) median diurnal variations of BLH, CO and radiation during the entire measurement period.

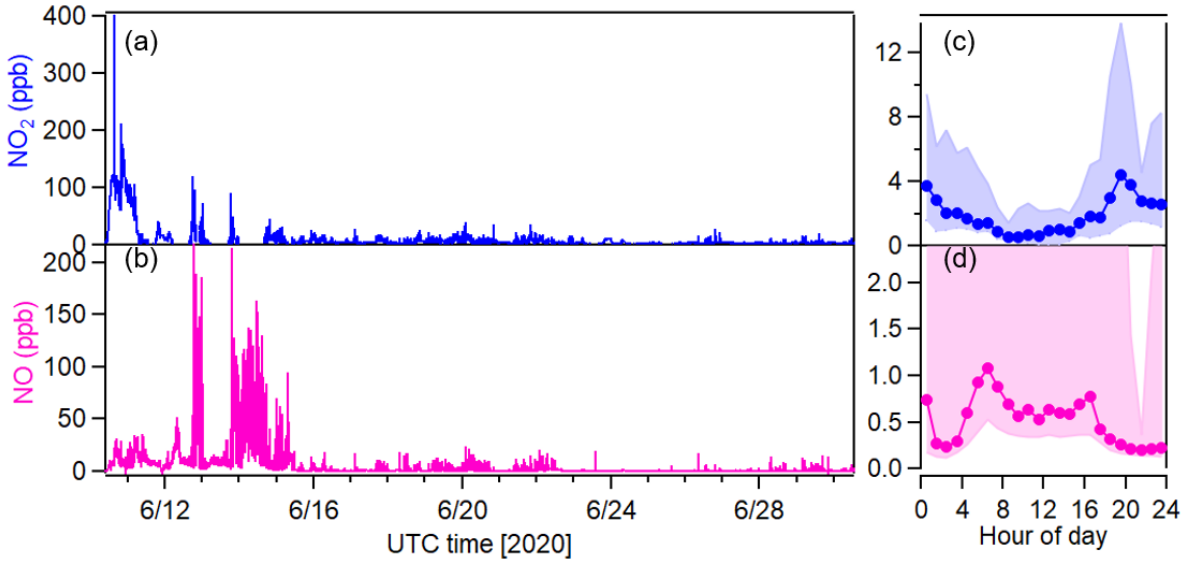

Figure S24. Time series of raw NO_2 and NO concentrations (a-b) and their median diurnal variations (c-d). Extremely high concentrations of NO_2 and NO (>100 ppb) show the errors of instrument.

Appendix B- List of publications during my PhD study

[1] **Song, J.,** Saathoff, H., Gao, L., Gebhardt, R., Jiang, F., Vallon, M., Bauer, J., Norra, S., Leisner, T., 2022. Variations of $PM_{2.5}$ sources in the context of meteorology and seasonality at an urban street canyon in Southwest Germany. Atmos. Environ. 282, 119147.

[2] Gao, L., **Song, J.,** Mohr, C., Huang, W., Vallon, M., Jiang, F., Leisner, T., Saathoff, H., 2022. Kinetics, SOA yields, and chemical composition of secondary organic aerosol from β-caryophyllene ozonolysis with and without nitrogen oxides between 213 and 313 K. Atmos. Chem. Phys. 22, 6001-6020.

[3] Vallon, M., Gao, L., Jiang, F., Krumm, B., Nadolny, J., **Song, J.,** Leisner, T., Saathoff, H., 2022. LED-based solar simulator to study photochemistry over a wide temperature range in the large simulation chamber AIDA. Atmos. Meas. Tech. 15, 1795-1810.

[4] Bertozzi, B., Wagner, R., **Song, J.,** Höhler, K., Pfeifer, J., Saathoff, H., Leisner, T., Möhler, O., 2021. Ice nucleation ability of ammonium sulfate aerosol particles internally mixed with secondary organics. Atmos. Chem. Phys. 21, 10779-10798.